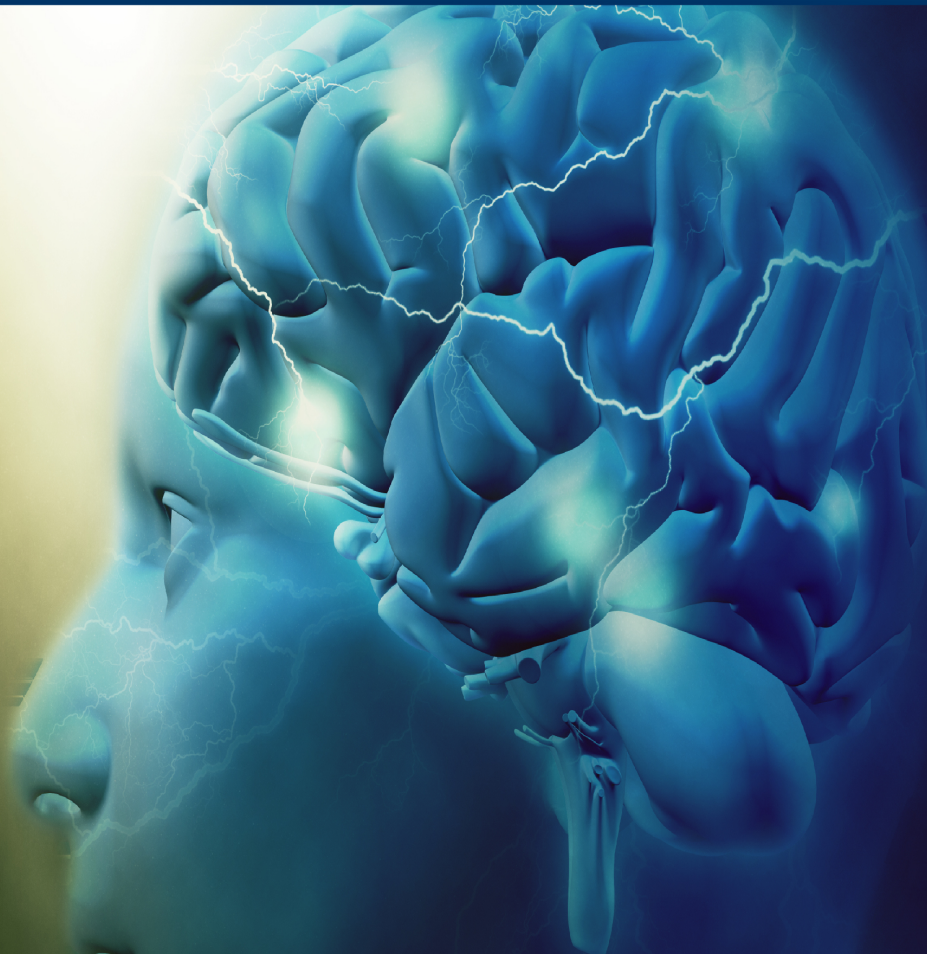


**PROCEEDINGS OF THE
3rd INTERNATIONAL CONFERENCE ON
BIOSIGNALS, IMAGES AND INSTRUMENTATION
16th - 18th MARCH, 2017**



ICBSII-2017

**DEPARTMENT OF BIOMEDICAL ENGINEERING
IN ASSOCIATION WITH
CENTRE FOR HEALTHCARE TECHNOLOGIES**

SSN COLLEGE OF ENGINEERING

OLD MAHABALIPURAM ROAD
KALAVAKKAM - 603110
TAMILNADU, INDIA

2017 International Conference on Biosignals, Images and Instrumentation (ICBSII - 2017)

Copyright © 2017 by the Institute of Electrical and Electronics Engineers, Inc. All rights reserved.

Copyright and Reprint Permission

Abstracting is permitted with credit to the source. Libraries are permitted to photocopy beyond the limit of U.S. copyright law, for private use of patrons, those articles in this volume that carry a code at the bottom of the first page, provided that the per-copy fee indicated in the code is paid through the Copyright Clearance Center, 222 Rosewood Drive, Danvers, MA 01923.

Other copying, reprint, or reproduction requests should be addressed to IEEE Copyrights Manager, IEEE Service Center, 445 Hoes Lane, P.O. Box 1331, Piscataway, NJ 08855-1331.

IEEE Catalog Number CFP17K33-USB

ISBN 978-1-5090-4979-0

Additional copies of this publication are available from

Curran Associates, Inc.

57 Morehouse Lane

Red Hook, NY 12571 USA

+1 845 758 0400

+1 845 758 2633 (FAX)

Email: curran@proceedings.com

Proceedings of the



3rd International Conference on
Biosignals, Images and Instrumentation
Department of Biomedical Engineering,
SSN College of Engineering



In association with

Centre for Healthcare Technologies

ICBSII - 2017
(16th – 18th March 2017)

Editorial Board

Chief Editor: Dr. A. Kavitha, Prof & HoD/BME

Co- Editors:

Ms. Delpha J. AP/BME

Ms. Laxmi N. AP/BME

Contents

Message from the Chief Patron	VII
Mrs. Kala Vijayakumar, President, SSN Institutions	
Message from the Patron	VIII
Dr. S. Salivahanan, Principal, SSN College of Engineering	
Convener's Message	IX
Dr. A. Kavitha, Professor & Head, BME	
Message from the Coordinators	X
Mrs. M. Dhanalakshmi AP/BME, Mrs. R. Nithya AP/BME	
Conference Organizing Committee	XII
Technical Advisory Committee	XIII
Review Committee	XIV
Student Organizing Team	XV

Chief Guest's Profile

Mr. Omar Saleh, Founder & CEO, Recycl3D	XVIII
Ms. Nicole McCallum, Executive Director, Recycl3D	XVIII

Keynote Speakers

Dr. G. Sudhir	XX
Biomedical engineering and spine surgery - where we are and what is the future	
Dr. Laxmi Iyer	XXI
Expanding horizons in the Biomedical Sciences	
Dr. Devanathan Raghunathan	XXII
My Journey across Academia and Entrepreneurship: Lessons Learnt	
Dr. Debdot Sheet	XXIII
Domain Adaptation for Learning with Interdependent and Non-Identically Distributed Data	
Mr. Hrushikesh Garud	XXIV
Methods of Segmentation for diagnosis of breast cancer cytology – An Integrated Image Pre-Processing and Nucleus Segmentation System	

Research Papers

1. Combinational neuro fuzzy and erosion rule based filter for detection and reduction of impulse noise	1
Rashmi Kumari, Anupriya Asthana, Vikas Kumar.....	
2. Thermal imaging based breast cancer analysis using BEMD and uniform RLBP	7
Vijaya Madhavi, T. Christy Bobby.....	
3. Diagnosis of diabetic retinopathy using texture features extracted from SLO images	14
Sri Vidhya. S, Kathirvelu. D.....	
4. Detection of Tuberculosis Bacilli from microscopic sputum smear images	19
Evangelin Sugirtha. G, Murugesan. G.....	
5. An fNIRs study to classify stages of learning from visual stimuli using prefrontal hemodynamics	25
Amiyangshu De, Amit Konar, Amalesh Samanta, Souvik Biswas, Piyali Basak.....	
6. Effect of disturbance in working memory performance: An fNIRs study	32
Souvik Biswas, Amiyangshu De, Amit Konar, Piyali Basak.....	
7. Retinal blood vessel extraction using graph tracer algorithm	38
Hepsiba.D, L.D.Vijay Anand.....	
8. An efficient clustering technique and analysis of infrared thermograms	42
R. Vishnupriya, N. Sri Madhava Raja, V.Rajinikanth.....	
9. Estimation of femur morphometric features for CBIR application	47
T. Christy Bobby.....	
10. Histogram Shifting Based Reversible Data Hiding With Controlled Contrast Enhancement	52
V.R.Vijay Kumar, V. Suresh Babu.....	
11. Contrast enhanced brain tumor segmentation based on Shannon's entropy and active contour	58
Priyadarshini. C, Nithysri. V, Pavithra. G, Sri Madhava Raja. N.....	
12. Feature extraction and analysis of renal abnormalities using fuzzy clustering segmentation and SIFT method	62
Aadhirai. S, Najumnissa Jamal.D.....	

13. Evaluation of symmetry plane using Genetic algorithm	
D. Chitradevi, Dr. S. Prabha	68
14. Geometric nonlinear diffusion filter based edge-map extraction and its validation of infrared breast images	
J ThamilSelvi, G Kavitha, C M Sujatha.....	73
15. A Versatile Hand Grip Design for Concise Arm and Hand Rehabilitation Robot for Stroke Patients	
Arnon Nontapha, Wimol San-Um	78
16. Development of thermistor based low cost high sensitive respiration rate measurement system using audio software with audio input	
Tarak Das, Sayanti Guha, Nisha Banerjee, Piyali Basak....	82
17. Quadcopter based technology for an emergency healthcare	
A. Josephin Arockia Dhivya, Dr. J. Premkumar.....	85
18. Development of real time ECG signal monitoring system for telemedicine application	
Mr.S.Bashyam. Dr.B.Ramachandran.....	88
19. Hairbrush for psoriasis scale removal	
Ravi kant kumar, Eunice Esther Lovely, M.Arпита Kshirsagar, Dr. J.B.Jeeva	92
20. Design of contactless power transfer for artificial heart	
Lidhiya Daniel, Thukkaram Sudhakar, Sheeba Abraham.....	95
21. Embedding pressure sensor in a footwear for checking the weight distribution during standing	
Nikita Ghosh, Saheli Guha, Sharmila Nageswaran	98
22. Experimental investigations on capacitive imaging of biological materials	
A. S. Sahana, A. Paramasivam, K. Kamalanand	102
23. FPGA based emotions recognition from speech signals	
B. Rajasekhar, M. Kamaraju, V. Sumalatha....	105
24. A study to differentiate normal and hypertensive subjects based on dynamic thermogram features	
Jayashree Ramesh, Dr.Jayanthi Thiruvengadam....	108
25. Analysis of neuromuscular control in human arm	
Jan Thomas, P.Vinupritha.....	112

26. Preliminary big data analytics of hepatitis disease by Random Forest and SVM using R- Tool	
Visali Lakshmi.P.R, Shwetha.G, N.Sri Madhava Raja.....	117
27. Finite Element Analysis of Palmaz –Schatz Stent and Express Stent Using Three Dimensional Models	
Keerthana. S, Visalakshi.Cho	122
28. A preliminary study on the control of nano acrylamide polymerization reaction	
N. Priyadharshini, Kamalanand K... ..	125
29. A study on time and frequency domain analysis of two class motor imagery signals	
S. Sridevi, P. Karthikeyan, S. Ramakrishnan.....	127
30. Selection of dominant voice features for accurate detection of parkinson’s disease	
Spriha Chandrayan, Aarushi Agarwal, Mohammad Arif, Sitanshu S.Sahu.....	133
31. EEG signal analysis using sparse approximations	
Palakurthi Ravali, J.Sheshagiri Babu.....	137
32. Impact assessment of mental subliminal activities on the human brain through neurofeedback analysis	
Munyaradzi C. Rushambwa, Asaithambi Mythili	142
33. Diagnosis of Epilepsy- A systematic review	
Vetrikani.R, T.Christy Bobby.....	148
34. A Review on Systemic Approach of the Ultra Sound Image to Detect Renal Calculi Using Different Analysis Techniques	
V.Velmurugan, M.Arunkumar, P.Gnanasivam.....	153

*Dedicated
to
all Staff and Students
of
the Department of
Biomedical Engineering*

From the Chief Patron

Mrs. Kala Vijayakumar

President, SSN Institutions



The SSN Group of Institutions provide a variety of stimulating environment for intellectual development, free-thinking and personal growth, challenging its students with dynamic learning opportunities and equipping them with the skills, insights, attitudes and practical experiences. Every aspect of SSN, from the campus to library is aimed at ensuring holistic development of its students. Programs offered at our college nurture qualities like leadership, kinship, discipline, organizational skills and managing diverse opinions, thoughts and point of view.

Biomedical Engineering as a discipline is truly multi-disciplinary and offers varied research avenues. The importance is two-fold when the technology is linked with healthcare. Taking cognizance of this fact, the BME department's initiative to host an International Conference certainly deserves appreciation.

With these few words, on behalf of the SSNCE administration, I congratulate BME and wish that the conference instill new thinking among the audience.

Mrs. Kala Vijayakumar
Chief Patron, ICBSII – 2017.

From the Patron

Dr. S. Salivahanan

Principal, SSN College of Engineering



The SSN Group of Institutions is ranked high among India's leading educational institutions providing quality education to students from all strata of society. The college aims towards not just developing knowledge but also instilling the right attitude and skills in the students for a holistic education relevant in a globalized context.

Biomedical Engineering is indeed a holistic discipline and successfully integrates engineering technology with healthcare. Diverse activities including the students and faculty have always strengthened the department in various aspects.

To add feather to the crown, the department is organizing the 3rd International Conference on Biosignals, Images and Instrumentation in a manner befitting the stream. I congratulate the entire team of biomedical department for planning this to perfection and wish them all success.

Dr. S. Salivahanan
Patron, ICBSII – 2017.

From the Convener

Dr. A. Kavitha

Professor & Head,
Department of Biomedical Engineering
SSN College of Engineering



It is with humongous pride that I present the 3rd International Conference on Bio-signals, Images and Instrumentation. To simply state that this feeling is shared by my colleagues and students would amount to a gross understatement. Words, however, can only achieve so much.

Biomedical engineering discipline is one which catalyzes interactions between biologists, physical scientists, and engineers to benefit medicine and human health. This serves society by conducting research that develops quantitative linkages across scales in the human body and uses that development to build new tools to improve human health. The outcomes of research assume a whole new level of importance and significance.

The department is frequently organizing workshops, seminars, project exhibitions and guest lectures on diverse concepts related to the core and inter-disciplinary subjects in biomedical engineering to equip the students in gaining a comprehensive knowledge of the industrial requirements to the fullest. Another event worthy of mention is the annual technical symposium 'Srishti' which is a repeat success. The department also publishes 'Synergy' a quarterly newsletter, accommodating the diverse activities happening in the department.

The 3rd International Conference on Bio-signals, Images and Instrumentation organized by SSN College of Engineering, is a multi-disciplinary academic event aimed at bridging the industry institution gap. The conference provides a platform for academics, students, clinicians and researchers to observe, discuss and showcase advancements in biomedical research.

They say teamwork divides the tasks and multiplies the success. I hope that the success of the conference instills a new exemplar in academia.

Dr. A. Kavitha
Convener, ICBSII – 2017.

From the Coordinators

Mrs. M. Dhanalakshmi

Assistant Professor,
Department of Biomedical Engineering
SSN College of Engineering



The International Conference will provide a wonderful forum to unveil the efforts of researchers, engineers and scholars.

This conference serves as a platform for various disciplines of medicine, engineering and healthcare and software in a single venue to elevate the medical and healthcare industry to generate standards, the academic programme provides great opportunity to share knowledge and wisdom with the eminent speakers from the world.

I extend my sincere gratitude to the management of SSN College of Engineering, Mrs.Kala Vijayakumar, President, SSN Institutions and Dr.S.Salivahanan, Principal, SSN College of Engineering for granting the department a wondrous opportunity to organize and conduct this prolific occasion helping us to take it forward to the global level.

Mrs. M. Dhanalakshmi
Secretary, ICBSII – 2017.

From the Coordinators

Mrs. R.Nithya

Assistant Professor,
Department of Biomedical Engineering
SSN College of Engineering



The aim of this International Conference is to create a platform for the exchange of ideas and spread of knowledge.

It is also aimed at emphasizing the advancements and current trends in the industry to make the undergraduate students converge their ideas in terms of project and project development.

The conference turned out to be a forum for scientists and researchers all over the world to share their ideas, experiences, findings and conclusions of their work in due course of their scientific research.

I extend my sincere gratitude to the management of SSN College of Engineering, Mrs.Kala Vijayakumar, President, SSN Institutions and Dr. S. Salivahanan, Principal, SSN College of Engineering for granting the department a wondrous opportunity to organize and conduct this prolific occasion helping us to take it forward to the global level.

Mrs. R. Nithya
Secretary, ICBSII – 2017.

Conference Organizing Committee

Chief Patron

Ms. Kala Vijayakumar, President, SSN Institutions

Patron

Dr. S. Salivahanan, Principal, SSN College of Engineering

Convener

Dr. A. Kavitha, Professor and HOD/BME

Coordinators

Mrs. M. Dhanalakshmi

Mrs. R. Nithya

Committee Members

Dr. V. Mahesh

Dr. S. Pravin Kumar

Dr. S. Guruprakash

Dr. L. Suganthi

Dr. R. Sivaramakrishnan

Dr. Sachin Gaurishankar Sarate

Mrs. B. Geethanjali

Dr. R. Subashini

Mrs. K. Nirmala

Mrs. J. Delpha

Mrs. N. Laxmi

Mrs. B. Divya

Mrs. Richa Malviya

Technical Advisory Committee

International Advisory Committee Members

- **Dr. Dinesh P Mital, Prof., Rutgers University, USA**
- **Dr. Steven Roodenrys, Prof., University of Wollongong, Australia**
- **Dr. Palaniappan Ramaswamy, Prof., University of Kent, UK**
- **Dr. Ram Chander Cheypala, PDF, Massachusetts Institute of Technology, USA**

National Advisory Committee Members

- **Dr. S. Ramakrishnan, Prof., IIT Madras**
- **Dr. Alok Ray, Prof., AIIMS Delhi**
- **Dr. Ramesh. R. Galigekere, Prof.& Head, BME, Manipal University**
- **Dr. Kumar Rajamani, Manager (Technical), Robert BOSCH, Bangalore**
- **Mr. Ranjith, Principal, Madras ENT Research Foundation (MERF), Chennai**
- **Dr. Hrushikesh Garud, Tech Lead, Texas Instruments, Bangalore**
- **Dr. Debdoot Sheet, Asst. Prof., IIT, Karagpur**

Review Committee

- **Dr. U.S Ragupathy**- Prof. and Head, Dept. of EIE, Kongu Engineering College, Erode
- **Dr. Christy Bobby Senthil** – Assoc. Prof , MS Ramaiah University, Bangalore
- **Dr. Mythili** – Assoc. Prof., VIT Vellore campus
- **Dr. G. Kavitha**- Asst. Prof (Sr. Grade), MIT, Anna University, Chennai
- **Dr. C. M. Sujatha**- Asst. Prof. (Senior Grade), Anna University, Chennai
- **Dr. K. Kamalanand** – Asst. Prof. – Instrumentation, MIT, Anna University, Chennai
- **Dr. Kayalvizhi** - HOD/BME, Agni College of Engineering, Chennai
- **Dr. Sri Madhavaraja N** - Assoc. Prof., St.Joseph's College Of Engineering, Chennai
- **Dr. A. Kavitha** – Prof. and HOD/BME, SSN College of Engineering, Chennai
- **Dr. N. Venkateswaran** - Prof., ECE, SSN College of Engineering, Chennai
- **Dr. PravinKumar. S** - Assoc. Prof, BME ,SSN College of Engineering, Chennai
- **Dr. Mahesh.V**- Assoc. Prof, BME , SSN College of Engineering, Chennai
- **Dr. Suganthi. L** - Assoc. Prof, BME ,SSN College of Engineering, Chennai
- **Dr. S. Karthika** - Assoc. Prof, IT, SSN College of Engineering, Chennai
- **Dr. Partibane. B** - Asst. Prof, ECE,SSN College of Engineering, Chennai
- **Mrs. K. Nirmala** - Asst. Prof, BME , SSN College of Engineering, Chennai
- **Mr. C. Vinoth Kumar** - Asst. Prof, ECE,SSN College of Engineering, Chennai

Student Organizing Team

Registration:

- Madhumithra S. K. - Final Year, UG
- Madhuvanathi S. - Final Year, UG
- Krriti R. - Final Year, UG
- Rosheema Bala J. B. - Final Year, UG
- Meena Nisha M. - Third Year, UG
- Viswanath S. - Second Year, UG

Conference Proceedings:

- Diana Chris A. – Final Year, PG
- Vaishalini Venkatraman – Final Year, PG
- Vardhini P. – Final Year, PG
- Vishnu Priya K. – Final Year, PG
- Chitra R. - Final Year, UG
- Mohamed Ajmal R. - Final Year, UG
- Surya Prakash D. - Final Year, UG
- Vijay ManiShankar L. - Third Year, UG
- Santhana Lakshmi A. - Third Year, UG
- Rathi Adarshi R. - Third Year, UG
- Kiran Kailash S. - Third Year, UG
- Haripriya R. - Third Year, UG
- Anjali S. - Third Year, UG

Accommodation:

- Monica A. - Final Year, UG
- Ganesh Kumar D. - Final Year, UG
- Thamizhamuthan S. - Final Year, UG
- Pragadeesh T. - Third Year, UG
- Annamalai M. - Third Year, UG
- Yaamini D. - Second Year, UG
- Prasanthini Palani Velu - Second Year, UG

Food Committee:

- Vaibhav M. - Final Year, UG

- Ganesh Kumar D. - Final Year, UG
- Gokularam I. - Third Year, UG
- Nithin Manoj- Third Year, UG
- Praveen Kumar G. - Second Year, UG

Hall Arrangements:

- Prathyusha R. - Final Year, UG
- Aathira Haridas - Final Year, UG
- HariPriya R. - Third Year, UG
- Om Prakash S. - Second Year, UG

Transport Arrangements:

- Sugirtha K.P.S.G. – Final Year, PG
- Mohamed Ajmal R. - Final Year, UG
- Gopichandran R. - Final Year, UG
- Chandramouli R. - Final Year, UG
- Balaraman D. - Third Year, UG
- Ashok Kumar S. K. - Third Year, UG

Culturals:

- Nova Belle P. N. - Final Year, UG
- Manasvi S. - Third Year, UG
- Pushpika S. - Third Year, UG

Momento:

- Divya Raghavi N. - Third Year, UG
- Sai Aarthi Ganesh- Third Year, UG

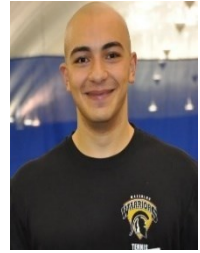
**3rd International Conference on Bio
Signals,
Images and Instrumentation
ICBSII 2017**

CHIEF GUESTS' PROFILE

The Chief Guests

Mr. OMAR SALEH

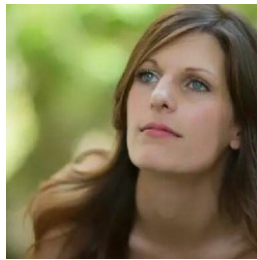
*Founder and CEO- RECYCL-3D
Calgary, Alberta, Canada.*



PROFILE:

Omar Saleh earned his B.A.Sc. in chemical engineering from the University of Waterloo in 2014. He is currently a Process EIT, Upstream Major Projects, Horizon Oil Sands.

The Horizon Engineering Solutions has a collaboration with SSN College of Engineering. The current consulting project with our college is *3D Prosthetic limb design and characterization*. The main objective of the project is to design a low cost prosthetic limb. Innovative ideas are incorporated which is not seen in the usual available prosthetic limbs. Many under graduate and post graduate students are working on the project.



Ms. NICOLE MCCALLUM

*Executive director- RECYCL-3D
Calgary, Alberta, Canada.*

PROFILE:

She received her Bachelor of Arts degree in Economics and Global studies from Wilfrid Laurier University and Masters' degree in Economics from Queen's University in 2010 and 2012 respectively.

Currently, she is a Sessional Lecturer in the College of Management and Economics (CME) at the University of Guelph. She received the Tri-Council Recognition award for attaining the honour of a SSHRC scholarship in 2010 from Queen's University. She has also received the Fitzroy, Badal and Ibrahim Education Award for her leadership and academic excellence and the Frank and Elsie Millerd Award in Economics for humanitarian achievement from Wilfrid Laurier University in 2010 and 2009 respectively. She has been given the Joseph-Armand Bombardier Master's Scholarship from Social Sciences and Humanities Research Council (SSHRC) for her research potential and academic performance. She has been awarded with the Audrey Joan McNiece Memorial Award for entrepreneurial and athletic leadership, innovation and achievement in 2009 from Wilfrid Laurier University.

**3rd International Conference on Bio
Signals,
Images and Instrumentation
ICBSII 2017**

KEYNOTE SPEAKERS' PROFILE

Biomedical Engineering and Spine Surgery – where we are and what is the future

Dr. G. Sudhir

Abstract:

The realm of spine surgery in India began with Lord Krishna correcting spinal deformity of his devotee as early as 3500 BC. In western world, reports for correction of spinal deformity is documented in Edwin Smith Papyrus in 1700BC. Since then the progress in the field of spine has been phenomenal in the western world but there hasn't been anything indigenously phenomenal from India.

At some point from our ancient Literature to today we have purposely removed our thinking hat and replace it with an in vogue hat and started following the crowd, unmindful of what the destiny might. Lack of trust in our literature or believing the rulers of our Land in the past, have propelled us to this point. With time we can see the reinstallation of our ancient believes in turmeric, salt, clove and coal scientifically in the western world. So it's time to remove our in vogue hat and put our thinking cap on. If we do so, we can see innumerable opportunities to create, innovate and have our own mark, especially when the potential of biomedical engineering is rightly tapped and put to use in the field of Spine Surgery.



Dr. G. Sudhir.

Spine Surgery
Fellowship in
Nottingham, QMC,
UK,
Fellow in EULAR,
Ortho Spine
Surgeon

Sudhir pursued MBBS from the Thoothukudi Government Medical College, under the Tamil Nadu Dr. MGR Medical University, and DNB in Orthopedics from the prestigious Ganga Medical Centre, Coimbatore, Tamil Nadu under National Board of Examinations. His high academic record includes many distinctions and gold medals like University second in pathology, top rank in anatomy, medicine, surgery, distinction in ophthalmology and pharmacology. He received Dr. Balu Sankaran Gold Medal for securing All India First Rank in DNB Orthopedics in 2011. To further pursue his passion, he entered FNB (Fellowship in National Board) in Spine Surgery in Sir Ganga Ram Hospital, New Delhi and excelled as the Best Outstanding Fellow. He has presented many papers, posters, and has participated in various State and National and International conferences. Currently, he is practicing in SRMC Hospital, Chennai. He is specialized to deal with all types of spinal pathologies like degenerative spinal disorders, spinal deformities, infections, tumors and fractures of spine.

Expanding Horizons in the Biomedical Sciences

Dr. Laxmi Iyer

Abstract:

Healthcare is one of the fastest growing sectors in India and globally. With the population in India expected to reach 1.4 billion by 2026, there is a vast scope for penetration and innovation. Add to that, there are a number of clinical and unmet medical needs of the ageing and burgeoning population that the country presents itself as an attractive market for entrepreneurs and investors alike.

My talk on “Expanding horizons in the biomedical sciences” will be focused on two main issues.

We live in a digitally communicated and a culturally divided world. Forced with unprecedented complexities from all corners including science and technology, this generation needs new skill sets- be it entrepreneurial skills or the ability to collaborate with others in different disciplines and culture, yet maintaining their own identity. We need to look at our biotech and biomedical science graduates and ask tough questions such as, “Are we preparing them for the world”. And what are some of the global competencies that the youth of our country requires?

I will be providing some insights on the future scope of biomedical sciences industry in the global healthcare landscape. Some of the futuristic focus areas include application of deep tech in healthcare, preventive healthcare, synthetic biology, sustainable food and needs-based innovations.



Dr. Laxmi Iyer,

Co-founder and
Managing Director
Biotechn. Asia
Singapore.

Laxmi Iyer is the Managing Editor and Co-founder of Biotechn. Asia, part of Biotech Media Pte Ltd, a Singapore-based media tech company that focuses on offering simplified, curated, fact-based news for all stakeholders in the biotech and healthcare ecosystem. She moved to Singapore from Mumbai in 2008 to do her Ph.D. in Virology from Nanyang Technological University and graduated in 2014.

During her Ph.D. she worked on the process of assembly of respiratory syncytial virus in macrophages and epithelial cells and has over 8 papers to her credit. She has been a science and conservation enthusiast all her life and was finally able to give some direction to it, when she co-founded her present company serendipitously. Rather than being the ultimate consumer of internet, she and a couple of friends decided to create good content and aimed to become the social glue of the biotech community- a one-stop solution for anyone who is looking for information related to biotech academia, industry and start-ups.

My Journey across Academia and Entrepreneurship: Lessons Learnt

Dr. Devanathan Raghunathan

Abstract:

Academia, and particularly Academic Research and Entrepreneurship are usually considered mutually exclusive and incompatible.

This talk will reflect on his experience of transitioning from research to working with startups, and how it is possible, and increasingly desirable that instead of transitioning, the academic and entrepreneurial experience can intersect and be amalgamated.

The discussion will centre upon the unique perceptions, and challenges faced by scientists, and technologists and how we can surmount this and have a foot in both the worlds.

The talk will conclude with a few pointers and suggestions that can better foster innovations, and entrepreneurship amongst students, researchers and even faculty in an academic setting.



**Dr. Devanathan
Raghunathan**

Chief Medical Officer,
Advanced First Aid
Research Pte. Ltd,
Singapore.

Devan works with Start-ups and SMEs in Strategic Planning and Business Development capacity. He Holds an MBA in Finance from S.P. Jain School of Global Management, in addition to an M.Tech in Knowledge Engineering from NUS Singapore, Ph.D. from the Max Planck Institute of Biophysical Chemistry, and a M.Sc. in Chemistry from IIT Madras. Devan has held appointments in academia and government before his foray into consulting and entrepreneurship and is based in Singapore. He is currently the Chief Medical officer at Advanced First Aid Research Pte Ltd, Singapore since November 2015.

Advanced First Aid Research Pte. Ltd. is a Medical Device company headquartered in Singapore. Their ethically-driven management, medical specialists and engineers are dedicated to maintaining world-class design practices and quality procedures in order to meet our customer expectations and international regulatory requirements. They continue to make progress in developing Advanced Wound Care Therapeutics to address the growing needs of wound markets related to burns, chronic infections, diabetic foot ulcers etc.

Domain Adaptation for Learning with Interdependent and Non-Identically Distributed Data

Dr. Debdoot Sheet

Abstract:

Machine learning based problem solving tasks in pattern recognition or computer vision are often faced with a challenge where the training data used to learn the model has its distribution different from the data on which the model is applied. Independent of the cause, any distributional change that occurs after learning a classifier can degrade the performance of such a learned system at test time. Domain adaptation is the science of mitigating such degradation effects. This talk would focus on presenting a simple introduction to the notion on distribution of data, independent and identically distributed (IID) and interdependent and non-identically distributed (INID) data, some common methods of domain adaptation with commonly used learning engines, and some test case scenarios where domain adaptation has had significant impact in practical situations.



Dr. Debdoot Sheet,

Assistant Professor,
Department of
Electrical Engineering,
IIT Kharagpur.

Debdoot Sheet is an Assistant Professor of Electrical Engineering at the Indian Institute of Technology Kharagpur and founder of Skin Curate Research. He was born in Kharagpur, India in 1986 and has spent his life across Kharagpur and Kolkata in India and Munich in Germany. He received the B. Tech degree in electronics and communication engineering in 2008 from the West Bengal University of Technology, Kolkata, MS and Ph.D. degrees from the Indian Institute of Technology Kharagpur in 2010 and 2014 respectively. His current research interests include computational medical imaging, machine learning, and visualisation. He is also a DAAD alumni and was a visiting scholar at the Technical University of Munich during 2011-12. He is also recipient of the IEEE Computer Society Richard E. Merwin Student Scholarship in 2012, the Fraunhofer Applications Award at the Indo-German Grand Science Slam in 2012, the GE Edison Challenge 2013, and the Young Alumni Achiever Award from IEM-UEM Kolkata in 2016. He is a member of IEEE, SPIE, ACM, IUPRAI and BMESI and serves

Methods of Segmentation for diagnosis of breast cancer cytology – An integrated image pre-processing and nucleus segmentation system.

Mr. Hrushikesh Garud

Abstract:

Computer vision (CV) systems for automated breast cancer diagnosis using Fine Needle Aspiration Cytology (FNAC) images are under development for a while now. Most of these CV systems implement the bottom-up way of diagnosis - "from evidence to the hypothesis." In the bottom-up manner of FNAC diagnosis, the process of segmentation of nuclei is critically important as the nucleus of a malignant cell is the place signs of malignancy can be observed. Automated nuclei detection and segmentation are well-studied problems in digital pathology and cytology. Though detection and segmentation of nuclei in cytology images are considered to be simpler than in histology, they still are the challenging problems due to high variability in images of breast FNAC. The variability is present due to the composition of the aspirated sample, underlying disease condition, quality and variability of slide preparation, and the imperfection of data acquisition process. This talk presents an integrated multistage ((image pre-processing and segmentation stages) system for accurate segmentation of isolated and closely separated nuclei from high magnification breast fine needle aspiration cytology (FNAC) images.



Mr. Hrushikesh Garud,

Technical Lead,
Advanced Driver
Assistance Systems,
Embedded Processing
Texas Instruments (I)
Pvt. Ltd.

Hrushikesh is the Senior Software engineer in Texas Instruments (I) Pvt. Ltd. in Bengaluru and a Doctoral researcher in IIT Kharagpur. He received his B.E degree in electronics from Dr.Babasaheb Ambedkar Marathwada University, Aurangabad in 2005, M.Tech in Electronics and Electrical Communication engineering and Ph.D in Medical Science and Technology from IIT Kharagpur, India in 2008 and 2013 respectively.

He has worked on the Computer Vision group, algorithm for HW accelerator design in the Multimedia Codecs Group (IVAHD3.0), Image signal processing algorithms development and compensated temporal noise filter for video cameras. His research interests include the algorithm development in Radiological imaging modalities, Image analysis system for breast FNAC diagnosis and enhancement in digital pathology. He has developed complete License Plate Recognition system for software implementation on TIs embedded system platforms. He extensively worked on selection of feature quantification techniques to maximize classification efficacy during translation of subjective into objective features.

**3rd International Conference on Bio signals,
Images and Instrumentation
ICBSII 2017**

RESEARCH PAPERS

Combinational Neuro Fuzzy and Erosion Rule Based Filter for Detection and Reduction of Impulse noise

Rashmi Kumari
JJTU, Jhunjhunu
Rajasthan, India
rashmi167k@gmail.com

Anupriya Asthana
JIMS, Greater Noida
U.P., India
a234asthana@gmail.com

Vikas Kumar
Sharda University, Greater Noida
U.P., India
prof.vikaskumar@gmail.com

Abstract—Multimedia usage is growing up day by day and visual information plays an important role in modern life. Contamination of digital images by impulse noise is still a challenging job for scientists. In this paper, a combinational neuro-fuzzy and erosion rule based filter has been proposed for identification and suppression of impulse noise, which works well when high density noise is present. In the first step, ANFIS (adaptive neuro-fuzzy system) has been applied to identify the impulse noise, and in the second step erosion rule has been used to replace the value for contaminated pixel. ANFIS helps to retain the fine information of the image, even when the images are highly contaminated by impulse noise and use of erosion rule gives the estimated value for pixel replacement. Experimental results indicate the fruitfulness of the presented technique by visual and statistical analysis.

Keywords—Image processing, Fuzzy logic, Neural network, ANFIS, Impulse noise, Erosion rule.

I. INTRODUCTION

Digital image processing applies computer algorithms for the processing of digital images. Noise detection and reduction are the main steps of these algorithms as images usually get contaminated by addition of noises during image capturing and transmission process. When the values of pixels changed randomly and replaced by any unwanted value then the image is considered as contaminated image. Noise reduction is very essential as it affects the subsequent image processing task as segmentation, object recognition etc. While removing the noise, it is necessary to retain the important details of the image.

Among several types of noises, fixed-valued impulse noise occurs when the value of contaminated pixels are changed with values equal to minimum “0” or maximum “255” of the defined range with same probability. This noise is commonly termed as the “salt-and-pepper” noise. From conventional mean and median filters to soft computing methods, numerous modifications have been done on techniques of image filters. Nonlinear filters have tendency to blur fine features of the image while reducing the noise.

Median filter is the simplest technique of noise reduction and there are several modified median filters have been studied in the literature, which show significant improvement in result. At high value of noise, decision based algorithm

generates streaks in recovered images due to continuous replacement. A new fast method is proposed by Srinivasan and Ebenezer to avoid the streaks [1]. In decision based unsymmetrical filter, unsymmetrical median value has been used instead of the neighborhood pixels. In case of trimmed filter, mostly pixel values are extremes values (either zero or 255) and the trimmed mean value will be again the extreme values, which is noise only. A modified decision based unsymmetric trimmed filter is proposed to avoid this lack where the mean value has been calculated [2]. A modified mean filter is also proposed by the Benazir and Imran for enhancement of image [3]. A combination of adaptive weight and trimmed median filter is also studied for better outcome in presence of high density noise [4].

Since the development of soft computing techniques several filters have been proposed on fuzzy concept and neural network. Fuzzy logic based filters minimize the uncertainty so it is helpful in taking decision of noise detection [5]. Neural networks have already been used for the denoising process [6-7]. The special network which is used commonly is known as CNN, where gradient based learning has been applied. Convolution neural network has been shown very effective on multiple tasks such as traffic sign recognition and handwritten digit recognition [8].

As neural network has special feature to learn from examples and fuzzy logic deals with uncertainty. So, combinations of Fuzzy Inference System (FIS) and Adaptive Neural Network (ANN) (such as ANFIS) have been found very useful and it is applied several times by scholars in various engineering and scientific research areas to deal with problems of real world. Combined applications of fuzzy logic and neural networks have been implemented many times to solve the problems of digital image processing in past few years [9].

A number of researchers have also worked on the mathematical morphology based tools in image processing and analysis. The basic mathematical morphology operations are dilation, erosion, opening and closing. Edward and Charles presented a simple closed-form expression for erosion, dilation and convolution [10]. Binary E&D (Erosion and Dilation) has been used in real-time surveillance system by Hugo et al [11].

A novel neuro-fuzzy erosion filter (NFEF) has been presented in this paper, where combinational neuro-fuzzy concept has been used to identify the presence of noise and mathematical morphological erosion rule is used to suppress the identified noise. Section II of this paper gives the brief description of neuro-fuzzy architectures. Concept of erosion rule in image processing is given in section III. The next part is section IV, which explains the working of the presented model and experimental results are presented in section V which shows the significant improvement over the traditional method in presence of high density noise. Section VI is concluding the presented method.

II. NEURO-FUZZY ARCHITECTURES

Neuro-Fuzzy computing has attracted the attention of numerous researchers of different fields for solving real world complex problems. The neuro-fuzzy term was introduced by integrating of these two paradigms fuzzy logic and neural network. Researchers used to combine these tools in different manners, so that sometimes confusion generated on the exact way of working of neuro-fuzzy systems. ANN learns the presented inputs by improving the interconnections between layers of neurons.

The term neuro-fuzzy can be defined in general, as a type of system designated for fuzzy controller type structure where neural network is used to regulate the fuzzy sets and rules repetitively with the set of pair of data vectors of input and output. This kind of system looks like a neural network first where parameter learning takes place and at execution time, it works like a fuzzy system. However, both techniques have some advantages as well as disadvantages too individually. But when they mixed together results are better than the each isolated techniques. The combination of FIS and ANN can be categorized as:

- (a) Concurrent Neuro-Fuzzy model
- (b) Cooperative Neuro-Fuzzy model
- (c) Fully Fused Neuro-Fuzzy model

The fuzzy system and the neural network work together continuously, in the concurrent model. In co-operative model, the neural network learning methods decides the membership function of fuzzy inference system from the set of training data. It can be considered as preprocessor. In fully fused neuro-fuzzy model, learning algorithms of neural network are utilized to decide the fuzzy inference parameters. These systems have the feature of sharing data structures and knowledge representations. Several models are proposed in literature which seem analogous in essence, but they have basic dissimilarity. Neural network representation is more suitable as it allows visualization of flow of data through the system and the error signals that are used to revise its parameters. This advantage permits to evaluate the different models or to envisage structural differences.

Among all available models, ANFIS has been used for the detection of noisy pixel in this proposed model. It has a five layered architecture. In the first hidden layer, the input variables are fuzzified and the T-norm operation (fuzzy operators) is performed to determine the rule antecedent part

in the second hidden layer. Fuzzy rule base or rule strengths are normalized in the third layer. Fourth layer decides the consequent parameters. Fifth layer determines the final output by taking account of all the incoming input signals. The input membership parameters are decided by the backpropagation learning method and least mean square method is used for determination of consequent parameters.

III. CONCEPT OF EROSION

Dilation and erosion are the fundamental concepts of mathematical morphology. Here we have used the concept of erosion to suppress the impulse noise. In erosion rule, the central pixel is changed by the darkest pixel in the vicinity of filter. A portion of gray-scale image is taken as input matrix for applying erosion rule as shown in fig.1. Structuring format of 1x3 is considered and its center pixel is changed by the minimum pixel value in its vicinity (filter structural element).

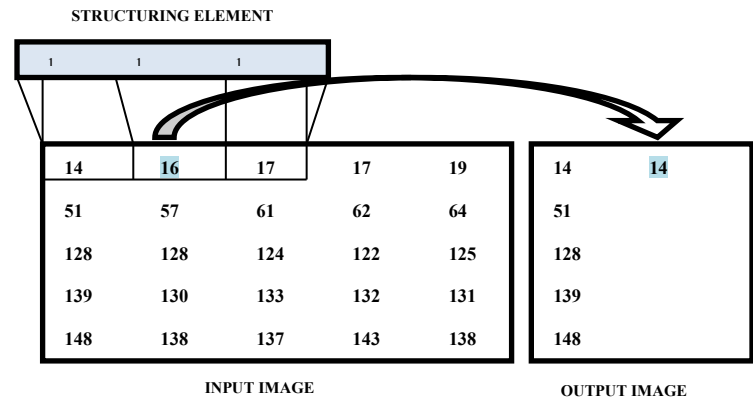


Fig.1 Erosion Rule

Here, centre pixel of filter structure is '16' and '14' & '17' as its neighboring pixel values. Since, '14' is the minimum value among all three values of the filter structure, so the center pixel is now replaced by this pixel value i.e. '14'. This will generate a new dilated output matrix of image.

This method is perfect for removing "salt noise" by ensuring that key features are relatively sharp. Therefore, in our proposed method to reduce the impulse noise, all detected corrupted pixels are converted into salt noise only i.e. pixel value of '1'. Then erosion rule is applied to replace these pixels by the minimum value in their vicinity and it works well on both salt and pepper noise.

IV. PROPOSED MODEL

As there are uncertainties in noise, to identify the noisy pixel and to keep preserve the minute information. ANFIS has been used in the proposed filter model (NFEF). For the training of ANFIS mentioned three parameters have been used [12].

- A. Intensity difference (ID)
- B. Average Intensity Difference (AID)
- C. Four Adjacent Intensity Difference (FAID)

These parameters are defined on the window pixels by considering the centre pixel has to be checked by ANFIS.

A. Intensity Difference (ID)

This parameter is calculated by taking the differences of centre pixel and its neighborhood in window pattern of size 3x3. T is expected to be high in flat region of image, though the edge pixels can also produce the high value of intensity difference.

$$ID = \sum_{i=1}^3 \sum_{j=1}^3 |A(2,2) - A(i, j)| \tag{1}$$

Here (i, j) ≠ (2, 2) and A(i, j) represents the pixel intensity.

B. Average Intensity Difference (AID)

It is another parameter to aid the impulse noise detection. As it is difference of centre pixel and average of all neighborhood pixels, it will generate the smaller value as compared to ID.

$$AID = \left| A(2,2) - \frac{\sum_{i=1}^3 \sum_{\substack{j=1 \\ (i,j) \neq (2,2)}}^3 A(i, j)}{8} \right| \tag{2}$$

C. Four-Adjacent Intensity Difference (FAID)

Four adjacent pixels situated vertically and horizontally are used to calculate the next value FAID which is used for impulse noise detection. This parameter would assist to make difference between the noise pixel and edge pixel. FAID is defined as:

$$FAID = \sum_{i=-1}^1 \sum_{j=-1}^1 \left| 4 \times A(i, j) - A(i-1, j) - A(i+1, j) - A(i, j-1) - A(i, j+1) \right| \tag{3}$$

A training image of 81x81 pixels is generated artificially by using random pixels to train the neural network. The all three inputs ID, AID and FAID are fed to the ANFIS as shown in fig. 2. Total 27(3³=27) rules will be generated in rule base as it has three inputs, which are as follows:

Rule 1: If ID is M₁₁ and AID is M₂₁ and FAID is M₃₁
Then O₁ = F₁ (ID, AID, FAID)

Rule 2: If ID is M₁₁ and AID is M₂₁ and FAID is M₃₂
Then O₂ = F₂ (ID, AID, FAID)

Rule 3: If ID is M₁₁ and AID is M₂₁ and FAID is M₃₃
Then O₃ = F₃ (ID, AID, FAID)

Rule 4: If ID is M₁₁ and AID is M₂₂ and FAID is M₃₁
Then O₄ = F₄ (ID, AID, FAID)

Rule 5: If ID is M₁₁ and AID is M₂₂ and FAID is M₃₂
Then O₅ = F₅ (ID, AID, FAID)

Rule 27: If ID is M₁₃ and AID is M₂₃ and FAID is M₃₃
Then O₂₇ = F₂₇ (ID, AID, FAID)

Where M_{ij} = jth membership function of the input
O_K = The output of Kth rule
F_K = Kth output membership function

Here the value of i, j, and K varies as i=1, 2, 3, j=1, 2, 3, K= 1, 2, 3 ..., 27.

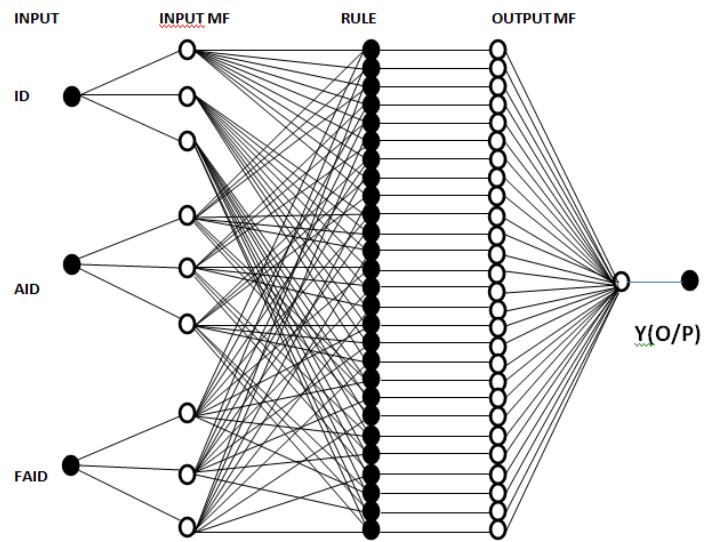


Fig.2 ANFIS network for Noise Detection

The output of the ANFIS is the weighted average of the all individual outputs. The weight factor W_K of the rules is as calculated as follows:

$$W_1 = M_{11}(\text{ID}) \cdot M_{21}(\text{AID}) \cdot M_{31}(\text{FAID})$$

$$W_2 = M_{11}(\text{ID}) \cdot M_{21}(\text{AID}) \cdot M_{32}(\text{FAID})$$

$$W_3 = M_{11}(\text{ID}) \cdot M_{21}(\text{AID}) \cdot M_{33}(\text{FAID})$$

$$W_4 = M_{11}(\text{ID}) \cdot M_{22}(\text{AID}) \cdot M_{31}(\text{FAID})$$

$$W_{27} = M_{13}(\text{ID}) \cdot M_{23}(\text{AID}) \cdot M_{33}(\text{FAID})$$

The output of ANFIS is

$$Y = \frac{\sum_{K=1}^{27} W_K O_K}{\sum_{K=1}^{27} W_K} \tag{4}$$

ANFIS has been trained here by taking the input and output pair of data and by using the above parameters. By use of testing pair of data, the accuracy of the ANFIS can be tested. ANFIS detects the noisy pixels from the data. Then the erosion rule has been applied on the sliding window and the contaminated pixels are changed by the minimum value in the vicinity. Flowchart for presented model is depicted in fig.3.

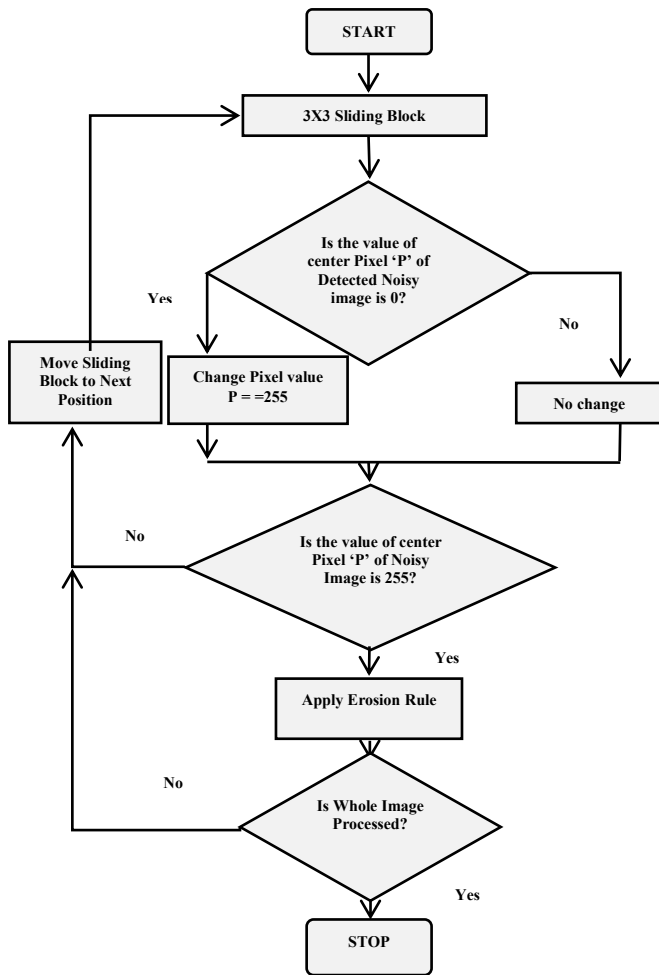


Fig.3 Flowchart for Proposed Model

Algorithm for detection and removal of impulse noise is given below for the presented model:

- Step 1) A standard test image is selected for the execution of algorithm. Impulse noise is added on it to generate a corrupted image.
- Step 2) ID, AID and FAID parameters are given as input of ANFIS for the training.

- Step 3) ANFIS detects the impulse noise and output of the ANFIS generates a new image containing only noise pixels.
- Step 4) Noise removal process is applied after identifying the corrupted pixel. If the window size is 3x3 and 'P' is the centre pixel then-

Case 1) If it is corrupted, i.e. P=0 or P=255 by the detection procedure, first there is need to convert centre pixel as 'P=255' if the value of "P=0". Value of would be unchanged in case of "P=255". After this the minimum value concept of erosion rule is applied on window of 3x3 size.

Case 2) If value of P is between 0 to 255, then it is a noise free pixel and left unchanged.

$$P = \begin{cases} \min(N), & \text{If pixel is corrupted} \\ \text{No change,} & \text{if pixel is not corrupted} \end{cases}$$

Where, N= Window size (3x3).

- Step 5) Above mentioned steps are repeated till the entire image is recovered.

Illustration: Suppose a corrupted 3X3 window is:

Case 1)

	163	162	162
N=	162	255	162
	161	162	163

As the center pixel of 'N' is detected as contaminated so the proposed filter is applied on this window by taking minimum value of 'N' (i.e. erosion rule) which gives (161). The corrupted center pixel of 'N' is replaced by this recovered value as:

P= Minimum (N),

	163	162	162
R=	162	161	162
	162	162	163

Where, 'R' is the recovered 3X3 matrix.

Case 2)

	163	162	162
N=	162	0	162
	162	160	163

$$N_1 = \begin{matrix} 163 & 162 & 162 \\ 162 & 255 & 162 \\ 162 & 160 & 163 \end{matrix}$$

As the type of noise is pepper '0' in first matrix, the centre pixel will be converted to '255', which generates new matrix 'N₁' and then the erosion rule has been applied to replace the value of corrupted pixel by minimum of its vicinity i.e. '160'.

P= Minimum (N), Recovered matrix R is as:

$$R = \begin{matrix} 163 & 162 & 162 \\ 162 & 160 & 162 \\ 162 & 160 & 163 \end{matrix}$$

V. EXPERIMENTAL RESULTS

Five standard test images have been chosen for the performance evaluation of the presented filter. The algorithm is tested at various noise densities and value of PSNR and MSE has been measured for every execution. Table I and Table II show the obtained results of MSE and PSNR for the gray scale test images. PSNR for the Lena image has been also compared with the conventional mean and median filter of size 3x3 for the comparative study of the proposed filter and the obtained result is mentioned in table III.

TABLE I VALUES OF PSNR AT DIFFERENT NOISE DENSITIES

Image	Value of PSNR at Noise Density						
	10%	20%	30%	40%	50%	60%	70%
Pout	31.74	28.92	27.07	25.46	24.18	21.45	17.45
Pirate	30.21	27.35	25.73	24.48	23.18	20.73	17.19
Lena	28.88	25.3	23.58	22.41	21.28	19.4	16.71
Coin	32.54	30.18	28.41	27.41	26.49	24.61	21.83
Cameraman	26.87	23.88	22.47	21.1	20.05	18.44	15.73

TABLE II VALUES OF MSE AT DIFFERENT NOISE DENSITIES

Image	Value of MSE at Noise Density						
	10%	20%	30%	40%	50%	60%	70%
Pout	43.52	83.36	127.79	184.88	248.52	465.49	1.17E+03
Pirate	61.82	119.77	173.62	231.82	312.41	549.293	1.24E+03
Lena	105.81	191.64	284.85	372.85	483.74	746.5	1.38E+03
Coin	36.22	62.41	93.96	118.1	145.94	2.25E+02	4.27E+02
Cameraman	133.41	266.39	367.1	504.79	648.2	931.97	1.74E+03

TABLE III PSNR COMPARISON WITH OTHER FILTERS

Noise %	PSNR Comparison (Lena Image)		
	Median 3X3	Mean 3X3	Proposed 3X3
10	28.47	22.76	28.88
20	25.89	20.25	25.3
30	22.19	18.48	23.58
40	18.09	17.08	22.41
50	14.93	15.93	21.28
60	12.08	13.22	19.4
70	9.88	11.02	16.71
80	8.1	7.34	13.09
90	6.62	5.9	9.09

It has been observed from the results that this proposed filter is working very well in presence of high densities of noise. PSNR above noise density 50% is showing recognizable difference over the PSNR values obtained from conventional 3X3 Median and 3X3 Mean filters. For visual analysis the original, noisy image, detected noise and recovered images by this proposed filter are shown in fig.4.

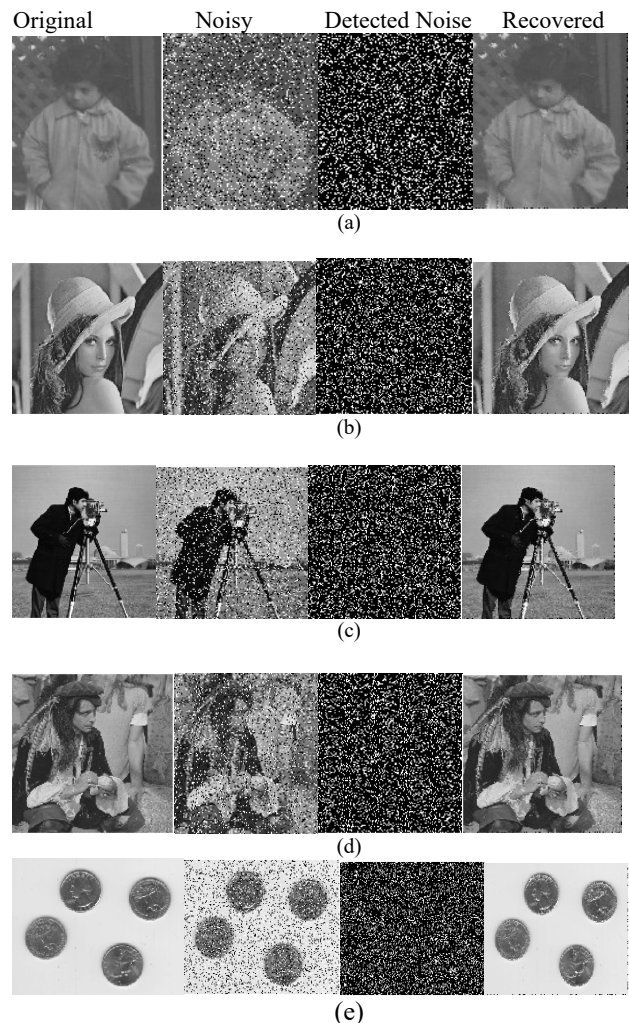


Fig.4. Proposed noise removal filter output for (a)Pout Image (b)Lena Image (c)Cameraman Image (d)Pirate Image (e)Coin Image

VI. CONCLUSION

A novel two step filter model has been proposed in this paper. ANFIS has been used to detect the noise at first step and then the slightly modified erosion rule has been applied at the second step to recover the corrupted image. ANFIS has been trained by the three parameters named as ID, AID and FAID to make the distinction between the edge pixels and noisy pixels. The experimental results of the proposed model show that this filter works much better in presence of high density noise. There is enough scope to model the morphological rule for the image denoising process with some modifications so that it can perform better than the all existing filters.

REFERENCES

- [1] K.S.Srinivasan, D.Ebenezer, "A New Fast and Efficient Decision-Based Algorithm for Removal of High-Density Impulse Noises", IEEE Signal Processing Letters, Vol.no:14, pp.189 - 192, 2007.
- [2] S. Esakkirajan, T. Veerakumar, Adabala N. Subramanyam, and C. H. Premchand, "Removal of High Density Salt and Pepper Noise Through Modified Decision Based Unsymmetric Trimmed Median Filter", IEEE Signal Processing Letters, Vol. 18, No. 5, May 2011
- [3] T.M.Benazir, B.M.Imran, "Removal Of High And Low Density Impulse Noise Using Modified Median Filter", International Conference on Recent Trend in Engineering & Technology (ICRTET 2012),pp.5-8, December 2012, Bangalore, INDIA.
- [4] M. Nooshyar, & M. Momeny, "Removal of high density impulse noise using a novel decision based adaptive weighted and trimmed median filter" In 8th IEEE Iranian Conference on Machine Vision and Image Processing (MVIP), pp. 387-391, 2013.
- [5] H.Xu, G. Zhu, H. Peng, D. Wang. "Adaptive fuzzy switching filter for images corrupted by impulse noise," Pattern Recognit.Lett., vol. 25 , pp 1657-1663, 2004.
- [6] J. Jiang, P. Trundle, J. Ren "Medical image analysis with artificial neural networks" Computerized Medical Imaging and Graphics, pp. 617-631, 2010.
- [7] SuoYishuang, Huanping Hong; Chen Gang "Research on the Visual Image Processing Based on Neural Network", Computer Modeling and Simulation, ICCMS '10. Second International Conference, IEEE Xplore, pp.22-24, 2010.
- [8] P. Sermanet and Y. LeCun. Traffic Sign Recognition with Multi-Scale Convolutional Networks. In Proceedings of International Joint Conference on Neural Networks (IJCNN), 2011.
- [9] Sheng-Fu Liang, Shih-Mao Lu, Jyh-Yeong Chang "A Novel Two-Stage Impulse Noise Removal Technique Based on Neural Networks and Fuzzy Decision", IEEE Transactions on Fuzzy Systems, Vol. 16, No.4, 2008.
- [10] Edward R. Dougherty, Charles R. Giardina, "Closed-Form Representation of Convolution, Dilation, and Erosion In The Context of Image Algebra", IEEE 1998.
- [11] Hugo Hedberg, FedrikKristensen, Peter Nilsson and Viktor Owall, "A Low Complexity Architecture for Binary Image Erosion and Dilation using Structuring Element Decomposition", 2005 IEEE.
- [12] Rashmi Kumari, Deepak Gambhir, Vikas Kumar, "Intensity Difference Based Neuro- Fuzzy System for Impulse Noisy Image Restoration", IEEE conf. International Conference on Signal Processing & Integrated Networks (SPIN), Amity University, Noida, 20-21 Feb, 2014

Thermal Imaging Based Breast Cancer Analysis Using BEMD and Uniform RLBP

Vijaya Madhavi
Department of ECE

East Point College of Engineering and Technology,
Bengaluru-560049.

vijayamadhavi79@gmail.com

T. Christy Bobby
Department of ECE

M.S. Ramaiah University of Applied Sciences,
Bengaluru-560058.

christy.ec.et@msruas.ac.in

Abstract— Breast cancer is the foremost cause of morbidity and mortality among womenfolk. India has 17% of world's population suffering from breast cancer. World Health Organization's International agency for Research on Cancer (IARC) estimates that more than 4,00,000 women die every year due to breast cancer. Thus early identification of breast cancer plays a vital role in reducing the mortality rate. Medical infrared thermography is gaining popularity as it can detect abnormality at an early stage when compared to mammogram. In this work an attempt has been made to distinguish healthy and pathological subjects using Bidirectional Empirical Mode Decomposition (BEMD) and uniform Rotated Local Binary Pattern (RLBP). Frontal thermogram images are pre-processed using anisotropic diffusion filtering which preserves sharp edges, fine details and effectively removes noise. Level set segmentation technique is applied on pre-processed image to obtain the required Region Of Interest (ROI). The delineated ROI's are subjected to BEMD where the image is decomposed into Intrinsic Mode Functions (IMFs) and a residue. IMF1 is considered for further processing as it contains maximum edge information about the image. Texture analysis is performed on IMF1 using uniform RLBP technique to obtain feature vector comprising of 59 unique elements. The dimensionality of features is reduced to 20 using Kernel Principal Component Analysis (KPCA). The subjects are classified using Least Square Support Vector Machine (LSSVM) classifier with different kernel functions and the classifier results are evaluated based on classifier performance measures. Analysis is performed on 43 healthy and 24 cancerous subjects chosen from DMR (Database of Mastology Research) database. The experimental results obtained by LSSVM classifier using Radial Basis Function (RBF) kernel with $\sigma^2=0.5$ and $\gamma=1$ outstands by achieving 89% accuracy. Hence the proposed system effectively distinguishes healthy and pathological subjects.

Keywords— Thermogram, BEMD, IMF, RLBP, LSSVM

I. INTRODUCTION

Breast cancer develops from tissues in mammary gland and is due to proliferation of cells. The world health organization's International Agency for Research on Cancer (IARC) estimates that it affects one in eight women in their life time and more than 4, 00,000 women die each year and is increasing because majority of the cases are diagnosed in later stages, justifying research on early diagnosis. Early detection increases survival rate and reduces the extent of surgical procedures [1].

There are various breast imaging techniques used for identifying breast cancer such as mammogram, ultrasound, thermogram and breast MRI. Mammogram is an X-ray image of the breast and detects breast lesions using low dose of radiation. It is a gold standard widely used in clinical application due to its low cost and low scan time but has limitation of low sensitivity to dense breasts, fails to detect cancer in early stage and poses risk for patients who go for

frequent mammogram due to radiation exposure. Mammogram looks at anatomical or structural part of the body [4].

Thermogram is based on temperature sensing and makes use of Infra-Red (IR) cameras to measure and map heat from the surface of the breast. It uses infrared radiation emitted by body to measure temperature and notice difference in the heat distribution pattern. Metabolic activity in cancerous and pre-cancerous tissues is higher than normal tissue because tumors require more nutrients causing increased blood flow resulting in increased regional surface temperature. Hence blood flow in vessel and high temperature indicate the existence of pre-cancerous and cancerous cells. Thermogram identifies physiological changes and can detect abnormality 8 to 10 years before mammogram can detect [4]. Thermogram is effective in detecting cancer in all age groups including pregnant or nursing women, of varying breast size, with or without breast implants and breast with dense tissues. Availability of high sensitive infrared cameras producing high resolution images and advancement in image processing techniques lead to the success rate of thermal image analysis in medicine.

Anisotropic filtering is a non-linear diffusion process used for edge detection and scale space representation of images [5]. In this method smoothing operation was performed on image to suave intra-regions in the image and preserve inter-region edges by considering local gradient information. The local gray-level variance and the gradient information were considered to preserve both edges and minute details and to filter out noise in the diffusion. The diffusion constant is chosen independent of space location to encourage intra region smoothing. It has been extensively used for edge detection, edge enhancement, image filtering, image smoothing, image enhancement, target tracking, defect detection and texture segmentation [6].

Active contour or level set is an implicit deformable model based on Partial Differential Equation (PDE) approach wherein curves are defined to move towards the desired boundaries to perform image segmentation. The benefits of variational level set over traditional level set is that larger time step is used to solve PDE so as to speed up curve evolution, eliminates costly re-initialization process and is computationally efficient. Level set segmentation is known to be versatile, robust, accurate and efficient as it can handle sharp corners and cusps. Level set segmentation without re-initialization is robust to noise and weak boundaries and is commonly used for medical image segmentation [9].

Empirical Mode Decomposition (EMD) approach was initially introduced for complex nonlinear and non-stationary signals. Later it was extended to 2D space so as to operate on images and is known as Bidirectional Empirical mode

decomposition (BEMD) or 2D Empirical mode decomposition (2D EMD). BEMD decomposes an image into set of bi-dimensional IMFs (BIMFs) based on oscillation or local frequency information and a bi-dimensional residue (BR). BEMD decomposition is data driven and IMF's are locally orthogonal that represent every frequency of local data. BIMF1 reflects majority of the high frequency information of the input image and can be used alone for further analysis [10]. BEMD is used in wide range of applications such as texture image analysis and segmentation, image denoising and enhancement, edge detection, fractal analysis and image compression [11].

Texture features derives efficient and compact quantifiable texture description and could provide hints for categorizing patterns. Local Binary Pattern (LBP) is a texture analysis approach most effectively and recurrently used texture descriptor that proficiently captures the local structure but is not rotation invariant. Hence Rotation invariant LBP (RLBP) is used to overcome the inability of LBP to deal with rotation changes. In uniform RLBP, uniformity in the pattern is utilized using dominant direction to extract more discriminative information. The dominant direction is defined as the index of the neighboring pixel whose variation from the central pixel is maximum and rotates the weights with regard to dominant reference direction to obtain P discrete values [13].

Principal Component Analysis (PCA) is a used for dimensionality reduction and is defined as a technique used to transform set of observations of correlated variables into set of linearly uncorrelated variable values termed as principal components which are lesser than the number of original variables. PCA is linear, costly and inefficient to represent complicated data in linear subspace effectively. Kernel PCA is a nonlinear form of PCA for dimensionality reduction of complicated data structure, making use of different kernel methods such as linear, polynomial and RBF to simplify computation [15]. Kernel PCA is computed using kernel matrix and is computationally simple.

Least square support vector machine (LSSVM) is a supervised learning scheme that transmutes input data into high dimensional feature space using various kernel functions such as linear, Radial Basis Function(RBF) and polynomial such that the transmuted data becomes more distinguishable than that of original data. SVM contains inequality constraints, hence is solved using quadratic programming methods and are often time-consuming. Least square SVM works with least square cost function, contains equality constrictions, henceforth the solution is obtained by solving a system of linear equations [16]. LSSVM is first trained to build a classification model which is further used in testing phase to classify subjects as healthy or sick.

II. METHODOLOGY

A. Thermogram Database

In this work, images are taken from Database of Mastology Research (DMR) containing frontal thermogram images acquired using FLIR SC-620 IR camera having a resolution of

640x480 pixels [14]. The dataset contains images from wide age group ranging from 29 to 85 years, containing breasts of different sizes such as medium, large and asymmetric breast size. Demographics of the subjects are shown in table 1.

Total number of subjects (n) – 67

Total number of healthy/normal subjects (nor) – 43

Total number of sick/abnormal subjects (ab) – 24

TABLE 1
DEMOGRAPHICS OF THE SUBJECTS

Age Range	Normal(nor)	Abnormal(ab)
29-50 years	07	11
51-70 years	31	12
71-85 years	05	01

The flow diagram representing framework for thermal image analysis is presented in fig. 1.

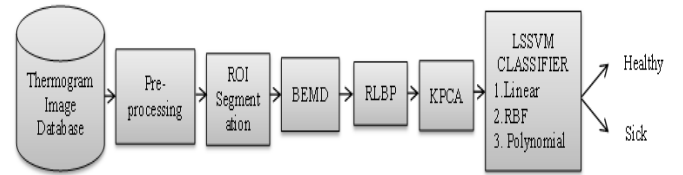


Fig.1 Framework for thermal image analysis

B. Pre-processing

Analysis of breast thermogram is a challenging task as they are images having low signal to noise ratio and less contrast. Input image is very large (640x480), so cropping of image is done to roughly remove unwanted regions. Pre-processing involves conversion from RGB to grayscale, image cropping to remove unwanted regions such as neck region, arms and region below infra-mammary fold and enhancement using anisotropic diffusion. Anisotropic diffusion is the modified form of linear

$$\frac{\partial g_t}{\partial t} = \text{div}[C_t \cdot \nabla g_t(x, y)]$$

(1)

where $g_t(x, y)$ is image at time t , div represents divergence operator, $\nabla g_t(x, y)$ is the gradient of the image and C_t is conduction coefficient. Suitable choice of C_t is done to smooth intra-regions in the image and retain inter-region edges. Minor variations in intensity such as noise will be well smoothed while edges with enormous intensity transitions are effectively preserved.

C. Region of Interest Segmentation

Region Of Interest (ROI) segmentation is performed using level set segmentation by providing few initial points manually around the desired ROI. The evolution equation of the level set function is given by

$$\frac{\partial \phi}{\partial t} + F \nabla \phi = 0$$

(2)

Depending on initial contour position; the initial value of level set function $\phi(x, y, t=0)$ is built. The value of ϕ is adjusted over time to obtain the contour given by

$\phi(x(t), y(t), t) = 0$. In-order to perform segmentation of images, the speed function F depends on image data and level set function ϕ . Active contours or snakes are dynamic curves that move towards sharp transitions of the object. To obtain these curves we define an external energy that can move the zero level curves toward the boundaries of the object. Let F be an image, and g be the edge function given as

$$g = \frac{1}{[1 + |\nabla G_\sigma * F|^2]} \quad (3)$$

where G_σ is the Gaussian kernel with standard deviation σ . External energy for a function $\phi(x, y)$ drives zero level set towards the edges of the object given by

$$\varepsilon_{g,\lambda,v}(\phi) = \lambda L_g(\phi) + v A_g(\phi) \quad (4)$$

$$L_g(\phi) = \int_{\Omega} g \delta(\phi) |\nabla \phi| dx dy \quad (5)$$

$$A_g(\phi) = \int_{\Omega} g H(-\phi) dx dy \quad (6)$$

where $v = \text{constant}$, $\lambda > 0$, δ represents dirac function and H represents Heaviside function. Total energy is given by

$$\varepsilon(\phi) = \mu P(\phi) + \varepsilon_{g,\lambda,v}(\phi) \quad (7)$$

The term $\mu P(\phi)$ castigates the deviance of ϕ from a signed distance function during its evolution. Pectoral region is an important region for breast cancer analysis as it is reported that 50 percentage of breast cancer is sited in this region [7]. Hence care has been taken to include pectoral region as well as breast region as ROI excluding neck region, arms and region below infra-mammary fold. Hence ROI segmentation aims to separate breast region from the remaining portion of the body.

D. BEMD

BEMD is performed on ROI in order to decompose an image into finite number of BIMF's. The process of extracting the BIMFs one by one having the highest to the lowest local spatial variations of the data is known as sifting process. The two properties that BIMFs followed are

1. The number of zero crossings is equal to the number of extrema points or differs by only one.
2. The local maxima envelopes and minima envelopes are symmetric around the envelope mean.

Steps for bi-dimensional shifting process is

1. Identify extrema of image F using geodesic operator based morphological reconstruction.
2. Connect all the maxima/minima points to produce 2D envelope.
3. Calculate local mean $m1$ by averaging both the envelopes
4. Calculate BIMF by subtracting mean from image, $h1 = F - m1$
5. Repeat steps 1 to 4 using $h1$ as BIMF

The sifting process concludes when the envelope mean is close to zero. The BEMD process is accomplished when there is no more extrema points present in the residue. Stopping criterion of sifting process can be obtained by restraining the size of the

standard deviation calculated from two successive sifting results.

E. Uniform RLBP

Texture features play a vital role in quantitative assessment of breast thermogram. Uniform RLBP is computed using dominant direction and is defined as the index in the circular neighbourhood for which the difference is maximum given by

$$D = \arg \max_{p \in (0,1,\dots,P-1)} |g_p - g_c| \quad (8)$$

where g_c is gray-level value of the centre pixel, g_p is gray-level value of its neighbour, p is the index of the neighbour, R is the radius of the circular neighbourhood and P is the number of neighbours. The weights related to the pixels in the neighbourhood are circularly shifted with respect to the dominant direction. The lowest weight is associated with the index corresponding to D and is subsequently increased in clockwise direction. RLBP of a pixel with radius R in circular neighbourhood and P number of neighbours is given by

$$RLBP_{R,P} = \sum_{p=0}^{P-1} s(g_p - g_c) 2^{\text{mod}(p-D,P)} \quad (9)$$

In uniform LBP, the obtained binary code must contain at the most two transitions from 0 to 1 and vice-versa. Implementation is done using lookup table of elements where the table maps the non-uniform patterns into a single bin and all others in separate bins. The uniform RLBP pattern is given as $U(RLBP, P)$ where $U(\)$ is the lookup table that defines a mapping from binary pattern to a uniform pattern. For P neighbours, the lookup table $U(\)$ consists of $2P$ elements and $P(P-1)+3$ different outputs corresponding to the uniform patterns. Texture analysis is performed by computing uniform RLBP of IMF1 and is useful in detecting local features for texture classification.

F. Kernel PCA

Processing high dimensional data is computationally intensive and also exhibits data redundancy posing difficulty in real time processing. Hence we go for dimensionality reduction where in high dimensional data is represented in lower dimension subspace resulting in reduced computation cost. The supremacy of kernel methods is that there is no need to compute projected new features explicitly. Given the training dataset, the kernel matrix can be constructed directly from it and can be used to compute principal components.

Principal components are computed using

$$y_k(x) = \sum_{i=1}^N a_{ki} k(x, x_i) \quad (10)$$

where $k(x, x_i)$ is the kernel matrix containing relative distance between all data points and is symmetric and positive semi-definite, a_k is a column vector of a_{ki} given as $a_k = [a_{k1}, a_{k2}, \dots, a_{kN}]^T$

G. Least Square SVM

Given the training dataset X_k, Y_k where $k = 1, 2, \dots, M$ where M is number of training samples, X_k is the feature vector, Y_k is class labels of training set. $Y_k \in \{-1, +1\}$ is the target class label. SVM algorithm tries to find an optimum hyper-plane given by $\omega^T x + b = 0$ where ω is the vector of hyper plane coefficients and b is a bias term, with the maximal margin to separate two different classes. Least square SVM is reformulation of standard SVM given by

$$\text{Min}_{\omega, b, e} \omega^T \omega + \gamma \sum_k e_k^2 \quad (11)$$

subjected to equality constraint

$$y_k (\omega^T \phi(x_k) + b) = 1 - e_k \quad \text{for } k=1, \dots, M \quad (12)$$

Lagrangian is given by

$$L(\omega, b, e; \alpha) = j(\omega, e) - \sum_{i=1}^N \alpha_i \{y_i [\omega^T \phi(x_i) + b] - 1 + e_i\} \quad (13)$$

Conditions for optimality are: $\partial L / \partial \omega = 0$; $\partial L / \partial b = 0$; $\partial L / \partial e_k = 0$; $\partial L / \partial \alpha_k = 0$; Eliminating ω , we get solution for α , b . Kernel κ is defined as the inner product in a feature space based on some mapping ϕ given by

$$\kappa(x, y) = \langle \phi(x), \phi(y) \rangle \quad (14)$$

For linear kernel, the kernel function is defined as

$$\kappa(x_i, x_j) = x_i^T x_j \quad (15)$$

For polynomial of degree d , the kernel is defined as

$$\kappa(x_i, x_j) = (x_i^T x_j + c)^d \quad (16)$$

The RBF kernel on two samples x_i and x_j represented as feature

$$\text{vectors in some input space, is defined as } \kappa(x_i, x_j) = \frac{e^{-\|x_i - x_j\|}}{2\sigma^2} \quad (17)$$

where σ is Gaussian RBF kernel's bandwidth. Least square SVM is trained using training set to learn the characterization for each texture class and is used to classify subjects as healthy and abnormal.

Classification performance measures/metrics such as sensitivity, specificity, accuracy, Negative Predictive Value (NPV), Positive Predictive Value (PPV), F1 score and misclassification rate is computed for linear, RBF and Polynomial kernel functions for varying values of σ^2 and regularization parameter γ . Classifier performance is evaluated using confusion matrix and Receiver Operating Characteristic (ROC). Confusion matrix or contingency table represents the count of correct and incorrect predictions made by the classification model compared to the count of actual outcomes in the data.

ROC is the graphical approach for displaying trade-off between true positive rate along x-axis and false positive rate along y-axis and is useful for evaluation of classifier performance. Area under ROC curve (AUC) is a measure of quality of classification model with value lying between 0 and 1. Here AUC is used to evaluate the classification performance of textural features extracted using RLBP.

III. RESULTS AND DISCUSSION

In this work, thermogram images (N=67) are taken from DMR database having a resolution of 640x480 pixels. Fig. 2(a) shows normal image and fig. 2(b) shows abnormal image taken from thermogram image database.

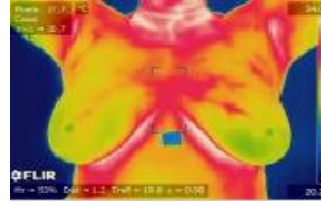


Fig. 2(a) Normal Image

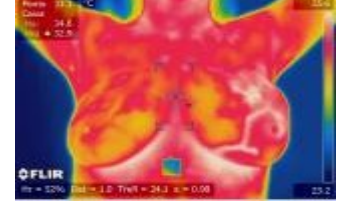


Fig. 2(b) Abnormal Image

Anisotropic diffusion is performed on cropped grayscale image to smooth the image and to retain the edges. Number of iterations, $n=15$, conduction coefficient, $c=20$, $\lambda=0.25$ and an optional input is 1 to preserve high contrast edges. The normal and abnormal pre-processed image is shown in fig. 3(a) and fig. 3(b) respectively.

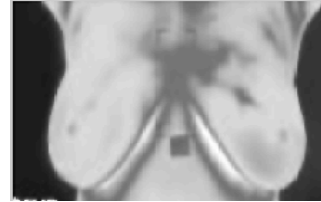


Fig. 3(a) Normal pre-processed image

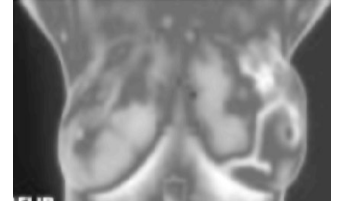


Fig. 3(b) Abnormal pre-processed image

Gradient ∇f of the anisotropic diffused image is computed to extract edge information from the image shown in fig. 4(a) and fig. 4(b) for normal and abnormal case.



Fig. 4(a) Normal gradient image

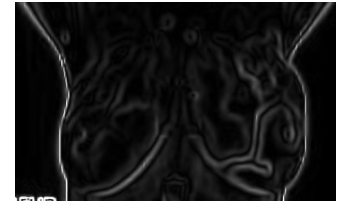


Fig. 4(b) Abnormal gradient image

Level set segmentation without re-initialization is applied on the obtained gradient image with few initial seed points selected manually around desired ROI. ROI is the region from axilla to infra-mammary fold. Level set segmentation output containing holes and gaps, so morphological dilation and closing operation is performed using circular disk of radius 2 as structuring element to fill the holes and gaps so as to obtain binary mask. Finally the binary mask is multiplied with the pre-processed image to obtain ROI. The obtained ROI contains blank horizontal and vertical lines which are removed to obtain final segmented ROI for normal and abnormal case shown in fig.5.

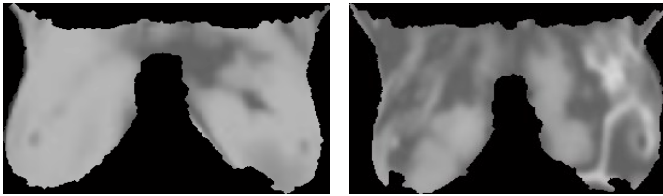


Fig. 5(a) ROI Segmentation (Normal case)

Fig. 5(b) ROI Segmentation (Abnormal case)

Bidirectional empirical mode decomposition is performed on segmented ROI and standard deviation less than 0.2 is considered as the stop criterion to obtain IMF1, IMF2, IMF3 and a residue image as shown in fig. 6. For further analysis, uniform RLBP is computed for IMF1, IMF2, IMF3 and residue with (P, R) = (8, 1) to detect local texture features.

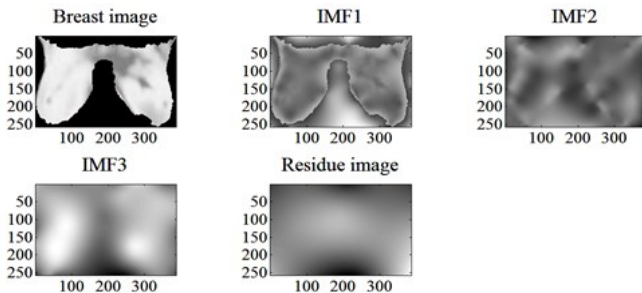


Fig. 6 BEMD computation: IMF1, IMF2, IMF3 and residue image

Fig. 7 represents histogram of uniform RLBP of IMF1, IMF2, IMF3 and residue. It is clearly evident that histogram of uniform RLBP of IMF1 contains maximum information compared to histogram of uniform RLBP of IMF2, IMF3 and residue image. Hence 59 uniform patterns representing histogram of uniform RLBP of IMF1 are considered for further processing.

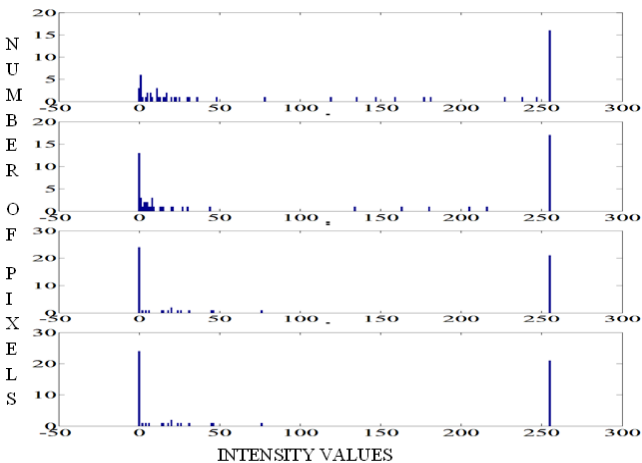


Fig.7 Histogram of uniform RLBP of IMF1, IMF2, IMF3 and residue image

Kernel PCA with polynomial kernel type having $d=0.0005$ and reduced dimension as 20 is considered for dimensionality reduction as it provides maximum discrimination compared to other type of kernels. The reduced 20 uniform RLBP features of IMF1 are passed through LSSVM. LSSVM is trained with 30 normal and 18 abnormal breast images and testing is performed on 24 normal and 11 abnormal subjects using linear,

RBF and polynomial kernel. The performance of LSSVM is evaluated for different values of σ^2 for RBF kernel and different values of regularization parameter γ for all kernel types using leave one out cost function. Performance measures are determined for all the kernel types and are tabulated in table 2. From table 2 and fig. 8, we can observe that performance of RBF kernel is satisfactory compared to linear and polynomial kernel. Also AUC of RBF kernel is greater than 0.8 whereas AUC of linear and polynomial kernel is around 0.6.

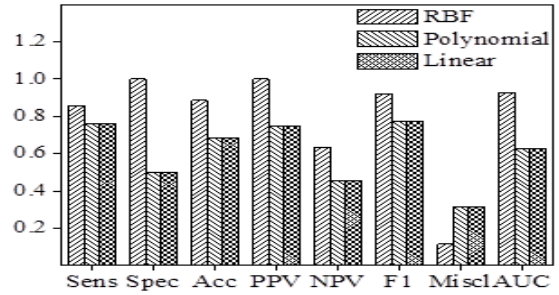


Fig. 8 Bar graph for performance measures of LSSVM for different kernels

On comparing performance of RBF kernel for different values of σ^2 and γ shown in table 3 and fig. 9, we can observe that for RBF3 with $\sigma^2=0.5$ and $\gamma = 1$, accuracy is 89% and AUC is 0.93.

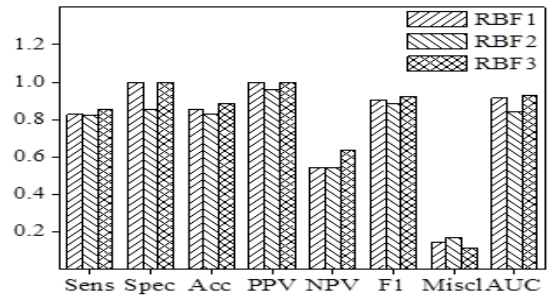


Fig. 9 Bar graph for performance measures of LSSVM using different parameters for RBF kernel

The confusion matrix and ROC curve for RBF3 kernel ($\sigma^2=0.5$ and $\gamma = 1$) is shown in fig. 10 and fig.11.

CONFUSION MATRIX		
Output Class	0	1
0	7 20.0%	4 11.4%
1	0 0.0%	24 68.6%
	100% 0.0%	85.7% 14.3%
Target Class	0	1

Fig. 10 Confusion matrix of LSSVM using RBF3 kernel

TABLE 2 PERFORMANCE MEASURES FOR LSSVM

Kernel	Sensitivity (%)	Specificity (%)	Accuracy (%)	PPV (%)	NPV (%)	F1 Score	Misclassification rate%	AUC
RBF	83	100	86	100	55	0.91	14	0.91
	82	86	83	96	55	0.88	17	0.84
	86	100	89	100	64	0.92	11	0.93
Linear	76	50	69	79	45	0.78	31	0.63
	75	45	66	75	45	0.75	34	0.60
Polynomial	76	50	69	79	45	0.78	31	0.63
	75	45	66	75	45	0.75	34	0.60

TABLE 3 RBF KERNEL FOR VARYING VALUES OF σ^2 AND γ

RBF Kernel	σ^2	γ	Accuracy (%)	AUC
RBF1	0.2	10	86	0.91
RBF2	1	1	83	0.84
RBF3	0.5	1	89	0.93

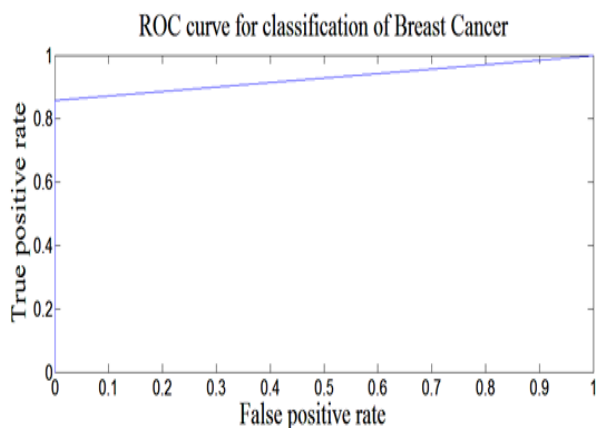


Fig.11 ROC of LSSVM using RBF3 kernel

IV. CONCLUSION

Breast cancer which is a significant health concern can be detected at early stage by processing and analysis of thermal images using BEMD and uniform RLBP features. Using this approach, classification accuracy of 89% is achieved by LSSVM classifier using RBF kernel with $\sigma^2=0.5$ and $\gamma=1$. The results obtained can be improved by extracting and combining different category of features and this work can be further extended to identify suspicious region in the abnormal breast image. Also more accurate and precise results can be obtained by processing and analysing multimodal breast images.

REFERENCES

- [1] American Cancer Society's Breast cancer facts & figures 2013-2014, [Online]. Available: <https://old.cancer.org/acs/groups/content/@research/documents/document/acspc-042725.pdf>
- [2] Fact sheet: Breast thermography, [Online]. Available: <http://www.longevitythermography.com/pdfs/factsheetthermographyforkindoweb1.pdf>
- [3] E. O. Rodrigues et al., "Comparing results of thermographic images based diagnosis for Breast diseases", in *proc. 21st IWSSIP 2014*, 12-15 May 2014, p. 39-42.
- [4] E.Y.K Ng, LN. Ung and F.C.Ng, "Statistical analysis of Healthy and Malignant breast thermography", *J. medical Eng. Technology*, pp. 253-263, Nov. 2001.
- [5] P. Perona and J. Malik, "Scale-space and edge detection using anisotropic diffusion", *IEEE Trans. Pattern Anal. Mach. Intell.*, pp. 629-639, July 1990.
- [6] J. Weickert, *Anisotropic Diffusion in Image Processing*, vol. 1, B. G.Teubner Stuttgart, 1998.
- [7] M. A. S. Ali et al., "Detection of breast abnormalities of Thermograms based on New segmentation method", in *proc. FedCSIS*, 2015, p. 255-261.
- [8] U. R. Gogoi et al., "Breast Abnormality detection through Statistical feature analysis using Infrared Thermogram", in 2015 ISSACC, 2015.
- [9] C. Li, C. Xu, C. Gui and M. D. Fox, "Level set evolution without reinitialization: a new variational formulation", in *Proc. IEEE comp. soc. CVPR '05*, 2005, p. 430-436.
- [10] Y. Lu, C. Huang, J. Wang and P. Shang, "An improved Quantitative analysis method for plant cortical microtubules", *The Scientific World Journal*, vol. 2014, Mar. 2014.
- [11] J.C. Nunes, Y. Bouaounce, E. Delechelle, O.Niang and Ph. Bunel, "Image analysis by bidimensional empirical mode decomposition", *J. on Image and vision computing*, vol. 21, pp.1019-1026, Nov. 2003.
- [12] G. Udaykumar, C.M. Sujatha and S. Ramakrishnan, "Analysis of Trabecular structure in Radiographic bone images using empirical mode decomposition and support vector machine", in *proc. 38th Annual NEBEC'12*, Mar. 2012, p. 376-377.
- [13] R. Mehta and K. Egiazarian, "Rotated Local Binary Pattern (RLBP) – Rotation Invariant Texture Descriptor", in *Proc. ICRAM2013*, Feb. 2013, p. 497-502.
- [14] L.F. Silva et al., "A New Database for Breast Research with Infrared Image", *J. of Medical Imaging and Health Informatics*, vol. 4, no. 1, pp. 92-100, Mar. 2014.
- [15] Al-waisy, "Multi-View face detection based on kernel principal component analysis and kernel support vector techniques", *Int. J. on Soft computing*, vol. 2, no. 2, May 2011.

- [16] J.A.K. Suykens and J Vandewalle, "Least Squares Support Vector Machine classifiers", *J. Neural Processing Letters*(1999), vol. 9, Issue 3, pp. 93-300, June 1999.
- [17] S.S.Suganthi and S.Ramakrishnan, "Anisotropic diffusion filter based edge enhancement for segmentation of breast thermogram using Level Sets", *Biomedical Signal Processing and control*, vol. 10, pp. 128-136, March 2014.
- [18] P. Samui and T. G. Sitharam, "Application of least square support vector machine in seismic attenuation prediction", *ISST J. of Earthquake Technology*, vol. 46, No. 3-4, pp. 147-155, Sept-Dec 2009.
- [19] K. Pelckmans et al., "LS-SVMlab: a MATLAB/C toolbox for least squares Support Vector Machines", Internal Report 02-44, ESAT-SISTA, KU Leuven (Leuven, Belgium), October 2002.

Diagnosis of Diabetic Retinopathy using Texture Features extracted from SLO images

Sri Vidhya S

Department of Biomedical Engineering,
SRM University,
Chennai, India.
sri05vidhya@gmail.com

Kathirvelu D

Department of Biomedical Engineering,
SRM University,
Chennai, India.
kathir297@gmail.com

Abstract—Diabetic retinopathy can affect the vision partially or completely in many diabetic patients. Scanning laser ophthalmoscopes (SLOs) are used for early detection of retinopathy. It uses the technique of confocal laser scanning microscope for di-agnostic imaging of retina of the human eye. The retinal image analysis is used as a preliminary diagnostic method to identify abnormal retinal conditions. The study is aimed to extract the texture features from the SLO images and thereby to implement a neural network classifier system to diagnose normal and abnormal retinal conditions. The study involved 30 participants, among which n=10 were normal and n=20 were abnormal. The captured SLO images were initially preprocessed using the gaussian filter to perform noise removal. The pre-processed image was transformed into super-pixels of size 200 pixels. Subsequently, the GLCM technique was implemented to extract the 22 texture features of the image. Among the extracted texture features, 16 features demonstrated statistically significant difference at the level ($p < 0.05$) between the normal and diabetic groups. A neural network classifier was trained to identify the diabetic retinal images. The neural network classifier could identify the diabetic subjects at an accuracy, sensitivity and specificity of about 86.7%, 80% and 90% for those features that exhibited statistically significant at $p < 0.05$.

Index Terms—Retinal image, super-pixel, texture features, neural network.

I. INTRODUCTION

Diabetic retinopathy is a severe eye disease that affects many diabetic patients causing blindness. According to the World Health Organization, in India the cases of diabetes would reach to 80 million by 2030. Only limited data are available for the occurrence of diabetic retinopathy in our country. The Chennai Urban Rural Epidemiology Study reported 17.6% prevalence of diabetic retinopathy in Chennai and Aravind Comprehensive Eye Study reported 10.5% prevalence of diabetic retinopathy in South India [1]. Retina, which is a thin layer that lines back of the eye, is located near the optic nerve. It receives light through lens and convert it into neural signals. These signals reach the brain for visual recognition. Since retina plays an important role in vision, retinal images can be used for the

diagnosis of healthy and diseased retina [2]. The SLO images are two dimensional retinal scans. It could contain artifacts other than retinal area. Exclusion of these artifacts is the pre-processing step prior to the extraction of features. Optometrists and ophthalmologists rely on image operations and diagnose it based on domain knowledge. The automatic detection of the retinal disease is carried out by image processing technique which involves the basic three steps of segmentation, feature extraction and classification. Automation in analysis is a time effective task. Various algorithms are used for the detection of diseased region.

Simple linear iterative clustering (SLIC) is a linear iterative clustering algorithm in which it is used for super-pixel segmentation. It performs local clustering of pixels. Compared to that of the GS04, QS09, TP09, SLIC provides equal segmentation. GS04 and QS09 do not control the number of super-pixels. GS04 is slow compared to the speed of SLIC for images less than 0.5 million pixels while TP09 is also slower by about 10 times than SLIC for 481x321 pixel images [4]. SLIC is a gradient ascent based algorithm. Graph based segmentation (GS) and Quick shift segmentation (QS) results in uncontrolled number of super-pixel generation. Turbo-pixel (TP) based segmentation provides controlled number of super-pixel but at a slower rate. Since we need the super-pixel number to be in control SLIC is implemented.

The Gray Level Co-occurrence Matrix (GLCM) method extracts statistical texture features. The texture features are computed from the statistical distribution of intensities at specified positions relative to each other in the image [5]. A number of texture features can be extracted from GLCM. In our case a 22 texture features were extracted among which only the significant features were used for classification process.

Several researchers [6-12] have studied the diagnosis of retinal disorders using the texture features extracted using MATLAB and obtained a quantitative results in differentiating the normal and abnormal conditions. The study was aimed to extract the texture features of the SLO retinal images and to implement a neural network classifier system.

II. METHODOLOGY

The retinal image quality assessment algorithm proposed here begins with a pre-processing phase. It comprised of 10 normal and 20 diabetic data obtained from a Private eye hospital (Chennai, Tamilnadu, India). The data flow diagram is shown in Fig.1

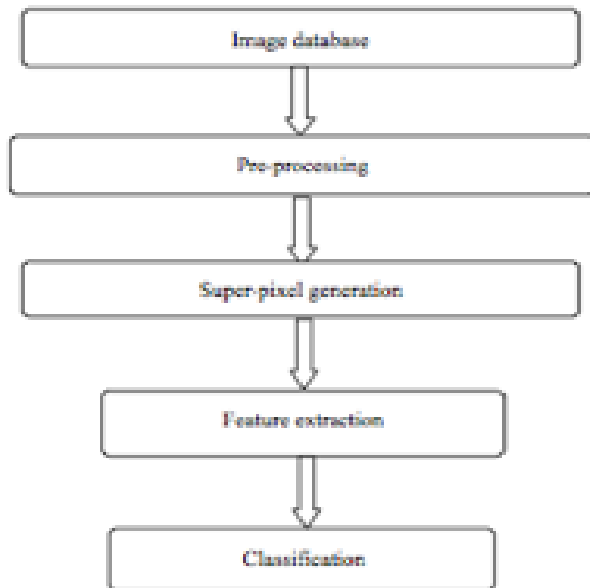


Fig. 1: Data Flow Diagram

It is divided into four stages: pre-processing, segmentation by super-pixel generation, feature extraction using GLCM and network classification. The pre-processing stage is concerned with the removal of noise in the images. In the super-pixel generation stage, the images are grouped into small regions of pixel size 200. In the feature extraction stage, the texture features from the super-pixel segmented images are extracted. Finally, classifier stage performs the automatic classification between the normal and diseased conditions.

A. Pre-processing

The retinal image size is reduced by cropping and contributes to a reduction of the processing time. The artifacts present in the images are removed by the application of gaussian filter.

B. Generation of Super-pixels

The images after pre-processing are grouped into small regions called super-pixels. The feature vector generation for super-

pixel are computationally efficient than that of feature vector generated per pixel. The complexity for image processing task was reduced. In certain cases the super-pixels generated using other methods are uncontrolled. But the number of super-pixels needed to be controlled in our case. Since the watershed approach generates super-pixels for artifacts, we use simple linear iterative clustering. The super-pixel size was set to be 200.

C. Feature Generation

Next to the generation of super-pixels, the texture features are to be generated. We differentiate between the normal and diseased condition using texture based features. GLCM matrix was obtained for super-pixel generated image. It determines the frequency of occurrence of a pixel *i* adjacent to other pixel of value *j*. Four angles $\theta = 0^\circ, 45^\circ, 90^\circ, 135^\circ$ are used for observing the adjacency of the pixel. The extracted texture features which are calculated using GLCM matrix are Autocorrelation, Cluster shade, Cluster prominence, Contrast, Energy, Entropy, Dissimilarity etc.,. A total of about 22 texture features were extracted.

D. Texture features definition

Autocorrelation - It exhibits a linear dependence between same index in the obtained Gray Level Co-occurrence Matrix.

Cluster Shade - It measure the skewness in the Gray Level Co-occurrence Matrix.

Cluster Prominence - It provides the peak in Gray Level Co-occurrence Matrix around the mean for non-symmetry.

Contrast - It shows texture fineness in the local variations.

Correlation - It exhibits a linear dependence between same index in the obtained Gray Level Co-occurrence Matrix.

Difference Entropy - It provide the higher weight on index entropy value difference.

Dissimilarity - It provided the greater weights of Gray Level Co-occurrence Matrix probabilities away from the diagonal.

Energy - It returns the variance in the GLCM.

Entropy - It provide a low value for an irregular Gray Level Co-occurrence Matrix texture randomness. Homogeneity - It provides the closeness among the element distribution in the diagonal of the Gray Level Co-occurrence Matrix.

Information Measures 1 - It measures the Entropy. Information Measures 2 - It measures the Entropy.

Inverse Difference Normalized - It inverses the contrast normalization.

Inverse Difference Moment Normalized - It normalize the homogeneity.

Maximum Probability - It provides the maximum value of Gray Level Co-occurrence Matrix.

Sum average - It results the higher weights to higher index of marginal Gray Level Co-occurrence Matrix.

Sum Entropy - It results the higher weight on higher sum of index entropy value.

from average value of Gray Level Co-occurrence Matrix.

Sum of Variance- It is the higher weights that differ from entropy value of marginal Gray Level Co-occurrence Matrix.

E. Feature selection

The features (Energy, Entropy, Dissimilarity, Contrast, Inverse difference, correlation, Homogeneity, Autocorrelation, Maximum probability, Sum of Squares, Sum Average, Sum Variance, Difference variance, Difference entropy, Maximal correlation coefficient, Inverse difference normalized (INN)) exhibited statistically significance difference at the level ($p < 0.05$) between the normal and diabetic groups.

F. Classifier Construction

The extracted features are then used to construct the binary classifier. The result of such a classifier is to represent either the “normal” or “abnormal” group. Artificial Neural Network (ANN) have been applied. It has three blocks : input, hidden and output layer. In our case we use only one hidden layer compressing of ten neurons. The network was trained for significant level $p < 0.05$.

G. Image Post-processing

The image may be misclassified for isolated super-pixels. To refine the super-pixels morphological closing operation was performed.

III. RESULTS AND DISCUSSION

The SLO images obtained was processed using the proposed approach using MATLAB 2016 prototype and the result for the normal and diabetic retinal conditions are displayed in Fig.2 and Fig.3.

The 22 texture features were extracted from the processed images. Some of the features such as Autocorrelation, Cluster shade, Cluster prominence, Contrast, Energy, Entropy, Dissimilarity etc., were extracted. These texture features were analyzed and the difference between the normal and diabetic values were studied. Table: 1 indicates the texture features extract- ed from retinal image for the total population (N=30).

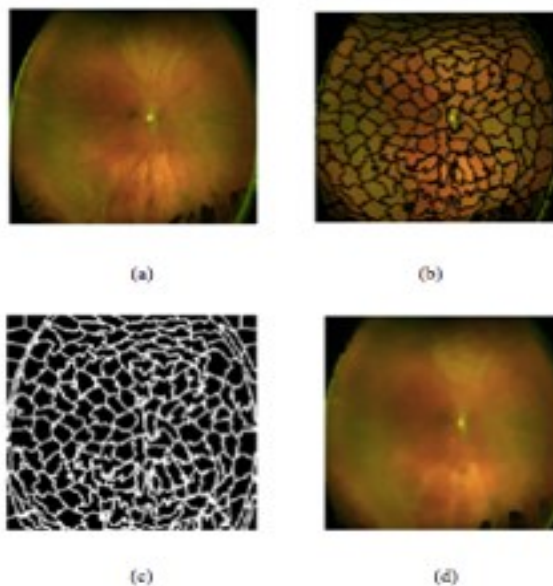


Fig. 2: Normal retinal image: (a) input image (b) superpixel (c) label (d) postprocessing

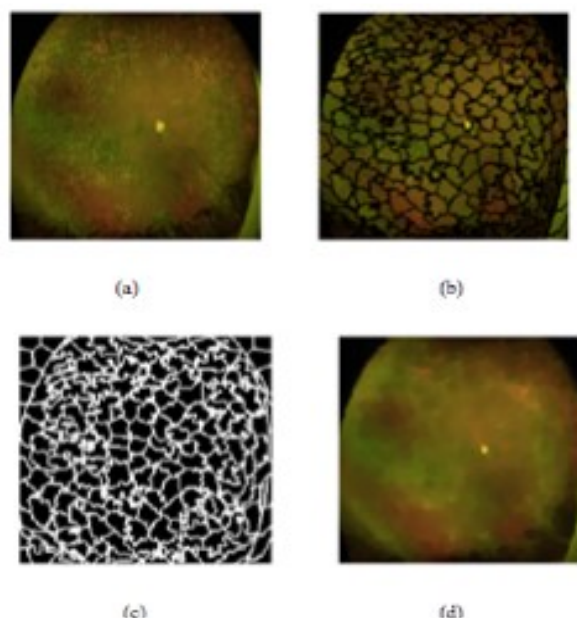


Fig. 3: Abnormal retinal image: (a) input image (b) superpixel (c) label (d) postprocessing

TABLE I. TEXTURE FEATURES EXTRACTED FOR THE TOTAL POPULATION (N=30)

TEXTURE FEATURES	NORMAL (Mean±SD)	ABNORMAL(Mean±SD)	p-value
Autocorrelation	5.59±1.24	4.28±1.00	0.0112*
Contrast	1.33±0.50	0.89±0.03	0.0235*
Correlation	0.51±0.04	0.58±0.05	0.0006**
Correlation	0.51±0.04	0.58±0.05	0.0006**
Cluster Prominence	49.31±38.06	40.32±22.42	0.5035
Cluster Shade	5.07±3.19	5.17±3.04	0.9299
Dissimilarity	0.57±0.11	0.45±0.11	0.0089**
Energy	0.17±0.02	0.22±0.06	0.0039**
Entropy	2.18±0.18	1.98±0.24	0.0154*
Homogeneity	0.80±0.03	0.84±0.03	0.0056**
Homogeneity	0.78±0.03	0.82±0.04	0.0049**
Maximum probability	0.29±0.07	0.37±0.08	0.0142*
Sum of squares	6.17±1.45	4.67±1.12	0.0118*
Sum average	4.39±0.44	3.81±0.47	0.0034**
Sum variance	11.31±3.09	8.31±2.21	0.0162*
Sum entropy	1.72±0.16	1.59±0.18	0.0589
Difference variance	1.32±0.50	0.88±0.31	0.0239*
Difference entropy	0.97±0.10	0.85±0.12	0.0058**
Information measure of correlation1	-0.33±0.03	-0.34±0.05	0.4599
Information measure of correlation2	0.79±0.07	0.74±0.05	0.0805
Inverse difference normalized (INN):	0.94±0.01	0.96±0.01	0.0047**
Inverse difference moment normalized:	0.98±0.02	0.99±0.01	0.1236

* p<0.05 and ** p<0.01

From the results predicted from the Matlab software, significant difference exist between the two groups for the following features: Energy, Entropy, Dissimilarity, Contrast, Inverse difference, correlation, Homogeneity, Autocorrelation, Maximum probability, Sum of Squares, Sum Average, Sum Variance, Difference variance, Difference entropy, Maximal correlation coefficient, Inverse difference normalized (INN) ($p < 0.05$). The neural network classifier could identify the diabetic subjects at an accuracy, sensitivity and specificity of about 86.7%, 80% and 90% at $p < 0.05$ using BPN respectively.

Siva et al [7] in their study employed Dennis Gabor translates and Support vector machine (SVM) classifier for retinal image classification. The sensitivity and specificity

were 76% and 99.8%. In our case using SVM sensitivity and specificity was obtained as 78.7% and 82.6% respectively. Maule et al [9] in their study implemented partition of ROI as traditional, exudates, vessels and optic disc prior to texture feature extraction. Haleem et al [10] in their study implemented sequential forward selection approaches and filter approach for feature selection. They proposed a combined feature selection using sequential forward selection and filter approach to utilize all the extracted features. In our case, significant level of $p < 0.05$ was used for feature selection and 16 features were utilized for network classification.

IV. CONCLUSION

Based on the results of the study it is evident that there is a statistical significant difference between the texture features extracted from normal and diabetic SLO images. The proposed system performed with an accuracy, sensitivity and specificity of 86.7%, 80% and 90% at $p < 0.05$ using BPN respectively. Therefore, the texture features extracted from SLO images can be used for classifying normal and abnormal subjects. The major limitation of the study is that it involves smaller sample size.

REFERENCES

- [1] Yorston, David. "Retinal diseases and VISION 2020." *Community Eye Health* 16.46 (2003): 19-20.
- [2] Nazimul, Hussain, Khanna Rohit, and Hussain Anjli. "Trend of retinal diseases in developing countries." *Expert Review of Ophthalmology* 3.1 (2008): 43-50.
- [3] Baben et al, 'Retinal Area Detector for Classifying Retinal Disorders from SLO Images', *IJRST –International Journal for Innovative Research in Science & Technology* | Volume 3 | Issue 04 | September 2016 ISSN (online): 2349-6010.
- [4] Achanta et al, 'SLIC Superpixels', EPFL Technical Report 149300.
- [5] Albregtsen (2008), 'Statistical Texture Measures Computed from Gray Level Co-occurrence Matrices', Image Processing Laboratory Department of Informatics University of Oslo.
- [6] Girardi et al(2015), 'Role of GLCM Features in Identifying Abnormalities in the Retinal Images', *I.J. Image, Graphics and Signal Processing*, 6, 45-51 Published Online May 2015 in MECS (<http://www.mecspress.org/>) DOI: 10.5815/ijigsp.2015.06.06.
- [7] Sivakumar et al(2011), 'Classification and Detection of Retinal Diseases', *International Conference on Signal, Image Processing and Applications With workshop of ICEEA IPCSIT vol.21 IACSIT Press, Singapore*.
- [8] Deepthimaris et al(2013), 'Detection and Feature Extraction of Abnormal Retinal Vessels in Diabetic Retinopathic Images', *National Conference on System Design and Information Processing - 2013*.
- [9] Maule et al(2015), 'A review on GLCM feature extraction in Retinal Image', *IJAR CET Volume 4 Issue 9, sep*.
- [10] Haleem et al, 'Supapixel based Retinal Area Detection in SLO Images', *Lecture Notes in Computer Science*.
- [11] Mohanaiah et al(2013), 'Image Texture Feature Extraction Using GLCM Approach' *International Journal of Scientific and Research Publications*, Volume 3, Issue 5, May 1 ISSN 2250-3153.
- [12] Geetanjali et al(2016), 'Automatic Detection of True Retinal Area and Diagnosing Retinal Disease using SLO Images', *IJAR CCE International Journal of Advanced Research in Computer and Communication Engineering ISO 3297:2007 Certified Vol. 5, Issue 7, July*.

Detection of Tuberculosis Bacilli from Microscopic Sputum Smear Images

Evangelin Sugirtha G
Dept of Computer Science and Engg.
St. Joseph's College of Engineering
Chennai, India
evangelinesugirtha@gmail.com

Murugesan G
Dept of Computer Science and Engg.
St. Joseph's College of Engineering
Chennai, India
murugesh02@gmail.com

Abstract— Tuberculosis is a contagious illness caused by the *Mycobacterium Tuberculosis*, also known as Koch bacillus. Many developing countries follow the manual method for diagnosing TB, which causes false alarms in the detection of TB positive and negative. In order to reduce the intervention of human we have developed an effective algorithm as an automated system for the detection of tuberculosis bacilli. This paper proposes a color segmentation and classification approach for automatic detection of *Mycobacterium Tuberculosis*, which causes TB from the image of Ziehl-Nielsen stained sputum smear obtained from a bright microscope. Segment the bacilli called candidate bacilli using its characteristics from the image using Particle Swarm Optimization technique, depending on pixel intensities. The candidate bacilli are then grouped together using connected component analysis after using morphological operations. Detection of Tuberculosis bacilli from sputum smear by random forest technique is a prominent method used in diagnosing the tuberculosis by classifying the subject samples. The combination of particle swarm optimization and random forest classification provides better results and correct diagnosis in term of infection level. The experimental result shows that our approach is significantly better compared to the existing approaches.

Keywords— *Particle swarm optimization; Random Forest Classification; Ziehl Neelsen staining; Sputum smear imag; Canny Edge detector*

I. INTRODUCTION

Tuberculosis is an infectious disease caused by *Mycobacterium bacillus*, so called as *Mycobacterium tuberculosis*, a multi-systemic communicable disease. *Mycobacterium* is a rod-shaped bacillus of length 2 to 4 μm and breadth 0.2 to 0.5 μm of size [1]. These bacteria usually affect lungs, but they can also infect other parts of the body too. TB is spread from person to person through the air usually when a person cough, spit or sneeze. They propel the tiny droplets containing tubercle bacilli into the air. A person needs to inhale only a few of these bacilli to become infected. TB is a major global health problem and it causes illness among millions of people every year and ranks alongside the human immunodeficiency virus (HIV) as a leading cause of death worldwide. TB, mostly affects adults in their productive years. However, all age groups are at risk. 1 Million Children (0-14 years of age) fell ill with TB, and 170,000 children died from

the disease in 2015 according to World Health Organization (WHO) report 2016. There are two methods used to identify the *Mycobacterium bacilli* through coloring agents: with a sputum smear and with a sputum culture. Also, there are two staining methods proposed in the literature, they are Ziehl Neelsen (ZN) staining and auramine staining methods. Sputum smears microscopy using the ubiquitous ZN stain. The primary diagnostic strategy for active tuberculosis (TB) is being expressed the good opinion by the World Health Organization.

The sputum smear is collected from TB suspecting patient in the morning. Ziehl –Neelsen staining process is used to stain the sputum smear. It uses the component to stain as the 0.5% carbol fuchsin, 25% sulfuric acid or 3% acid alcohol and methylene blue solution. The bacilli region is stained as red color by a ZN staining method. The stained slides are captured by conventional microscope. Nikon eclipse 80I microscopy at 100x magnification is used, MA88-300 digital camera attached to a microscope for image acquisition. It will produce the vivid 640X480 images. The taken images were stored in the JPEG format. This paper aims to detect TB bacilli from Ziehl Neelsen stained (ZN stained) sputum smears, using an algorithm comprising segmentation of candidate bacillus objects and classification of segmented objects.

Image segmentation is a low-level image processing work aiming at partitioning an image into homogeneous regions [2]. In this proposed method, we use particle swarm optimization for the thresholding based segmentation. The PSO technique is a stochastic method to find the neighborhood optimal thresholds by reducing their cross entropy between original image and its threshold version. In this algorithm, entropy criterion has been used as fitness value and near optimal threshold value has been searched out through maximizing the normal entropy function.. The PSO technique has been used to solve the problem of thresholding based segmentation. After segmentation, we perform the post processing method as edge detection and morphological processing.. We use a canny operator for edge detection [2]. Canny edge detector uses a multilevel algorithm to detect a wide limits of edges in the image. It has set of image processing tasks as: smoothing the image with Gaussian filter, computing the gradient using partial derivative, find the magnitude and orientation of gradient, non-maxima suppression, double thresholding. The

morphological operations such as closing and opening operation are performed based on concatenation of dilation and erosion to provide structure for the detected edges. Then using connected component labeling method, we count number of objects in the image. For connectivity of object, we can assign 4 or 8 for binary images. The feature extraction parameters like eccentricity and axis length are calculated for each bacillus. Classification is a next steps to classify each bacilli based on feature extraction metrics and conditions.

Random forests are an ensemble learning method that uses the results from many different models to calculate a response [4]. In most cases the result of an ensemble model will be better than the result from any one of the individual models. In the case of random forests, several decision trees are created (grown) and the response is calculated based on the outcome of all of the decision trees

The types of diagnosis of TB, recent advances for the diagnostic algorithm and detection of pulmonary tuberculosis are given in [8]. In clinical practice, rapid TB diagnosis and early detection of pulmonary TB continues to be challenging for clinicians. New technology has arrived and implemented to detect the TB. In Smear Microscopy, collect sputum smear as inputs to staining procedure. Sputum smear can be stained to detect the acid bacilli in the Mycobacterium tuberculosis for diagnosis of tuberculosis. The method of hot Ziehl- Nielsen staining techniques are discussed in [9][10]. It uses the Carbol fuschin solution. Then it uses the decolorizing agent as 25% sulfuric acid and 3 %acid alcohols. Then it is allowed to dry with light source. Then it will capture with light microscope and it's sent to the system in the format of JPEG. Medical diagnosis and treatment is an intellectual process. There are three major potential benefits of automated diagnosing system. (1) Upgraded safety of patients (2) enhanced efficiency in health care outcomes and (3) improved quality of care. A fully automatic detection system can automatically analyze the presence of TB Bacteria quickly from focusing images. It can be processed by the set of process as image segmentation, feature extraction and pattern recognition. The paper [2] describes about the segmentation of bacilli in the image PSO technique is used to threshold the pixel in the image and uses the parameter such as fitness value and weight factors to segment the red bacilli. The segmented image is post processed by the edge detection and morphological processing. Random Forest, like decision trees, can be used to solve classification and regression problems, but it is able to overcome the drawbacks with single decision trees [8]. The paper [11] reviewed the whole microscopic image processing method and suggest the random forest technique as well as genetic algorithm. It provides the best results compared to the neural network and it will be the most advanced one [6].

This paper is organized as follows. Section 2 explains the each step elaborately in pseudocode algorithmic manner. Section 3 provides the experimental results and configuration of experiments. It also explains the metric used in the systems. Section 4 discusses the method to automate the TB Bacilli detection.

II. METHODS AND MATERIALS

The sequence of steps to be performed to detect the bacilli are follows:

- (i) Image acquisition
- (ii) Image segmentation
- (iii) Image post processing
- (iv) Image classification

A. Image Acquisition

The first and foremost step of image processing is image acquisition. In this paper, we have used ZN stained images to identify the TB bacilli and which is recommended by WHO. The ZN stained image is obtained from the Ziehl-Neelsen Sputum smear Microscopy image Data Base (ZNSM-iDB) is a repository for smear microscopy digital images obtained from three different microscopes. The images are in JPEG format and there is no limitation in the size of the image. The images are then undergoing image preprocessing steps to correct the non-uniform background illumination and convert the image into binary form so that we can perform analysis on image foreground objects.

B. Image Segmentation

Once the image acquisition and the preprocessing process are over, then image is ready to be processed further. The next step in the image processing is image segmentation to divide the whole image into number of regions or objects. The level of subdivision always depends on the problem of interest, where the segmentation gets over when the object of interest in the problem is isolated. In general the image segmentation algorithms are based on the main two properties of intensity values: discontinuity and similarity. In this paper we have used the Particle Swarm Optimization (PSO) algorithm to segment the bacilli from the image. PSO is a similarity based thresholding algorithm. PSO is a population-based optimization method modeled after the simulation of social behavior of birds in a flock [2]. It is initialized with a group of random particles (solutions) and then searches for optima by amending generations. Each particle is flown through the search space having its position adjusted based on its distance from its own personal best position and the distance from the best particle of the swarm. The performance of each particle, i.e. how close the particle is from the global optimum, is measured using a fitness function which depends on the optimization problem.

Each particle, i , aviates through an n -dimensional search space, R^n , and maintains the following information:

- x_i , the current position of i^{th} particle (x - vector),
- B_i , the personal best position of i^{th} particle (c - vector), and
- v_i , the current velocity of i^{th} particle i (v - vector)

$$b_i(t+1) = \begin{cases} b(t) & \text{if } f(x_i(t+1)) \geq f(b_i(t)) \\ x_i(t+1) & \text{if } f(x_i(t+1)) < f(b_i(t)) \end{cases} \quad (1)$$

If the position of the global best particle is denoted by g_{best} , then:

$$g_{best} \in \{b_1(t), b_2(t), \dots, b_m(t)\} = \min\{f(b_1(t)), f(b_2(t)), \dots, f(b_m(t))\} \quad (2)$$

The velocity updates are calculated as a linear combination of position and velocity vectors. Thus, the velocity of particle i is updated using equation (3) and the position of particle i is updated in (4).

$$v_i(t+1) = w v_i(t) + c_1 r_1 (p_i(t) - x_i(t)) + c_2 r_2 (g_{best} - x_i(t)) \quad (3)$$

$$x_i(t+1) = x_i(t) + v_i(t+1) \quad (4)$$

In the formula, w is the inertia weight [2], c_1 and c_2 are the acceleration constants, r_1 and r_2 are random numbers in the range $[0,1]$ and V_i must be in the range $[-V_{max}, V_{max}]$, where V_{max} is the maximum velocity. The RGB image segmented by PSO is shown in Fig. 3 (b). The segmented image is in the RGB format. The blue component of the image will be extracted to get the red bacilli alone. Then it will be post processed by the canny edge detector and morphological processing.

C. Image Postprocessing

After segmentation, Image has to be processed by contrast enhancement to highlight the bacilli alone. For post processing, we perform the operation such as edge detection and morphological processing. In edge detection, canny operator is used to detect the edges. In morphological operation, opening and closing operations are used to get the structure of bacilli and the number of bacilli, eccentricity and axis length.

1) *Canny Edge Detection*: Canny edge detection is a multi-step algorithm that can detect edges with noise suppressed at the same time. The following steps are used to perform canny edge detection operation.

Step 1: Smooth the image with a Gaussian filter to reduce noise and unwanted details and textures which optimize the trade-off between noise filtering and edge localization.

$$I' = g(x, y) * I \quad (4)$$

where

$$g(x, y) = \frac{1}{\sqrt{2\pi\sigma^2}} e^{-\frac{x^2+y^2}{2\sigma^2}} \quad (5)$$

Step 2: Compute the gradient magnitude using approximation of partial derivatives. The edges should be marked where the gradients of the image has large magnitude

$$\nabla g = \begin{bmatrix} \frac{\partial g}{\partial x} \\ \frac{\partial g}{\partial y} \end{bmatrix} = \begin{bmatrix} g_x \\ g_y \end{bmatrix} \quad (6)$$

(7)

$$S = \nabla(g * I)$$

$$= (\nabla g) * I = \begin{bmatrix} g_x \\ g_y \end{bmatrix} * I$$

Since

$$\begin{bmatrix} g_x * I \\ g_y * I \end{bmatrix}$$

Let $h = g$ then the two dimensional Gaussian becomes

$$h_x(x, y) = \frac{\partial h(x, y)}{\partial x} = \frac{-x}{\sqrt{2\pi\sigma^4}} e^{-\frac{x^2+y^2}{2\sigma^2}} \quad (8)$$

$$h_y(x, y) = \frac{\partial h(x, y)}{\partial y} = \frac{-y}{\sqrt{2\pi\sigma^4}} e^{-\frac{x^2+y^2}{2\sigma^2}} \quad (9)$$

Step 3: Find the magnitude and orientation of gradient vector $S = [S_x \ S_y]$ Using any gradient operators (Roberts, Sobel, Prewitt, etc.) to get

$$\text{Magnitude } M(x, y) = \sqrt{S_x^2(x, y) + S_y^2(x, y)} \dots \quad (10)$$

$$\text{Direction } \theta(x, y) = \tan^{-1} \left(\frac{S_y(x, y)}{S_x(x, y)} \right) \quad (11)$$

Step 4: Find the threshold M

$$M_T(x, y) = \begin{cases} M(x, y) & \text{if } M(x, y) > T \\ 0 & \text{otherwise} \end{cases} \quad (12)$$

Where T is so chosen that all edge elements are kept while most of the noise is suppressed.

2) *Morphological Operations*: The detected edges will be processed by morphological processing. Dilation and erosion are often applied to an image in concatenation. Open operation is an erosion followed by a dilation The open operation breaks this connections and clears isolated pixels with binary values of 1. In image processing, closing is, together with the opening, the basic work horse of morphological noise removal. Opening removes small objects, while closing removes small holes. Number of components can be calculated by connected component labeling method

D. Feature Extraction

Using the component labeling method, we found the number of objects of interest. To find the number of objects, it uses 8 connected component labeling method in binary image (refer Fig. 2(e)). connected component labeling method is performed as follows.

Step 1: Read the binary image(Fig. 2(e)) and run length encode the input binary image.

Step 2: Scan the run assigning preliminary labels equivalence in a local equivalence table.

Step 3: Hence the number of 1's in the binary image local equivalence table connect with the likely neighborhood pixel with 8 directions, such as east, west, north, south, northeast, southeast, northwest and southeast. Resolve the equivalence class

Step 4: Relabeled the runs based on the resolved equivalence class.

For each bacilli, we have to calculate the feature extraction parameters. Select the feature extraction parameter as eccentricity, compactness, area, perimeter, minor axis length and major axis length. Set the threshold value for eccentricity at 0.65. Set the threshold value for the axis ratio as 1.25 to detect the TB Bacilli. This part is essential to classify and detect the bacilli.

E. Image Classification

By using feature extraction parameters, the next step is classification process. Here we use a Random Forest Classification, Random forests or random decision forests are an ensemble learning approach for classification, regression and other tasks, that operate by constructing a collection of decision trees at training time and outputting the class that is the process of the classes (classification) or mean prediction (regression) of the individual trees. Random decision forests correct for the decision tree's habit of overeating to their training set. To classify each bacilli, calculate the axis length, eccentricity area within bacilli and build a classification tree based on the criteria as axis ratio should be in the range of 1.25 and eccentricity as 0.65. The following are the steps used to perform random forest classification process

- For each tree in forest
 - a. Take a bootstrap sample of data.
 - b. Randomly select variables.
 - c. For each variable selected, find the split point which minimizes Mean square error.
 - d. Split the data using variables with the lowest Mean Square Error.
- Repeat steps (b) to (d) until some stopping condition is satisfied or all the data is exhausted.
- Repeat this process to build several trees .

To make a prediction, run an observation on several trees and average the predicted values from all the trees. Or find the most popular class of the majority voting method. Hence classification trees will be built by using a feature extraction parameters and the condition to satisfy the characteristics of the TB bacilli.

Building Classification Tree

- Step 1. Calculate Axis length ratio as Major Axis Length / Minor Axis Length
- Step 2. Set the threshold value for the axis ratio should be above the range of 1.25.
- Step 3. Calculate the eccentricity
- Step 4. Calculate μ and σ of each object.
- Step 5.** Calculate area, if it is between the ranges of $1.5\sigma \pm \mu$. then it is definite bacilli.

The outcomes received from the classification tree, we need to accumulate each of the positive TB bacilli to conclude that whether the images are taken from the TB affected person or not by counting the number of TB bacilli in the smear image.

F. Proposed System

The procedure for detection of TB Bacilli using image processing technique is follows.

- Step 1. The input image is acquired through conventional microscope and Ziehl Nielsen Staining method

- Step 2. The bacilli region present in the image is segmented using Particle Swarm Optimization and the blue component is extracted .Fig. (b) (c).
- Step 3. For segmented images edges are detected using the canny operator. Fig. (d)
- Step 4. Morphological operation such as opening, closing image is carried out to focus only on bacilli alone and remove artifact. Fig. (e).
- Step 5. Through connected component labeling method, number of objects in the image are found.
- Step 6. The feature extraction parameters such as axis length, eccentricity are used to classify bacilli by building classification trees.
- Step 7. Aggregate the several classification trees for each bacillus, based on smear result table, detect the patients have a TB or not .

III. EXPERIMENTAL RESULTS AND ANALYSIS

In order to prove the correctness of the proposed method, 50 tissue slide images are stored to detect the TB bacilli. To acquire the image, Nikon eclipses 80I microscopy at 100x magnification is used, MA88-300 digital camera attached to ocular on a microscope for image acquisition. It will produce the vivid 640X480 images.

A. Performance Metrics

For a set of images, we assign the values for arguments such as predefined PSO population for multi-segmentation $N=150$. Individual weight of particles is 0.8, social weight of particles is 0.8, inertial factor as 1. 2. The edge operators are used to detect the edges of the bacilli by using pixel gradient. Set the pixel gradient value as 0.5. If a pixel gradient is higher than the *upper* threshold, the pixel is accepted as an edge. If a pixel gradient value is below the threshold, it is rejected. If the pixel gradient is between the two thresholds, then it will be accepted only if it is connected to a pixel that is above the *upper* threshold.

Then the morphological processing as opening and closing operation are to concatenate the dilation and erosion methods. The Connected component labeling method can be used to count number of objects in the image and it assigns the 8 connectivity to connect the same likelihood pixels. For feature extraction, we used the parameters, eccentricity, axis length of the bacilli with the threshold value of eccentricity as 0.90 and axis length ratio as 2.50. From the given image, the proposed system found that there are 30 numbers of bacilli, its eccentricity and axis length ratio are tabulated in the following Table 1 and Table 2.

TABLE 1. Metrics for TB bacilli detection

Bacillus	Eccentricity	Area	Axis length ratio
1	0.9410	41	2.95
2	0.9557	98	3.39
3	0.7720	47	1.57
4	0.6190	19	1.27
5	0.6717	58	1.34
6	0.5106	53	3.98
7	0.6614	12	1.33
8	0.7464	23	1.50
9	0.5585	98	1.20
10	0.9605	171	3.59
11	0.9681	113	5.22
12	0.9815	98	2.78
13	0.9768	28	1.61
14	0.8436	34	1.86
15	0.9750	98	4.49
16	0.9785	118	4.84
17	0.9214	105	2.57
18	0.9474	61	3.12
19	0.4933	98	1.14
20	0.7198	62	1.44
21	0.8855	26	2.26
22	0.9763	107	3.86
23	0.8207	112	4.66
24	0.7852	15	1.67
25	0.8000	40	1.21
26	0.5620	32	1.92
27	0.9659	53	2.87
28	0.9375	106	3.80
29	0.8000	15	1.67
30	0.8000	15	1.67

Classification Tree

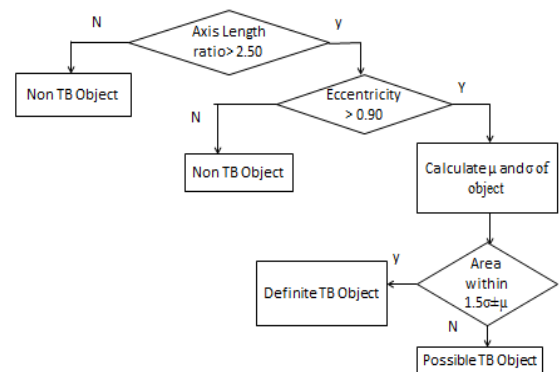


Fig. 1. Classification Tree for Identification of TB

According to feature extraction parameter, we build a classification tree for each bacillus. Then it aggregates the each classification to detect the bacilli based on tuberculosis grading chart. A Random forest technique is used to classify the bacilli. After choosing the data eccentricity, axis length and area, we perform CART (classification and Regression tree) algorithm [7]. The bold face values from the area column of the above table are the value of the TB bacillus which is the object of interest in this paper. Due to the presence of enough number of bacilli one can conclude that the samples are taken from the TB affected person.

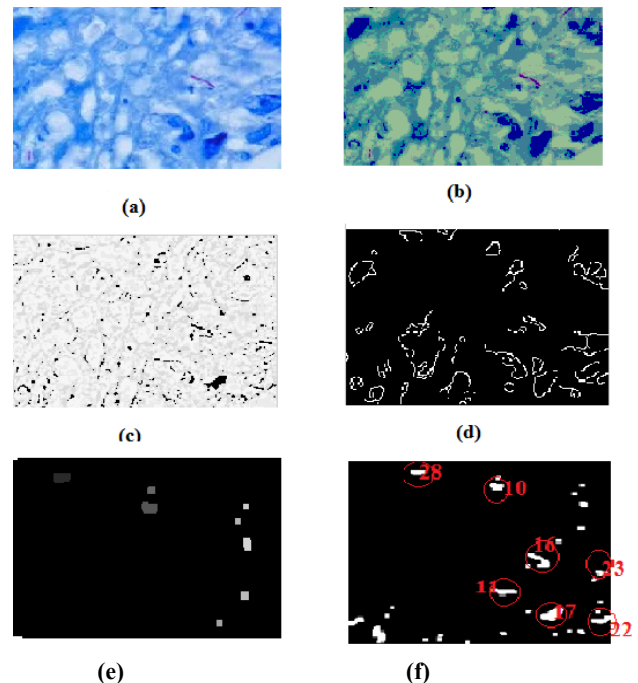


Fig. 2. (a) sputum smear image (input image), (b) PSO Segmented image. (c) blue component extraction, (d) edge detection and (e) morphological operation. (f) TB bacilli is rounded with red color circle(output image).The Definite TB object is detected and rounded by red circle.

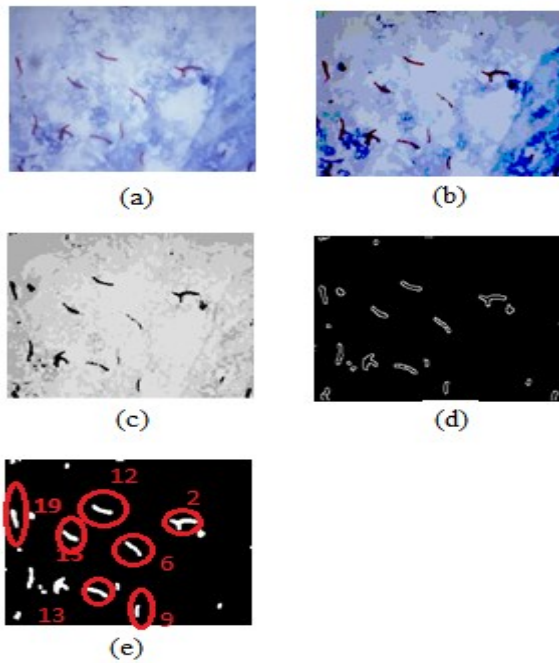


Fig. 3. (a) sputum smear image (input image), (b) PSO Segmented image. (c) blue component extraction, (d) edge detection and (e) morphological operation.

TABLE 2 .Metrics for Tuberculosis Detection

Bacillus	Eccentricity	Area	Axis length ratio
1	0.9410	41	2.95
2	0.9557	105	3.39
3	0.7720	47	1.57
4	0.6190	19	1.27
5	0.6717	58	1.34
6	0.9681	113	3.98
7	0.6614	12	1.33
8	0.7464	23	1.50
9	0.5585	171	1.20
10	0.9605	98	3.59
11	0.5106	23	2.78
12	0.9815	120	5.22
13	0.9768	112	4.66
14	0.8436	34	1.86
15	0.9750	118	4.49
16	0.9785	98	4.84
17	0.9214	98	2.57
18	0.9474	61	3.12
19	0.4933	175	1.14
20	0.7198	62	1.44
21	0.8855	26	2.26

IV. CONCLUSION

Microscope imaging and digital image processing of microscope images has opened up new realms of medical research and brought about the possibility of advanced clinical diagnostic procedures. This paper proposes a novel approach to the detection of Tuberculosis Bacilli from ZN stained sputum images using Particle Swarm Optimization algorithm for image segmentation and Random Forest algorithm for image classification. The proposed method of detection of tuberculosis bacilli through digital image processing has witnessed a better result compared to the experiment results. In this work, automated analysis on enhancing the diagnostic relevance of tuberculosis is comprehensively analyzed using pre-processing, segmentation, feature extraction, separation of overlapping bacilli. Artificial intelligence based classification leads to speedup the diagnosis, to improve the accuracy and to reduce the workload of laboratory technicians. In future, the image level classification can be extended to slide level classification so that 10 to 100 images are analyzed per slide. Also, severity analysis depends on the number of bacilli present in an image which could be performed.

REFERENCES

- [1] Ciero Fierreira Fernandes, Costa Filho, Campus Levy, Clahidek de Matos Xavier, Luciana Botinelly Mendonca Fujimoto and Marly Guimaraes Fernandes Costa, "Automatic identification of tuberculosis, Mycobacterium", Research on Biomedical Engineering, 2015, Vol. 31, pg.33-43.
- [2] Fahd Mohsen Hadhoud, Kamal Mostafa and Khalid Amin, "A new image segmentation based on Particle Swarm Optimization", International Arab journal of Information Technology, 2012, Vol 9, No. 5, pg. 487-493.
- [3] Ned Horning, "Random Forests :An algorithm for image classification and generation of continuous field data sets", International Conference on Geoinformatics for Spatial Infrastructure Development in Earth and Allied Sciences, 2010. Pg. 1-6.
- [4] Osman M.K, F. Ahmad, Z. Saad and M. Y. Mashor, H. Jaafar, "A Genetic Algorithm-Neural Network Approach for Mycobacterium Tuberculosis Detection in Ziehl-Neelsen Stained Tissue Slide Images", Proceeding of the International conference on Intelligent Systems Design and Applications (ISDA), 2010, pg. 1229-1234.
- [5] Rani Ooman Panicker, Biju Soman, Gagan Saini & Jeny Rajan, "Review of Automatic methods Based on Image Processing Techniques based for Tuberculosis detection from microscopic sputum smear Images" Journal of Medical Systems, 2016, Vol. 40, No.17, pg.1-13.
- [6] Rohit Nayak, Vishnu Prasad Shenoy and Ramesh R. Galigeke, " New algorithm for automatic assessment of the degree of TB-infection using images of ZN-stained sputum smear" Proc. of International Conference on Systems in Medicine and Biology (ICSMB), Kharagpur, 2010, pg. 294-299.
- [7] Salem Ayas and Murat Ekinci, "Random forest – based tuberculosis bacteria classification in images of ZN Stained Sputum Smear Samples", Signals, Image and Video Processing, 2014. Vol.8, No. 1, pg. 49-61.
- [8] Yon Ju Ryu.M.D, "Diagnosis of pulmonary Tuberculosis : Recent Advances and Diagnostic Algorithm", Tuberculosis and Respiratory Diseases, 2015, Vol.78, No.2, pg. 64-71.
- [9] Zingue dezemon, Claude Mambo Muvuny and Otu Jacob, (2014), "Staining techniques for detection of acid fast bacilli: what hope does fluorescein diacetate vitality staining technique represent for the monitoring of tuberculosis treatment in resource limited setting", Trends in Bacteriology, 2014, Vol.1, No. 1, pg. 1-6.
- [10] Civic Kose, Rengul Cetin Atlay and A. Enis Cetin, "Special issue on microscopic image processing", Signals, Image and Video Processing, 2014. Vol.8, No. 1, pg. 1-3.

An fNIRs Study to Classify Stages of Learning from Visual Stimuli Using Prefrontal Hemodynamics

Amiyangshu De¹, Amit Konar¹, Amalesh Samanta²

¹Dept. of Electronics and Telecommunication Engg.

²Dept. of Pharmaceutical Technology.

Jadavpur University, Kolkata, India.

amiyangshu_de@yahoo.com, konaramit@yahoo.co.in,
asamanta61@yahoo.co.in.

Souvik Biswas³, Piyali Basak³

³School of Bioscience and Engineering

Jadavpur University, Kolkata, India.

souvikbiswas.res@gmail.com, piyalibasak@gmail.com.

Abstract— A wide range of research exists on fMRI imaging and psychological assessment based memory and/or learning studies. However, absence of literature is observed in fNIRs based memory and learning research. This paper provides a novel study of prefrontal hemodynamic changes of subjects engaged in multiple trial paired-associate learning. The direct measure of prefrontal hemodynamic is collected by fNIRs machine. The raw signals are pre-processed (to filter out artifacts) to extract 144 features for each feature pool which are reduced to 36 using principal component analysis (PCA). From three pools of features, the most relevant feature pool is sorted out considering algorithms' classification performance. Learning stages are classified from 'ZERO' learning using three conventional classifiers (RBF-SVM, LSVM and LDA). Experimental analysis reveals RBF-SVM algorithm has the highest performance in classification of learning trials which reaches over 93%. Analysis of hemodynamic features shows greater total hemoglobin load in orbitofrontal (OFC) and medial prefrontal cortex (mPFC) in initial learning trials which shifts to dorsolateral (DLPFC) and ventrolateral prefrontal cortex (VLPFC) areas when learning is complete. We also observe the engagement of working memory in initial learning stages. This findings also can be useful to justify low learning ability among individuals with neurovascular deficits.

Keywords— *fNIRs, Hemodynamic-response, Paired-associate learning, Independent component analysis, RBF-SVM, LSVM, LDA.*

I. INTRODUCTION

Cognitive studies based on brain computer interface (BCI) research is drawing immense interest due to its capacity in revealing biological basis of different cognitive processes. Involvement of brain areas depends on the complexity of cognitive processing – different cognitive tasks involve different brain areas. However, cognitive task performance naturally depends on the supply of oxygenated blood to the specific brain regions [1]. Measurement of oxyhemoglobin (HbO) and deoxyhemoglobin (HbR) provides information about engaged brain areas in cognitive processes. A Functional Near Infrared Spectroscopy (fNIRs) machine

records oxyhemoglobin and deoxyhemoglobin concentration in brain areas over which its head-band is mounted. The present study tries to measure the prefrontal cortex (PFC) hemodynamic changes during paired-associate learning tasks from fNIRs signals.

Very few research clearly demonstrate the role of prefrontal cortex in learning behavior and memory. Also, low number of literature is available on the role of working memory in learning and memorization. Fletcher *et al.* reports the learning related neuronal responses in prefrontal cortex from fMRI study [2]. Gregory *et al.* reports the role of medial prefrontal cortex in memory retrieval and inferencing [3]. Euston *et al.* shows the role of medial frontal cortex in memory and decision making whereas, long time ago Asaad *et al.* demonstrated the neural activity of primate prefrontal cortex during associative learning [4-5]. Preston and Eichenbaum reviews the interplay of hippocampus and prefrontal cortex in memory [6]. Winocur and Moscovitch shows the role of hippocampus and prefrontal cortex in memory and learning using rat models [7]. Zhang *et al.* demonstrates the role of working memory in learning [8]. Low working memory performance in learning among children with developmental disorders is reported by Alloway and Archibald which is further investigated by Maehler and Schuchardt [9-10]. In addition, Salazar *et al.* shows content specific fronto-parietal synchronization in visual working memory tasks [11].

However, recent studies have not reported the relation between learning and changes in hemodynamic response – more specifically how hemodynamic parameters change from the beginning to the learning completion. How the neurovascular coupling changes during different cognitive activities (like learning and recall) is not yet clearly investigated. So, a functional near infrared spectroscopy study can produce an insight to understand the learning mechanism that further can provide a guideline to adopt personalized learning strategies for persons with different kinds of brain damage.

The paper aims to classify learning stages from formulated hemodynamic features. The recorded fNIRs data is filtered and preprocessed to remove artifacts. Three pools of features, each containing nine features, are constructed and feature

extraction is performed. A principal component analysis based technique reduces the feature dimension which is fed into different conventional classification algorithms to classify different learning stages from the 'ZERO' learning stage. Additional merit of the paper is biological implication to report the activated brain regions involved in learning and recall processes.

The paper is organized in the following ways: section II gives theoretical framework of learning and recall, principle of fNIRs device, and methods undertaken for normalization of data, data point reduction and classification. Section III contains experiments and results. Section V concludes the experimental outcomes.

II. PRINCIPLES AND METHODOLOGY

This section provides the principles, tools and techniques for the experiment. The followings are included in this section: (A) biological basis of learning and role of working memory, (B) principles of fNIRs, (C) normalization of fNIRs signals, (D) principal component analysis based feature reduction and (E) feature classification.

A. Biological basis of learning and role of working memory

Prefrontal brain regions and working memory plays important role in learning. But, when it is learned and information is transferred to long term storage, so, a subject can perform independent of working memory. Rehearsal (or recall) has important role in memory consolidation [12-13] Working memory performance is mostly related to prefrontal cortex (PFC) [14] But, functional differences is observed – left frontal cortex gets activated in verbal working memory tasks whereas, right frontal cortex is active in working memory tasks related to space. In addition lower brain areas are related to ventrolateral prefrontal cortex (VLPFC) and higher brain areas are associated with dorsolateral prefrontal cortex (DLPFC) [15]. We can also reports higher engagement of medial prefrontal cortex (mPFC) in different learning and memory performances. Orbitofrontal cortex is also involved in tasks related to sensory memory and affective processing. fMRI study shows the involvement of DLPFC in maintenance of working memory and long term memory performance [12].

B. Principles of Functional Nearinfrared Spectroscopy

The results from functional near-infrared spectroscopy show good correlation with PET and fMRI studies. The principle of fNIRs is based on the light absorption capacity of the biological tissues of the brain. As blood oxygen demand changes in different cognitive tasks, the light absorption capacity of oxyhemoglobin (HbO) and deoxyhemoglobin (HbR) also vary according to their concentration change. A near infrared light source transmit light of 700-900 nm that is absorbed, scattered and transmitted by the brain tissues. A linear relationship between light absorption (in nerve tissues) and prefrontal hemodynamic is obtained from fNIRs data through the application of modified Beer-Lamberts' law [16].

C. Normalization of Raw data

Scaling of the recorded data is done using the following technique: Let M_{HbO} and M_{HbR} be the oxyhemoglobin (HbO) and deoxyhemoglobin (HbR) concentrations respectively, measured in mili-mol/liter. Let $^{Max}M_{HbO}$ and $^{Min}M_{HbO}$ be the maximum and minimum concentration of HbO in a session. Considering a max-min technique of normalization, we get normalized values for HbO and HbR.

We normalize M_{HbO} by

$$M_{HbO} = \frac{(M_{HbO} - ^{Min}M_{HbO})}{(^{Max}M_{HbO} - ^{Min}M_{HbO})} \quad (1)$$

Similarly, M_{HbR} normalized by

$$M_{HbR} = \frac{(M_{HbR} - ^{Min}M_{HbR})}{(^{Max}M_{HbR} - ^{Min}M_{HbR})} \quad (2)$$

The parameters used in the last equation has similar meaning to those defined for M_{HbO} . This transformation returns normalized M_{HbO} and M_{HbR} in [0, 1]. We found this technique converts all the data in normal distribution.

D. Noise Removal

We undertake a digital bandpass filter (Chebyshev) with a pass band of 0.1-0.4 Hz to eliminate undesirable noises arise from different physiological artifacts like heart beat (1-1.5 Hz) respiration and Meyer's wave (<0.1 Hz) [17].

E. Feature Extraction

Three pools of features containing nine features in each of them is constructed. The nine features are constructed from 16 channel fNIRs data to get nine features/channel, i.e. a total of $16 \times 9 = 144$ features per set. Each participant undergoes 5 different sets of paired-associate learning. Hence for 10 participants the total feature matrix has a dimension of 50×144 . The three pools of features are described below:

Feature Set 1.

- 1) Mean value of HbO concentration.
- 2) Standard deviation of HbO concentration.
- 3) Skewness of HbO concentration.
- 4) Entropy of HbO concentration.
- 5) Mean value of total hemoglobin concentration.
- 6) Mean value of oxygen demand (HbO-HbR).
- 7) Standard deviation of total hemoglobin (HbO+HbR).
- 8) Skewness of total hemoglobin concentration.
- 9) Entropy of total hemoglobin concentration.

Feature Set 2.

- 1) Mean value of HbR concentration.
- 2) Standard deviation of HbR concentration.
- 3) Skewness of HbR concentration.
- 4) Entropy of HbR concentration.
- 5) Mean value of total hemoglobin concentration.
- 6) Mean value of oxygen demand (HbO-HbR).
- 7) Standard deviation of total hemoglobin (HbO+HbR).
- 8) Skewness of total hemoglobin concentration.
- 9) Entropy of total hemoglobin concentration.

Feature Set 3.

- 1) Mean value of total hemoglobin concentration.
- 2) Mean value of HbO concentration.
- 3) Mean value of oxygen demand.
- 4) Standard deviation of oxygendemand.
- 5) Standard deviation of total hemoglobin.
- 6) Skewness of total hemoglobin.
- 7) Skewness of oxygen demand.
- 8) Entropy of HbO concentration.
- 9) Entropy of HbR.

F. PCA based feature reduction

The advantage of using PCA is for a better resolution and improved classification of the data. We considered top 25% ranked (from PCA) features. Let us consider a matrix of n feature vectors for a stimulus s is represented by:

$$D_s = \left[\begin{array}{c} \bar{d}_1, d_2, \dots, \bar{d}_n \\ \vdots \\ \bar{d}_1, d_2, \dots, \bar{d}_n \end{array} \right]_{n \times E} \quad (1)$$

Thus, for p instances we construct matrix M such that,

$$P = \left[\begin{array}{c} D_1 \\ D_2 \\ \vdots \\ D_r \end{array} \right] = \left[\begin{array}{c} \bar{d}_1, d_2, \dots, \bar{d}_n \\ \bar{d}_1, d_2, \dots, \bar{d}_n \\ \vdots \\ \bar{d}_1, d_2, \dots, \bar{d}_n \end{array} \right]_{r \times E} \quad (2)$$

PCA reduces the matrix P into $m_{r \times e}$ such that $e < E$. The PCA steps are:

- 1) Each feature vector is adjusted by subtracting the average value of feature from each of its elements to have a zero mean. Thus the obtained matrix is stored as P' .
- 2) Next step is to find the Eigen Vectors. The Eigen Vectors can be found by the following equation:

$$c = \frac{1}{-E} P'^T P' \quad (3)$$

Find the Eigen vectors (\vec{V}) such that, $C\vec{V} = \lambda\vec{V}$, where $\det(C - \lambda I) = 0$.

- 3) Now, we project the data points along with principal components as the Eigen vectors is the principal components (\vec{PC}).

$$\psi = \vec{PC} \times P' \quad (4)$$

The projected data $\psi_{r \times E}$ is reduced to $\psi'_{r \times e}$ where the selected data points are related to highest Eigen values [18].

F. Classification of learning trials using RBF-SVM, LSVM, LDA.

Radial basis function support vector machine (RBF-SVM), linear support vector machine (LSVM) and linear discriminant analysis (LDA) are considered to classify learning states from the 'ZERO' learning state.

- (i) Linear Discriminant Analysis (LDA):

It is one of the frequently used classifier in brain computer interface (BCI) research. LDA algorithm is used to find an allocated vector ψ in the specified feature dimensions such that the desired target classes can be divided into distinct groups which maintain an effective variance. This characteristic can be obtained by Fisher's Criterion (Equation 5):

$$X(\psi) = \frac{\psi^T S_b \psi}{\psi^T S_w \psi} \quad (5)$$

Where, S_b and S_w are scatter matrices of between-class and within-class respectively and represented as following (Equation 6 and 7):

$$S_b = (a_1 - a_2)(a_1 - a_2)^T \quad (6)$$

$$S_w = \sum_{d_w \in \tau_1} (d_w - a_1)(d_w - a_1)^T + \sum_{d_w \in \tau_2} (d_w - a_2)(d_w - a_2)^T \quad (7)$$

Here, τ_1 and τ_2 are two distinct classes; a_1 and a_2 indicate the group means of the respective classes and d_w denotes samples. If a vector ψ satisfies equation 5, it can be represented as the following generalized Eigen value problem (Equation 8):

$$S_w^{-1} S_b \psi = \lambda \psi \quad (8)$$

Hence, the optimal vector ψ is now Eigen vector that corresponds to the largest Eigen values of $S_w^{-1} S_b \psi$. The optimal vector ψ can be obtained by the following formula (Equation 9):

$$\psi = S_w^{-1} (a_1 - a_2); \text{ until } S_w^{-1} \text{ is non-singular.} \quad (9)$$

- (ii) Linear Support Vector Machines (LSVM):

SVM algorithm tries to find the maximum distance within the hyperplane and support vectors. The equation of separating 2D hyperplane is as follows (Equation 10):

$$g(x) = cx = k \quad (10)$$

Where, c is defined as weight vector and k is considered as bias. Optimal solution of c can be calculated by minimizing the cost function (Equation 11):

$$Q(c, \xi) = \frac{1}{2} \|c\|^2 + a \sum_{\ell} \xi_{\ell} \quad (11)$$

When it satisfies the following conditions (Equation 12):

$$(x_{\ell}^T c + b) > -\xi_{\ell} \text{ for } n_{\ell} = +1$$

and,

$$(x_{\ell}^T c + b) > -1 + \xi_{\ell} \text{ for } n_{\ell} = -1 \text{ where } \xi_{\ell} > 0 \forall \ell \quad (12)$$

Where $\|c\|^2 = c^T c$, and a is the parameter of positive regularization, ξ_{ℓ} is error in training event, n is the number of wrongly classified samples, and p_{ℓ} is the marked class for the ℓ sample.

- (iii) RBF-Support Vector Machines (RBF-SVM):

RBF-SVM is an improved SVM algorithm where the kernel function is modified with radial basis function of Gaussian type. RBF kernel can be defined by the following equation (Equation 13):

$$K(d_i, d_j) = \exp(-\gamma \|d_i - d_j\|^2), \text{ where } \gamma > 0 \quad (13)$$

Where, $\|d_i - d_j\|^2$ is the Euclidean distance and γ can be obtained as:

$$\gamma = \frac{1}{2\sigma^2} \quad (14)$$

Here, σ is termed as a free parameter.

III. EXPERIMENTS AND RESULTS

This section demonstrates experimental set up, results of the experiments and their justification.

A. Experimental Set-up

Ten right handed student volunteers, aged between 20 to 29 years, are selected for this experiment. All of them have normal or corrected to normal vision. A paired associate learning task containing eight Hiragana scriptures and their corresponding meanings in a string of two English letters are presented. Each learning stimulus has a span of 3 seconds and a total 24 seconds for a complete learning trial. Total recall task spans for 16 seconds and 2 seconds for each cued recall. This paired associate learning and cued recall task is repeated for six times. Each participant performs this tasks on 5 different stimulus sets. Two minutes rest is provided between two successive trials. The sample stimulus for paired-associate learning is demonstrated in Fig.1. whereas, the scheme of stimulus presentation is shown in Fig.2.

Learning		Recall	
Paired-association		Cued-recall	
け	ke	も	?
か	ka	ふ	?
そ	so	ぬ	?
す	su	ち	?
ぬ	nu	そ	?
ち	ti	す	?
も	mo	け	?
ふ	fu	か	?

Fig.1. Sample of paired-associate learning used in prefrontal hemodynamic analysis in learning and recall tasks.

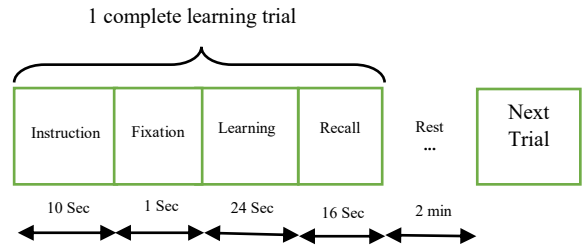


Fig. 2. Presentation of stimulus during paired-associate learning and recall task.



Fig.3. Prefrontal hemodynamic analysis of a subject performing paired-associate learning and recall task.

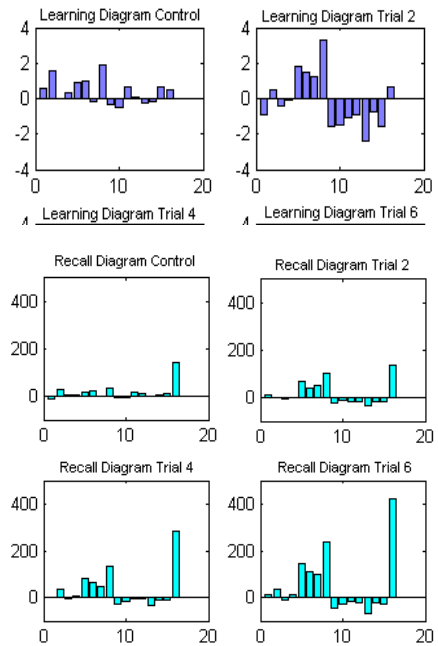


Fig 5. Mean values of Blood Oxygen demand in different voxels during successive trials of recall (trial zero, two, four, and six). Compared to the control ('ZERO') learning state, the blood oxygen demand increases during successive trials of recall. Voxel 9 and 16 are found to be the most involved prefrontal areas during recall performance.

A continuous wave near-infrared spectroscopy (fNIRS 1100) is used for data acquisition. The 4-emitter and 10-detector fNIRS band forms 16 channels which has a sampling frequency of 2 Hz and penetration depth of 1.25cm. Data



acquisition and visualization is performed using COBI studio software. For each instance hemodynamic data is recorded after removal of baseline. Fig.3. shows capturing of hemodynamic data during paired associate learning.

The change in oxygen demand (HbO-HbR) during trials of learning and recall shows higher oxygen requirement in initial trials of learning which falls down when learning is complete, i.e. when subjects gain 100% accuracy in recall. The blood oxygen demand during recall shows the similar trend of learning. However the involved brain areas of activation are different in recall tasks. Fig.4 and Fig. 5 demonstrate the change in oxygen demand during performing learning and recall tasks.

B. Classification of Learning

The PCA based feature reduction technique lowers the feature dimension from 50×144 to 50×36. Table I reports the classification accuracy after PCA based feature reduction. Radial Basis Function Support Vector Machine (RBF-SVM), Linear Support Vector Machine (LSVM), Linear Discriminant Analysis (LDA) are the three considered classification algorithms for all the three sets of features. Table I shows RBF-SVM outperforms all the other classification algorithms. In addition, feature set 3 provides the best classification accuracy (93.75 for RBF-SVM). From Table I we can observe classification accuracy increases in successive trials of learning considering ‘ZERO’ learning vs. ‘n’-th trials of learning which is possibly due to high diversification of features’ character from ‘ZERO’ learning stage with increase in trial number.

TABLE I. MEAN % ACCURACY OF CLASSIFICATION

Feature Set 1			
INPUT vs. TARGET	RBF-SVM	L-SVM	LDA
‘zero’ vs. 1	61.79	58.56	37.82
‘zero’ vs. 2	65.32	65.29	62.17
‘zero’ vs. 3	64.57	70.11	62.97
‘zero’ vs. 4	85.33	72.31	71.00
‘zero’ vs. 5	88.64	74.06	77.03
‘zero’ vs. 6	90.23	78.50	78.33
Feature Set 2			
INPUT vs. TARGET	RBF-SVM	L-SVM	LDA
‘zero’ vs. 1	48.81	52.94	50.05
‘zero’ vs. 2	62.33	61.75	58.61
‘zero’ vs. 3	69.02	63.19	60.17
‘zero’ vs. 4	78.50	68.66	65.24
‘zero’ vs. 5	77.19	73.56	69.86
‘zero’ vs. 6	85.42	78.25	76.25
Feature Set 3			
INPUT vs. TARGET	RBF-SVM	L-SVM	LDA
‘zero’ vs. 1	66.13	57.31	59.02
‘zero’ vs. 2	68.78	68.75	65.62
‘zero’ vs. 3	74.81	70.88	68.11
‘zero’ vs. 4	87.50	75.00	73.00
‘zero’ vs. 5	88.06	73.79	74.97
‘zero’ vs. 6	93.75	86.25	81.25

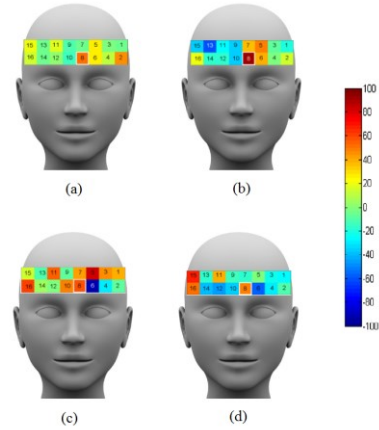


Fig 6. Mean value of total hemoglobin concentration in different voxels during successive learning trials (trial zero (a), two (b), four (c), and six (d)).

C. Classifiers’ ranking from Friedman Statistical Test

Friedman test provides ranking of the algorithms for each data set. Null hypothesis assumes the algorithms are no better than any one of them and hence cannot be ranked. For feature set 1, Friedman statistical score is computed as 8.33 which is

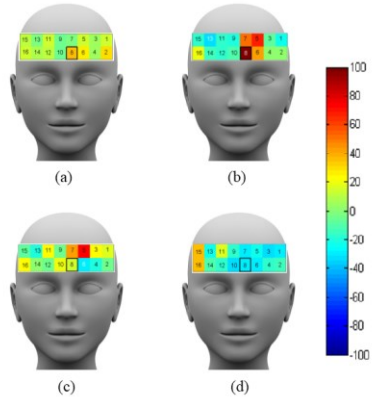


Fig 7. Mean value of total hemoglobin concentration in different voxels during successive recall trials (trial zero (a), two (b), four(c), and six (d)).

greater than $\chi^2_{2,0.05} = 5.991$ at 2 degree of freedom and 95% confidence level. Thus null hypothesis is rejected suggesting that classifiers can be ranked according to their classification accuracies. Similarly for feature set 2 and 3, Friedman statistical scores are 7.0 and 10.33 which rejects the null hypothesis. Hence, RBF-SVM ranks 1, LSVM ranks 2 and LDA ranks 3 considering their average classification accuracies (considering their nearest integer values).



D. Biological Implication of Results

Fig.6 and 7 show the engaged brain areas during learning and recall stages. A voxel plot approach is used to design a 2×8 matrix of voxel plot representing the 16 fNIRs channels using MATLAB 2015b. From Fig.6 we can report the high involvement of mPFC and OFC in initial stages of learning. However the cognitive load shifts to left DLPFC and left VLPFC in learning completion. Here, OFC involves in attention, where mPFC involves decision making and consolidation of memory. In learning completion the role shifts to planning and execution (for DLPFC and VLPFC). Fig. 7 shows activation of mPFC that supports retrieval of information from long term memory and its consolidation. In addition, when the information is learned the activation falls down and shifts to right DLPFC and right VLPFC – fetching more focus on execution which is observed in latter recall trials [19-20].

E. Descriptive Statistics of Accuracy and Response time

Table 2 reports the mean, standard deviation and variance of accuracy during recall which shows accuracy during recall reaches 100% for all the subjects in 6th trial. Fig. 8 shows the change in recall accuracy in successive trials. From Fig. 9 we can observe that higher trial numbers lowers response time in recall for the subjects considering the hits for correct response only. Lowering in response time (in mili sec) suggests low efforts in recall when learning is complete.

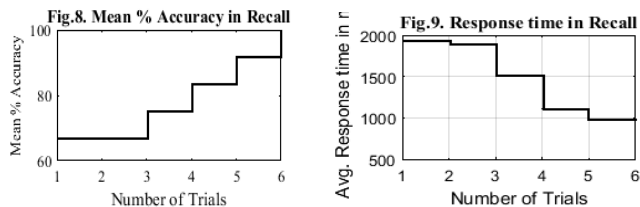


Table 2. Mean, Standard deviation and Variance of Percentage Accuracy during Recall Tasks

	Trial1	Trial2	Trial3	Trial4	Trial5	Trial6
Mean	66.66	66.66	75	83.33	91.66	100
Std	6.46	6.46	0	6.46	6.46	0
Variance	34.72	34.72	0	34.72	34.72	0

IV. CONCLUSION

This paper proposes an approach to classify learning stages in paired-associate learning tasks. Response time and percentage accuracy of correct response are taken as supportive measures for this classification problem. Considering the best feature set to produce highest classification accuracy, we find feature set 3 is the optimum. A PCA based feature reduction techniques produces highest classification accuracy for RBF-SVM algorithm which reaches almost 94% for feature set 3. Considering the

[12] R. S. Blemenfeld and C. Ranganath, "Dorsolateral Prefrontal Cortex Promotes Long Term Memory Formation through its Role in Working Memory Organization," *The Journal of Neuroscience*, pp. 916-925, 2006.

[13] N. Unsworth, "On the division of working memory and long term memory and their relation to intelligence: A latent variable approach," *Acta*

biological implications from this paper, it is observed that OFC and mPFC play important role in initial learning stages. However the cognitive load shifts to DLPFC and VLPFC brain regions in learning complication. This outcomes suggest shift in brain areas involvement during learning trials - from beginning to learning completion. However, due to sluggish response of fNIRs device we can't examine brain response changes in time domain. An fNIRs-EEG based approach may solve this limitation in near future.

ACKNOWLEDGMENT

We acknowledge the funding provided by University Grant Commission, India for the project "University with Potential for Excellence (UPE)" in the program Cognitive Science (Phase II) granted to Jadavpur University, India.

REFERENCES

- [1] H.-J. Kim, H.-K. Park, D.-W. Lim, M.-H. Choi, H.-J. Kim, I.-H. Lee, H.-S. Kim, J.-S. Choi, G.-R. Tack and S.-C. Chung, "Effects of oxygen concentration and flow rate on cognitive ability and physiological responses in the elderly," *Neural Regeneration Research*, pp. 264-269, 2013.
- [2] P. Fletcher, C. Buchel, O. Josephs, K. Friston and R. Dolan, "Learning Related Neuronal Responses in Prefrontal Cortex Studied with Functional Neuroimaging," *Cerebral Cortex*, pp. 168-178, 1999.
- [3] P. J. Gregory, D. N. Christopher, M. D. Madison and D. M. Smith, "The Medial Prefrontal Cortex is Critical for memory retrieval and resolving inferences," *Learning and Memory*, pp. 201-209, 2013.
- [4] D. R. Euston, A. J. Gruber and B. L. McNaughton, "The role of medial prefrontal cortex in memory and decision making," *Neuron Review*, pp. 1057-1070, 2012.
- [5] W. F. Asaad, G. Rainer and E. K. Miller, "Neural activity in the primate prefrontal cortex during associative learning," *Neuron*, pp. 1399-1407, 1998.
- [6] A. R. Preston and H. Eichenbaum, "Interplay of Hippocampus and Prefrontal Cortex in Memory," *Current Biology*, pp. 764-773, 2013.
- [7] G. Winocur and M. Moscovitch, "Hippocampal and Prefrontal Cortex Contributions to Learning and Memory: Analysis of Lesion and Aging Effects on Maze Learning in Rats," *Behavioural Neuroscience*, pp. 544-551, 1990.
- [8] Y. X. Zhang, D. R. Moore, J. Guiraud, K. Molloy, T.-T. Yan and S. Amitay, "Auditory Discrimination Learning: Role of Working Memory," *PLOS One*, 2016.
- [9] T. P. Alloway and L. Archibald, "Working Memory and Learning in Children with Developmental Coordination Disorder and Specific Language Impairment," *Journal of Learning Disabilities*, pp. 251-262, 2014.
- [10] C. Maehler and K. Schuchardt, "Working memory functioning in children with learning disabilities: does intelligence makes a difference?," *Journal of Intellectual Disability Research*, vol. 53, 2008.
- [11] R. Salazar, N. Dotson, S. Bressler and C. Gray, "Content Specific Fronto-Parietal Synchronization during Visual Working Memory," *Science*, vol. 338, pp. 1097-1100, 2012.
- [12] R. S. Blemenfeld and C. Ranganath, "Dorsolateral Prefrontal Cortex Promotes Long Term Memory Formation through its Role in Working Memory Organization," *The Journal of Neuroscience*, pp. 916-925, 2006.
- [13] N. Unsworth, "On the division of working memory and long term memory and their relation to intelligence: A latent variable approach," *Acta Psychologica*, pp. 16-28, 2010.
- [14] A. H. Lara and J. D. Wallis, "The Role of Prefrontal Cortex in Working Memory," *Frontiers in System Neuroscience*, 2015.
- [15] A. M. Owen, "The functional organization of working memory processes

- within human lateral frontal cortex: the contribution of functional neuroimaging," *The European Journal of Neuroscience*, pp. 1329-1339, 1997.
- [16] S. M. Coyle, T. E. Ward and C. M. Markham, "Brain computer interface using simplified functional nearinfrared spectroscopy system," *Journal of Neural Engineering*, vol. 4, no. 3, pp. 219-226, 2007.
- [17] N. Naseer and K.-S. Hong, "fNIRs based brain computer interface: a review," *Frontiers in Human Neuroscience*, vol. 9, p. article 3, 2015.
- [18] R. Kar, A. Konar, A. Chakraborty, B. Sen Bhattacharya and A. K. Nagar, "EEG source localization by memory network analysis of subjects engaged in perceiving emotions from facial expressions," in *IJCNN*, 2015.
- [19] J. D. E. Gabrieli, R. A. Poldrack and J. E. Desmond, "The role of left prefrontal cortex in language and memory," *PNAS*, vol. 95, pp. 906-913, 1998.
- [20] A. Collins and E. Koechlin, "Reasoning, Learning and Creativity: Frontal Lobe Function and Human Decision Making," *PLOS Biology*, vol. 10, no. 3, p. e1001293, 2012.

Effect of Disturbance in Working Memory Performance: An fNIRs Study

Souvik Biswas
School of Bio Science and
Engineering,
Jadavpur University,
Kolkata, India.
souvikbiswas.res@gmail.com.

Amiyangshu De, Amit Konar
Department of Electronics and
Telecommunication Engg.,
Jadavpur University,
Kolkata, India.
amiyangshu_de@yahoo.com
konaramit@yahoo.co.in

Piyali Basak
School of Bio Science and
Engineering,
Jadavpur University,
Kolkata, India.
piyalibasak@gmail.com

Abstract—This paper demonstrates a near infrared spectroscopic study of understanding effect of disturbance on working memory performance. Embedded prefrontal hemodynamic characters are obtained from recorded data which is filtered and preprocessed by adopting a mean normalization technique. Furthermore, a ReliefF algorithm based feature selection is adopted to sort out the most prominent feature set. A comparative study is drawn to demonstrate the effectivity of the proposed framework by comparing classifiers accuracy which shows that our proposed framework outperforms other conventional principal component analysis (PCA) based feature selection and classification techniques. In addition, correlations among different learning conditions, as well as recall conditions are calculated to demonstrate how diverse conditions (without and with disturbances) alter prefrontal hemodynamics. In addition, a voxel plot approach shows the changing oxyhemoglobin concentrations during different recall tasks (with and without disturbance during learnings). The novelty of this paper lies in understanding the role of disturbance during encoding of information which affects recall performance in working memory tasks.

Keywords— *Working memory, disturbance, near infrared spectroscopy, ReliefF algorithm, LSVM, LDA, kNN.*

I. INTRODUCTION

In the twenty first century BCI research takes a significant leap in understanding cognitive process and most specifically in the domain of memory – how it is formed, consolidated and retrieved. Yet, after the advancement in brain imaging techniques and signal processing, the complete understanding of memory processes are not revealed. This area of research is perhaps growing day by day from its interdisciplinary approach. Changing hemodynamics in brain tissues could be a productive estimation to justify cognitive performance during different tasks which can be demonstrated from the notion that higher cognitive tasks need more energy consumption and increased cortical blood supply. This neurobiological basis provides the platform for near infrared spectroscopy (fNIRs) to be an effective tool of brain imaging. In addition, its low cost, portability, spatial resolution and non-invasive character comes out as added advantages over other conventional tools.

An fNIRs device records signals of confined cortical activities in a depth of few centimeters. In the past decade, Carlson *et al* [1] experimented the role of music and white noise on working memory performance in monkeys. In addition, Fine and Minnery demonstrate the role of salience effect on working memory performance [2]. Furthermore, we can report the recent research by Ning Ng *et al.* that reveal effect of noise and working memory capacity on memory processing of speech in audiology research [3]. However, the role of disturbance in working memory performance is still not well explored.

Recent studies have not explained the changing role of prefrontal hemodynamics during working memory performance in different noisy environments. As for information, working memory is one of the most heuristic and important concept in cognitive psychology which demonstrate a multicomponent interrelated systems as proposed by Baddeley and Hitch [4]. They hypothesized a limited capacity system that share information between processing and storage. Concurrent processing of different information leads to a loss from short term storage. In addition, attention plays an important role during working memory performance. Hence disturbance during encoding or addition of newer information could alter the working memory capacity and the performance decreases with concurrent increase in processing loads [5].

As we can know, the most involved brain area for working memory performance is related to prefrontal cortex, henceforth, an fNIRs study can contribute significantly in understanding the changing hemodynamic parameters of working memory performance in different noisy environments. In addition, this device is appropriate to record prefrontal hemodynamic data.

In this paper we try to understand the role of disturbance in working memory performance from the embedded characters in the recorded signals. If we can understand the process of information encoding in working memory without and with disturbance, it could add another feather in BCI-memory research. Furthermore, the role of encoding variation (in different noisy conditions) in recall performance is investigated.

This paper aims to understand varied working memory performance from fNIRs signals adopting a mean normalized preprocessing of recorded signals. The second novelty lies in a *ReleifF* algorithm based feature selection technique rather than conventional principal component analysis (PCA). Supportively, a correlation study is carried out among different encoding (learning) and recall trials to demonstrate the changing hemodynamic characters.

We organize the paper in the following ways. Section II (PROPOSED FRAMEWORK) consists of preprocessing and mean normalization of the data sets, feature extraction, a *ReleifF* algorithm based feature selection and feature classification using different conventional classifiers. Section III demonstrates experimental set up, whereas section IV contains different results from the analysis of experimental data. Section V concludes this paper.

II. PROPOSED FRAMEWORK

A. Preprocessing

Several artifacts and noise are incorporated within the recorded signals when an experiment is conducted. These noises can be grouped into two different classes, i) Physiological Noise and ii) Experimental Noise. A number of physiological noises like heartbeat, respiration, blood pressure fluctuation, Mayer Waves [6] etc. occur during the experiment. Similarly, experimental noises are generated through motion artifacts, which can cause dislocation of the optodes. This kind of artifacts can be seen in the fNIRs signal as a spike.

Reduction of these noises can be done using various adaptive filtering processes. In this paper, we have used Chebyshev band pass filter with cut off frequencies 0.1 Hz to 0.6Hz, so that all major noises can be removed. Additionally, ICA is used to filter out other noises embedded within the signal [6]. ICA helps in the restoration of original hemodynamic data from noisy data by isolating the main Independent Components (IC) and later on accumulating the ICs along with their primary IC using derived associated weights of their t values.

B. Proposed mean normalization of Recorded Datasets:

To extract the best probable feature set we have adjusted the raw data matrix in such a way that the differences between two distinct classes can be maximized. For this purpose we have computed the mean of the each voxel (column of the raw data set) for each class by:

$$\bar{m}_{j,c} = \frac{\sum_{i=1}^n x_{i,j}}{n}, \text{ where, } x_{i,j} \in c \quad (1)$$

Where i is row index n is number of rows, and j is column index for class c thus $x_{i,j}$ represents data point. After the computation of mean of each voxel we have computed the mean of all the voxel by the following equation:

$$\bar{m}_{t,c} = \frac{\sum_{j=1}^p \bar{m}_{j,c}}{p} \quad (2)$$

Where, p is the number of columns in the raw dataset and $\bar{m}_{t,c}$ is the mean of all the voxels for class c . Now, again the mean of the population is computed by taking the average of $\bar{m}_{t,c}$ for all the classes. Thus the output becomes:

$$\bar{m}_T = \frac{\bar{m}_{t,1} + \bar{m}_{t,2} + \dots}{T} \quad (3)$$

Where, T is the total number of classes and $\bar{m}_{t,1}, \bar{m}_{t,2}, \dots$ are the mean of the all voxels for each class. Now, the data matrix is multiplied with a gain function G to maximize the distance between two different classes. Thus, G can be defined as:

$$G = |\bar{m}_T| + 1 \quad (4)$$

To explain it mathematically, let us consider the data matrix for class c is,

$$B = \begin{bmatrix} y_{1,1} & y_{1,2} & \dots & \dots \\ y_{2,1} & y_{2,2} & \dots & \dots \\ \vdots & \vdots & \ddots & \vdots \\ y_{i,1} & y_{i,2} & \dots & \dots \end{bmatrix}_{i \times j} \quad (5)$$

Where, y is the feature element. The gain G is multiplied with the feature matrix B to produce H , which is further considered for feature extraction:

$$H = G \times B = G \times \begin{bmatrix} y_{1,1} & y_{1,2} & \dots & \dots \\ y_{2,1} & y_{2,2} & \dots & \dots \\ \vdots & \vdots & \ddots & \vdots \\ y_{i,1} & y_{i,2} & \dots & \dots \end{bmatrix}_{i \times j} \quad (6)$$

C. Feature Extraction

Feature extraction from the recorded data sets is an important step for classification problems. We take 9 features from the set of preprocessed and mean normalized fNIRs data. The following features are considered for this experiment:

- i) Mean of oxyhemoglobin concentration
- ii) Mean of deoxyhemoglobin concentration
- iii) Mean of total hemoglobin concentration
- iv) Standard deviation of oxyhemoglobin concentration
- v) Standard deviation of deoxyhemoglobin concentration
- vi) Standard deviation of total hemoglobin concentration
- vii) Skewness of oxyhemoglobin concentration
- viii) Skewness of deoxyhemoglobin concentration
- ix) Skewness of total hemoglobin concentration

The dimensions of both the raw HbO and HbR data were $11 \times 16 \times 40$, where 11 represents number of participants, 16 represents number of channels and 40 represents the samples.

As, for each participant 5 distinct trials are taken, the dimension of the raw data becomes $55 \times 16 \times 40$. To extract first feature set we take mean HbO concentration data of the subjects recorded by each channel. Therefore, the dimension of first feature becomes 55×16 . Similarly, for rest of the features we have extracted the 16 features for 11 participants, which finally presents a feature matrix of 55×144 .

D. RelieF Algorithm based Feature Selection

Relief algorithm estimates quality of attributes according to best differentiable values between instances that are near to each other. We have extracted the features from a mean adjust data matrix in such a way that the computation of this differences between two distinct classes can be maximized, this helps in the selection of best probable features. The pseudo code for classical RelieF algorithm is given below [7]:

RelieF Algorithm

Input: Vector of attributes (matrix D) and class values for each training instances.

Output: Vector W (weight estimation of the qualities of the attributes)

begin

Set all weights $W(D) = 0$;

For $i=1$ to p **do begin**

 randomly select an instance R_i ;

 find k nearest hits H_j ;

for each class $c \neq \text{class}(R_i)$

 from class c find k nearest misses $M_j(c)$;

for $D=1$ to t **do**

$W[D] :=$

$$W[D] = \frac{\sum_{j=1}^k \text{diff}(D, R_i, H_j)}{pk} + \sum_{c \in \text{class}(R_i)} \frac{P(c)}{1 - P(\text{class}(R_i))} \frac{\sum_{j=1}^k \text{diff}(D, R_i, M_j(C))}{pk}$$

end

end

E. Feature Classification

In this paper, feature classification of the selected features is performed using Linear Support Vector Machines (LSVM), Linear Discriminant Analysis (LDA) and k-Nearest Neighbors (kNN) algorithms to understand role of disturbance in working memory performance.

i) Linear Support Vector Machines (LSVM)

SVM algorithm is a binary classifier which tries to find the maximum differences within the support vectors and separating hyperplane. The following equation defines the hyperplane [8].

$$S(x) = Gx + D \quad (7)$$

Where, G is the weight vector and D is bias. By minimizing the cost function we can find the optimal solution of G :

$$Q(G, \varphi) = \frac{1}{2} G^2 + f_r \sum_{\ell}^n \varphi_{\ell} \quad (8)$$

When it satisfies the following conditions:

$$(x_{\ell} G + D) > 1 - \varphi_{\ell} \text{ for } n_{\ell} = +1 \quad (9)$$

and,

$$(x_{\ell} G + D) > -1 + \varphi_{\ell} \text{ for } n_{\ell} = -1 \text{ Where } \varphi_{\ell} > 0 \forall \ell \quad (10)$$

Where $\|G\|^2 = G^T G$, f_r is the parameter of positive regularization, φ_{ℓ} is training error, n is the number of misclassified samples, and p_{ℓ} is the level of the input class for the ℓ -the sample.

ii) Linear Discriminant Analysis (LDA)

LDA algorithm is one of the widely used classifier in BCI research. LDA algorithm tries to find a vector \mathcal{G} within the input feature set so that the target classes can be divided into distinct groups with an effective variance [9]. This characteristic is obtained by Fisher's Criterion:

$$H(\mathcal{G}) = \frac{\mathcal{G}^T E_b \mathcal{G}}{\mathcal{G}^T E_w \mathcal{G}} \quad (11)$$

Where, E_b and E_w are scatter matrices of between-class and within-class respectively. It is represented as following (Equation 6 and 7):

$$E_b = (s1 - s2)(s1 - s2)^T \quad (12)$$

$$E_w = \sum_{d_w \in L1} (d_w - s1)(d_w - s2)^T + \sum_{d_w \in L2} (d_w - s1)(d_w - s2)^T \quad (13)$$

Here, $L1$ and $L2$ are two distinct classes; $s1$ and $s2$ is the group means of each classes and d_w denotes samples. If a vector \mathcal{G} satisfies equation 11, it can be represented as the following generalized eigenvalue problem:

$$E_w^{-1} E_b \mathcal{G} = \psi \mathcal{G} \quad (14)$$

Hence, the optimal vector \mathcal{G} is now eigenvector that corresponds to the largest eigenvalues of $E_w^{-1} E_b \mathcal{G}$. The optimal vector \mathcal{G} can be obtained by the following formula:

$$\mathcal{G} = E_w^{-1} (s1 - s2), \text{ Until, } E_w^{-1} \text{ is nonsingular.} \quad (15)$$

iii) k-Nearest Neighbor (kNN)

The k-nearest neighbors (kNN) algorithm figures out nearest neighbors within the feature space. Classifier performance depends on the following parameters: (i) appropriate cost of k and, (ii) and appropriate similarity function. In kNN algorithm, primarily it finds out the closest k instances belong to class d_k , and then allows k to vote for the class of d_k [10]. The algorithm depends on the following equations:

$$f(l_i) = \arg \max_k \sum_{p_j \in kNN} f(p_j, d_k) \quad (16)$$

$$f(l_i) = \arg \max_k \sum_{p_j \in kNN} \sigma(l_i, p_j) f(p_j, d_k) \quad (17)$$

Now, l_i is the test point, p_j belongs to class d_k , $\sigma(l_i, p_j)$ is similarity function within l_i and p_j .

III. EXPERIMENTAL SETUP

A. Participants

Eleven healthy student volunteers took part in this experiment. They all have normal or corrected to normal vision and all aged between 20-29 years. All the participants are assigned to three different sets of learning and recall tasks with distinct levels of disturbance (Fig. 1). All the participants are informed about the experimental objective and possible limitations. Experimental data for each instance is recorded after removal of base line.

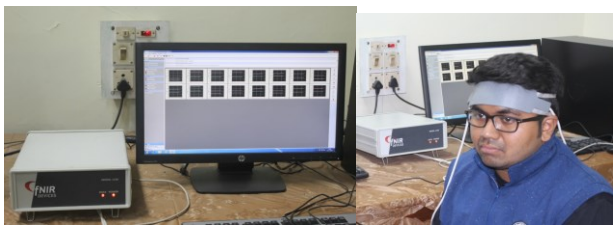


Fig. 1. Performing an fNIRs recording during this experiment.

B. Learning and Recall Task for Working Memory

Each participants are presented with 3 sets of less-common word list of 10 words. The stimulus is presented over the computer screen over an initial fixation dot. Each trial was conducted with different disturbance conditions embedded in the presented stimulus. fNIRs signal is recorded after removal of the baselines for each instances. Learning period spans for 20 seconds followed by a 20 second free recall span. Sufficient time is provided between each trials to nullify the ceiling effects. The stimulus presentation scheme is shown in Fig 2.

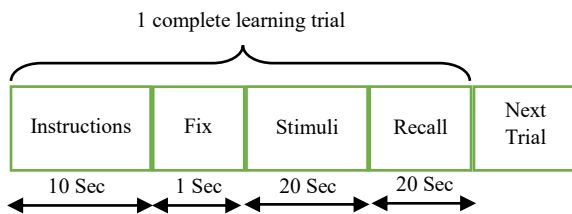


Fig. 2. Timeline of Stimuli presentation during experiment.

C. Data Acquisition

The total experimental procedure is conducted at Artificial Intelligence Laboratory, Jadavpur University over a period of 20 days. The prefrontal hemodynamic is recorded using fNIRs 1100 consisting of 4 emitter and 10 recorded which form 16

channels. This fNIRs system has a recording frequency of 2 Hz and the IR light penetrates into 1.25 cm of cortical tissues. The data acquisition and visualization is performed using COBI studio software.

IV. RESULTS

A. Classification Results

Top 25% of the feature matrix according to the ranking of ReliefF based feature selection technique is considered as Proposed Framework (PFW) is taken for classification. The feature matrix is reduced from 55×144 to 55×36 for each class. The percentage accuracy of classification has been given in Table I. From the table we can observe that disturbance (L3) after encoding is more diverse than disturbance during encoding (L2) of information in working memory task. Both the task is compared to a reference zero disturbance stage (L1). Diversification of hemodynamic features in different tasks reports change in classifiers' performance. A comparative study is carried out for PFW-LSVM based classification with PCA based LSVM, LDA and kNN to justify its effectiveness.

TABLE I. PERCENTAGE ACCURACY OF CLASSIFICATION RESULTS

Instances	PFW-LSVM	PCA-LSVM	PCA-LDA	PCA-kNN
Learning				
L1 vs. L3	75.00	69.40	63.50	51.50
L1 vs. L2	90.62	84.60	68.90	75.18
Recall				
R1 vs. R3	71.50	68.81	54.50	37.40
R1 vs. R2	87.50	74.20	81.30	68.60

Table II. reports the specificity and sensitivity obtained for the proposed classification technique (PFW-LSVM) which is obtained from the confusion matrix.

TABLE II. CLAASIFIER'S PERFORMANCE (LSVM)

Instances	%Accuracy	Sensitivity	Specificity
Learning			
L1 vs. L2	90.62	100	87.5
L1 vs. L3	75	66.66	37.5
Recall			
R1 vs. R2	87.5	100	66.5
R1 vs. R3	71.5	78.33	37.5

B. Statistical Validation of Classifiers' Ranking.

Let us consider that null hypothesis as no distinction in classifiers performance among the classification algorithms. But, Friedman's statistical test score is 9.9 which is higher than $\chi^2_{3,0.05} = 7.815$ at 95% confidence level and with 3 degree of freedom. Hence, the null hypothesis is rejected and classifiers are ranked according to their average classification

accuracies. Table III reports classifiers ranking considering equation 18.

TABLE III. RANKING OF THE CLASSIFIER

Instances	Rank of the classifiers			
	PFW - LSVM	PCA - LSVM	PCA - LDA	PCA - kNN
L1 vs. L2	1	2	3	4
L1 vs. L3	1	2	4	3
R1 vs. R2	1	2	3	4
R1 vs. R3	1	3	2	4
$\sum R_i$	4	9	12	15
R	1	2.25	3	3.75

The statistical validation is performed by computing chi square from the following equation.

$$\chi^2 = \frac{12}{pd(d+1)} \left[\sum_{i=1}^p (\sum R_i)^2 \right] - 3p(d+1) \tag{18}$$

Here, p is the number of instances = 4, d is the number of algorithms that is 4, degree of freedom (F) is considered as $d-1$, henceforth $F=3$ and R is the ranking of the classifiers as mentioned in Table. III [11].

C. Biological Implication of Experimental Results

The mean HbO concentration is plotted in a 2x8 matrix voxel plot using MATLAB 2015b. This plot represents the 16 channel positions of the fNIRs head band. From Fig. 3 we can observe that HbO concentration vary in recall performances with different learning conditions. Fig 3. (a) represents the recall in zero disturbance learning where medial prefrontal cortex (mPFC) and partial activation of dorsolateral (DLPFC) and ventrolateral prefrontal cortex (VLPFC). The voxel activation (Fig 3. (b)) during recall for encoding with disturbance shows additional involvement of orbitofrontal cortex (OFC) along with the early mentioned brain areas

which suggest more effort is given to recall the encoded information. The HbO concentration areas are widely spread for disturbance after encoding which is shown in Fig. 3. (c). It shows higher HbO concentration requirement in recall. However, wide range of brain areas get involved. The above mentioned brain areas are mostly related to working memory performance and learning. Here, we can observe variability of engagement pattern of prefrontal cortex when a subject performs in different noisy conditions [12-14].

D. Correlation Coefficients

Measure of Linear dependence of two random variables are known as the correlation coefficient. If each of the variable contains S scalar observations, then the Pearson correlation coefficient is [15]:

$$\rho(X,Y) = \frac{1}{S-1} \sum_{i=1}^S \left(\frac{X_i - \mu_X}{\sigma_X} \right) \left(\frac{Y_i - \mu_Y}{\sigma_Y} \right) \tag{19}$$

Where, μ_x and σ_x represents the mean and standard deviation for variable X , respectively, and μ_y and σ_y are the mean and standard deviation for variable Y . Table IV reports the correlation coefficient of different learning and recall instances. The correlation coefficient is computed from the mean values of oxyhemoglobin. We can observe poor positive correlation among L1 and L2 which gets stronger considering L1 and L3. This result means encoding with disturbance has wide variability from learning without disturbance. However, the correlation coefficients for recall tasks show different scores – a poor correlation among without disturbance and disturbance after encoding stage.

TABLE IV. CORRELATION COEFFICIENT

Learning		Recall	
L1 vs. L2	0.4344	R1 vs. R2	0.4317
L1 vs. L3	0.6926	R1 vs. R3	0.3662

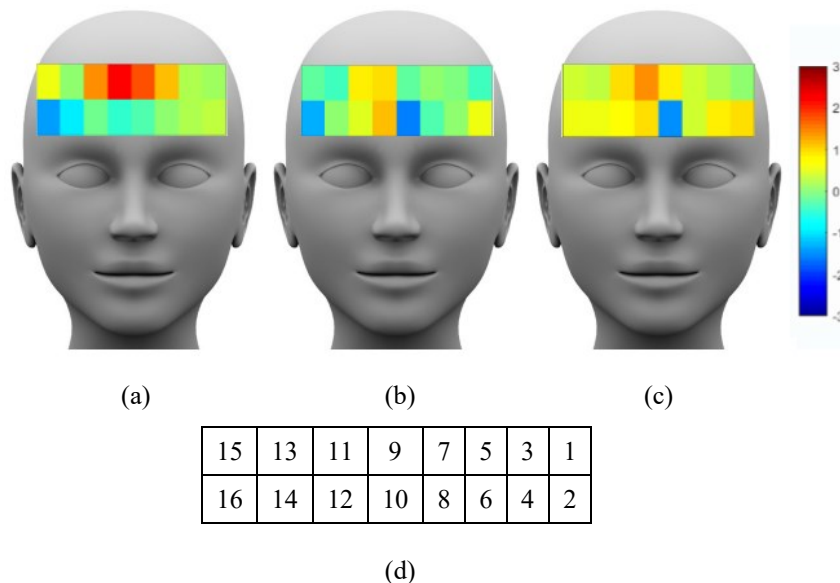


Fig. 3. Voxel plot of mean of oxyhemoglobin (HbO): (a) Recall task for learning without disturbance, (b) Recall task for learning with disturbance during encoding, (c) Recall task for Learning with disturbance after encoding, (d) Channel position of fNIRs head-band.

E. Descriptive Statistics of recall accuracy

Average percentage accuracy during recall tasks for each participants and the corresponding variance and standard deviation for correct responses are represented in the following Table V. Compared to the working memory task with zero disturbance, the performance accuracy for task with disturbance after encoding is more affected than those when disturbance is applied during encoding.

TABLE V. STATISTICAL MEASURES OF PARTICIPANTS PERFORMANCE DURING RECALL TASKS OF DIFFERENT TASK CONDITIONS.

Participant s	Task 1 (without disturbance)	Task 2 (disturbance during encoding)	Task 3 (disturbance after encoding)
	Correct Recall among 10 words	Correct Recall among 10 words	Correct Recall among 10 words
1	7	5	2
2	6	4	2
3	8	4	3
4	5	5	3
5	7	3	3
6	7	2	2
7	6	4	1
8	5	4	3
9	5	5	3
10	7	3	4
11	7	3	2
Average	6.363	3.818	2.545
Variance	0.9586	0.8760	0.6115
Standard deviation	0.9791	0.9359	0.7820
Percentage accuracy	63.63%	38.18%	25.45%

V. CONCLUSION

This paper proposes a novel approach of understanding role of disturbance in working memory performance. The proposed feature selector-classifier provides higher classification accuracies (which reaches almost 91%) than conventional PCA based feature selection-classification approach. Considering the biological implication from the experimental analysis, we observe different prefrontal brain areas' involvement during recall tasks for verbal working memory with varied encoding strategies (without and with disturbance). Some recall tasks need more attention where others require learning, memorization and execution strategies. Hence the activation of OFC, mPFC and DLPFC variation is observed. Correlation coefficients among HbO concentration between different learning and recall trials show hemodynamic correlation is least for learning with disturbance and recall in disturbance after encoding conditions compared to corresponding zero disturbance conditions. However, an improved time domain analysis is still required to understand the encoding and recall strategies adopted by the brain in different noisy conditions.

ACKNOWLEDGMENT

We are thankful to University Grant Commission (UGC) for providing the fund for this research from University with Potential for Excellence (UPE) Phase II Project in Cognitive Science, granted to Jadavpur University, Kolkata.

REFERENCES

- [1] S. Carlson, P. Rama, D. Artchakov and I. Linnonkoski, "Effect of music and white noise on working memory performance in monkeys," *Neuro Report*, vol. 8, pp. 2853-2856, 1997.
- [2] M. S. Fine and B. S. Minnery, "Visual Saliance Affects Performance in Working Memory Tasks," *The Journal of Neuroscience*, vol. 29, pp. 8016-8021, 2009.
- [3] E. H. Ning Ng, M. Rudner, T. Lunner, M. S. Pederson and J. Ronnberg, "Effect of Noise and Working Memory Capacity on Memory Processing of Speech for Hearing-aid User," *International Journal of Audiology*, vol. 52, pp. 433-441, 2013.
- [4] A. Baddeley, S. D. Salla, T. W. Robbins and A. Baddeley, "Working Memory and Executive Control and Discussion," *Philosophical Transactions: Biological Science*, vol. 351, pp. 1397-1404, 1996.
- [5] P. Barrouillet, S. Bernardin, S. Portrat, E. Verguawe and V. Camos, "Time and Cognitive Load in Working Memory," *Journal of Experimental Psychology*, vol. 33, no. 3, pp. 570-585, 2007.
- [6] N. Naseer and K. Hong, "fNIRS-based Brain-Computer Interfaces: A review," *Frontiers in Human Neuroscience*, vol. 9, 2015.
- [7] M. Robnik-Skinoja and I. Kononenko, "Theoretical and empirical analysis of ReliefF and RReliefF," *Machine Learning*, no. 53, pp. 23-69, 2003.
- [8] C. Burges, "A tutorial on support vector machines for pattern recognition," *Knowl. Discov. Data. Min*, pp. 121-167, 1998.
- [9] S. Mikay and G. Ratsch, "Fisher Discriminant Analysis With Kernels," in *IEEE Conference on Neural Networks for Signal Processing IX*, 1999.
- [10] M. Pal, A. Khasnobish, A. Konar, D. N. Tibarewala and R. Janarthan, "Classification of Deformable and Non-Deformable Surfaces by Tactile Image Analysis," in *International Conference on Control, Instrumentation, Energy & Communication (CIEC)*, 2014.
- [11] D. J. Sheskin, *Handbook of Parametric and Nonparametric Statistical Procedures*, 2nd ed., CHAPMAN & HALL/CRC, 2000.
- [12] C. E. Curtis and M. D'Esposito, "Persistent activity in the prefrontal cortex during working memory," *Trends in Cognitive Sciences*, vol. 7, no. 9, pp. 415-423, 2003.
- [13] D. R. Euston, A. J. Gruber and B. L. McNaughton, "The Role of Medial Prefrontal Cortex in Memory and Decision Making," *Neuron*, vol. 76, pp. 1057-1070, 2012.
- [14] M. A. Staal, *Stress, Cognition, and Human Performance: A literature Review and Conceptual Framework*, Hanover, MD: NASA Centre for AeroSpace Information, 2004.
- [15] R. Fisher, *Statistical Methods for Research Workers*, 13th ed., Hafner, 1958.

Retinal Blood Vessel Extraction Using Graph Tracer Algorithm

Hepsiba.D

Assistant Professor-EIE
Dept. of Electrical Technology
Karunya University
Coimbatore, Tamil Nadu, India

L.D.Vijay Anand

Assistant Professor-EIE
Dept. of Electrical Technology
Karunya University
Coimbatore, Tamil Nadu, India

Abstract—The true blood vessels in a retina are major and effective part to identify the cardiovascular disease (CVD) in human. Retinal blood vessel morphology is related to the risk of cardiovascular diseases. In this paper the identification of true vessel structure of retinal image is done using the retinal image processing system. The colour fundus retinal image is converted to Gray image for better results in the processing. A clear image of segmented vessel is obtained through Kirsch template method. The vessel structure is extracted and tracking of blood vessels from optimal forest is done by using graph tracer algorithm. The performance analysis is done between the manual segmented retinal image and the retinal image segmented using Kirsch template method.

Keywords—Cardiovascular disease, Retinal images, vessel segmentation, optimal forest.

I. INTRODUCTION

The retina is a light-sensitive layer of tissue, lining the inner surface of the optic. The optics of the eye create an image of the visual world on the retina (through the cornea and lens), which does much the same role as the film in a camera. The accurate and automated analysis of vessel morphology is a valuable instrument in medical imaging since it is applicable to many diagnostic processes. Retinal blood vessel morphology can be an important indicator for diseases such as diabetes, high blood pressure, and coronary artery disease. Both the arteries and veins of the retina are generally binary trees, whose attributes can be considered either locally or globally. Measurable geometrical changes in diameter, branching angle, length of the retinal blood vessel, cause these diseases. The detection and measurement of retinal blood vessels can be employed to measure the severity of disease, as part of the procedure of automated diagnosis of disease or in the judgment of the progression of therapy.

Retinal fundus images provide important data for early detection of many retinal and systemic diseases. A retinal image provides information of the happening within the human body. In particular, the state of the retinal vessels has been presented to reflect the cardiovascular status of the physical structure. Measurements to quantify retinal vascular structure and

properties provide better diagnostic capabilities for the risk of cardiovascular diseases. Most of the process is involved to segment and extract the vessels from retinal images. There are many methods for the segmentation and extraction of blood vessel from retinal image.

This paper describes the segmentation and tracing of blood vessel. Retinal blood Vessel extracted image is used for diagnostic purposes. In the medical field retinal images are utilized to detect the cardiovascular disease, hypertension and strokes.

II. SYSTEM OVERVIEW

A. Input Image

Retinal image is generally aided by the public availability of the annotated Digital Retinal Images for Vessel Extraction (DRIVE) databases. Pixel feature classification and identification of elongated structures has been highly successful in the detection of large and medium retinal vessels. The input image is a color image which is also called as fundus image.

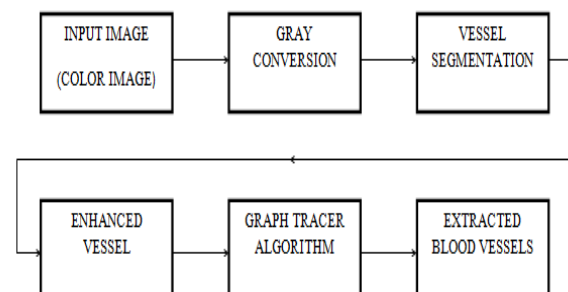


Fig. 1. Retinal Image Processing System

B. Gray Conversion

The input color image is converted to gray image using gray conversion. Gray image carries only intensity information. The black and white, are composed exclusively of gray shades, varying from black which is the weakest intensity to the strongest intensity which is white. Due to this process no loss of data is caused.

C. Vessel Segmentation

The process in which the image is divided into multiple parts is called Image segmentation. It is done to identify objects or other relevant information in digital images. Enhancement or Thresholding based algorithms are fast in nature and most suitable for parallelization. [1]. Kirsch template method is a non-linear edge detector that finds the maximum edge strength in a few predetermined directions. The edge magnitude of the Kirsch operator is calculated as the maximum magnitude across all directions. The edge direction is defined by the mask that produces the maximum edge magnitude.

D. Enhancing And Extracting of Retinal Blood Vessel

The vessel extraction process is to extract the vessels from the segmented retinal image. This process is used for sharpening the image because the segmented image may have noise information. Therefore, to clear the noise vessel extraction process is used. And the vessel extraction is obtained by graph tracer algorithm to find bifurcations and crossovers. The feature extraction method of the Graph tracer algorithm is having capability to identify bifurcations and crossovers presented in retinal images. This algorithm identifies the vessel accurately and it can identify more blood vessels at the same time.

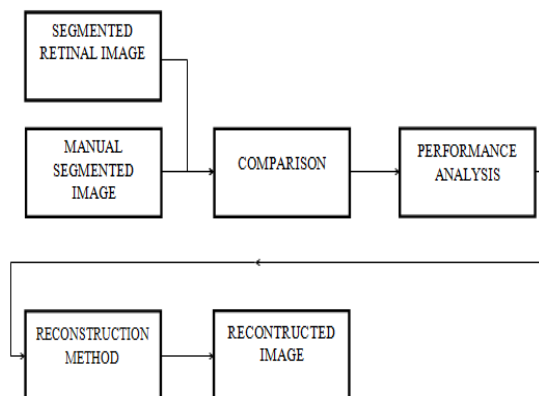


Fig. 2. Performance Analysis System

Manual segmented retinal images have been given in the DRIVE database with retinal color fundus images. The segmented images are exactly matched with the retinal fundus images. The manual segmented images are mostly used to analyze with automatically segmented image for measuring the performance of the system.

Automatic segmented and manually segmented retinal images are used to analyze the retinal image processing system. Sensitivity and specificity are the parameters that decide the accuracy of the system. The statistical measures for the performance of a binary classification test are found by the sensitivity and specificity.

III. IMAGE PROCESSING RESULTS

Retinal images are segmented and extracted by Kirsch template algorithm. [3]. The system performance is analysed and accuracy of the system is measured. The input image, taken for processing is the retinal image in TIFF format as shown in Fig. 3. The color fundus image is converted to gray image, as the vessel extraction and vessel tracing is a time consuming process in a color image. The gray conversion is done for reducing the process time of vessel segmentation and extraction. Gray image is obtained by the gray conversion of the color image. Gray image carries only intensity information. The gray image conversion process is done by using commands in MATLAB. The color image determined by an RGB combination of color densities is converted to gray image by eliminating the red and blue components of a color image as shown in Fig. 4.



Fig. 3. Retinal Image

Kirsch template method is used to segment the blood vessel from gray image as shown in Fig. 4. Kirsch template method is a non-linear edge detector that finds the maximum edge strength in a few predetermined directions

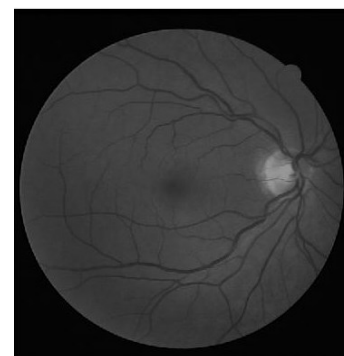


Fig. 4. Gray Converted Image

The operator takes a single kernel mask and rotates it in 45 degree increments through all 8 compass directions. The edge magnitude of the Kirsch operator is calculated as the maximum magnitude across all directions. The edge direction is defined by the mask that produces the maximum edge magnitude. Kirsch template Segmented image is shown in Fig. 5.

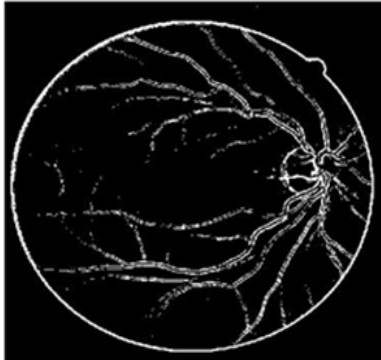


Fig. 5. Vessel Segmentation using Kirsch Template Method

Vessel enhancing process is to extract the vessels from the segmented retinal image. In the segmented image each element has different intensities and by using edge detecting command the segmented image is smoothened. The extracted elements are used to form another matrix of an image which is called vessel enhanced image shown as in Fig. 6.

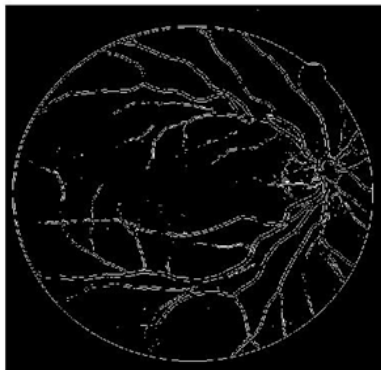


Fig. 6. Vessel Enhanced Image

The vessel extraction is obtained by graph tracer algorithm to remove noise pixels and to produce a clear vessel image. The feature extraction method of the Graph tracer algorithm is having capability to identify bifurcations, crossovers and removes noise present in the retinal images. This algorithm identifies the vessel accurately and at the same time it can identify more blood vessels. The vessel extracted image is shown in Fig. 7. After blood vessel extraction, the system analyses to measure the accuracy of extracted images.

The segmented image is compared with manually segmented image to find the accuracy of the image and performance of the system by measuring the values of sensitivity and specificity. [5]. Kirsch template Segmented image is shown in Fig. 5 and the manual segmented image is shown in Fig. 8.

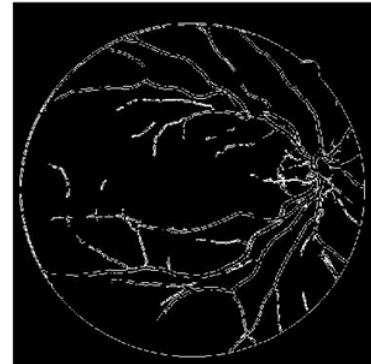


Fig. 7. Vessel extracted image

Morphological reconstruction is a method for extracting meaningful information about shapes in an image. Reconstruction image is obtained by using segmented (Kirsch Template) image and manual segmented image. Essentially a generalization of flood-filling, morphological reconstruction processes an image, called the marker, based on the characteristics of another image, which is called as mask [4].

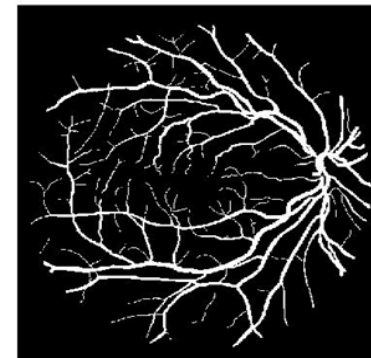


Fig. 8. Manual Segmented Image

The high points, or peaks, in the marker image specify where processing begins. The peaks spread out, or dilate, while being forced to fit within the mask image. The reconstructed image for Kirsch Template method is shown in Fig. 9.



Fig. 9. Reconstructed Image for Kirsch Template

The performance of the image processing system for 20 different retinal images is shown in terms of Sensitivity, Specificity and Accuracy in Table-1. The average system performance for the image processing system is shown in Table-2.

TABLE I. PERFORMANCE OF IMAGE PROCESSING SYSTEM

Images	True Positive Rate (Sensitivity)	False Positive Rate (1-Specificity)	Accuracy
Image-1	0.2805	0.0365	0.9025
Image-2	0.3142	0.0317	0.9013
Image-3	0.3426	0.0335	0.9091
Image-4	0.2996	0.0289	0.9097
Image-5	0.3777	0.0347	0.9127
Image-6	0.2634	0.0303	0.9007
Image-7	0.2636	0.0315	0.9115
Image-8	0.3583	0.0292	0.9269
Image-9	0.2936	0.0344	0.9049
Image-10	0.2769	0.0367	0.901
Image-11	0.242	0.0323	0.9075
Image-12	0.3001	0.0348	0.9161
Image-13	0.2927	0.0307	0.9081
Image-14	0.246	0.0324	0.894
Image-15	0.3031	0.0348	0.9069
Image-16	0.3445	0.0335	0.9058
Image-17	0.2689	0.33	0.9106
Image-18	0.3236	0.0348	0.9096

Image-19	0.2703	0.0317	0.8927
Image-20	0.3749	0.0441	0.9051

TABLE II. AVERAGE PERFORMANCE OF IMAGE PROCESSING SYSTEM FOR KIRSCH TEMPLATE METHOD

Method	True Positive Rate (Sensitivity)	False Positive Rate (1-specificity)	Accuracy
Kirsch Template Method	0.3749	0.0441	0.9269

IV. CONCLUSION

The retinal image processing system uses a TIFF file format retinal image to extract the vessel. The input retinal image given to the image processing system undergoes various processes, such as vessel segmentation, vessel enhancement and vessel extraction. The system performance is measured by calculating sensitivity and specificity. The automatically generated segmented image using Kirsch Template is compared with manual segmented image and finally the reconstructed image is obtained.

REFERENCES

- [1] E. Grisan, A. Pesce, A. Giani, M. Foracchia, and A. Ruggeri, "A new tracking system for the robust extraction of retinal vessel structure", IEEE Eng. Med. Biol. Soc., Sep. 2004, vol. 1, pp. 1620-1623.
- [2] H. Azegrouz and E. Trucco, "Max-min central vein detection in retinal fundus images", IEEE Int. Conf. Image Process., Oct. 2006, pp. 1925-1928.
- [3] H. Li, W. Hsu, M. L. Lee, and T. Y. Wong, "Automatic grading of retinal vessel caliber", IEEE Trans. Biomed. Eng., vol. 52, no. 7, pp. 1352-1355, Jul. 2005.
- [4] Sushil Kumar, Millie Pant, A.K. Ray, "2D Maximum Entropy Method for Image Thresholding Converge with Differential Evolution", Advances in Mechanical Engineering and its Applications (AMEA) 189 Vol. 2, No. 3, 2012, ISSN 2167-6380.
- [5] M. Martinez-Perez, A. Highes, A. Stanton, S. Thorn, N. Chapman, A. Bharath, and K. Parker, "Retinal vascular tree morphology: A semiautomatic quantification," IEEE Trans. Biomed. Eng., vol. 49, no. 8, pp. 912-917, Aug. 2002.
- [6] T.Y.Wong, F. M. A. Islam, R. Klein, B. E.K.Klein, F.Cotch, C.Castro, A. R. Sharrett, and E. Shahar, "Retinal vascular calibre, cardiovascular riskfactors, and inflammation: The multi-ethnic study of atherosclerosis (MESA)", Invest Ophthalm. Vis. Sci., vol. 47, no. 6, pp. 2341-2350, 2006.

An Efficient Clustering Technique and Analysis of Infrared Thermograms

R. Vishnupriya¹,

Department of Electronics and
Instrumentation Engineering,
St. Joseph's College of Engineering,
Chennai 600 119, Tamilnadu, India
vishnupriyarameshkumar@gmail.co
m.

N. Sri Madhava Raja²,

Department of Electronics and
Instrumentation Engineering,
St. Joseph's College of Engineering,
Chennai 600 119, Tamilnadu, India .

V. Rajinikanth³

Department of Electronics and
Instrumentation Engineering,
St. Joseph's College of Engineering,
Chennai 600 119, Tamilnadu, India
;rajinikanthv@stjosephs.ac.in.

Abstract— This work proposes an efficient clustering technique for the localization of normal and abnormal tissues using the thermal data obtained from Digital Infrared Thermal Imaging. 10 normal and abnormal raw thermograms are preprocessed and by using K-means clustering, the heat patterns of the thermograms are clustered into various objects using the Euclidean distance metric. Further, breast thermograms are analysed, extracting the region of abnormality by utilizing the fuzzy nature of these thermograms. Features extracted from the simulations conducted on breast thermograms are compared and a distinctive variation is observed. These features can be used efficiently to identify normal and abnormal tissues.

Keywords— *Thermograms; cdata; L*a*b space; K means Clustering; fuzzy; feature extraction.*

I. INTRODUCTION

Breast cancer has become one of the most important health problem in women. When X ray, C.T, Ultrasound and M.R.I. etc., are tests of anatomy, E.M.G. is a test of motor physiology, Digital Infra-red breast thermal imaging technique records temperature changes in blood flow and displays them as thermal patterns. Extensive research have been carried out and they prove that infrared thermography is an adjunct to mammography as it is non invasive, passive, radiation free technique, safe for all ages and genders.

The relationship between thermal signatures and breast cancer [1, 2] has been shown in the recent literature. The cancerous tissues and the lesions surrounding them show increased vascular flow and metabolic rate than normal tissues [3]. The accuracy of thermography depends upon the symmetry of the breasts' temperature, temperature stability, physiological state, and menstruation [4]. Gore and Xu observed that highly sensitive infrared cameras are distinct enough to record the local temperature distribution of a breast with tumor [5].

Medical images in Gray scale are displayed using color scales with the rapid growth in digital imaging [6]. A pseudo-color based coding presented in uniform color space preserves all the information of gray scale images that prevents any distortion [7]. Mostly preferred pseudo color coding are HSV

and L*A*B color space. L*a*b* space consists of a luminosity layer L*, a chromaticity layer a* and a chromaticity layer b* that helps to improve the visual perception and cognitive ability [8]

In thermal imaging due to the difficulties in automatic segmentation, asymmetric analysis is done with human intervention. Before extracting the features for quantitative analysis, segmentation of breast tissues is performed. Analysis of thermograms can be carried out by extracting the region of abnormality. Hence N. Golestani et al [9] has suggested the clustering of the thermo vascular heat patterns in breast thermogram using Fuzzy K means, Fuzzy C means and Level set methods. Based on the shape, size and borders of the ROI, abnormality was detected. Utilizing the fuzzy nature of the thermograms and by implementing fuzzy C- means and K-means segmentation various heat patterns of breast thermogram have been clustered [10]. Depending upon the sensitivity of the IR camera the number of clusters increases. To segment the abnormal patterns an Improved Particle Swarm Optimization (IPSO) algorithm [11] based on Otsu's bi-level and multi-level thresholding has been proposed. Similarly, modified algorithms [12, 13] were applied to extract the hottest region of breast thermogram which could help in detecting the temperature changes and suspicious tissue characteristics.

To evaluate the effectiveness of textural information possessed by mass regions features based on gray-level co-occurrence matrices are used. Tan et al. [14] used texture features to study the ocular thermograms in young and elderly subjects. Hairong Qi et al investigated features that support detection of asymmetry. By this approach the false positive rate gets reduced during diagnosis and increase chances of disease cure and survival [15]. Kaviya et al [16] in their work enhanced the thermal image using overall brightness local contrast adaptive equalization (OBLCAE) algorithm which is better even for low illumination color image after segmentation. Feature extraction matrix has been generated by applying GLCM over the enhanced image.

This paper is organized as follows: A review of the previous work description on the related problem is discussed in Section 1. Section 2 gives an overview of the color based segmentation algorithm (K-means clustering). Numerical experimental results and discussions of the simulated results obtained from normal and abnormal thermograms are presented in Section 3. Section 4 presents the concluding remarks of the work and its future enhancements.

II. METHODOLOGY

In this study, the segmentation of abnormal tissues from thermograms is done by K-means clustering. The raw thermal images obtained in cdata form are converted to rgb. The tissues in rgb space are converted to lab space that enables us to quantify the differences made visually. Using K-means clustering the heat patterns of the thermogram is clustered into various objects using the Euclidean distance metric by which the hidden patterns and grouping of dataset is enhanced. Energy, correlation, contrast and homogeneity are extracted from the immune patterns of both normal and abnormal thermograms after segmentation. Features extracted from the segmented hottest pattern for both normal and abnormal patients are compared before and after segmentation. The features extracted contribute towards asymmetric analysis.

A. Database

With the use of latest medical thermography equipment DITI - SCT640 Digital Infrared thermal Camera specially designed for medical gp, equine & animal husbandry, 10 normal and 10 abnormal raw breast thermograms were obtained from Digital Infrared Thermal Imaging. In healthy subjects, the thermo vasculature is consistent. Current systems record these thermal patterns with a sensitivity of 0.01°C by DITI. The image capture process is highly performed by certified thermographer.

B. K-Means Clustering

Primarily, a color based segmentation techniques of breast thermal images is modeled and the features extracted from the obtained clusters are compared with the thermograms before segmentation. Segmentation of breast thermal images helps in detecting the abnormal cases and determining the degree of severity of a malignant tumour. Since malignancy type of tumors are associated with higher temperature than healthy breasts and benign tumors types, this study is focused in detecting the hottest/suspected regions of abnormal breasts [17, 18]. Using an algorithm based on K-means algorithm, few empty clusters may be segmented in the result but this is one seems to be an effective unsupervised learning techniques for clustering. It partitions M data points to N disjoint subsets S_j where $j=1, 2, \dots, K$.

It is based on minimization of the objective function

$$J = \sum_{j=1}^k \sum_{n \in S_j} ||x_n - \mu_j||^2 \quad (1)$$

where x_n , representing n^{th} data points (vector form) in S_j and μ_j is the geometric centroid of data points.

The algorithm consists of the following steps:

1. The thermograms obtained were in cdata form which has been converted to RGB .

2. The tissues in RGB space are transformed to lab space that enables us to quantify the differences made visually. The L*a*b* color space contains luminosity layer, 'L*' channel. Two other chromaticity layers 'a*' and 'b' channels respectively. All of the color information is present in the 'a*' and 'b*' layers only. In order to distinguish the color differences we use lab space.
3. Selecting a value of cluster N, and further by implying K-means clustering algorithm to the thermograms, information can be clustered based on the heat patterns.
4. We aim to define the n centroids for N clusters. Each point in the heat pattern belonging to thermogram is associated with the nearest centroid. The variation between the considered two colors is estimated using Euclidean distance metric.

Euclidean distance is given by

$$d(p, q) = \sqrt{(p_1 - q_1)^2 + (p_2 - q_2)^2} \quad (2)$$

where $d(p, q)$ is the distance between the centroid and the point q .

5. When no point is pending, we assign each object based on minimum distance to the nearest centroid and early grouping is done.
6. Once we obtain the n new centroids, a new binding is to be performed between the same data points and the nearest new centroids. This process is repeated until no changes in the centroids are possible.

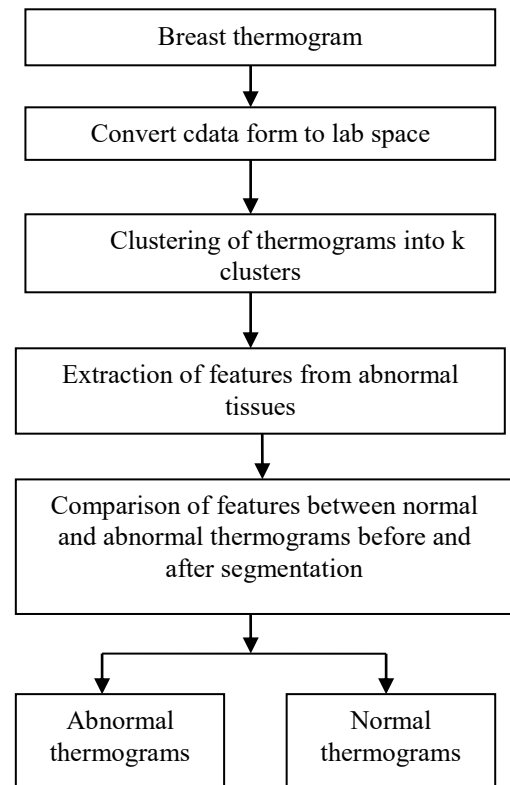


Fig 1: Workflow representation of the clustering technique and extraction of features from the breast thermograms

By this procedure, color segmentation of both normal and abnormal thermal images is performed. After finding the hottest regions, the prime features of gray level co-occurrence matrix are obtained from those regions. The procedure

involved in the clustering technique and classification of normal and abnormal thermograms are depicted in the figure 1.

III. RESULTS AND DISCUSSION

Sample breast thermograms for 3 normal and 3 abnormal cases that are preprocessed into RGB space from cdata form is shown the in figure 2(a) and 3(a) respectively.

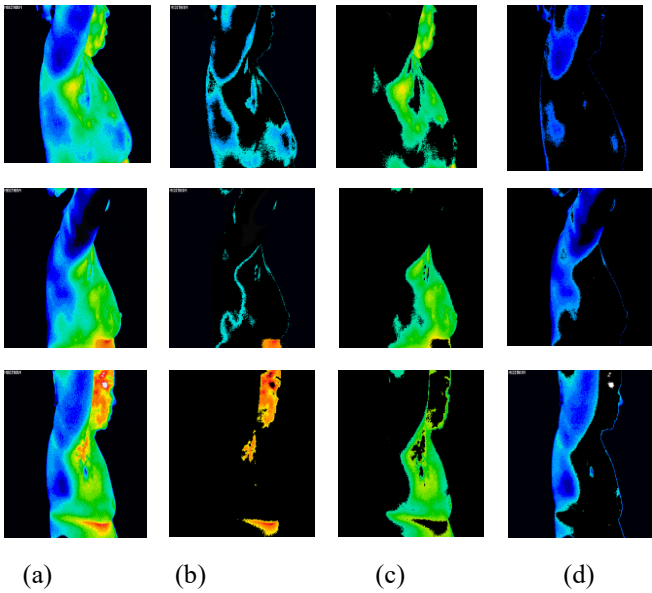


Fig 2: Representative normal image converted from cdata to RGB (a) and their corresponding red cluster (b), green cluster (c) blue cluster (d)

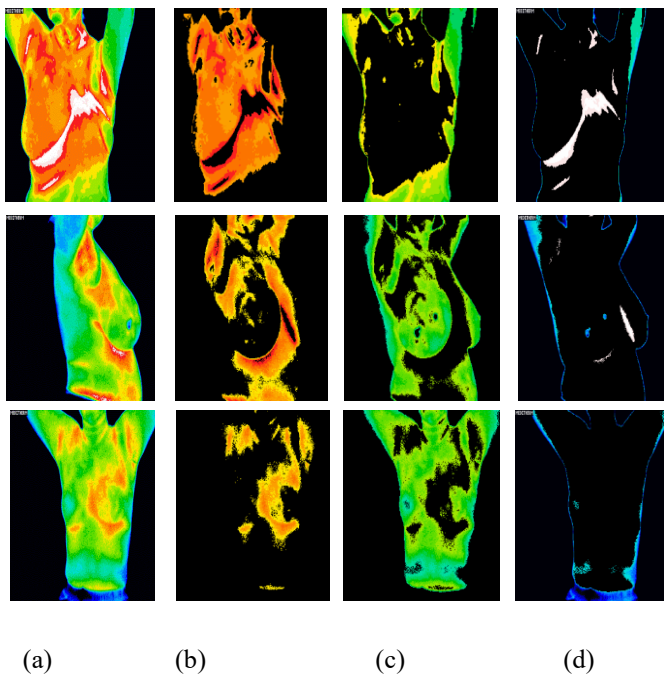
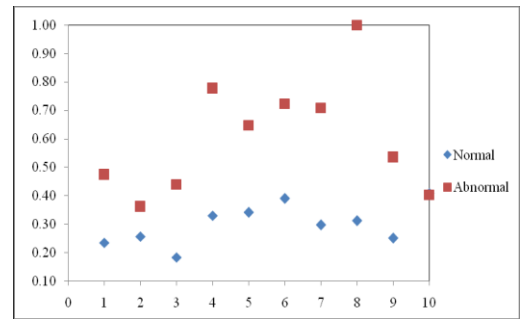
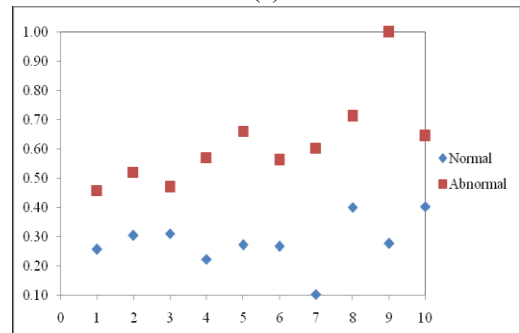


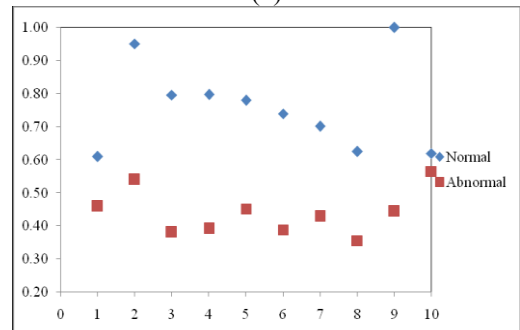
Fig 3: Representative abnormal image converted from cdata to RGB (a) and their corresponding red cluster (b), green cluster (c) blue cluster (d)



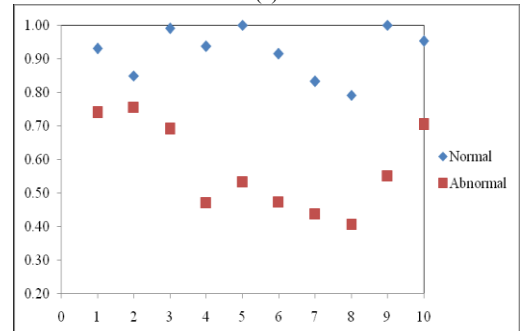
(a)



(b)



(c)



(d)

Fig 4: Scatterplot of variation in contrast between normal and abnormal thermograms before segmentation (a) variation in contrast between normal and abnormal thermograms after segmentation (b) variation in energy between normal and abnormal thermograms before segmentation (c) variation in energy between normal and abnormal thermograms after segmentation (d)

The different colors in thermograms represent the temperature gradients and are assigned in the image from black to white. The dark red color represents highest temperature compared to nearby tissues. It is seen that the presence of cancerous tissue and increased metabolic activity introduces asymmetric pattern when compared to normal breast thermograms.

In this work, an efficient clustering technique: Fuzzy K-means (FKM) for the segmentation of various breast thermograms is applied to both normal and abnormal thermal images. The various heat patterns for each case are clustered. Several methods to extract features were employed in order to detect any abnormality condition from breast thermograms. Texture of the abnormal patterns of any thermogram may be examined by determining the gray-level co-occurrence matrix (GLCM), otherwise termed as gray-level spatial dependence matrix.

The prime features of GLCM describe the correlation in intensity of pixels that are next to each other in space. This feature forms the basis for effective classification of thermograms whether it is normal or complicated by malignant tissues. For this, 10 normal and abnormal breast thermograms having pathology in either of the left or right breasts were subjected to clustering and feature extraction. These features are normalized and analyzed quantitatively. Normalised values of the statistical features extracted from thermograms in both the groups are shown in Table 1. The relationship between features varies depending upon the underlying properties of the thermogram under consideration.

TABLE I. COMPARISON OF FEATURES IN THE NORMAL AND ABNORMAL THERMOGRAMS BEFORE AND AFTER SEGMENTATION

Normal	Contrast		Correlation		Energy		Homogeneity	
	Bef Seg	After Seg	Bef Seg	After Seg	Bef Seg	After Seg	Bef Seg	After Seg
1	0.23	0.26	0.91	0.99	0.61	0.93	0.94	0.98
2	0.26	0.30	0.92	0.99	0.95	0.85	0.97	1.00
3	0.18	0.31	0.87	0.99	0.80	0.99	0.96	0.99
4	0.33	0.22	0.76	0.99	0.80	0.94	0.98	0.99
5	0.34	0.27	0.94	0.99	0.78	1.00	0.98	1.00
6	0.39	0.27	0.85	0.96	0.74	0.91	0.92	0.98
7	0.30	0.10	0.84	0.99	0.70	0.83	0.99	0.99
8	0.31	0.40	0.92	0.99	0.63	0.79	0.94	0.98
9	0.25	0.28	0.75	0.99	1.00	1.00	0.99	1.00
10	0.41	0.40	0.69	0.99	0.62	0.95	0.96	0.98
Ab-normal	Contrast		Correlation		Energy		Homogeneity	
	Bef Seg	After Seg	Bef Seg	After Seg	Bef Seg	After Seg	Bef Seg	After Seg
1	0.47	0.46	0.96	0.99	0.46	0.74	0.97	0.97
2	0.36	0.52	0.97	1.00	0.54	0.76	0.98	0.99
3	0.44	0.47	0.88	0.98	0.38	0.69	0.95	1.00
4	0.78	0.57	0.96	0.99	0.39	0.47	0.94	0.94
5	0.65	0.66	0.97	1.00	0.45	0.53	0.94	0.94
6	0.72	0.56	0.97	1.00	0.39	0.47	0.94	0.94
7	0.71	0.60	0.97	1.00	0.43	0.44	0.93	0.94
8	1.00	0.71	0.94	0.99	0.36	0.41	0.91	0.91
9	0.53	1.00	0.95	0.99	0.44	0.55	0.91	0.92
10	0.40	0.64	0.95	1.00	0.57	0.70	0.95	0.96

The difference between maximum and minimum energy is higher in the hottest cluster of abnormal thermograms after

segmentation than normal thermograms. More prominent anisotropic distribution in abnormal thermograms differs the energy by 25.20% after segmentation from the raw thermograms before segmentation. This is evident from the change in magnitude from 0.41 to 0.76 after

The numerical features extracted describe the local patterns and shows a range of variation in the thermal patterns before and after segmentation. As all clustering and classification techniques are statistical methods, sufficient data is required for obtaining significant results.

The features analyzed are related with the help of boxplot and scatterplots as shown in figure 4 and 5. The severity of the disease for each case is represented and compared. As there is weak correlation in abnormal thermograms, normal thermograms show high homogeneity. From the table 1 we observe that the heat patterns are weakly correlated before segmentation. The underlying temperature distribution of thermograms shows significant variation in energy. As energy depends upon the amount of information present in different orientations it is clearly distinct in both normal and abnormal tissues before and after segmentation.

The difference between maximum and minimum energy is higher in the hottest cluster of abnormal thermograms after segmentation than normal thermograms. More prominent anisotropic distribution in abnormal thermograms differs the energy by 25.20% after segmentation from the raw thermograms before segmentation. This is evident from the change in magnitude from 0.41 to 0.76 after segmentation.

The local changes in the information for normal images are less than 0.50 in a range between 0.18 and 0.41 before segmentation whereas its value drops down between 0.10 and 0.40 after segmentation. High percentage contrast difference of 8.95% before segmentation and 15.44% after segmentation among normal and abnormal is observed.

As the changes in the vascular patterns is not consistent, depending upon the severity of the abnormal conditions prevailing in the thermogram the average energy and contrast values across the considered images esteem to be high. The results show that normal and abnormal thermograms results with a normalised average energy difference of 3.92% before segmentation and 1.13% after segmentation. Similarly, among the different pathological conditions, maximum variation is observed from normalised contrast before and after segmentation.

IV. CONCLUSION

In this work, an attempt is made to quantify the abnormality in breast thermograms using the prime GLCM Features. For this experimentation, the clusters are obtained using the raw breast thermograms collected from DITI. The healthy breast regions are grouped as normal and breast regions with pathology as abnormal using an efficient K means clustering



technique. Due to abrupt changes in pixel intensities the two groups shows considerable variations in terms of average energy and contrast. The results show that the derived features are highly correlated and homogenous after segmentation.

In summary, it is shown that these features quantify the structural or contrast nature of the image. It appears that these features could support automated and early diagnosis of breast cancer. Though, the results are reported with robustness of the features, on adding feature selection and classification will help us diagnose the type of cancer which leads to further improvements. These features makes the algorithm suited for real time online (live processing) and can be applied to computer assisted diagnosis.

ACKNOWLEDGMENT

We would like to acknowledge and extend our gratitude to the DITI Imaging Founder & CEO Mr.A.M.Shahul Hameed and its certified thermographer Ms.Hemalatha-CCT1 USA for supporting this work in collecting thermograms of normal and abnormal patients.

REFERENCES

- [1] Gautherine, M., and Gros, C., "Contribution of infrared thermography to early diagnosis, pretherapeutic prognosis and post irradiation follow-up of breast carcinomas", *Med. Mundi*. vol 21:pp 135–149, 1976.
- [2] Gros, C., Gautherine, M., and Bourjat, P., "Prognosis and post therapeutic follow-up of breast cancers by thermography". *Bibl. Radiol*. vol 6: pp 77–90, 1975.
- [3] Fok, S. C., Ng, E. Y. K., and Tai, K., "Early detection and visualization of breast tumor with thermogram and neural network", *J. Mech. Med. Biol*. vol 2: pp 185–195, 2002.
- [4] Ng, E. Y. K., Chen, Y., and Ung, L. N., "Computerized breast thermography: Study of Image segmentation and temperature cyclic variations", *Intl. J. Med. Eng. Technol*. vol 25:pp 12–16, 2001.
- [5] Gore, J. P., and Xu, L. X., "Thermal imaging for biological and medical diagnostics, biomedical photonics handbook". CRC, Boca Raton, 2003.
- [7] Li, H., and Burgess, A. E., "Evaluation of signal detection performance with pseudo-color display and lumpy backgrounds." *J Med Syst* vol 34: pp 35–42, 2010.
- [8] Zhou, X., Zhang, C., & Li, S. "A perceptive uniform pseudo-color coding method of SAR images", *International Conference on Radar, CIE, IEEE*, vol 23,pp. 1–4, Oct. 2006.
- [9] Connolly, C., and Fliess, T., "A study of efficiency and accuracy in the transformation from RGB to CIELAB color space", *IEEE Transactions on Image Processing*. vol 6:pp 71046–1048, 1997
- [10] N. Golestani, M. Tavakol, E.Y.K.Ng: "Level set Method for Segmentation of Infrared Breast Thermograms", *EXCLI Journal*, pp 241-251,2014.
- [11] EtehadTavakol M, Sadri S, Ng EYK. "Application of K- and fuzzy c-means for color segmentation of thermal infrared breast images". *J Med Syst*. vol 34: pp 35–42,2010 [PubMed].
- [12] N Sri Madhava Raja, S Arockia Sukanya, Y Nikita, "Improved PSO based multi-level thresholding for cancer infected breast thermal images using Otsu" *Procedia Computer Science*, vol 28,pp 524-529, 2015.
- [12] Sowmya B, Bhattacharya S, "Color image segmentation using fuzzy clustering techniques". *Annual IEEE*. pp 41–45, 2005.
- [13] Pakhira MK. "A modified k-means algorithm to avoid empty clusters". *Int J Rec Trends Engin*. vol 1: pp 220–226, 2009.
- [14] Tan JH, Ng EYK, Acharya UR.,"Study of normal ocular thermogram using textural parameters". *Infrared Phys Technol.*, vol 53, issue 2, pp 120-126,2010.
- [15] Hairong Q, Kuruganti PT., "Detecting breast cancer from thermal infrared images by asymmetry analysis". *Eng Med Biol*. Vol 2: pp 1155–1156, 2002.
- [16] C. Kaviya, M. Sundaram, T. Pandiselvi, "Study of color image enhancement for analysis of breast thermograms" *International Conference on Computing Technologies and Intelligent Data Engineering (ICCTIDE)*, 7-9 Jan. 2016.
- [17] Bezdek, J. C., "Pattern recognition with fuzzy objective function algorithms". Plenum, New York, 1981.
- [18] <http://mathworld.wolfram.com/K-MeansClusteringAlgorithm>.
- [19] B.Balasuganya, Telagarapu Prabhakar, S.Poonguzhali "An Evaluation of Different Feature Extraction Methods for Classification of Tumor in Breast Ultrasound Images" *International Conference on Computation of Power, Energy, Information and Communication*, ISBN: 978-1-4673-6406- 5, April 2013.
- [20] B.Balasuganya, "Contourlet Based Feature Extraction Method for Classification of Breast Cancer using Thermogram Images", *International Journal of Scientific & Engineering Research*, Volume 5, Issue 4, April-2014 285 ISSN 2229-5518.
- [20] Haralick RM, Shanmugam K, Dinstein I, "Textural features for image classification", *IEEE Trans Syst Man Cybern*, vol 3:pp 610–621,1973.
- [21] Sheeja V. Francis & M. Sasikala & S. Saranya, "Detection Of Breast Abnormality From Thermograms Using Curvelet Transform Based Feature Extraction", *J Med Syst* (2014) 38:23.
- [22] S. S. Suganthi & S. Ramakrishnan, "Analysis of Breast Thermograms Using Gabor Wavelet Anisotropy Index" *J Med Syst* (2014) 38:101.

Estimation of Femur Morphometric Features for CBIR Application

T. Christy Bobby

Department of Electronics and Communication Engineering

M.S.Ramaiah University of Applied sciences-Bangalore

christy.ec.et@msruas.ac.in

Abstract— Recently, it has been demonstrated that morphology of the trabecular bone and morphometric of the proximal femur provide important and useful information for the diagnosis of osteoporosis and femoral fractures. In this work, human femur radiographic bone images are classified using morphometric features derived from the segmented bone. Femur bone structure from 2D X-ray radiograph is segmented using active contour method and morphometric measurements such as head diameter, head height, neck diameter, intertrochanteric distance, proximal femur length and neck length are calculated in pixel values. From the measured morphometric distances, six morphometric ratios are calculated. These ratios are examined to discriminate normal and abnormal bone and used for classification. Neural network based statistical tools such as Extreme Learning Machine (ELM) and Evolutionary Extreme Learning Machine (E-ELM) are utilized to automate the classification. The results show that the E-ELM classifier performance in terms of accuracy (98%) is higher when compared to ELM classifier. This proposed method could be used as adjoin method for Quantitative Ultrasound (QUS) to identify the disorders such as osteoporosis and femoral fractures.

Keywords—*Human femur, Trabecular structure, CBIR, Sharpness features*

I. INTRODUCTION

Osteoporosis and femoral fractures in the elderly population are the major health dilemma allied with increased mortality, morbidity and healthcare cost. Thus for prevention of proximal femoral fractures, understandings of the causes and bone strength features are essential. Trabecular bone morphology and morphometric measurements of the proximal femur are considered as significant and useful factors for screening and diagnosis of femoral fractures and osteoporosis [1]. Previous studies have outlined the influence of various morphological, morphometric and functional features of the cortical and trabecular bones are utilized both in diagnosis and therapy in femur bone fractures. Obtaining these informations from image without human intervention or manual editing remains a goal to avoid inconsistency present in the manual analysis [2, 3].

Image segmentation plays an imperative role in medical images, such as X-ray, Computed Tomography (CT), Ultrasound (US) and Magnetic Resonance Imaging (MRI). In particular, image segmentation may be considerably difficult for low intensity contrast images with a smoothly varying intensity, noise and weak edges. Due to these above features some of the established segmentation techniques such as clustering, edge detection, thresholding and region growing

face substantial difficulties. To address these complexities, deformable contour approach known as active contour snakes model has been used as one of the most versatile technique for medical image segmentation. In Snakes model the object boundary is represented as an energy minimization procedure [4] which intern describe an object edge as a parameter curve or surface. The curves are influenced by both an internal and external forces. A snake can find object boundaries after proper initialization [5]. The active contour models have the capability to realize sub pixel accuracy and thus it provide closed and smooth boundaries even for low contrast images.

In this paper, femur bone is segmented from the low contrast X-Ray images using variational formulation of level set function. This method completely purges the need of the re-initialization process by forcing the level set function to be close to a signed distance function [6,7].

Conventionally, radiologists or physicians analyse and judge the severity of the ailment on the basis of their training and experience. But many times human intervention will have certain degree of variability in image elucidation. Thus the design of automated image analysis tool may serve to reduce the variability and provide accurate information to support clinical decision-making systems [8]. Artificial Neural Networks (ANN) has been applied widely to automate the biomedical screening and diagnostic systems. The ANN based Extreme Learning Machine (ELM) is an efficient learning algorithm is used in Single-hidden Layer feed Forward Neural network (SLFN). This algorithm makes the selection of hidden neurons weights very fast using Moore-Penrose (MP) generalized inverse problem. Also, MP over comes many drawbacks such as stopping criteria, learning rate, learning epochs, and local minima faced by gradient-based learning methods. However, ELM needs more number of hidden neurons due to the random determination of the input weights and hidden biases [9]. To eliminate redundancy in the hidden nodes and to achieve satisfactory performance, Evolutionary Extreme Learning Machine (E-ELM) has been designed by combining both ELM and Differential Evolution (DE) [10].

In this work, femur bone structure from 2D X-ray radiographs is segmented using active contour method. The Morphometric measurements such as Head Diameter (HD), Head Height (HH), Neck Diameter (ND), Intertrochanteric Distance (ID), Proximal Femur Length (PFL) and Neck Length (NL) are measured from the segmented normal and abnormal proximal femur images. And also six morphometric ratios such as Sphericity (SP), Head-Neck Ratio (HNR),

Proportionality (PP), Head–Neck Scale (HNS), Head–Neck Transition (HNT) and Trochanter–Head Ratio (THR) are calculated using the derived morphometric measurements [11]. These ratios are examined to distinguish normal and abnormal bone and used as inputs to the ELM and E-ELM classifiers. The performance of the classifiers is analysed using classification accuracy.

II. METHODOLOGY

Digitized pelvis X-ray images ($N = 60$) are considered for this analysis. To improve the contrast, the digital radiographs are enhanced using Adaptive Histogram equalization (AHE) technique. The proximal femur bones from the background muscle are segmented using Active Contour using Level set method.

A. Segmentation using Active Contour Level set Function:

In level set formulation, the active contours are denoted by C : $C(t) = \{(x, y) | \phi(t, x, y) = 0\}$, where $\phi(t, x, y)$ is level set function. The general level set evolution equation of the level set function ϕ is,

$$\frac{\partial \phi}{\partial t} + F |\nabla \phi| = 0 \quad (1)$$

The function F represents the speed function. For segmentation of the image, F depends on the complexity of the image and the level set function ϕ . For the given level set function ϕ the gradient flow progress equation is given by:

$$\frac{\partial \phi}{\partial t} = \mu [\Delta \phi - \text{div}(\frac{\nabla \phi}{|\nabla \phi|})] + \lambda \delta(\phi) \text{div}(g \frac{\nabla \phi}{|\nabla \phi|}) + \nu \delta(\phi) \quad (2)$$

Where $g = \frac{1}{1 + |\nabla G_o * I|^2}$ is image gradient, δ is a regularized version of one dimensional dirac measure, deviation of ϕ from a signed distance function is controlled by the effect of μ and ν is a correctness term and it is a force pushing the curve towards the object, where $\mu > 0$, $\nu > 0$, $\lambda > 0$ [7].

B. Ratiometric calculation using Morphometric Features

From the segmented image using active contour level set the morphometric parameters such as head diameter, head height, neck diameter, intertrochanteric distance, proximal femur length and neck length are calculated in pixel values [11]. The parameters are calculated as the average value three consecutive trials. From the above derived parameters the six ratios such as SP, HNR, PP, HNS, HNT and THR are calculated as

$$\begin{aligned} \text{Sphericity(SP)} &= \text{HH} / 0.5\text{HD} \\ \text{Head Neck Ratio (HNR)} &= \text{HD/NL} \\ \text{Proportionality (PP)} &= \text{PFL/ID} \\ \text{Head Neck Scale (HNS)} &= \text{HH/NL} \\ \text{Head Neck Transition (HNT)} &= \text{HD/ND} \end{aligned}$$

$$\text{Trochanter Head Ratio (THR)} = \text{ID/HD}$$

These ratios are examined to distinguish normal and abnormal bone and used as an input to the classifiers.

C. Classification using ELM and EELM classifiers:

Training SLFNs with K hidden neurons and activation function $g(x)$ is used to learn N distinct samples, where x_i is the inputs and t_i is the targets. In ELM, the nonlinear system has been converted to a linear system using the following equation:

$$H\beta = T \quad (5)$$

where H is the hidden-layer output matrix, β is the output weights matrix and T targets matrix. The output weight is computed as Least-Square (LS) solution to the given linear system. The minimum norm LS to the linear system is

$$\hat{\beta} = H^\dagger T, \quad (6)$$

where H^\dagger is the MP generalized inverse of matrix H . Using DE and MP generalized inverse, the population in E-ELM is randomly generated. It consists of input weights and hidden biases.

$$\theta = \begin{bmatrix} w_{11}, w_{12}, \dots, w_{1k}, w_{21}, w_{22}, \dots, w_{2k}, \dots, w_{n1}, \\ w_{n2}, \dots, w_{nk}, \dots, b_1, b_2, \dots, b_k \end{bmatrix} \quad (7)$$

All w_{ij} and b_j are randomly initialized within the range of $[-1, 1]$. The subsequent output weights are computed by using the MP generalized inverse and evaluated using Root Mean Squared Error (RMSE) value of cost function (E)

$$E = \sqrt{\frac{\sum_{j=1}^N \|\sum_{i=1}^K \beta_i g(w_i \cdot X_j + b_i) - t_j\|_2^2}{mN}} \quad (8)$$

The fitness to the RMSE validation set is used to save time. In next step, all individuals in the population are calculated using mutation, crossover and selection steps of DE.

In the selection step, the mutated vectors are compared with the original vectors, and the vectors with better fitness values are retained to the next generation. Further to improve the generalization performance of selection criteria, one more criteria is added into the selection. In this selection strategy, smaller norm value of output weights $\|\beta\|$ is considered and the calculation of new population $\theta_{i, G+1}$, is described as follows:

$$\theta_{i, G+1} = \begin{cases} \mu_{i, G} & \text{if } f(\theta_{i, G}) - f(\mu_{i, G}) > \varepsilon f(\theta_{i, G}), \\ \mu_{i, G} & \text{if } |f(\theta_{i, G}) - f(\mu_{i, G})| < \varepsilon f(\theta_{i, G}) \text{ and} \\ \|\beta^{\mu_{i, G}}\| < \|\beta^{\theta_{i, G}}\|, \\ \theta_{i, G} & \text{else,} \end{cases} \quad (9)$$

Where, $f(\cdot)$ is the fitness function and ε is a preset tolerance rate. Once the new population is generated, the DE process is repeated until a preset maximum learning epoch is completed [12]. The accuracy of classification models with different type of activation functions such as sigmoidal, sine, hardlim, triangular basis and radial basis functions for varying

number of epochs from 100 to 1000 is estimated and analyzed. Accuracy is ratio of sum of True Positives (TP) samples and True Negatives (TN) samples to total number of samples used for testing. The TP and TN are the cases where the abnormal is classified as abnormal and normal classified as normal, respectively [13].

III. RESULTS AND DISCUSSIONS

Typical pre-processed radiographic images of normal and abnormal femur trabecular bones are shown in Fig 1 (a) and (b) respectively. The femoral head region of the anterior-posterior pelvis images are overlapped with thigh bone and muscles. Thus, the segmentation of femur bone from the background in radiographic image is very difficult task.

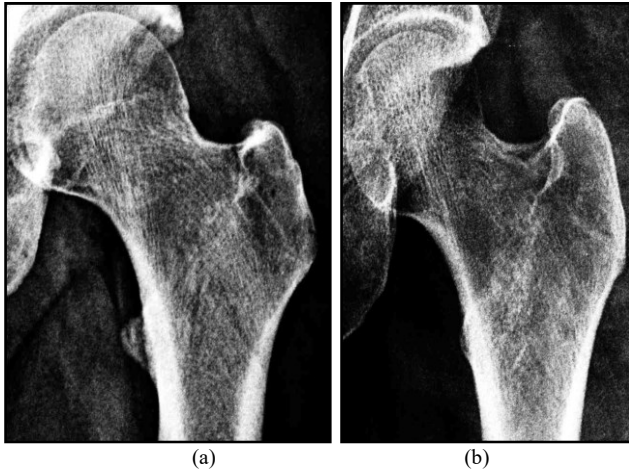


Fig. 1 Typical normal (a) and abnormal (b) femur bone image

Fig 2 (a) and (b) shows the normal and abnormal femur bone images with the detected edge using active contour model for 250 iterations. Fig 3 (a) and (b) shows the corresponding segmented images with background suppressed. Fig 4 shows the measured morphometric parameters such as head diameter, head height, neck diameter, intertrochanteric distance, proximal femur length and neck length are calculated in pixel values from the segmented femur bone images.

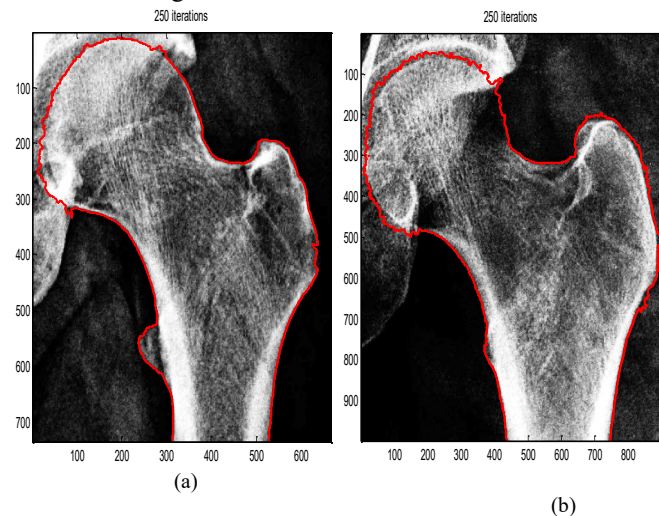


Fig 2 Normal femur bone (a) Abnormal femur bone (b) with contour

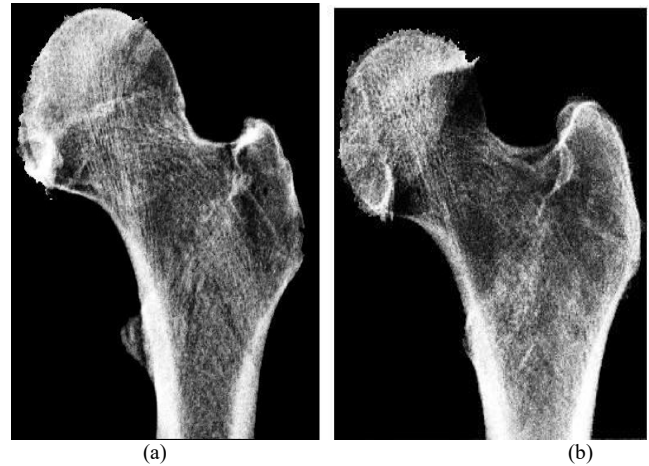


Fig 3 Segmented (a) normal femur bone and (b) abnormal femur bone

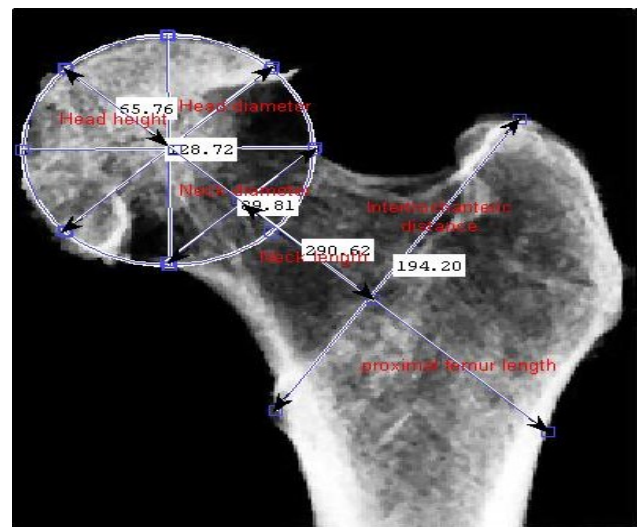


Fig. 4. Definitions of the head diameter, head height, neck diameter, intertrochanteric distance, proximal femur length and neck length

Fig. 5 shows the scattergram of morphometric ratios for various normal and abnormal images. The table 1 shows the mean values of the morphometric ratios and their statistical significance values. Except head neck scale ratio all other morphometric ratios have clear demarcations between normal and abnormal images and statistically highly significant values. Also the ratio metric values for abnormal images are high except head neck ratio. It is clear from the results that the abnormal images shows morphometric changes due to some pathology and hence it could be used for the classification of normal and abnormal images. The sphericity ratio shows high difference between normal and abnormal values compare with other ratios. This could be due to more geometrical variations occur in the femoral head compare with other regions in the abnormal femur bone. Since sphericity is derived from the head height and the head radius. Except head neck scale ratio all other morphometric ratios employed for classification to achieve better performance.

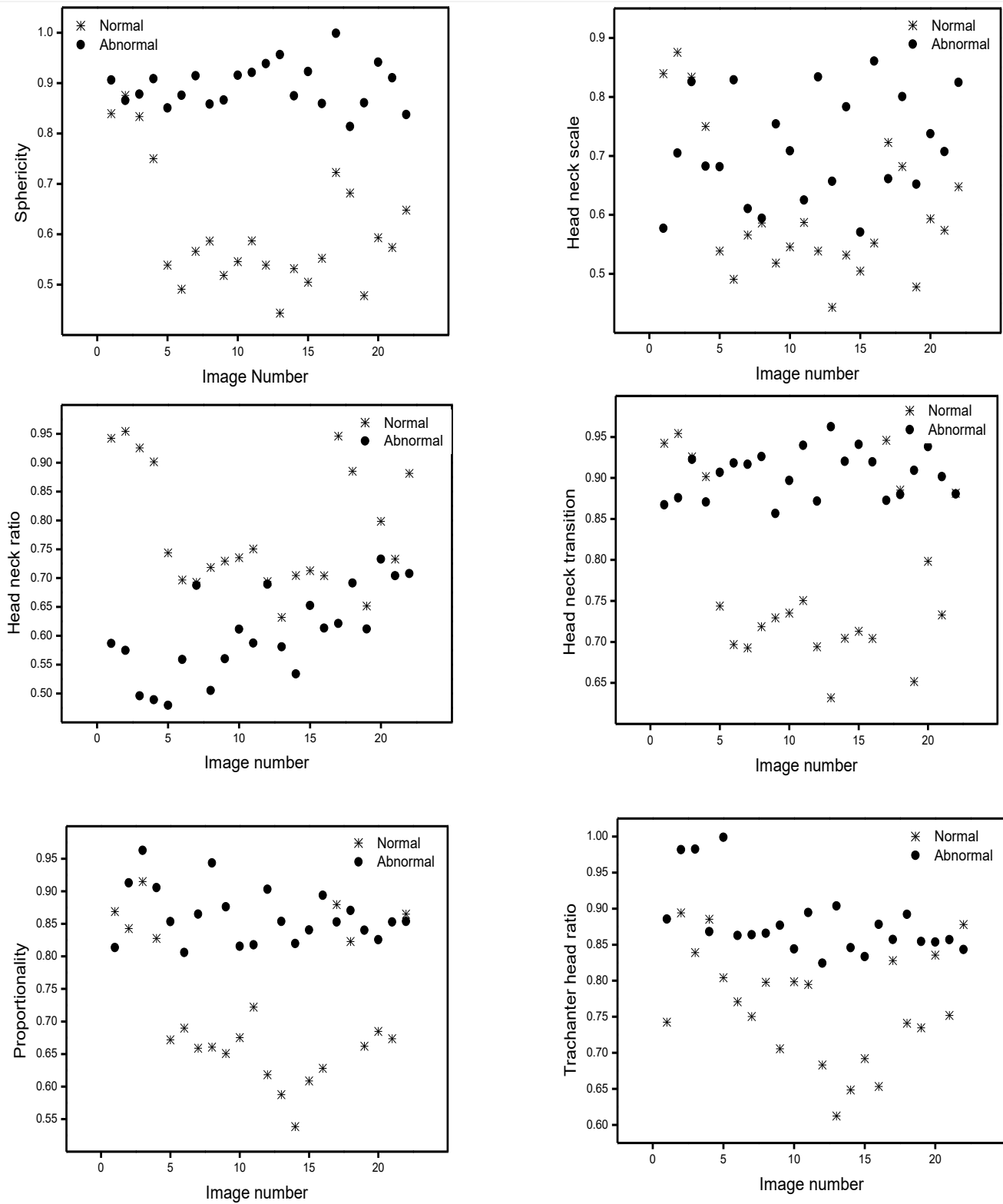


Fig. 5 Scattergram of Morphometric ratios derived from normal and abnormal femur bones

TABLE 1
NORMALISED MEAN VALUES OF THE
MORPHOMETRIC RATIOS AND THE SIGNIFICANT VALUES OF
NORMAL AND ABNORMAL IMAGES

Morphometric ratios	Normalised mean values		Significant value
	Normal	Abnormal	
Sphericity	0.626	0.867	P < 0.0001
Head-neck ratio	0.788	0.673	P < 0.0001
Proportionality	0.728	0.836	P < 0.0001
Head-neck scale	0.626	0.637	P = 0.0028
Head-neck transition	0.788	0.883	P < 0.0001
Trochanter-head ratio	0.785	0.851	P < 0.0001

Table 2 shows the accuracy of classification models with different activation functions such as Sigmoidal, Sine, Hardlim, Triangular basis (TBF) and Radial Basis Functions (RBF). ELM classifier exhibits maximum accuracy of 83% for sigmoidal and sine activation functions. Compare with ELM, E-EELM produced high classification accuracy. Thus it is observed from the results E-ELM model using RBF performs efficiently in terms of accuracy (98%).

TABLE 2
ACCURACY OF ELM AND E-ELM FOR DIFFERENT
ACTIVATION FUNCTIONS

Activation Function	Accuracy (%)	
	ELM	EELM
Sigmoidal	83	95
Sine	83	95
Hardlim	66	95
TBF	58	95
RBF	75	98

IV. CONCLUSION

Characterization of femur bone quantity and quality has received considerable attention due to its sensitivity to hormonal, mechanical, and therapeutic effects. In this work, morphometric features are derived to classify normal and abnormal femur bones using conventional radiographs. Among the six morphometric ratios, five features showed better differentiation of normal and abnormal images. The

results demonstrate that it is possible to differentiate and classify normal and abnormal images using morphometric ratios. Also it is seen that the E-ELM classifier uses RBF activation function showing better classification accuracy (98%). Hence it appears that classification of femur image using morphometric analysis could be used as an index for automated image analysis using Content Based Image Retrieval (CBIR) system and gross abnormality detection.

REFERENCES

- [1] Y. Maeda et al., "Comparison of femoral morphology and bone mineral density between femoral neck fractures and trochanteric fractures", *Clin. Orthop. Relat. Res.*, vol. 469, issue 3, pp. 884-889, Mar. 2010.
- [2] Zhao L.J. et al., "Genome-wide association study for femoral neck bone geometry", *J. of Bone and Mineral Res.*, vol. 25, issue 2, pp. 320-329, Feb. 2010.
- [3] P. Cerveri et al., "Towards automatic computer-aided knee surgery by innovative methods for processing the femur surface model", *The Int. J. of Med. Robotics and Computer Assisted Surg.*, vol. 6, issue 3, pp. 350-361, Sep. 2010.
- [4] M. Kass, A. Witkin and D. Terzopoulos, "Snakes: Active Contour Models", *Int. J. of computer vision*, vol. 1, issue 4, pp. 321-331, 1988.
- [5] J. Cheng, Y. Liu, R. Jia, W. Guo, "A New Active Contour Model for Medical Image Analysis—Wavelet Vector Flow", *IAENG Int. J. of Applied Mathematics*, vol. 36, issue 2, May 2007.
- [6] K. K. Shyu, V. T. Pham, T. T. Tran and P.L. Lee, "Unsupervised active contours driven by density distance and local fitting energy with applications to medical image segmentation", *Machine Vision and Appl.*, vol. 23, issue 6, pp. 1159-1175, Nov. 2012.
- [7] C. Li, R. Huang, Z. Ding, C. Gatenby, D. N. Metaxes and J. C. Gore, "A level set method for image segmentation in the presence of inhomogeneities with application to MRI", *IEEE Trans. on Image Process.*, vol. 20, issue 7, pp. 2007-2016, July 2011.
- [8] A. Kassner, R. E. Thornhill, "Texture analysis: a review of neurologic MR imaging applications", *American J. on Neuroradiology*, pp.809-816, May 2010.
- [9] N. Liu, H. Wang, "Ensemble Based Extreme Learning Machine", *IEEE Signal Process. Lett.*, vol. 17, no. 8, pp. 754-757, Aug. 2010.
- [10] H. T. Huynh, Y. Won, *The Use of Evolutionary Algorithm in Training Neural Networks for Hematocrit Estimation*, *Evolutionary Computation*, Wellington Pinheiro dos Santos (Ed.), INTECH Open Access Publisher, 2009.
- [11] S. Schumann, M. Tannast, L. P. Nolte, G. Zheng, "Validation of statistical shape model based reconstruction of the proximal femur—A morphology study", *Medical Engineering & Physics*, vol. 32, issue 6, pp. 638-644, July 2010.
- [12] Q. Y. Zhu, A. K. Qin, P. N. Suganthan, G. B. Huang, "Evolutionary Extreme Learning Machine", *Pattern Recognition*, vol. 38, issue 10, pp.1759-1763, Oct. 2005.

Histogram shifting based reversible data hiding with controlled contrast Enhancement

V.R.VijayKumar
Department of ECE
Anna University Regional centre
Coimbatore, Tamilnadu
vr_vijay@yahoo.com

V. Suresh Babu
Department of ECE
Christ The King Engineering
Coimbatore, Tamilnadu
sureshvece@gmail.com

Abstract—In this paper, we present an improved reversible data hiding algorithm for digital images based on the histogram shifting technique which can accurately recover the original image after extracting the hidden data. The highest two peaks in the histogram of host image are selected for data embedding. This embedding process is repeated again and again, to attain larger embedding capacity. In addition, a Controlled Contrast Enhancement (CCE) is performed to get good visual perception. In order to verify the robustness of the proposed method various attacks such as impulse noise, shearing, rotation, and scaling are considered. The proposed algorithm efficiently removes the various attacks on the watermarked image and efficiently recovers the original and embedded data. The better performance of the proposed method over existing methods in terms of PSNR, SSIM and embedding rate is demonstrated.

Keywords— Controlled Contrast Enhancement, Histogram Shifting, Reversible Data Hiding, Watermarking.

I. INTRODUCTION

In recent years, the world of growing technology security is of utmost concern. With the increase in cyber crime, providing only system security is not sufficient. Security provided to secret information using data hiding also most important [1]. Data hiding is applied widely to the fields of ownership protection, content authentication, secret communication and telemedicine. Lot of data hiding methods has been proposed for the purpose of achieving imperceptibility, high capacity, robustness and confidentiality. Imperceptibility indicates that embedded images should be perceptually inconspicuous [2]. Robustness means the ability of correctly extracting embedded image after enduring different types of attacks (e.g., noise addition, scaling, rotation, shearing, cropping). Confidentiality refers to the fact that data is not exposed to the illegal user [3].

The well known data hiding method is the Least Significant Bit (LSB) substitution [4]. This method directly replaces the right most insignificant bit of host media. But this method is irreversible method of data hiding. In quality-sensitive applications such as military imaging, medical imaging, high precision systems in scientific research, law enforcement, and remote sensing where a small loss can lead to significant difference in final „decision making“ process [5]. Nevertheless, the irreversible data hiding techniques are hard to satisfy many circumstances of quality-sensitive

applications. Recently, reversible data hiding (RDH) is widely used, which can extract the embedded bits, and also restore the original cover image without any error [6][7]. Among all the reversible data hiding techniques, difference expansion, histogram shifting, prediction error methods are most widely applicable. Histogram-based technique presented the secret message is embedded into the histogram bin of host media [8]. Difference expansion method [9] creates pixel differences are used to embed data; this is because of high redundancies among the neighboring pixel values in natural images. The prediction error method generate a residual image to explore the similarity of neighboring and residual image, which arrives from the difference between central pixel and its neighboring pixels, is used to hide the information [10]. However, in presented method some distortion may occur and most of the schemes allow only a limited payload size.

To overcome these drawbacks, we propose a robust reversible data hiding based on the histogram shifting technique. Here, the two peak points in the histogram (from host media) are selected for data embedding. This process is repeated again and again. When a large number of bits are embedded, image contrast is over-enhanced, which introduces annoy perception visually. The perfection in visual quality of the image is also an important concern in the data hiding. The proposed scheme has large embedding capacity with good visual perception using the Controlled Contrast Enhancement (CCE). Eventually, contrast enhancement provides good visual quality up to certain limit. Relative contrast error (RCE) is used to keep the contrast enhancement in optimum level so that the image contrast comforts the typical visual perception. Threshold is used to control the CCE based on the host image. After embedding the secret information, embedded image subjected to several attacks and the robustness of the proposed scheme is tested. This algorithm is more suitable for test images as well as medical images.

Thus, the cover image and embedded data is perfectly extracted with better quality.

The rest of this paper is prepared as follows. In Section 2, different existing methods for reversible data hiding are described. The proposed method is presented with three part of explanation in Section 3, followed by the experimental

results and comparison with various images in Section 4. Conclusion is addressed in Section V.

II. BACKGROUND WORK

HS-based algorithm is the most important work of RDH, in which the peak of image histogram is utilized to embed data. In this method, each one pixel value is modified at most by 1, and thus the visual quality of marked image is guaranteed [1]. In 2015, Hao Tian Wu et al. proposed a data hiding algorithm [1] with the property of contrast enhancement. This method utilizes the two peak points of the image histogram to embed the secret information into the image. The peak point is a pixel values containing the most number of occurrences in the image, and hence can embed large number of data. So this embedding process is repeated again and again. It can be make out that the contrast of host images was gradually enhanced through splitting more histogram peaks in this algorithm. But more differences were initiated in brightness and structural similarity.

Dinu Coltuc et al. proposed a RDH algorithm based on contrast mapping technique [2], which is also a familiar method. In that paper, the whole host image will be partitioned as pixel pairs, using the reversible contrast mapping (RCM) transform for pixel position. But, in this method the embedded bit rate is much less than the histogram based RDH.

The same author latter proposed another RDH algorithm [3], named, prediction-based reversible watermarking. Prediction based reversible watermarking uses median edge detector (MED), gradient-adjusted prediction (GAP), and a simplified GAP (SGAP) are used for global optimization. In that paper, SGAP outperformed all other prediction methods.

III. PROPOSED WORK

In this section, we propose a modified data hiding scheme based on histogram shifting technique. In order to enhance the embedding capacity of the proposed method, we use adaptively control the degree of contrast enhancement based on the host image because the embedding capacity may vary for different images. This approach is more suitable to the medical images and test images. The design of the proposed system is shown in Figure 1.

A. Embedding process

Initially, a original gray scale image I of size MxN is taken. The pixels which cause underflow/overflow can be distinguished by employing a location map. Then the histogram of host image is calculated which indicates number of incidences in the host image with gray level value p. Select the pairs of peak represented with P_L and P_H where the minor peak value is P_L, and P_H is the superior peak [12]. For data embedding, the next pixel values of peak are shifted to create vacant spaces while the peak values are manipulated to carry hidden data by filling those vacant spaces. The secret data bit stream S_i = [0,1] embedded on peaks based on the formula as given below,

$$p'' = \begin{cases} p - 1 & \text{for } p < P_L \\ P_L - S_i & \text{for } p = P_L \\ p & \text{for } P_L < p < P_H \\ P_H - S_i & \text{for } p = P_H \\ p + 1 & \text{for } p > P_H \end{cases} \quad (1)$$

Where p'' is the embedded pixel value. However, embed huge number of bits with utilizing more peak pairs from the modified histogram. This same process can be repeated again and again. The last peak pair value and number of peak pair values are stored in the LSB of first 16 pixel values of first row

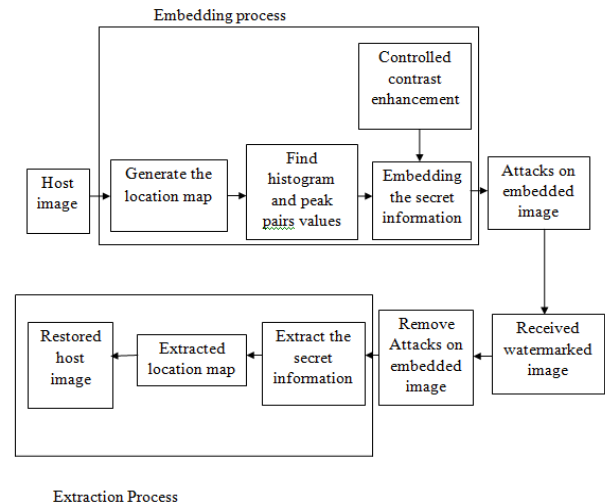


Figure.1 Block diagram of proposed method

of embedded image. The relative contrast error (RCE) is used for estimating the contrast enhancement of image for avoiding exasperate visual perception and the formula is given by,

$$RCE = \frac{std_e - std_o}{R - 1} + 0.5$$

(2)

Where L value is 256 for an 8 bit grayscale image std_o indicate the standard deviations of original image and std_e is standard deviation of enhanced images. In this process, set the threshold value to control the amount of contrast enhancement. Here, the threshold T value has chosen based on the host media. Because, embedding capacity may vary from one image to another image. Hence, this adjustable threshold is best fitting which is able to provide an assurance to the enhanced image has acceptable visual quality. The embedding operation is performed again and again until the relative contrast error attain nearer to the threshold T. Arithmetic Encoding is used to compress the location map for reducing the size and embed into the image mutually with the secret data. The location map is generated to remember their locations of embedded position and avoid the overflows and underflows due to histogram modification.

Algorithm for data embedding

- STEP 1: Select the host image
- STEP 2: Generate the location map
- STEP 3: Calculate the histogram of the host image
- STEP 4: Find the highest two peak points from the histogram
- STEP 5: Embedding secret information on LSB of two peak points
- STEP 6: Check whether CCE exceed the level of threshold
- STEP 7: Attacks are occur on embedded image



B. Removal of attacks on embedded image

Robustness indicates the ability of correctly extracting watermarks after suffering different kinds of attacks. The most classical data hiding leads to permanent distortions and facing many risks such as illegal accessing and unauthorized tampering. Scaling, rotation, shearing [11] and noise addition these are the frequently occurring attacks in the data hiding field. In this paper deals with these attacks and restored through various methods. The following are the different stages involved in the removal of the attacks.

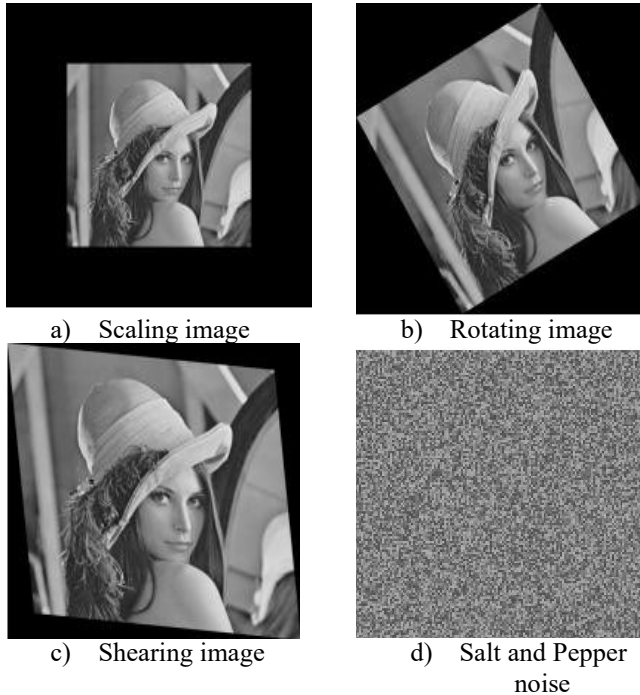


Figure 2. Various attacks and its results on embedded image

Switching median filter

The switching median filter is a well known nonlinear filter to eliminate the impulse noise in the smooth regions as well as the detail regions in image. The salt and pepper noise is efficiently removed using this filter. The filter, first detect which pixels are noisy pixels in an image. Replacing the noise pixels, with an appropriate values using median filter, while all other noise free pixels unchanged. Assume $\{x_{i-L}, x_{i-L+1}, \dots, x_{i-1}, x_{i+1}, \dots, x_{i+L}\}$ represent the input pixels in the $(2L+1) \times (2L+1)$ sliding window and $x_{i,j}$ is the current pixel which is locating at position (i,j) in the image. The recovery formula as given below,

$$y_{i,j} = \begin{cases} x_{med} & \text{for } x_{i,j} = 0 \\ x_{med} & \text{for } x_{i,j} = 255 \\ x_{i,j} & \text{otherwise} \end{cases} \quad (3)$$

Where, $x_{med} = \text{med}\{x_{i-L}, x_{i-L+1}, \dots, x_{i-1}, x_{i+1}, \dots, x_{i+L}\}$ and, is the filtered pixel locating at position (i,j) .

Geometric transformation

Geometric transforms permit the elimination of geometric distortion in an embedded image. It has correlation between embedded and scaled (or rotated) version of embedded images. It collect the matching points between the two images and maps the pixels (x,y) into a new location (x'',y'') . Assume $sc = \cos(\theta)$, $ss = \sin(\theta)$, geometric transform formula i.e.,

$$[x' \ y' \ 1] = \begin{bmatrix} s & -ss & 0 \\ ss & sc & 0 \\ 0 & 0 & 1 \end{bmatrix} [x \ y \ 1] \quad (4)$$

From this, recover the angle (A) and theta (D) of image.

$$A = \sqrt{-SS \ SS + SC^2} \quad (5)$$

$$D = \tan(-ss/sc) (180/\pi) \quad (6)$$

This method is a simple and accurate restoration method for scaling as well as rotation of embedded image.

Shearing matrix

Efficiently retrieve the embedded image from sheared version of embedded image using shearing matrix. Shearing slides of the one edge of an image beside the X or Y axis, creating a parallelogram. An X direction shear slides an edge along the X axis, whereas a Y direction shear slides an edge along the Y axis. The amount of the shear is controlled through a shear angle. Create a shear matrix [12] based on the shearing position of embedded image. Apply the shearing matrix on the coordinates of embedded image. Note that after geometric attacks, an interpolation process is generally needed for images. Hence, forming the new x and y coordinates using linear interpolation and reshape the image. The proposed method achieves satisfactory robustness under all these attacks.

C. Extraction algorithm

The extracting procedure is reverse process of the embedded procedure. The recovery procedure requires the information of the embedded image. Hence, we can retrieve the embedded bit stream s_i , by extracting the last peak-pair and length of location map (L) from the LSBs of 16 excluded pixels in first row of the image. The last hidden information can extract by using last peak pairs and the previous peak-pairs can be obtained by,

$$s = \begin{cases} 1, & \text{if } p = P_L - 1 \\ 0, & \text{if } p = P_L \end{cases} \quad (7)$$

$$s = \begin{cases} 0, & \text{if } p = P_H \\ 1, & \text{if } p = P_H + 1 \end{cases}$$

Where “ s ” is the i -th bit stream value extracted from the watermarked image p “. The extraction operations are performed in the same order as that of the embedding operations. We can decode the location map for retrieve the cover image. The location map gives the location information of all modified pixel values. The following operation is performed on every pixel counted in the histogram to recover its original value,

$$p = \begin{cases} p' + 1, & \text{for } p' < P_L - 1 \\ P_L, & \text{for } p' = P_L - 1 \\ P_H, & \text{for } p' = P_L \\ p' - 1, & \text{for } p' > P_H + 1 \end{cases}$$

Where, p is recovered host image. Then, repeat this image restoration by the extracted peak pairs until the pixel values between the superior peak and the minor higher peak points are shifted back by 1 closer to the peak to their original location. Lastly, the peak points are replaced back into the recovered image.

Algorithm for data extraction

- STEP 1: Receive the embedded image
- STEP 2: Perform de-embedding iteratively
- STEP 3: Check the CCE value if it is exceeding the value of threshold the iteration will be stop
- STEP 4: Extract the location map
- STEP 5: Extract the host image and secret information without any distortion

IV. RESULTS AND DISCUSSION

The analysis and implementation of the proposed algorithm is carried out in MATLAB R2013b on the OS windows 8. Different standard test images and medical images with 512x512 sizes are analyzed with performance metrics. The data to be embedded can be numerical, alphabetical and image form. The cover image as well as the embedded bits is exactly recovered from the embedded image with better visual quality from human vision point of view. This can claim with respect to the Peak Signal to Noise Ratio (PSNR), Structural Similarity (SSIM) and visual inspection (the ultimate) performance metrics.

$$PSNR = 10 \log_{10} \frac{R^2}{MSE}$$

$$MSE = \frac{\sum_{M,N} [I_1(m,n) - I_2(m,n)]^2}{M \cdot N}$$

Where, R=255, $I_1(m, n)$, $I_2(m, n)$, M and N are original image, reconstructed image.

$$SSIM = \frac{2\mu_x \mu_y + c_1}{\mu_x^2 + \mu_y^2 + c_1} \frac{2\sigma_{xy} + c_2}{\sigma_x^2 + \sigma_y^2 + c_2} \quad (11)$$

Where, μ_x average of x, μ_y average of y, σ_{xy} covariance of x & y, $c_1 = k_1 L^2$, $c_2 = k_2 L^2$, L=dynamic range of the pixel value, default coefficients $k_1=0.01, k_2=0.03$. Fig. 3 shows the result of the lena test image which is 512 by 512, 8 bits per pixel (bpp), and grayscale as taken as the host image. And, logo as embedding which demonstrates that the proposed scheme makes the secret information of proposed scheme imperceptible. The visual result of lena image as shown below.

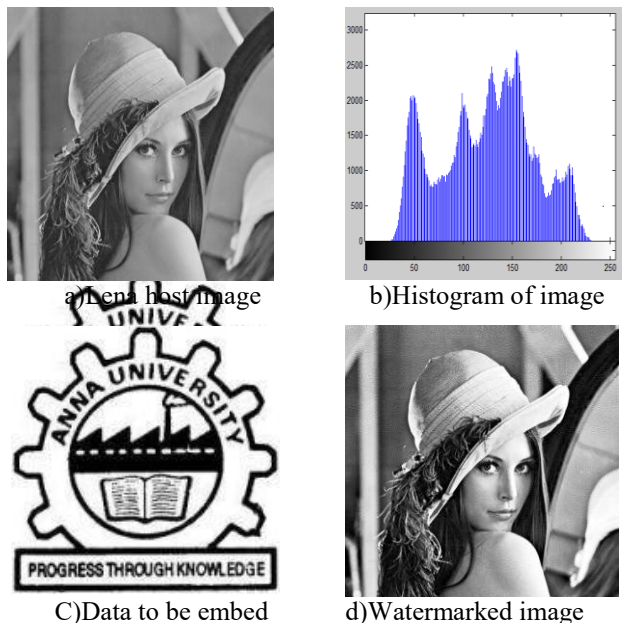
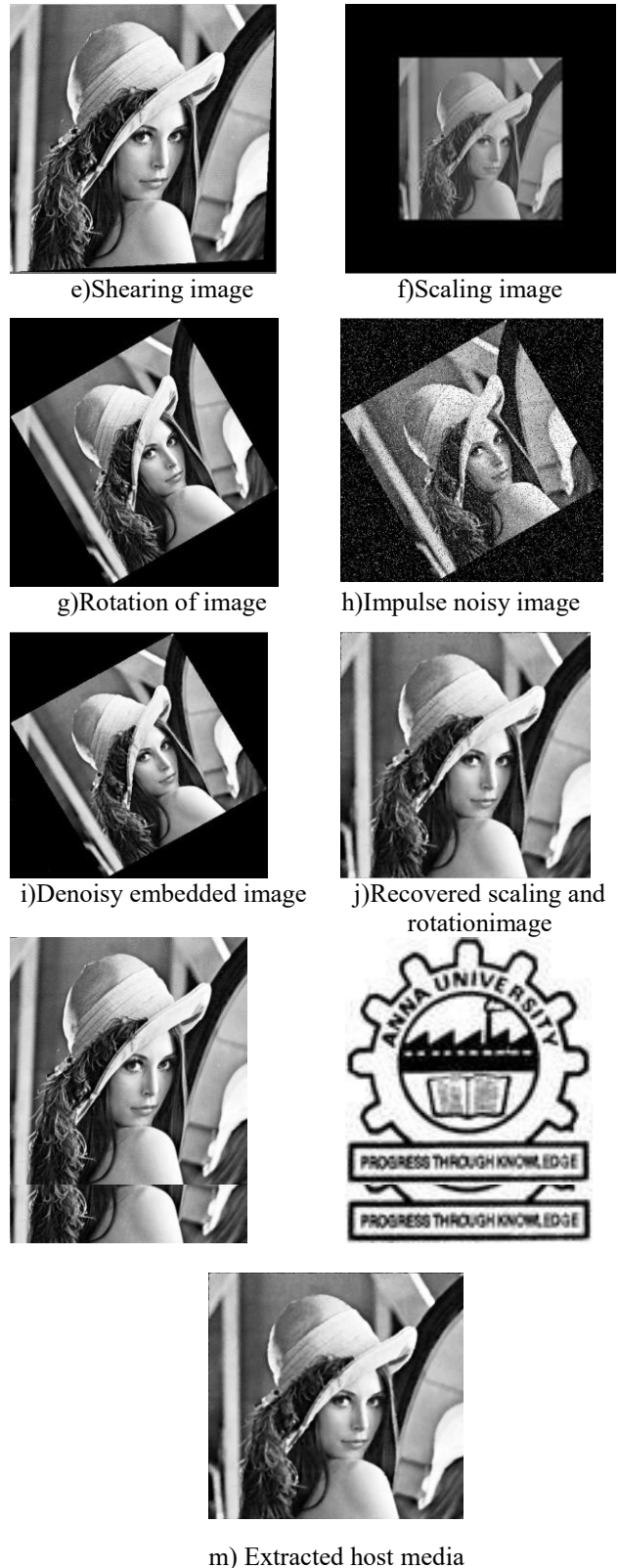


Figure 3. The output result of proposed work.

The proposed method is more suitable for various test images as well as medical images. Recently, most hospitals have already established the electronic medicinal information to make healthcare better, safer, and more efficient. Also telemedicine techniques help to eliminate distance barriers. Hence, the proposed method developed for medical image also. The visual results for the different images are shown below.

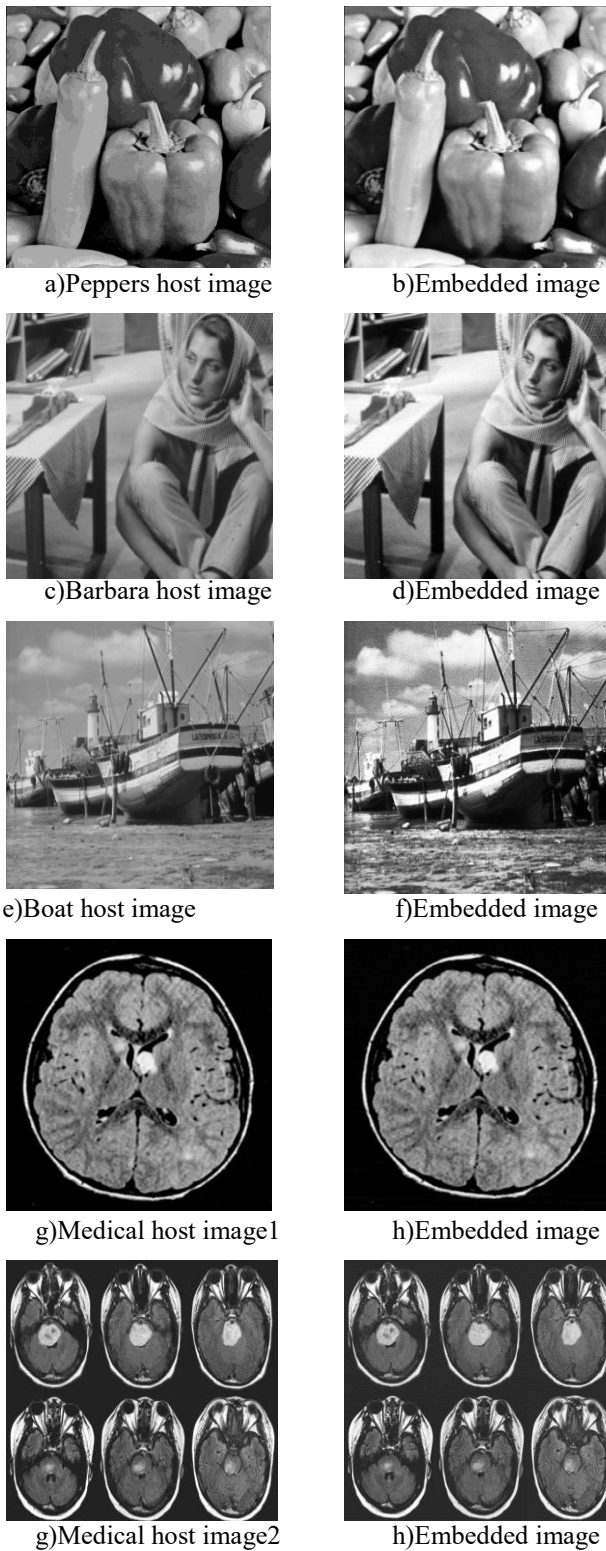


Figure 4. Output result with various images

Performance comparison

The performance indices PSNR, SSIM, and number of embedding bits are calculated by averaging the results obtained from various images. In this proposed work, the threshold value of relative contrast error is set as adaptively based on the host media which can guarantee the enhanced image has good visual quality as well as can embed large amount of data. Furthermore, the proposed method is robust against the common attacks. In this way, it can improve the accuracy of recovered noisy image.

Table 1 shows the PSNR value for five test images with different methods. One can observe that the PSNR for these five test images are all higher than other methods. The PSNR value of proposed work is higher around 2dB over the other existing method.

Table 1 Comparison of PSNR value with different images

Various Image method	Lena	Peppers	Barbara	Boat	Man
Zu tian et al. [17]	30.245	29.310	26.332	27.842	29.456
Tianrui Zong et al.[14]	33.452	32.986	27.211	29.369	31.425
Y Hu et al. [15]	32.643	33.894	23.475	28.037	29.227
Proposed method	34.254	34.378	25.170	30.064	31.216

Table 2 shows the SSIM values for five test images. It indicates similarity between original and recovered images. It shows the output of the proposed work as good visual quality.

Table 2 Comparison of SSIM value with different images

Images	Lena	Peppers	Barbara	Boat	Man
Methods					
Y Hu et al. [15]	0.8238	0.8798	0.7924	0.7501	0.8372
Proposed method	0.8905	0.8614	0.7822	0.8169	0.8302

Table 3 shows the maximum embedding rate of the proposed work. In this proposed method can embed significant bits. The embedding range is improved approximately 0.5% over the existing method.

Table 3 Embedding rate of proposed work

various images method	Lena	Peppers	Barbara	Boat	Man
Proposed work(bpp)	0.8	0.8	0.61	0.83	0.77

In this method, the secret message is extracted without any loss of data and distortion through the data process. The data extraction is achieved effectively through the parameters such as PSNR, SSIM and number of embedding bits. It is clearly shows that for all images proposed method gives highest PSNR values among the compared methods. The average PSNR gain is up to 2.00dB compared with existing algorithm. In addition to that, the embedding capacity of proposed work also improved approximately 0.5% over the existing method.

The proposed method can more accurately recover the image through the attacks removal algorithm. Besides, the computation complexity of the proposed scheme is also very small as it presently deals with the shifting and searching operations.

V. CONCLUSION

An efficient data hiding algorithm based on histogram shifting is presented. In this work, embedding operation is performed based on histogram shifting. This can embed significantly large amount of data. When a huge number of bits are embedded, image contrast is over-enhanced; it is controlled by controlled contrast enhancement method. Furthermore, the robustness of the proposed algorithm is verified using various attacks. The cover image as well as the embedded bits is exactly recovered from the embedded image with better visual quality. Experimental results in terms of PSNR, SSIM and Embedding rate is significantly demonstrate better performance of the proposed method.

REFERENCES

- [1] Hao-Tian Wu, Jean-Luc Dugelay, and Yun-Qing Shi, "Reversible Image Data Hiding with Contrast Enhancement", in *IEEE SIGNAL PROCESSING LETTERS*, VOL. 22, NO. 1, JANUARY 2015.
- [2] D.Colcuc and M. Chassery, "Very fast watermarking by reversible contrast mapping", *IEEE Signal Process. Lett.*, vol.14,no.4,pp. 255–258, 2007.
- [3] C. Dinu, "Improved embedding for prediction-based reversible watermarking", *IEEE Trans. Inf. Foren Secur.*, vol. 6, no. 3, pp. 873–882, 2011.
- [4] R. Chandramouli and Nasir Memon, "Analysis of LSB based image steganography techniques", In *Image Processing, Proceedings.2001 International Conference on, IEEE*, vol. 3, pp. 1019-1022, 2001.
- [5] I. Dragoi and D. Colcuc, "Local prediction based difference expansion reversible watermarking", *IEEE Trans. Image Process.*,vol.23,no.4, pp. 1779–1790, 2014.
- [6] Z.C. Ni, Y.Q. Shi, N. Ansari and W. Su, "Reversible data hiding", *IEEE Trans. Circuits Syst. Video Technol.*,vol.16,no.3,pp.354–362, 2006.
- [7] W. Hong and T.-S. Chen, "Reversible data embedding for high quality images using interpolation and reference pixel distribution mechanism," *J. Vis. Commun. Image R.*,vol. 22, pp. 131–140, 2011.
- [8] S.F. Chiou and M.S. Hwang, "A capacity enhanced reversible data hiding based on SMVQ," in *Imaging Science Journal* 59(1), pp. 17-24, 2010.
- [9] B. Ou, X. Li, Y. Zhao, R. Ni, and Y.Q. Shi, "Pairwise prediction-error expansion for efficient reversible data hiding," *IEEE Trans. Image Process.*, vol. 22, no. 12, pp. 5010–5021, 2013.
- [10] Li Yang, F.C. Chang, and Yu Jing, "Reversible Data Hiding Algorithm Based on Prediction Error", *IEEE Trans. Consumer Electron.*,vol. 53, no. 2, pp. 629–636, 2010.
- [11] H.C. Lu, Y.P. Chu and M.S. Hwang, "A new steganographic method of the pixel value differencing", *Journal of Imaging Science and Technology* 50(5), pp. 424-426, 2006.
- [12] Z. Ni, Y.Q. Shi, N. Ansari, W. Su, Q. Sun and X. Lin, "Robust lossless image data hiding designed for semi-fragile image authentication," *IEEE Transactions on Circuits Systems for Video Technology* 18, pp. 497-509,2008.
- [13] S. Han, Fujiyoshi and M.H. Kiya, "A Reversible image authentication method without memorization of hiding parameters," *IEICE Transactions* E92-A(10), pp. 2572-2579, 2009.
- [14] Tianrui Zong and Yong Xiang, "Robust Histogram Shape-Based Method for Image Watermarking," *IEEE trans. on circuits and systems for video technology*, vol. 25, no. 5, pp. 717-729, 2015.
- [15] Y. Hu, H.K Lee and J. Li, "DE based reversible data hiding with improved overflow location map," *IEEE Transactions on Circuits Systems for Video Technology*, vol.19-21, pp. 250-260, 2009.
- [16] Hao-Tang Chan, Wen-Jyi Hwang and Chau-Jern Cheng, "Digital Hologram Authentication Using a Hadamard-Based Reversible Fragile Watermarking Algorithm", *Journal of display technology*, vol. 11,no.2, pp. 193-203, 2015.
- [17] Zu tian, "Reversible data hiding by difference expansion," *IEEE Trans. Multimedia and security*, 18, pp. 467-471, 2002.
- [18] Guangyong Gao and Yun-Qing Shi, "Reversible Data Hiding Using Controlled Contrast Enhancement and Integer Wavelet Transform,"*IEEE Signal Processing Letters*, vol.22, no.11, November 2015.
- [19] C. W. Honsinger, P. W. Jones, M. Rabbani, and J. C. Stoffel, "Lossless recovery of an original image containing embedded data," *U.S. Patent*6 278 791, 2001.
- [20] C. Deng, X. Gao, X. Li, and D. Tao, "Local histogram based geo-metric invariant image watermarking," *Signal Process.*, vol. 90, no. 12,pp. 3256–3264, 2010.
- [21] H. C. Wu, N. I. Wu, C. S. Tsai and M. S. Hwang, "Image steganographic schemes based on pixel-value differencing and LSB replacement methods", *IEEE Proc. Vision Image Signal Processing*, 152, pp. 611-615, 2005.

Contrast Enhanced Brain Tumor Segmentation based on Shannon's Entropy and Active Contour

Priyadharshini. C*
Department of
Electronics and
Instrumentation
Engineering St. Joseph's
College of Engineering,
OMR, Chennai 600119,
India
*priya.dharshini.1996c@
gmail.com

Nithysri. V
Department of
Electronics and
Instrumentation
Engineering
St. Joseph's College of
Engineering, OMR,
Chennai 600119, India

Pavithra. G
Department of
Electronics and
Instrumentation
Engineering
St. Joseph's College of
Engineering, OMR,
Chennai 600119, India

Sri Madhava Raja. N**
Department of
Electronics and
Instrumentation
Engineering
St. Joseph's College of
Engineering, OMR,
Chennai 600119, India
**nsrimadhavaraja@stjo
sephs.ac.in

Abstract—In this paper, a novel computer procedure is proposed to assist the brain tumor image examination. This approach enhances and extracts the contrast improved tumor core section from a two dimensional Magnetic Resonance Image (MRI) integrating the Bat Algorithm (BA), Shannon's multi-thresholding, and Active Contour (AC) based segmentation. Firstly, BA assisted multi-thresholding is executed to improve the tumor core section of the brain MRI dataset. Later, the tumor core is extracted using the AC segmentation approach. The proposed methodology is tested on the well-known BraTS MRI dataset. The success and the clinical significance of the proposed approach are verified using image similarity values and statistical measures. The experimental results confirm that the proposed approach presents a great performance when compared with the ground truth, suggesting that it might have real world practical implications with a clinically significant impact.

Keywords- Brain tumor; bat algorithm; active contour; image similarity index.

I. INTRODUCTION

In medicine, computer aided disease assessment is widely adopted to examine anatomical and pathological sections from clinical images [1]. These imaging procedures will support the premature detection and diagnosis of various diseases, also helping to reduce the morbidity and mortality rates. The literature presents a considerable number of image segmentation schemes to examine clinical images [1-3].

Brain Tumor (BT) is one of the major cancers in human community and the early diagnosis of BT will improve the survival rate [4]. The accuracy of tumor extraction from the

brain Magnetic Resonance Image (MRI) mainly depends on the chosen image segmentation method. Due to its significance, a wide number of brain image segmentation procedures have been recently proposed to autonomously extract the tumor region from the MRI. Chaddad proposed a Gaussian mixture model feature extraction method from brain

MRI images [4]. Khandani et al. outlined the force data clustering algorithm based BT segmentation scheme [5]. Chaddad and Tanougast discussed about multi-level thresholding based tumor extraction from MRI brain dataset [6]. Maksoud et al. implemented a segmentation procedure based on a hybrid clustering technique [7]. Panali et al. proposed a two-stage approach to segment the MRI brain region [8]. Srivastava et al. proposed a methodology to preprocess the MRI images using a non-local averaging procedure [9]. Abdullah et al. developed a MatLab framework to segment tumor from MRI [10]. A number of other alternatives can be found in [11-13]. All the above discussed procedures are implemented to segment a specific modality based images. In the proposed approach, the contrast brain MRI is chosen for the study.

This paper proposes a computer aided segmentation methodology to identify the tumor from the 2D brain MRI database. Initially, a global thresholding scheme based on Shannon's entropy is adopted to enhance the tumor region in the brain MRI. In order to improve the multi-thresholding accuracy, Shannon's entropy is integrated in the Bat Algorithm (BA). Later, the Active Contour (AC) segmentation procedure is adopted to extract the tumor core from BT image.

The performance of proposed methodology is evaluated using the BraTS MRI dataset [27, 29], being confirmed with a relative examination between the segmented tumor region and the ground truth offered by an expert member. The

experimental results indicate that the proposed approach is efficient in obtaining a high similarity index value [6], as well as other statistical measures [14,15]; the average values of Jaccard, Dice, precision, sensitivity, specificity and accuracy suggest that this approach is clinically significant.

II. METHODOLOGY

This section describes the adopted methodology.

A. Bat Algorithm (BA)

The traditional Bat Algorithm (BA) was originally proposed by Yang by mimicking the bio-sonar characteristics of microbats [16-18]. BA is described by a discrete equation system comprising the velocity renewal (Eq.1), the position renewal (Eq. 2), and the frequency vector updates (Eq. 3), as shown below:

$$V_i^{(t+1)} = V_i^{(t)} + (X_i^{(t)} - G_{best}) \cdot F_i \quad (1)$$

$$X_i^{(t+1)} = X_i^{(t)} + V_i^{(t+1)} \quad (2)$$

$$F_i = F_{min} + (F_{max} - F_{min}) \cdot \beta^t \quad (3)$$

where $V_i^{(t+1)}$ and $X_i^{(t+1)}$ represent the velocity and position of the agent (or solution) i for the next iteration (t), F_{min} is the minimum frequency and F_{max} is maximum frequency.

From Eq.1, one can observe that velocity renewal relies predominantly on the frequency update. Throughout the heuristic investigation, a new result for every bat is produced based on the subsequent relation:

$$X_{new} = X_{old} + \varepsilon A^t \quad (4)$$

where ε = arbitrary digit of the range [-1,1] and A is the intensity of bats' discharged sound throughout the investigation of a new "area" (set of positions leading to a set of solutions).

The arithmetical illustrations for intensity alteration are shown below:

$$A_i^{(t+1)} = \alpha_i A_i^{(t)} \quad (5)$$

$$r_i^{(t+1)} = r_i(0) [1 - \exp(-\gamma_i t)] \quad (6)$$

In this work, and based in the literature in the topic, the BA parameters are assigned as follows:

Number of bats = 20; search dimension = 3; iterations = 1000; stopping criteria = $J(t)_{max}$; frequency vector constant $\beta = [0,1]$; ε is a random value between [-1,1]; $A_0 = 10$ and $A_{min} = 1$ (which decays in steps of 0.1); $\alpha^1 = \gamma^1 = 0.75$.

B. Shannon's Entropy

In information theory, entropy is normally considered to measure the uncertainty of a variable [19]. The details regarding Shannon entropy can be found in Paul and Bandyopadhyay's work [19].

Let us consider a brain MRI image of size $M \times N$. Then, the gray value of the pixel with coordinates (x,y) can be expressed as $f(x,y)$, for $x \in \{1,2,\dots,M\}$ and $y \in \{1,2,\dots,N\}$. Let L be the number of gray levels of image I_0 and the set of all gray levels $\{0,1,2,\dots,L-1\}$ can be symbolized as G , in such a way that:

$$f(x,y) \in G \forall (x,y) \in image \quad (7)$$

The normalized histogram of the image can be represented as $H = \{h_0, h_1, \dots, h_{L-1}\}$.

In the proposed work, a tri-level threshold is considered. Hence, the above equation can be written as;

$$H(T) = H_1(T) + H_2(T) + H_3(T) \quad (8)$$

$$T^* = \max_T \{H(T)\} \quad (9)$$

in which T^* is the optimal threshold.

Shannon's entropy should satisfy Eqn. 9. In this paper, the optimal threshold value is attained by using the BA.

C. Active Contour Segmentation

This section presents the essential segmentation practice to extract the tumor core from the multi-threshold brain MRI image. In this paper, the Active Contour (AC) segmentation proposed by Houhou et al. [20] and Bresson et al. [21] is adopted. The AC has three necessary steps, namely: *i*) boundary exposure; *ii*) preliminary active contour; and *iii*) ultimate active contour which tender minimized energy.

In this work, the variable snake model is considered to track similar pixel groups in the preprocessed image based on the energy minimization concept. The energy function of the snake can be described as:

$$\min_C \left\{ E_{GAC}(C) = \int_0^{L(C)} g(|\nabla I_0 C(s)|) ds \right\} \quad (10)$$

where ds is the Euclidean component of length and $L(C)$ is the length of the curve C which satisfies $L(C) = \int_0^{L(C)} ds$. The parameter g is an edge indicator, which will disappear based on the object boundary defined as:

$$g(|\nabla I_0|) = \frac{1}{1 + \beta |\nabla I_0|^2} \quad (11)$$

where I_0 represents original image and β is an arbitrary constant. The energy value rapidly decreases based on the edge value and gradient descent criterion [22, 23].

This procedure is mathematically represented as:

$$\partial_t C = (kg - \langle \nabla_g, N \rangle) N \quad (12)$$

where $\partial_t C = \partial C / \partial t$ represents the deformation in the snake model, t is the iteration time, and k , N are the curvature and normal for the snake 'C'. In this procedure, the snake silhouette is continuously corrected till minimal value of the energy; E_{GAC} is achieved.

D. Performance Metrics for Processed image

The preprocessed image quality is assessed using typical image metrics, such as Root Mean Square Error (RMSE), Pixel Signal to Noise Ratio (PSNR) and Structural Similarity Index (SSIM) [24-26]. The accuracy of the medical image segmentation is commonly confirmed using a relative analysis with the expert segmented image, known as the Ground Truth (GT). During this procedure, the image performance metrics, such as Jaccard Index (JI), Dice Index (DI), False Positive (FP) rate and False Negative (FN) rate, are computed [6]. Additionally, well-known performance index, such as precision, sensitivity, specificity, and accuracy, are also considered to analyze the segmented tumor core [14, 15].

III. RESULTS AND DISCUSSION

This section presents the experimental result of the proposed research work using the contrast enhanced T₁ modality (T_{1c}) image of brain tumor MRI dataset [27, 28]. During this study, two different patient test image dataset with an image dimension of 216 x 160 is considered.

Firstly, tri-level threshold based on BA and Shannon function is implemented on the chosen test image. This procedure divides the entire image into three threshold levels based on the optimal threshold value (T*) and enhance the abnormal region (tumor) by grouping similar pixels. Later, the enhanced tumor region is extracted using the AC segmentation approach. Finally, the segmented tumor region is compared with the ground truth and the image quality, similarity and statistical measures are computed and analyzed to justify the significance of the proposed two-stage automated computer brain tumor segmentation procedure.

Fig. 1 depicts the results obtained with the test image 'Data1_95' (patient1's data with slice number 95). Fig. 1 (a) shows the 216 x 160 sized gray scale test image, Fig. 1 (b) depicts the histogram, Fig. 1 (c) presents the tri-level thresholded image. Fig. 1 (d), (e) and (f) show the active contour segmentation, extracted tumor and the ground truth offered by an expert member, respectively. A similar procedure is implemented for the other test images considered in this study and the results are summarized in Table I.

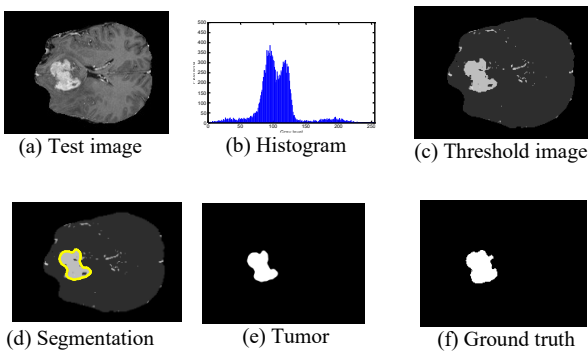


Figure 1. Result obtained for the test image Data1_95

TABLE I. SEGMENTATION RESULT FOR MRI DATASET

	Test image	Threshold image	Tumor	Ground truth
Data1_100				
Data1_105				
Data2_75				
Data2_85				
Data2_95				

TABLE II. IMAGE SIMILARITY MEASURE VALUES

Image	JI	DI	FP	FN
Data1_95	0.8279	0.9059	0.0118	0.1623
Data1_100	0.8397	0.9129	0.0254	0.1390
Data1_105	0.8032	0.8909	0.0416	0.1634
Data2_75	0.9399	0.9690	0.0505	0.0126
Data2_85	0.8979	0.9462	0.1042	0.0085
Data2_95	0.8963	0.9453	0.1015	0.0127
Average	0.8675	0.9284	0.0558	0.0830

TABLE III. STATISTICAL MEASURE VALUES

Image	Precision	Sensitivity	Specificity	Accuracy
Data1_95	0.9954	0.9988	0.8715	0.9330
Data1_100	0.9942	0.9978	0.8876	0.9411
Data1_105	0.9914	0.9961	0.8619	0.9266
Data2_75	0.9993	0.9974	0.9874	0.9924
Data2_85	0.9996	0.9955	0.9915	0.9935
Data2_95	0.9997	0.9976	0.9873	0.9924
Average	0.9966	0.9972	0.9312	0.9631

Table III shows that proposed two stage automated approach offered the following values of JI, DI, FP and FN :the average values of JI and DI are greater than 0.86 (ie. 86%) and the FP and FN are lesser than 0.085 (ie. 8.5%). Table IV presents the average statistical measures obtained with the proposed study. The average values of precision, sensitivity and accuracy are greater than 96% and the specificity is greater than 93 %. From the results of Table II and Table IV, one can

observe that, the proposed approach is clinically significant and it can be used as an automated tool to segment and analyze the tumor region of brain MRI dataset.

IV. CONCLUSION

Anovel computer assisted automated segmentation and analysis of the tumor region from the brain MRI is proposed and discussed. The proposed approach adopts a two-step process, such as the Bat Algorithm assisted using Shannon's entropy tri-level thresholding and followed by the Active Contour segmentation method. During the experimental work, the tumor core is extracted from the test image dataset and is then validated against the ground truth images from the BraTS dataset. The experimental results confirm that the average values of image quality measures, similarity measures and statistical measures are better (ie. > 85%). Hence, this approach can be used to extract the tumor core from the clinical brain tumor MRI recorded with T_{1C} modality.

ACKNOWLEDGEMENT

The authors would like to acknowledge the constant support and the guidance of Dr. Michael S. Couceiro, Ingeniarius, Rua Coronel Veiga Simão, 3025-307, Coimbra, Portugal for the research work.

REFERENCES

- [1] Abder-Rahman Ali, Micael Couceiro, Ahmed Anter, Aboul-Ella Hassanien, "Particle swarm optimization based fast fuzzy C-Means clustering for liver CT segmentation," *Applications of Intelligent Optimization in Biology and Medicine*, Intelligent Systems Reference Library, vol.96, pp. 233-250, 2015.
- [2] N. Sri Madhava Raja, G. Kavitha, and S. Ramakrishnan, "Analysis of vasculature in human retinal images using particle swarm optimization based Tsallis multi-level thresholding and similarity measures," *Lecture Notes in Computer Science*, vol. 7677, pp.380-387, 2012.
- [3] K. Kamalanand, and S. Ramakrishnan, "Effect of gadolinium concentration on segmentation of vasculature in cardiopulmonary magnetic resonance angiograms," *Journal of Medical Imaging and Health Informatics*, vol. 5, pp.1-5, 2015.
- [4] A. Chaddad, "Automated feature extraction in brain tumor by magnetic resonance imaging using gaussian mixture models," *International Journal of Biomedical Imaging*, vol. 2015, Article ID 868031, 11 pages, 2015.
- [5] M.K. Khandani, R. Bajcsy, R. and Y. P. Fallah, "Automated segmentation of brain tumors in MRI using force data clustering algorithm," *Lecture Notes in Computer Science*, vol. 5875, pp. 317-326, 2009.
- [6] A. Chaddad, and C. Tanougast, "Quantitative evaluation of robust skull stripping and tumor detection applied to axial MR images," *Brain Informatics*, vol.3, no.1, pp.53-61, 2016.
- [7] E. Abdel-Maksoud, M. Elmogy, and R. Al-Awadi, "Brain tumor segmentation based on a hybrid clustering technique," *Egyptian Informatics Journal*, vol.16, pp. 71-81, 2015.
- [8] T. K. Palani, B. Parvathavarthini, and K. Chitra, "Segmentation of brain regions by integrating meta heuristic multilevel threshold with markov random field," *Current Medical Imaging Reviews*, vol.12, no.1, pp. 4-12, 2016.
- [9] A. Srivastava, V. Bhateja, H.Tiwari, S.C. Satapathy, "Restoration algorithm for gaussian corrupted MRI using non-local averaging", *Advances in Intelligent Systems and Computing*, vol.340, pp 831-840, 2015.
- [10] A. A. Abdullah, B. S.Chize, Z. Zakaria, "Design of cellular neural network (CNN) simulatorbased on Matlab for brain tumor detection", *Journal of Medical Imaging and Health Informatics*, vol. 2, pp. 296-306, 2012.
- [11] M.C. Jobin Christ., and R.M.S. Parvathi, "A survey on MRI brain segmentation", *Advances in Intelligent Systems and Computing*, vol. 166, pp.167-177, 2012.
- [12] N. Gordillo, E. Montseny, and P.Sobrevilla, "State of the art survey on MRI brain tumor segmentation", *Magnetic Resonance Imaging*, vol.31, no. 8, pp. 1426-1438, 2013.
- [13] J. Liu, M. Li, J. Wang, F. Wu, T. Liu, and Y. Pan, "A survey of MRI-based brain tumor segmentation methods", *Tsinghua Science and Technology*, vol. 19, no.6, pp. 578-595, 2014.
- [14] H. Lu, A.C. Kot, and Y.Q. Shi, "Distance-reciprocal distortion measure for binary document images," *IEEE Signal Processing Letters*, vol. 11, no. 2, pp. 228-231, 2004.
- [15] R.F. Moghaddam, and M. Cheriet, "A multi-scale framework for adaptive binarization of degraded document images," *Pattern Recognition*, vol.43, No.6, pp. 2186-2198, 2010.
- [16] X.S.Yang, "Bat algorithm: literature review and applications", *Int. J. Bio-Inspired Computation*, vol. 5, no. 3, pp. 141-149, 2013.
- [17] V. Rajinikanth, and M.S. Couceiro, "Optimal multilevel image threshold selection using a novel objective function", *Advances in Intelligent Systems and Computing*, vol. 340, pp 177-186, 2015.
- [18] S. C. Satapathy, N.S.M. Raja, V. Rajinikanth, Amira S. Ashour, Nilanjan Dey, "Multi-level image thresholding using Otsu and chaotic bat algorithm", *Neural Computing and Applications*, doi:10.1007/s00521-016-2645-5, 2016.
- [19] S. Paul, and B. Bandyopadhyay, "A novel approach for image compression based on multi-level image thresholding using shannon entropy and differential evolution," *2014 IEEE Students' Technology Symposium (TechSym)*. Kharagpur: IEEE; pp.56-61, 2014.
- [20] N. Houhou, J-P. Thiran, and X. Bresson, "Fast texture segmentation model based on the shape operator and active contour," *IEEE Conference on Computer Vision and Pattern Recognition, CVPR 2008*, Anchorage, AK, pp.1 - 8, 2008.
- [21] X. Bresson, S. Esedoglu, P. Vanderghenst, J-P. Thiran, and S. Osher, "Fast global minimization of the active contour/snake model," *J. Math. Imaging Vis.*, vol.28, no.2, pp. 151-167, 2007.
- [22] D. Bibicu, L. Moraru, and A. Biswas, "Efficient segmentation using active contours embedded in an image feature," *Journal of Medical Imaging and Health Informatics*, vol.5, no.2, pp. 241-247, 2015.
- [23] H. C. Kang, B. Kim, J.Lee, J.Shin, and Y-G. Shin, "Accurate four-chamber segmentation using gradient-assisted localized active contour model", *Journal of Medical Imaging and Health Informatics*, vol.5, no.1, pp. 126-137, 2015.
- [24] P. Ghamisi, M.S. Couceiro, J.A. Benediktsson, N.M.F Ferreira, "An efficient method for segmentation of images based on fractional calculus and natural selection," *Expert Systems with Applications*, vol. 39, no. 16, pp. 12407-12417, 2012.
- [25] V. Rajinikanth, and M.S. Couceiro, "RGB histogram based color image segmentation using firefly algorithm", *Procedia Computer Science*, vol.46, pp. 1449-1457, 2015.
- [26] N.S.M.Raja, V. Rajinikanth, and K. Latha, "Otsu based optimal multilevel image thresholding using firefly algorithm," *Modelling and Simulation in Engineering*, vol. 2014, Article ID 794574, 17 pages, 2014.
- [27] Menze et al., "The multimodal brain tumor image segmentation benchmark (BRATS)", *IEEE Transactions on Medical Imaging*, vol. 34, no.10, pp.1993-2024, 2015.
- [28] M. Kistler, S. Bonaretti, M. Pfahrer, R. Niklaus, and P. Büchler, "The virtual skeleton database: An open access repository for biomedical research and collaboration," *Journal of Medical Internet Research*, Vol.15, No.11, e245, 2013.
- [29] <http://braintumorsegmentation.org/>

Feature Extraction and Analysis of Renal Abnormalities using Fuzzy Clustering Segmentation and SIFT Method

Aadhirai. S

IEEE student member(ID-9402439)

PG student: EIE department

B.S.A. Crescent University

Chennai, India

aadhiraieic@gmail.com

Najumnissa Jamal.D

Professor: EIE department

B.S.A. Crescent University

Chennai, India

najumnissa.d@bsauniv.ac.in

Abstract—Ultrasound Imaging is one of the most widely used technique to provide information about renal diseases in kidney such as cyst, tumor and calculi. This paper aims to extract features from the different renal abnormalities to discriminate between the normal and abnormal conditions. Two filters, median and wiener filter are used to remove the speckle noise in US (ultrasound) images. A picture quality performance technique is implemented to identify the quality of the images. Peak to signal noise ratio (PSNR) and Mean squared error (MSR) is used to verify the enhanced images. The preprocessed images are then segmented using FCM (fuzzy c-means clustering technique) which yields better results to find Region of interest (ROI). The statistical features along with scale invariant feature transform (SIFT) features and Texture features are extracted and analyzed. It is found that features like Energy, Variance and kurtosis are seen to be higher in the normal kidney images than the renal abnormalities. The features can be used to discriminate between normal and abnormal renal conditions. The developed system is expected to provide support for the medical practitioners for decision making to provide an enhanced health care.

Keywords— *Kidney abnormalities, preprocessing technique, Peak to signal noise ratio (PSNR) and Mean squared error (MSE), Fuzzy c-means clustering (FCM) and scale invariant feature transform (SIFT).*

I. INTRODUCTION

Since ancient times, formation of kidney stone in humans became an unsolved problem and a wide research in this area has to be conducted [1]. A renal abnormality is one of the major risks in life and sometimes will lead to death if the disease is not diagnosed properly. There are many diagnostic techniques to identify the renal tumor, renal cyst and renal calculi. They are ultrasound, computer tomography (CT), and Magnetic resonance imaging (MRI). Ultrasound is the cheapest scanning technique when compared to above said techniques. Bharathi and Amirthaveni (2008) conducted a comparative study on 24 hour urinary composition between urinary stone formers and healthy volunteers from five cities of Tamil Nadu namely Coimbatore, Vellore, Madurai, Nagercoil and Tirunelveli. It was reported that there was a considerable

increase in incidence of kidney stone cases year by year (from 1869 to 3084) in Coimbatore while other admission centres of other cities showed marginal increase in admission rates [3]. Tamisselvi et.al detected renal calculi from images and developed a semiautomatic region growing algorithm using ultrasound kidney images [4]. K.Viswanath et.al used level set segmentation and ANN classification to detect kidney stone from ultrasound images [5]. Komal Sharma [6] proposed a computer assisted classification for classification of renal ultrasound images into a) normal b) medical renal disease (MRD),cyst, and the region of interest is cropped from the cortex region of the kidney and from regions inside renal cyst. [7] Detected the abnormalities in the kidney of renal calculi using a preprocessing method CANR (combinational approach of noise removing) for removal of noise in the US images and GLCM for the extraction of features. T. Mangayarkarasi et.al, developed a patient assistive Tool for detection of Abnormalities in kidney [9]. In this paper Ultrasound images for renal abnormalities is taken and filters like Median and Wiener filters are applied as a preprocessing tool to enhance the quality of the image. Then Fuzzy C means clustering is applied to the segmented region of Interest and statistical features, texture features using GLCM and SIFT features are extracted. These features are further analyzed for variation in the abnormalities and reported whether the image is normal or has renal abnormalities. The flow diagram of the work is shown in figure 1.

II. METHODOLOGY

A. Ultrasound images

7 normal and 21 abnormal ultrasound kidney images for each type were obtained with the help of medical doctor. The real time ultrasound kidney images for normal and with tumor, calculi and cyst were obtained from Sri Chakra scans, Chennai. All images with 512 x 512 pixels in size were acquired using Voluson ultrasound machine with 3.5MHz curved array transducer.

B. Preprocessing

In this work we have implemented two filters for removing the speckle noise for smoothing the images so that the clarity of the image is good. The performance metrics used to know about the quality of the images are peak to signal to noise ratio (PSNR) and mean squared error (MSE). PSNR is the quality measurement between the original image and denoised image. Peak to signal noise ratio (PSNR) is the ratio between

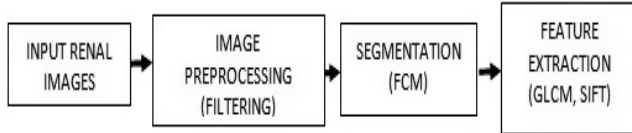


Fig 1. Flow diagram of the feature extraction method.

the maximum possible power and corrupting noise that affect representation of image. It is expressed as decibel scale.

The PSNR is used as measure of quality reconstruction of image. In Mean squared error if the value is low then the image quality is high and is also used to measure the degree of image distortion because they can represent the overall gray-value error contained in the image. With MSE or PSNR, only gray value differences between corresponding pixels of the original and distorted version are considered. MSE works well when the distortion is mainly caused by the contamination of additive noise. The higher the PSNR the quality of the image is good. Similarly the MSE value should be low so that it represents the quality of the image is enhanced [19,20].

III. SEGMENTATION

After the preprocessing technique segmentation is carried out to find the region of interest in the images the features are extracted from the segmented images. Segmentation is the process of partitioning an image into multiple segments, i.e. set of pixels, pixels in a region are similar according to homogeneity criteria such as color, intensity or texture, so as to locate and identify objects in an image. FCM is an iterative, unsupervised clustering algorithm and has been applied for medical images for segmentation. It involves number of clustering and subtractive clustering algorithm is used it is used to iterate by initialising optimization-based FCM algorithm. FCM is based on minimizing an objective function as shown in equation (1), with respect to fuzzy membership U , and set of cluster centroids.

Where u_{ij} represents the membership of pixel x_j in the i th cluster, v_i is the i th cluster center, $\|\cdot\|$ is a norm metric, and m is a constant. Clustering based segmentation is

implemented in our work which segments the image into clusters having pixels with similar characteristics [15, 16].

$$J = \sum_{j=1}^N \sum_{i=1}^c u_{ij}^m \|x_j - v_i\|^2, \quad (1)$$

$$u_{ij} = \frac{1}{\sum_{k=1}^c \left(\frac{\|x_j - v_i\|}{\|x_j - v_k\|} \right)^{2/(m-1)}}, \quad (2)$$

$$v_i = \frac{\sum_{j=1}^N u_{ij}^m x_j}{\sum_{j=1}^N u_{ij}^m}. \quad (3)$$

Where u_{ij} represents the membership of pixel x_j in the i th cluster, v_i is the i th cluster center, $\|\cdot\|$ is a norm metric, and m is a constant. Clustering based segmentation is implemented in our work which segments the image into clusters having pixels with similar characteristics [15].

IV. FEATURE EXTRACTION

A. Statistical Features

a) *Mean*: Mean is most basic of all statistical measure. Means are often used in geometry and analysis; a wide range of means have been developed for these purposes. In contest of image processing filtering using mean is classified as spatial filtering and used for noise reduction

b) *Skewness*: The Skewness characterizes the degree of asymmetry of a distribution around its mean. While the mean, standard deviation, and average deviation are dimensional quantities, that is, have the same units as the measured quantities x_j , the skewness is conventionally defined in such a way as to make it no dimensional. It is a pure number that characterizes only the shape of the distribution.

c) *Kurtosis*: The kurtosis is also a no dimensional quantity. It measures the relative peakedness or flatness of a distribution.

d) *Variance*: Variance finds the feature values are relatively high.

B. GLCM features

The gray-level co-occurrence matrix (GLCM) is also known as the gray-level spatial dependence matrix. It uses a statistical method for examining the texture, considering the spatial relationship of pixels. The GLCM functions are used for finding texture properties of an image by calculating the frequency of occurrence of pixel pairs with specific values and in a specified spatial relationship. The GLCM can be calculated on square matrix of relative frequencies in which two neighbouring pixels separated

by distance d at orientation q occur in the image, at two different gray levels. This results into a square matrix having the size of the largest pixel value in the image. It enables the representation of the relative frequency distributions of gray levels and describes the frequency of how often one gray level will appear in a specified spatial.

The GLCM features – contrast, correlation, energy and homogeneity are calculated [7]. The contrast measures the intensity contrast between a pixel and its neighbour on the entire image. The correlation is used to find a measure of how a pixel is correlated to its neighbour over the whole image [12]. The energy is using the homogeneous region from non-homogeneous regions. It is expected to be high if the frequency of repeated pixel pairs is high. The normalized co-occurrence matrix is denoted by total number of the occurrence of two neighbouring pixels between gray-intensity at vertical direction and angle. The homogeneity measures the closeness of the distribution of elements in the GLCM to the GLCM diagonal.

C. SIFT features

When all images are similar in nature (same scale, orientation, etc) simple corner detectors can work. But when images are of different scales and rotations, the Scale Invariant Feature Transform is used [13]. For any object there are many features, interesting points on the object that can be extracted to provide a "feature" description of the object. This description can then be used when attempting to locate the object in an image containing many other objects. SIFT image features provide a set of features of an object that are not affected by many of the complications experienced in other methods, such as object scaling and rotation. [17] While allowing for an object to be recognized in a larger image SIFT image features also allow for objects in multiple images of the same location, taken from different positions within the environment, to be recognized. SIFT features are also very resilient to the effects of "noise" in the image. The SIFT approach, for image feature generation, takes an image and transforms it into a "large collection of local feature vectors. Each of these feature vectors is invariant to any scaling, rotation or translation of the image.

V. RESULTS AND DISCUSSION

The images acquired from the clinics were resized to 256 X 256 pixels and one acquired sample image for cyst, calculi, tumor and normal kidney is shown in figure 2.

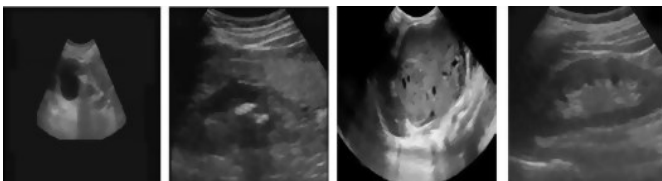


Fig. 2. Sample images of cyst, calculi, tumor and normal kidney

Then the image is subjected to preprocessing technique. Figure.3 shows median filter and wiener filter applied to the ultrasound renal images. From the figure 3, we can see that Wiener filter images are better than the Median filter as wiener filter carries out an optimal tradeoff between inverse filtering and noise smoothing. It removes additive noise and de-blurring concurrently [10]. The PSNR and MSE values from table.1, shows that the wiener filter has good noise smoothing than the median filter. Hence wiener filter is used in this study for denoising the images.

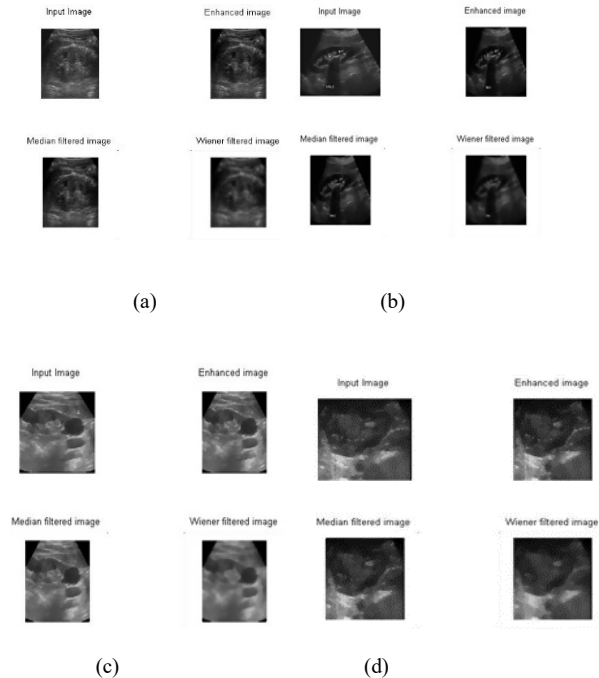


Fig. 3. Filter applied images a) Normal kidney b) Cyst c) Calculi d) Tumor

TABLE.1. COMPARISON OF PERFORMANCE METRICS

Image	Median Filter		Wiener Filter	
	PSNR (dB)	MSE	PSNR(dB)	MSE
Normal	147.92	0.02	159.78	0.01
Tumor	104.60	1.86	134.74	0.09
Calculi	64.72	1.00	68.89	0.98
Cyst	75.39	0.34	79.23	0.24

Then the denoised images are subjected to FCM clustering for segmentation for extracting the features. Figure.4 shows the clustered images to select the region of Interest to extract the necessary features [15]. The statistical features were extracted for the segmented images along with the GLCM features and SIFT features which are shown in Table 2 - 9.

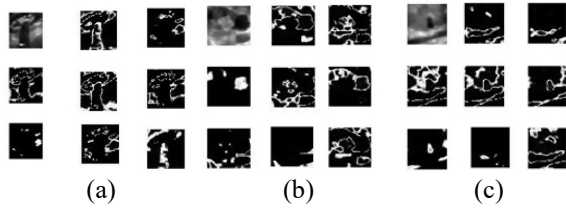


Fig: 4 FCM segmented images for a) Calculi b) Cyst c) Tumor

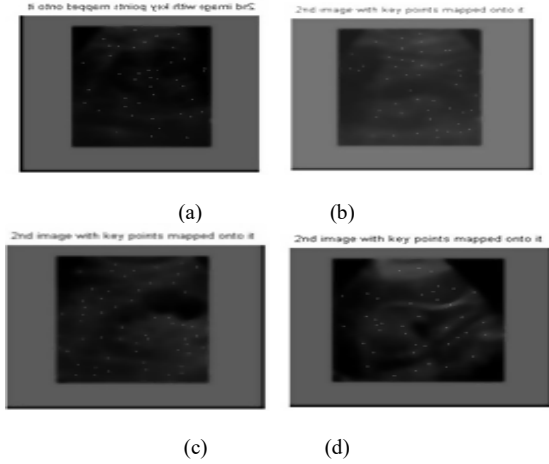


Fig. 5. SIFT key point extraction images of a) Normal Kidney b) Calculi c) Cyst d) Tumor

Table 2. SIFT and Statistical features for Renal Tumor

Tumor	F1	F2	F3	F4	F5	F6
Img1	0.074	175.35	19.26	-2.09	254.851	4.03E+03
Img2	0.074	165.86	17.80	-1.65	254.851	4.42E+03
Img3	0.070	177.76	19.71	-2.10	254.851	3.65E+03
Img4	0.074	152.07	17.15	-1.51	254.828	5.22E+03
Img5	0.075	152.27	17.30	-1.47	254.828	5.29E+03
Img6	0.066	179.79	13.64	-0.64	254.835	4.82E+03
Img7	0.069	136.42	13.58	-0.66	254.835	4.45E+03

F1) SIFT F2) Mean F3) Kurtosis F4) Skewness F5) Maximum probability F6) Variance.

TABLE 3. GLCM FEATURES FOR RENAL TUMOR

Tumor	F7	F8	F9	F10	F11	F12'	F13
Img1	-65.16	0.95	0.972	0.36	0.30	1.07E+03	39.56
Img2	-45.62	0.94	0.974	0.38	0.29	1.16E+03	36.98
Img3	-57.43	0.94	0.972	0.34	0.31	9.60E+02	38.89
Img4	-34.42	0.95	0.973	0.48	0.28	1.54E+03	34.42
Img5	-42.21	0.95	0.976	0.43	0.29	1.63E+03	34.68
Img6	-61.21	0.95	0.977	0.28	0.34	9.30E+02	40.93
Img7	-44.71	0.94	0.974	0.45	0.21	1.57E+03	27.91

F7) Cluster shade F8) Homogeneity F9) Correlation F10) Contrast F11) Energy F12) Cluster prominence F13) Auto correlation

TABLE 4. SIFT AND STATISTICAL FEATURES FOR RENAL CALCULI

Calculi	F1	F2	F3	F4	F5	F6
Img1	0.070	162.29	20.87	-1.93	254.85	4.77E+03
Img2	0.071	158.91	18.09	-1.92	254.85	4.56E+03
Img3	0.066	159.16	18.92	-1.96	254.85	4.88E+03
Img4	0.073	156.72	20.13	-1.81	254.85	4.85E+03
Img5	0.064	159.23	19.12	-1.76	254.83	4.64E+03
Img6	0.068	161.69	19.84	-1.91	254.85	4.55E+03
Img7	0.072	162.46	20.58	-1.09	254.84	4.54E+03

F1) SIFT F2) Mean F3) Kurtosis F4) Skewness F5) Maximum probability F6) Variance

TABLE 5. GLCM FEATURES FOR RENAL CALCULI

Calculi	F7	F8	F9	F10	F11	F12	F13
Img1	-52.88	0.96	0.97	0.39	0.33	1.52E+03	35.47
Img2	-57.86	0.96	0.97	0.42	0.35	1.66E+03	35.41
Img3	-50.51	0.96	0.98	0.31	0.34	1.54E+03	36.36
Img4	-66.97	0.97	0.97	0.40	0.36	1.56E+03	34.75
Img5	-63.61	0.96	0.97	0.39	0.35	1.69E+03	36.71
Img6	-47.03	0.96	0.97	0.39	0.34	1.55E+03	35.98
Img7	-47.85	0.96	0.97	0.40	0.34	1.58E+03	35.95

F7) Cluster shade F8) Homogeneity F9) Correlation F10) Contrast F11) Energy F12) Cluster prominence F13) Auto correlation

TABLE 6. SIFT AND STATISTICAL FEATURES FOR RENAL CYST

Cyst	F1	F2	F3	F4	F5	F6
Img1	0.068	161.48	19.71	-1.90	254.85	4.56E+03
Img2	0.067	161.19	20.99	-1.09	254.85	4.68E+03
Img3	0.065	163.96	19.44	-1.86	254.85	4.18E+03
Img4	0.072	166.33	19.69	-1.95	254.85	4.21E+03
Img5	0.062	163.08	21.02	-1.95	254.85	4.40E+03
Img6	0.067	171.70	20.04	-1.96	254.85	4.60E+03
Img7	0.074	164.43	20.07	-1.93	254.85	4.26E+03

F1) SIFT F2) Mean F3) Kurtosis F4) Skewness F5) Maximum probability F6) Variance

TABLE 7. GLCM FEATURES FOR RENAL CYST

Cyst	F7	F8	F9	F10	F11	F12	F13
Img1	35.98	0.964	0.976	0.47	0.27	1.80E+03	29.22
Img2	44.42	0.971	0.978	0.48	0.35	2.11E+03	29.81
Img3	79.46	0.969	0.977	0.45	0.29	1.98E+03	27.46
Img4	-19.99	0.960	0.974	0.43	0.26	1.43E+03	33.44
Img5	-58.95	0.966	0.981	0.34	0.35	1.51E+03	36.97
Img6	-67.19	0.968	0.978	0.40	0.36	1.65E+03	37.07
Img7	-47.11	0.963	0.979	0.34	0.33	1.27E+03	37.04

F7) Cluster shade F8) Homogeneity F9) Correlation F10) Contrast F11) Energy F12) Cluster prominence F13) Auto correlation

TABLE 8. SIFT AND STATISTICAL FEATURES FOR NORMAL IMAGES

Normal	F1	F2	F3	F4	F5	F6
Img1	0.074	161.84	20.86	-1.95	254.85	4.48E+03
Img2	0.066	155.34	20.93	-1.91	254.85	5.02E+03
Img3	0.071	161.71	20.87	-1.95	254.85	4.47E+03
Img4	0.066	156.70	21.24	-1.99	254.85	5.08E+03
Img5	0.073	161.79	20.83	-1.94	254.85	4.43E+03
Img6	0.064	156.91	21.39	-2.01	254.85	5.00E+03
Img7	0.069	156.28	20.25	-1.85	254.84	4.84E+03

F1) SIFT F2) Mean F3) Kurtosis F4) Skewness F5) Maximum probability F6) Variance

TABLE 9. GLCM FEATURES FOR NORMAL IMAGES

Normal	F7	F8	F9	F10	F11	F12	F13
Img1	- 56.74	0.964	0.977	0.407	0.344	1.50E+03	36.89
Img2	- 62.78	0.970	0.981	0.377	0.359	1.83E+03	36.21
Img3	- 56.97	0.964	0.977	0.411	0.343	1.50E+03	36.88
Img4	- 67.79	0.971	0.981	0.383	0.368	1.84E+03	36.58
Img5	- 56.71	0.962	0.978	0.388	0.340	1.49E+03	36.88
Img6	- 67.90	0.970	0.982	0.362	0.367	1.83E+03	36.60
Img7	- 59.63	0.967	0.979	0.382	0.345	1.57E+03	36.65

F7) Cluster shade F8) Homogeneity F9) Correlation F10) Contrast F11) Energy F12) Cluster prominence F13) Auto correlation

TABLE 10. FEATURES FOR NORMAL AND ABNORMAL IMAGES

Features	Normal	Renal Tumor	Renal Calculi	Renal Cyst
F1	0.069	0.072	0.069	0.070
F2	158.43	162.79	160.07	167.13
F3	20.97	16.92	19.65	19.86
F4	-1.94	-1.45	-1.77	-1.70
F5	254.85	254.84	254.84	254.85
F6	4746.66	4553.7	4683.9	4175.3
F7	-60.23	-48.16	-56.91	-31.39
F8	0.967	0.951	0.966	0.964
F9	0.979	0.974	0.978	0.978
F10	0.381	0.391	0.398	0.380
F11	0.351	0.281	0.349	0.330
F12	1605.72	1318.02	1589.68	1509.94
F13	36.77	35.28	35.730	35.34

F1) SIFT F2) Mean F3) Kurtosis F4) Skewness F5) Maximum probability F6) Variance F7) Cluster shade F8) Homogeneity F9) Correlation F10) Contrast F11) Energy F12) Cluster prominence F13) Auto correlation

From the features extracted the average values are calculated for each feature and tabulated in table. 10. From table.10, it is observed that the features for renal abnormalities are lesser than the normal kidney images. It is seen that the features SIFT, Mean and skewness is lower in normal images than for renal abnormal images. Similarly Kurtosis, Variance, correlation, energy, cluster prominence and autocorrelation values of the features of normal kidney images are seen to be higher than renal abnormalities. Energy and Cluster prominence is seen lower in renal tumor than other abnormalities and Mean, Variance and cluster shade features are lower in renal cyst than the other abnormalities. Maximum probability, Homogeneity and contrast have not many differences in the images used.

VI. CONCLUSION

In this work ultrasound images from 28 subjects is collected, the normal and abnormal of US kidney images are obtained and pre processed using wiener and median filter to remove the speckle noise in the US images. After the pre processing technique segmentation process was done to find the ROI in the US Images and to reduce the complex time to extract the features. Quality measure

performance is done to know the quality of image, quality performance PSNR and MSE was calculated. It measures the quality of image between the original image and the reconstructed image of filter used to remove the noise and how much the noise is removed in the image is known with the help of quality performance analysis. Features are extracted from the segmented images, for future extraction statistical features, GLCM features techniques. An attempt has been made to apply SIFT algorithm to the normal and kidney images. SIFT feature seems to discriminate the normal and kidney images. Certain features discriminate normal images from renal tumor, renal calculi and renal cyst. The results obtained show that the SIFT features and texture features could be used to classify renal abnormalities. The results obtained further show that classification of kidney stones by texture analysis method and SIFT method can be done. The future scope is to extract the features using SURF technique and the extracted key points are given as inputs to the classifier for classification.

ACKNOWLEDGMENT

The authors thank Sri Chakra Scan centre for providing the kidney images and professors of EIE department to carry out the research work.

REFERENCES

- [1] Ding Zuchun, "An Effective Keypoint Selection Algorithm in SIFT", International Journal of Signal Processing, Image Processing and Pattern Recognition Vol. 6, No. 2, April, 2013.
- [2] <http://www.shodhganga.com>.
- [3] Bharathi PS, Amirthaveni M, "Impact of nutritional intervention on urinary composition of stone formers", Indian J Nutr Dieted, 2008, 45: 169-175.
- [4] Yan Xu, Toshihiro Nishimura, "Segmentation of Breast Lesions in Ultrasound Images Using Spatial Fuzzy Clustering and Structure Tensors", International Journal of Computer, Electrical, Automation, Control and Information Engineering Vol: 3, No: 5, 2009.
- [5] P.R.Tamilselvi, "Detection of a Renal calculi using a semi automatic segmentation approach", International Journal of Engineering Science and Innovative Technology (IJESIT) Volume 2, Issue 3, May 2013.
- [6] Komal Sharma, jitendra virmani, "Classification of renal diseases using first and higher order statistics", international conference on computing for sustainable global development, IEEE, 2016.
- [7] Ranjith.M, "Extraction and Dimensionality reduction of features for renal calculi detection and artifact differentiation from segmented ultrasound kidney images", IEEE, 2016.
- [8] Prema T. Akkasaligar, Sunanda Biradar Classification of Medical Ultrasound Images of Kidney, International Journal of Computer Applications (0975 - 8887) International Conference on Information and Communication Technologies (ICICT- 2014,)pp 24 -28.
- [9] T.Mangayarkarasi, D .Najumissa, "Development of patient assistive Tool for detection of Abnormalities in kidney", Indian Journal of Science and Technology, Vol 8(24), IPL0324, September 2015, pp 1 -5.
- [10] Ming Zhang, Anxue Zhang, and Jianxing Li, "Fast and Accurate Rank Selection Methods for Multistage Wiener Filter", IEEE



- transactions on signal processing, vol. 64, no. 4, February 15, 2016 pp 973 -984.
- [11] Shuruthi.B, M.Siddapa, "Speckle noise reduction in ultrasound images-A review", International journal of engineering and research technology (IJERT), Vol.4 issue 02, February 2015.
- [12] R.Vinoth, K.Bommannaraja, "An enhanced ultrasound kidney image classification", biomedical research 2016, special issue: S46-S52.
- [13] Ding Zuchun, "An Effective Key point Selection Algorithm in SIFT", International Journal of Signal Processing, Image Processing and Pattern Recognition Vol. 6, No. 2, April, 2013.
- [14] Liya Kong, Qinghua Huang, Minhua Lu "Accurate Image Registration Using SIFT for Extended-Field-of-View Sonography", IEEE 2010.
- [15] Yan Xu, Toshihiro Nishimura, "Segmentation of Breast Lesions in Ultrasound Images Using Spatial Fuzzy Clustering and Structure Tensors", International Journal of Computer, Electrical, Automation, Control and Information Engineering Vol: 3, No: 5, 2009
- [16] Rajeshwar Dass, Priyanka, Swapna Devi, "Image Segmentation Techniques", International Journal of Electronics & Communication Technology, Vol.3, Issue 1, Jan-March 2012.
- [17] Dr.J.S.Leena jasmine, "Digital Image processing",First Edition,Magnus Pulations,June 2016.
- [18] <http://www.ultrasoundmedicine.com>
- [19] Tanzila Rahman,Mohammad Shorif Uddin, "Speckle Noise Reduction and Segmentation of Kidney Regions from Ultrasound Image",978-1-4799-6/13,2013 IEEE.
- [20] V.Damerjian, O.Tankyevych, N.Sough, E.Petit, "Speckle Noise Characterization Methods in Ultrasound Images-A review",Elsevier Masson,IRBM 35(2014) 202-213.

Evaluation of Symmetry Plane using Genetic Algorithm

D. Chitradevi
Research Scholar
Department of CSE
Hindustan Institute of Technology and Science
dcdevi@hindustaniv.ac.in

Dr. S. Prabha
Associate Professor
Department of ECE
Hindustan Institute of Technology and Science
sprabha@hindustaniv.ac.in

Abstract: Normal human brain is not perfectly symmetrical even it has a high degree of bilateral symmetry. Identification of plane of symmetry is a critical step in brain image analysis. Brain symmetry gives two hemispheres. This paper proposes a new method for evaluating best symmetry plane of brain images using Genetic Algorithm (GA) from Magnetic Resonance Images (MRI). MRI scan is the best modality for brain images, which helps to look for tumors and other diseases in the brain. Symmetry can be reflected in MR image representing axial/horizontal and coronal slices of the brain. Genetic algorithm is an optimization technique which helps to find the optimized solutions/feasible solutions. GA adopted to achieve better results, faster processing times and it is used in more applications. The GA optimization is performed using the selection, mutation and crossover. Major operations are preprocessing, random selection of coordinates and genetic algorithm. Morphological operators help to extract the region of interest from brain image and unwanted portions of MRI images are removed. This proposed method provides better symmetry value with an accuracy of 90%. This performance leads to good approximation of brain tumor segmentation.

Keywords: Symmetry plane, Genetic Algorithm, MR brain image, Optimization, bilateral symmetry, MRI

I. INTRODUCTION

Medical images are obtained by MRI (Magnetic Resonance Images). The MRI is the valuable tool for clinical and surgical environment. The automatic detection of this plane in brain images in magnetic resonance images (MRI) is a useful task. MRI tool helps to detect a different variety of conditions of the brain such as cysts, tumors, bleeding, swelling, developmental and structural abnormalities, infections, inflammatory conditions, or problems with the blood vessels. It can determine if a shunt is working and detect damage to the brain caused by an injury or a stroke. Normal human brains are high degree of bilateralsymmetry. Hence there is a need to find the symmetry. The mid-sagittal plane can

be defined as the plane that is the best to separates both brain hemispheres. The human brain marked symmetry across the sagittal plane. The left and right hemispheres are not exact mirror images. Internal hemispheric variation is called as asymmetry. Both hemispheres will have the variations, the variations within the individual much less than another object. Scientist have proved about the brain structure i.e generally, left handed people will have different shape of the brain similarly right handed people will have different shape of the brain. Left-handers will have more symmetrical brain but, right-handers have asymmetrical brain (left cerebral hemisphere is larger than the right). Symmetry is one of the geometric features for the brain. The real brains and their images do not get the exact symmetry. The symmetry can be computed by comparing of two hemispheres. The maximum value of symmetry measure is called as symmetry plane. Proposed system needs reflection symmetry. This work proposes correlation coefficient method to find the similarity between two hemispheres with help of genetic algorithm. The separation between two hemispheres can be detected in MRI which is easier than other scan like CT, PET etc. the orientation of the image is improved and maximizing the correspondence for the left and right side of the hemispheres.

II. RELATED WORKS

Many researches have been developed for finding symmetry. Khotanlou, et al. used fuzzy classification, symmetry analysis and spatially constrained deformable models to find symmetry [1]. Jayasuriya et al. identified the symmetry plane in Neuro images with the help of Intensity profile analysis [2]. Alexander et al. used downhill simplex method and global maximum optimization to get best symmetry plane [3]. Liu, Sheena Xin reviewed about symmetry and asymmetry analysis

[4]. Saddique et al. discussed about brain tumor segmentation using symmetry techniques such as hybrid (EHASA) [5]. Bala et al. calculated minimization or maximization of function [6]. Grigaitis et al. utilized hybrid method to find the symmetry with deviation angle until 25o [7]. Vasupradha et al. have discussed Particle swarm optimization and Enhanced Darwinian Particle Swarm Optimization [8]. Bala et al. discussed about Multi objective GA [9]. Kaushik et al used genetic algorithm for image segmentation [10]. Khattar et al. analyzed the genetic algorithm for travelling salesman problem. [11].Tuzikov, Alexander, used downhill simplex method to find the best symmetry plane [12]. Prima et al. have proposed block matching procedure to and local similarity measures to find the symmetry [13].

III. METHODS AND MATERIALS

Evaluations of Symmetry Plane: Proposed system uses MRI. Brain images are acquired with the help of Magnetic Resonance Image (MRI) scanning. There are number of methods has been proposed to identify the symmetry of the brain [1]. MRI scanned image can be read. Convert RGB to gray scale. To get accurate brain region, need to use morphological operations. Morphological operation helps to remove external parts (unwanted surroundings) of an MRI brain image. In this system morphological erosion operation was considered to extract the boundary of an image or ROI of brain image. Erosion with disk structuring element was used to smooth the brain borders by filling holes inside the brain region. ($g=f \ominus s$) Erosion also helps to disconnect the weakly connected regions/boundaries. Then, crop the filled brain image from the original image.

Genetic Algorithm

Genetic algorithm processes works on randomly generated population. Each generation will have new set of population obtained by the GA operators. It selects best individual based on fitness function i.e. close to objective by suppressing the weaker ones. Genetic algorithms have challenging operators to mimicking the natural process: Selection, Crossover, Mutation and recombination, used to get best solution of a problem [13].

The following steps are genetic algorithm processes [3]. Initial populations are two values i.e., y1 and y2.

algorithm using symmetry and active contour (HASA) and enhancement
HASA

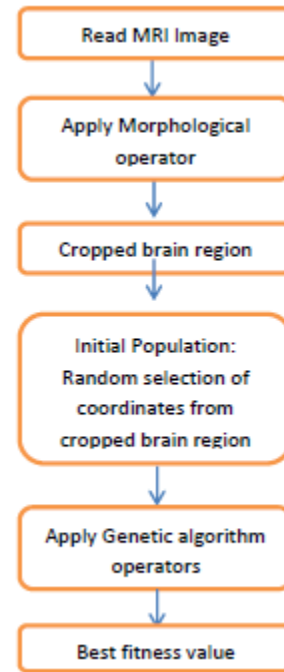


Fig. 1 Symmetry Plane Processing

Objective: max Y=similarity (A & B).

Y: Objective function

A: M x N matrix, B: M1 x N1 matrix

A : 1 and B : size of the row in a matrix.

1. *Initial Population*: For an instance, x1 is start row and x2 is row size (total number of rows in cropped brain image). Initial random populations are {y1,y2}. Bresenham’s line drawing algorithm can be used to draw line on the image with coordinate points [12]. There are three generic operations are performed to produce the next generation.

2. Find the fitness function value. The following table shows the input population with symmetry value (fitness value).

TABLE.1 POPULATIONS WITH FITNESS VALUE

Initial Populations		Fitness value
y1	y2	
10111111.11	10010100.11	8.7
11111111.10	1001100.10	8.8
1100000.11	1100100.10	8.6
1011111.10	10010100.11	8.5
10111010.1	10001100.10	7.6



For accurate result, fixed number of population size as 50. Select best individual from the fitness values based on selection methods. Roulette wheel selection method used for selecting the best individuals. The maximum fitness value will be the best solution for next generation. Each individuals of the population is evaluated using fitness function. Apply crossover operators to create an offspring. This can be represented as crossover rate Pc. Mutation operator is performed bit by bit, which is used to change some bits from selected individuals. Gaussian mutation used to mutate the chromosomes. Decode the string calculate the fitness function. Evaluate the fitness function to rely on objective function. Objective function is to find the best symmetry value. Symmetry can be found by using correlation coefficient method. With this method, the similarities found between two hemispheres are

$$r_1 = \frac{\sum(x_i - x_m)(y_i - y_m)}{\sqrt{\sum(x_i - x_m)^2} \sqrt{\sum(y_i - y_m)^2}}$$

'r' value lies between $-1 \leq r \leq +1$, X and Y two parts of an image with same size which is two hemispheres. Proposed system takes output as a positive correlation which gives strongly related data. From the number of individuals the next population are chosen, i.e fitting values are greater than the others. Greatest individual value can be selected for next generation (Select the new population replacing current population). This process can be repeated until it reaches the maximum or minimum optimum solution (objective function). Maximum symmetry is the best fitness value.

IV. RESULTS

This proposed system implemented using MATLAB. The dataset for the study was collected from National Centre for Image Guided Therapy and MR image database. Initially, input image was read and then it converted into gray scale to reduce the computational complexity for further processing. Brain region have been extracted through morphological operations based on structuring element. Masking was applied to get a binary image. Then, from the resultant image, the initial populations are generated and it was passing on to genetic algorithm operations for best optimized solutions.

The following parameters used for controlling the operations of GA [13]:

1. *Population Size*: One of the criteria chosen to get best optimized solution is population size or number of individuals. Initial population size was 20. In that,

small size of population got low performance. Increase in population size as 50 best solutions was found.

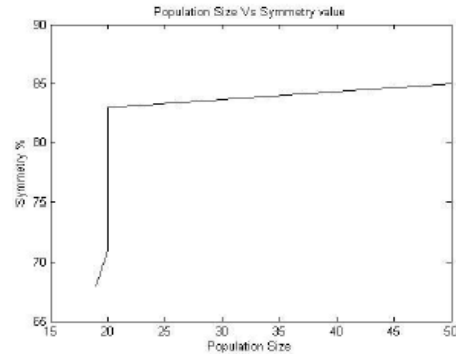


Fig.2 Population size with symmetry value

Fig.2 represents, increase in population size (50) gives best accuracy.

2. *Maximum Generations*: Initially population size and maximum generations was 20 & 50 respectively. To improve the accuracy, the population size was 50 and maximum generation as 80. But, best optimized symmetry value was found in 51 generation.

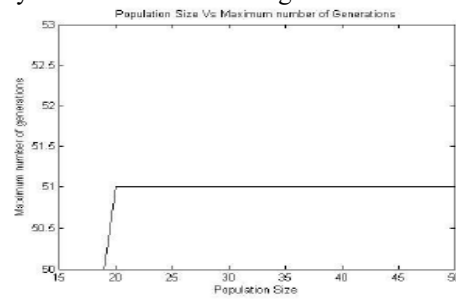


Fig.3 Population size vs Number of Generations

Fig.3 shows the maximum number of generations. In many cases number of generations are 51 even it has population size as 20 or 50. Population size is 20 performances in accuracy were low compared to 50. The high accuracy level achieved with a population size 50. The highest performance is 90% with population size 50 and total number of generations executed was 51.

3. *Stall Generations*: Maximum stall generations, stops the algorithm which finds average relative change in the best fitness function value. This system stops with high stall generations of 29.



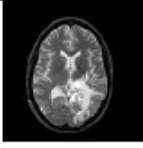

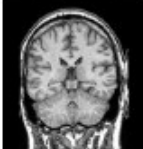

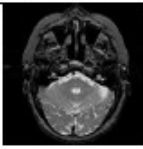
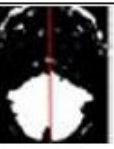
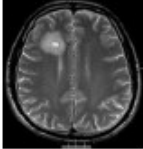

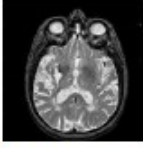

	a	b	c	d
1			180 x 133	0.8376
2			224 x 190	0.8508
3			223 x 185	0.8758
4			197 x 197	0.897486
5			194 x 152	0.859896

Fig. 4 a) Original Image b) Symmetrical Image c) Size of a symmetrical image d) best fitness value.

The size of each volume of input image limit is from 105 x 95 to 225 x 201. It used different plane of an image such as coronal image, horizontal image/axial image. Fig. 4 shows Original Image, after removing unwanted external parts drawn a line on the image (symmetry image), dimension of a symmetrical image, and best fitness value.

Fig. 5 shows best fitness value, population size, and current best individuals, individual values in the generations, expected values and stopping criteria. Fitness graph displays the best fitness value 89.74 and the mean value of the fitness 89.74. Score range is displayed in score histogram with the limit from 0 to 50.

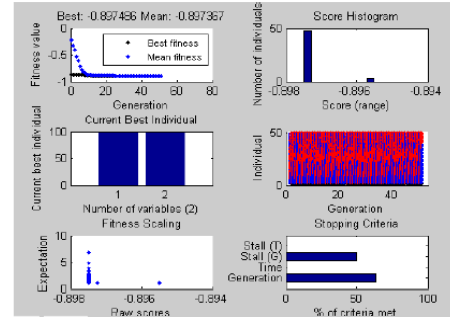


Fig. 5 GA output

Best optimized values have been shown in current best individual generation graph; it holds the value of y1 and y2. Stopping criteria's are stall generation value and percentage of stall generation.

V. DISCUSSION

The main objective of the proposed work was to identify the accurate result of symmetry in the brain region. Though many techniques are available for symmetry findings they result in maximum iteration and maximum time limit. GA can solve this problem and gives it best solutions. PSO will not have a crossover and mutation operation. Implementation of these two operations in GA helps to find best parent for next generations. Vijay et al. (2016) discussed PSO techniques using MRI. Comparing PSO with GA, GA yields best optimized solution than PSO. PSO gives 84% of accuracy with 68 numbers of generations. But for the same images, GA yields 90% of accuracy with 51 numbers of generations which is shown in the following table. GA helps in accurate detection of symmetry region.

Method	No. of generations	Performance in Accuracy
PSO	68	84%
GA	51	90%

VI. CONCLUSION

As a conclusion, the proposed algorithm method proves to be best symmetry. Symmetry plane is achieved by using genetic algorithm. This algorithm achieved good results with the highest performance of 90 % of symmetry value and the highest stall generation is above 30. Generally, symmetry plane is a useful feature for tumor identification. The proposed work has many advantages in comparison with other methods such as automation (in the

symmetry analysis method, a reduced generations is required to select the appropriate peaks) and it also works well for wide range of tumors.

REFERENCES

- [1] Khotanlou, Hassan, et al. "3D brain tumor segmentation in MRI using fuzzy classification, symmetry analysis and spatially constrained deformable models." *Fuzzy sets and systems* 160(10), pp. 1457-1473, 2009.
- [2] Jayasuriya, Surani Anuradha, and Alan Wee-Chung Liew. "Symmetry plane detection in neuroimages based on intensity profile analysis." *Information Technology in Medicine and Education (ITME), 2012 International Symposium*, vol. 2. IEEE, 2012.
- [3] Tuzikov, Alexander V., Olivier Colliot, and Isabelle Bloch. "Evaluation of the symmetry plane in 3D MR brain images." *Pattern Recognition Letters* 24, no. 14, pp. 2219-2233, 2009.
- [4] Liu, Sheena Xin. "Symmetry and asymmetry analysis and its implications to computer-aided diagnosis: A review of the literature." *Journal of biomedical informatics* 42(6), pp. 1056-1064, 2009.
- [5] Saddique, Mubbashar, Jawad Haider Kazmi, and Kalim Qureshi. "A hybrid approach of using symmetry technique for brain tumor segmentation." *Computational and mathematical methods in medicine*, 2014.
- [6] Bala, Anju, and Rajender Singh Chhillar. "A Paper on Multiple Objective Functions of Genetic Algorithm." *International Journal of Computer Applications* 119(10), 2015.
- [7] Grigaitis, Darius, and Mécislovas Meilunas. "Automatic extraction of symmetry plane from falx cerebri areas in CT slices." *Bildverarbeitung für die Medizin 2007*. Springer Berlin Heidelberg, pp. 267-271, 2007.
- [8] Vijay, Vasupradha, A. R. Kavitha, and S. Roselene Rebecca. "Automated Brain Tumor Segmentation and Detection in MRI Using Enhanced Darwinian Particle Swarm Optimization (EDPSO)." *Procedia Computer Science*, pp. 475-480, 2016.
- [9] Bala, Anju, and Rajender Singh Chhillar. "A Paper on Multiple Objective Functions of Genetic Algorithm." *International Journal of Computer Applications* 119(10), 2015.
- [10] Kaushik, Divya, et al. "Medical image segmentation using Genetic Algorithm." *image* 81(18), 2013.
- [11] Khattar, Sonam, and Puneet Gosawmi. "An Efficient Solution of Travelling Salesman Problem Using Genetic Algorithm." *International Journal of Advanced Research in Computer Science and Software Engineering*, 4(5), pp. 656-660, 2014.
- [12] Tuzikov, Alexander V., Olivier Colliot, and Isabelle Bloch. "Brain symmetry plane computation in MR images using inertia axes and optimization." *Pattern Recognition*, 2002. *Proceedings*. vol.1, IEEE, 2002.
- [13] Prima, Sylvain, Sébastien Ourselin, and Nicholas Ayache. "Computation of the mid-sagittal plane in 3-D brain images." *IEEE Transactions on medical Imaging* 21(2), pp.122-138, 2012.

Geometric Nonlinear Diffussion Filter Based Edgemap Extraction and its Validation of Infrared Breast Images

J ThamilSelvi

Department of Electronics and
Communication Engineering
Sri Sairam Engineering College
Chennai, India

thamilselvi.ece@sairam.edu.in

G Kavitha

Department of Electronics and
Communication Engineering
MIT Campus
Chennai, India

C M Sujatha

Department of Electronics and
Communication Engineering
Anna University, CEG Campus
Chennai, India

Abstract—Breast cancer is the leading cancer that affects women in the world. Early diagnosis of cancer prevents morbidity and mortality rate. Thermography is an additional tool for early diagnosis of breast cancer. Low contrast, poor Signal to Noise Ratio (SNR) and complex breast boundaries are the inherent limitation of breast thermal images which makes segmentation a challenging task. In this work, an attempt is made to extract edge map from Type-I and Type-II breast images using Geometric Non linear Diffussion Filter (GNLDF) method to aid accurate segmentation. GNLDF is an iterative nonlinear filter which reduces the noise and preserves the edges based on the local image topology. The extracted edge maps are validated against the input images using betametric and Gradient Magnitude Similarity Deviation (GMSD). Result showed that edge map extracted using GNLDF method is distinct for both types of images. The beta metric and GMSD values are found to be 0.29 and 0.004 indicating high resemblance of filtered image edges with the input images. GNLDF method has improved the SNR of Type-I and Type- II images by 35dB compared to Perona Malik method. Hence, the edge map extracted using GNLDF filter shall aid accurate segmentation of breast tissue to identify pathology for clinical interpretation and diagnosis.

Keywords: Breast thermography, GNLDF, Perona Malik, Beta metric, GMSD and SNR

I. INTRODUCTION

Breast cancer is second most common malignancy among women in the developing countries. World Health Organization estimated that by the year 2030, 27 million of women will be affected by breast cancer [1]. Early diagnosis of breast cancer prevents disability and death. There exists many potential imaging technique which aid detection of breast cancer. The mammography technique fails to detect cancer among young women and sensitivity is poor [2]. In modern imaging technique such as magnetic resonance image, computed tomography and ultrasound, patients are exposed to radiation and subjected to long duration diagnostic procedure [3]. Thermography is the promising tool for early diagnosis of

breast cancer. It is a functional and non-invasive imaging technique which captures the thermal variations of breast surface. These thermal variations are essential for the quantitative analysis and clinical interpretation [4, 5]. The extraction of breast tissue from other region plays indispensable role for clinical interpretation and analysis. Infrared images are of low contrast with poor SNR and amorphous in nature. The detection of lower breast boundaries and inframammary fold are challenging task for image analysis, segmentation and interpretation [6]. Hence necessary preprocessing technique is required to reduce the noise and preserve the sharp edges to aid accurate segmentation for analysis. Many edge detection techniques have been employed for the detection of the breast boundaries. The lower breast boundary detected using Canny and Hough Transform included the false edges [7]. Extraction of inframammary fold has been attempted using thresholding, border detection and cubic spline interpolation [8]. Due to the presence of noise in inframammary fold and lower breast boundaries, these conventional edge detection techniques fail [9]. In the linear and homogeneous diffusion filters such as median, hybrid median filter and Gaussian filter, important edges are blurred due to uniform smoothing at each location. [10, 11]. Total variation based denoising filter suffers from a stair casing effects in regions with gradual image variations [12]. Anisotropic diffusion filter (ADF) is one of the most widely used denoising and often used as edge detection technique in medical imaging [13-15]. ADF have good performance in denoising while preserving sharp edge features [16-18]. The diffusion coefficient is the function of gradient threshold and calculated in all four directions. Recently GNLDF is used to denoise the low dose X-ray imaging. In this method diffusivity parameter is independent of gradient threshold and diffusion depends on two local parameters. The diffusion coefficients are found either in horizontal or vertical direction.

In this work, an attempt is made to extract the edge map using GNLDF method [19]. This method incorporates the global

noise behaviour and the local topology of the pixel intensities to define new diffusivity functions. The extracted edge map is validated against Perona Malik edge map using Beta metric [19] and GMSD [21]. Further to evaluate the performance of GNLDF method, SNR is calculated and plotted.

II. METHODOLOGY

A. Database

Breast thermal images for this study are obtained from <http://visual.ic.uff.br/proeng> an online database of the project [20]. 35 images of Type-I with clear, distinguishable lower breast boundary and inframammary fold and 20 images of Type-II with indefinite lower breast boundary and complex inframammary fold are considered for this analysis.

B. Materials and Methods

To aid accurate segmentation, it is necessary to obtain the appropriate edge maps. The image enhancement and edge detection based on linear scale space technique is replaced by nonlinear diffusion filter. The GNLDF method is attempted to extract the edge map and compared with edge map extracted using PM model. The diffusion equation proposed by Perona Malik [19] is given by

$$\frac{\partial I(x, y, t)}{\partial t} = \text{div}[c(|\nabla I(x, y, t)|) \cdot \nabla I], t > 0 \quad (1)$$

$$I(x, y, 0) = I_0 \quad \text{when } t = 0$$

where $I(x, y, t)$ represents the image gray values at coordinate (x, y) , $c(\cdot)$ is the diffusivity coefficient, $|\nabla I|$ is the magnitude of image gradient and I_0 is the initial image. The diffusion coefficient is a monotonically decreasing non negative function and it is obtained using

$$c(x) = \exp[-(x/k)^2] \quad (2)$$

where 'k' is the noise threshold which controls the diffusion applied on the gradient direction and 'x' is gradient. Optimal choice of k is important for denoising. In this work, PM model 'k' is empirically chosen to be 5.

The diffusion coefficient depends on the neighborhood pixels taken from all four directions. In PM model the global 'k' is used to define the diffusivity function. For faster convergence and to remove noise at the edges, local image information needs to be considered.

Hence in GNLDF, a new diffusivity function either in horizontal or vertical direction is derived using global noise behaviour and local topology of pixel intensities as shown below

$$c(D_x, P_x) = \exp(-(D_x / P_x)^2) \quad (3)$$

D_x is the intensity difference along x- direction, derived using noise and edge pixels for window sizes of 3 x 3 and given by

$$D_x = \begin{cases} |I_E - I_W| - \delta & \text{if } |I_E - I_W| > \delta \\ 0 & \text{else} \end{cases} \quad (4)$$

where I_E and I_W are the intensities at east and west of neighboring reference pixel $\mathcal{S} \in \{0, \sigma\}$, ' σ ' is the standard deviation of the image noise. Median Absolute Deviation (MAD) is used to find δ .

Similarly the local noise behaviour ' P_x ' derived along x- direction is obtained using

$$P_x = I'_{s,x} - A_x \quad (5)$$

A_x is the average of neighboring pixels along east and west direction of reference pixel and obtained using

$$A_x = (I_E + I_W) / 2 \quad (6)$$

The new pixel intensity $I'_{s,x}$ along 'x' direction depends on the intensity difference and neighboring pixel average which is given by

$$I'_{s,x} = \begin{cases} (I_s - D_x) / 2 & \text{if } I_s > A_x \\ (I_s + D_x) / 2 & \text{if } I_s \leq A_x \end{cases} \quad (7)$$

where I_s is the intensity of image.

It is observed when $P_x \gg D_x$, 'c' is equal to 1 for noise pixel and allows big diffusion. Similarly for edge pixel $P_x \ll D_x$ and 'c' is equal to 0 which allows small diffusion. Hence GNLDF method is able to differentiate noise and edge pixel. The noise pixel is found to have higher or lower pixel values compared to the adjacent pixels with similar intensities. Similarly the edge pixel is found to be on inclining or declining slope. The stability of the above equation depends on the step size Δt . The diffusion converges at small step size.

C. Edgemap Validation

The edge map extracted from GNLDF and PM methods are validated using beta metric and GMSD. Beta metric measures resemblances of edge maps derived from original and filtered image defined by

$$\beta = \frac{D(\Delta I_n - \overline{\Delta I_n}, \Delta I_f - \overline{\Delta I_f})}{\sqrt{(\Delta I_n - \overline{\Delta I_n}, \Delta I_n - \overline{\Delta I_n})(\Delta I_f - \overline{\Delta I_f}, \Delta I_f - \overline{\Delta I_f})}} \quad (8)$$

$$D(s_1, s_2) = \sum_{i=1}^M \sum_{j=1}^N s_1(i, j) s_2(i, j) \quad (9)$$

where ΔI_n and ΔI_f are the edge maps of original I_n and filtered images I_f . $\overline{\Delta I_n}$ and $\overline{\Delta I_f}$ are the mean intensities of ΔI_n and ΔI_f .

GMSD computes the local quality metric by comparing the gradient magnitude maps of the input and filtered images.

$$GMSD = \sqrt{\frac{1}{N} \sum_{i=1}^N (GMS(i) - GMSM)^2} \tag{10}$$

where GMS is the gradient magnitude similarity map which depends on the gradient of original and filtered image, GMSM is the mean gradient magnitude similarity map. N is the total number of pixel.

III.RESULTS AND DISCUSSION

The typical infrared breast images of Type-I and Type-II images are shown in Fig 1.

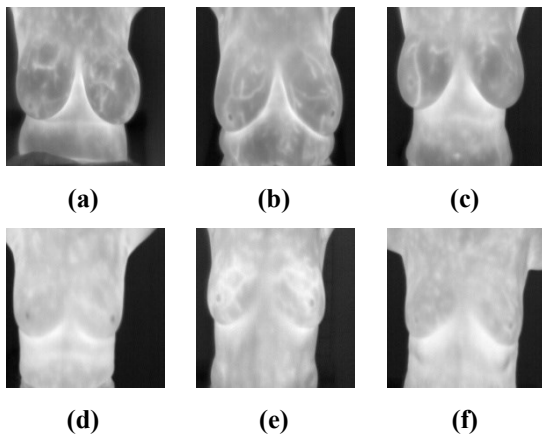
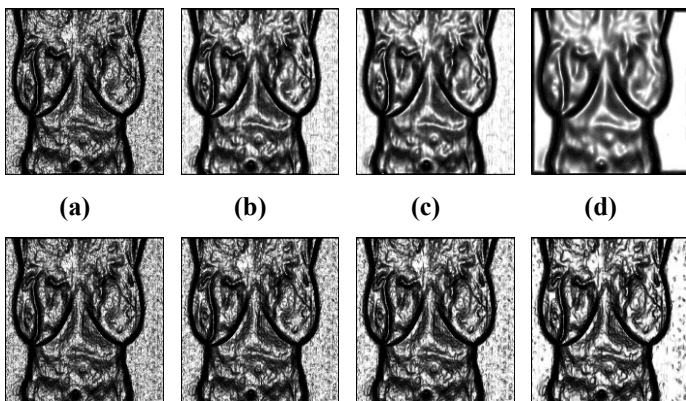


Fig 1 Typical breast images of (a-c) Type- I with clear lower breast boundary and inframammary fold (d-f) Type- II images with indefinite lower breast boundary and inframammary fold.

The Type -I images have visible lower breast boundary and inframammary fold and shown in Fig 1(a-c). The images with indefinite lower breast boundary and inframammary fold categorized as Type- II images are shown in Fig 1(d-f) respectively.

For varying number of iteration the edge maps of type-I images obtained using PM method and GNLDF techniques are shown in Fig. 2(a-d) and Fig 3 (a-d).



(e) (f) (g) (h)

Fig 2 Edgemaps for iterations 2, 4, 8 and 20 (a-d) PM model and (e-h) GNLDF model of Type-I images

It is observed from Fig2(a-d) and Fig3 (a-d) the PM based edge maps of Type-I and Type-II images are found to be visually good compared to GNLDF method. When number of iteration is less thick edges are observed at intra and inter

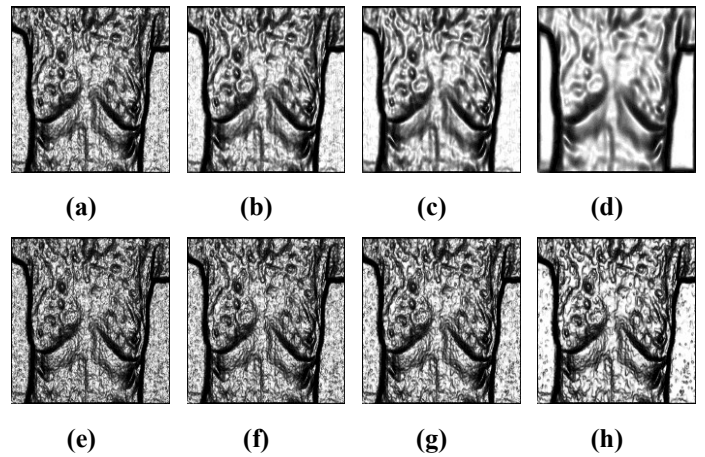


Fig 3 Edgemaps for iterations 2, 4, 8 and 20 (a-d) PM model and (e-h) GNLDF method of Type- II images

breast region. It is also observed that increase in number of iteration blurs the inter region and the sharp edges in PM model edge map compared to GNLDF method.

Similarly from Fig 2(e-h) and Fig 3(e-h), it is observed that the edge maps obtained using the GNLDF technique independent of global parameter 'k', the edge maps are found to be indistinguishable for varying iterations. The inter region and sharp boundaries are found to be preserved. The subjective evaluation may lead to improper segmentation. Hence using mean square error between the input and filtered images of PM and GNLDF method the appropriate edge maps of Type-I and Type- II images are found.

The average MSE of Type-I and Type-II images are observed to be high for PM model compared to GNLDF method edgemaps. The average MSE value of Type-I edge map obtained using PM and GNLDF methods are found to be minimum with 0.18(iteration 8) and 0.15 (iteration 4) respectively. Similarly the MSE value for Type-II images was found to be 0.19 (iteration 8) and 0.16(iteration 4)

For the PM and GNLDF method edge maps, the maximum MSE for Type-I images are found to be 0.28 and 0.18 respectively. For Type-II images 0.28 and 0.19 MSE value was observed. This may be due to partial removal of noise and insufficient diffusion process. The minimum average MSE value of GNLDF method is observed earlier (iteration 4) compared to PM model (iteration 8). This may be due to new nearest scheme which incorporated the noise and the pixel behavior in diffusion to differentiate them. Hence the edge

map of Type-I and Type-II images are extracted for the iterations 8 and 4 using PM and GNLDF method.

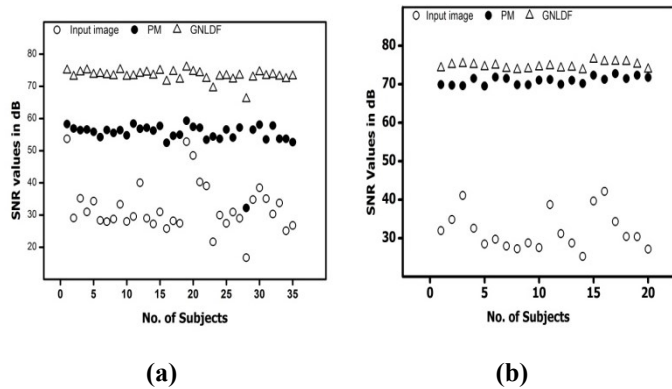


Fig. 5 SNR of Input, PM and GNLDF method a) Type-I images and b) Type-II images

The PM and GNLDF based edge maps of Type-I and Type-II images obtained for iterations 8 and 4 are validated using the beta metric and GMSD as shown in Fig (4).

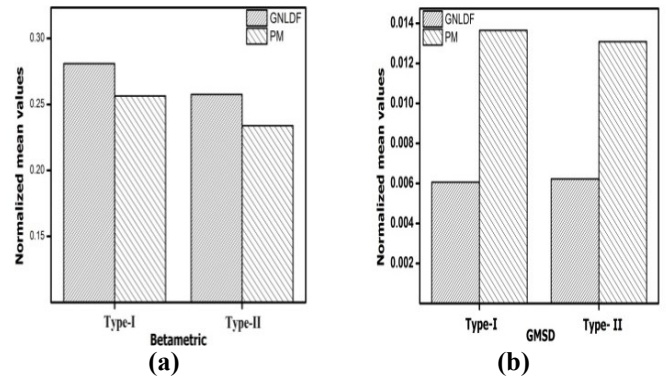
Fig. 4 Edge map validation index of PM and GNLDF methods (a) Betametric and (b) GMSD

The betametric measures the resemblance of the edge images derived from the original and filtered images. For both Type-I and Type-II images the betametric are high which may be due to well preserved edges in the GNLDF compared to Perona Malik model. Similarly GMSD which shows the range of distortion severities in the images are found to be low for GNLDF compared to PM model. From the values of betametric and GMSD it is observed that the proposed technique removes the noise and found to preserve the sharp edges. The performance of the extracted edge maps are further validated using SNR values of the input and filtered images obtained using PM and GNLDF methods. The SNR values of Type-I and Type-II images of input and filtered images obtained using PM and GNLDF methods are shown in Fig 5(a) and (b). From both the plots it is observed signal to noise ratio of the input images are low compared to filtered images and found to be scattered. This may be due to the presence of noise.

It is also observed from the plots, that maximum SNR values are observed for GNLDF filtered images. Compared to input images, the SNR of Type-I filtered images obtained using GNLDF methods are uniform and improved by 35dB respectively which is shown in Fig 5(a). The increased SNR value of GNLDF filtered image shows that noise is reduced and edges are preserved. It is also observed from Fig 5 (b), the SNR values of Type-II filtered images obtained from GNLDF methods have improved by 32 dB respectively. Hence GNLDF filter is capable of reducing the noise and also preserved the sharp edges near the lower breast boundaries and inframammary fold.

IV. CONCLUSION

Breast cancer is most prevalent cancer in the world. Early detection improves the survival rate. To aid accurate segmentation for analysis it is necessary to obtain the connected edges. In this paper, GNLDF method is employed to extract the edge map from Type-I and Type-II images and compared with edge map extracted using PM method. The



beta metric and GMSD values are used to validate GNLDF and PM method edge maps. Further to evaluate the performance, SNR is extracted from both diffusion model images. The results shows that the edge map extracted using GNLDF method is distinct near the inframammary fold even for weak boundary. Compared to PM model, the beta metric value is found to be high and GMSD value is found to be less for GNLDF diffusion method. GNLDF method is able to reduce the noise and edges are continuous and found to be preserved. For Type-I and Type-II images, it is observed that the average SNR of GNLDF has improved by 35dB and 32 dB in denoised image compared to input images. Hence GNLDF technique shall be used to extract the edge map which aids for accurate segmentation and analysis for clinical interpretation of the pathology.

REFERENCES

- [1] M. C. Araújo et al., "Interval symbolic feature extraction for thermography breast cancer detection," *Expert Syst. Appl.*, vol. 41, no. 15, pp.6728-6737, 2014.
- [2] S. Shen et al., "A multi-centrerrandomised trial comparing ultrasound vs mammography for screening breast cancer in high-risk Chinese women," *Br. J. Cancer*, vol. 112, no. 6, pp. 998-1004, 2015.
- [3] K. Das and S. C. Mishra, "Estimation of tumor characteristics in a breast tissue with known skin surface temperature," *J Therm Biol.*, vol. 38, no. 6, pp. 311-317, 2013.
- [4] R. S. Marques, "Automatic segmentation of breast in thermal images," M.S. dissertation, 2012.
- [5] J. P. S. De Oliveira et al., "Segmentation of infrared images: A new technology for early detection of breast diseases," *IEEE International Conference on Industrial Technology (ICIT)*, pp. 1765-1771, 2015.
- [6] N. Scales and C. Kerry, "Automated image segmentation for breast analysis using infrared images," In *26th Annual International Conference of the IEEE Engineering in Medicine and Biology Society*, 2004, vol. 1, pp. 1737-1740, 2004.



- [7] L. Motta et al., "Automatic segmentation on thermograms in order to aid diagnosis and 2D modeling," In Proceedings of 10th Workshop Informática Médica, vol. 1, pp. 1610-1619, 2010.
- [8] P. Gravel et al., "A method for modeling noise in medical images," IEEE Trans. Med. Imag., vol. 3, no. 10, pp. 1221-1232, 2004.
- [9] P. Kapoor and S. Patni, "Image segmentation and asymmetry analysis of breast thermograms for tumor detection," International Journal of Computer Applications, vol. 50, no. 9, 2012.
- [10] J. Weickert, "Anisotropic Diffusion in Image Processing", vol. 1, Teubner, Stuttgart, 1998.
- [11] S. M. Chao and D.M. Tsai, "An improved anisotropic diffusion model for detail- and edge-preserving smoothing," Pattern Recogn. Lett., vol. 31, no. 13, pp. 2012-2023, 2010.
- [12] S. Prabha et al., "Total variation based edge enhancement for level set segmentation and asymmetry analysis in breast thermograms," In 36th Annual International Conference of the IEEE Engineering in Medicine and Biology Society, August, 2014, pp. 6438-6441.
- [13] Y. Yongjian and S. T. Acton, "Speckle reducing anisotropic diffusion," IEEE Trans Image Process, vol. 11, pp. 1260-1270, 2002.
- [14] D. Mittal et al., "Enhancement of the ultrasound images by modified anisotropic diffusion method," Med BiolEnggComput, vol. 48, pp. 1281-1291, 2010.
- [15] G. Gerig et al., "Nonlinear anisotropic filtering of MRI data," IEEE Trans Medical Imaging, vol. 11, pp. 221-232, 1992.
- [16] P. Perona and J. Malik, "Scale-space and edge detection using anisotropic diffusion," IEEE Trans Pattern Anal Machine Intell, vol. 12, pp. 629-639, 1990.
- [17] J. Weickert, "A review of nonlinear diffusion filtering", In Lecture Notes in Computer Science, Scale-Space Theory in Computer Vision, Springer-Verlag 1997, 1252:3-28.
- [18] F. Catté et al., "Image selective smoothing and edge detection by nonlinear diffusion," SIAM Journal of Numerical. Analysis, vol. 29, pp. 182-193, 1992.
- [19] PROENG, Image Processing and Image Analyses Applied to Mastology, 2012
- [20] E. Michel-González et al., "Geometric nonlinear diffusion filter and its application to X-ray imaging," **Biomed Engineering Online**, vol. 10, no. 1, pp. 1, 2011.
- [21] W. Xue et al., "Gradient magnitude similarity deviation: a highly efficient perceptual image quality index," IEEE Transaction of Image Processing., vol. 23, no. 2, pp. 684-695, 2014.

A Versatile Hand Grip Design for Concise Arm and Hand Rehabilitation Robot for Stroke Patients

Arnon Nontapha
Intelligent Electronics Systems Research Laboratory
Master of Engineering Technology (MET) Program
Faculty of Engineering, Thai-Nichi Institute of Technology,
Bangkok, Thailand
Tel: (+66)-2-763-2600,
E-mail Address: arnonnontapha@gmail.com

Wimol San-Um
Intelligent Electronics Systems Research Laboratory
Master of Engineering Technology (MET) Program Faculty
of Engineering, Thai-Nichi Institute of Technology,
Bangkok, Thailand
Tel: (+66)-2-763-2600,
E-mail Address: wimol@tni.ac.th

Abstract—The number of stroke patients in Thailand has been increasing over 28,000 people annually. Most stroke patients have a problem on motion functional movement, resulting in serious disability and directly affecting to daily living ability. Rehabilitation for improving motion functional movements for post-stroke patients is therefore highly required. This paper subsequently presents a unique design of a hand grip which is compatible to concise arm and hand rehabilitation robot for post-stroke patients. Most rehabilitation robots have focused on mechanics of robot body and grip stick, but this work alternatively focuses on the design of a new stable gripper as a robot end, which provides full function for training of arm and hand muscles. The design covers a controllable hand stick, a hand ball, and a curvature part for complete exercise. The use of self-rehabilitation also embeds some sensors connecting to smart phones or tablets. Such complements motivate patients to increase repetition of movements with the record outcomes and feedback. The design of cost-effective 3-Dimensional to be implemented will also be introduced.

Keywords—Rehabilitation; Robot; Sensor; Hand Grip; Post-Stroke Patients; Hand and Arm Muscles

I. INTRODUCTION

Thailand is currently facing the increase of the stroke patients over 200,000 people annually, and those people died over 28,000 people, especially elderly people [1]. Most stroke patients have an effect on motion functional movement, which results in serious disability, directly affecting to activates of Daily Living (ADLs) such as eating bathing or dressing. Rehabilitation for improving motion functional movements for post-stroke patients is thereof relatively important for ADLs in practice [2]. Previous studies for solution regarding with design and development of rehabilitation devices for stroke therapy have extensively been reported. *Wansitta Kaewboon* [3] studied proposed the design for arm rehabilitation to regain functional movement focusing on triceps and infraspinatus muscles for Thai people through the use of the Electromyography (EMG) signal in order to measure and to evaluate muscle progression using Mean Square Root (RMS) and Mean Absolute Value (MAV). LabVIEW program was



(a) InMotion 2.0

(b) Arneo, Hocoma



(b) New hand-grip device for self-rehabilitation

Fig.1 Examples of hand grip stick robotic devices for motor training (a) End-effector type (InMotion 2.0 Interactive Motion Technologies, Watertown, MA, USA) [9], (b) Exoskeleton type (Arneo®, Hocoma, Switzerland)[10], (c) New hand-grip device for self-rehabilitation after stroke, Imperial College London [11].

employed to control both continuous passive motion (CPM) and Direct Exercise. The results showed the device can maintain velocity and function correctly in the way that RMS and MAV of the EMG signals are increased when force level increased for both triceps and infraspinatus muscle. *Ricardo Morales et al.* [4] presented the a new concept for multimodal assistive robot that can assist the stroke patients called “Patient-Tailored Assistance”, consisting of seven degree-of-

freedom for safe human-robot interaction. The proposed robot had considered the patients residual physical and cognitive of physical abilities. Moreover, the patient-tailored assistance robot can be adapted to each patient's individual characteristics and it can be used for reaching task for rehabilitation purpose. Additionally, the visual feedback as well as the level of robot assistance can be adapted to the user's global state by measuring users' performance through the physiological and biomechanical monitoring systems. The result showed that the robot can increase physical and cognitive abilities of stroke patients in performing daily living activities.

Moreover, *Zhibin Song et al.* [5] presented the design of the upper-limb exoskeleton rehabilitation device which was a human-machine interactive (HMI), which focuses on assistance and passive training by rehabilitation device. The

experiment utilised the EMG to verify and evaluate the muscle progress at biceps and triceps muscles, and inertial sensor was used to detect position, velocity, and acceleration strength. *Akhlaqor Rahman and Adel Al-Jumaily* [6] proposed the exoskeleton rehabilitation device which is the bilateral movement training for assisting stroke patients in order to extend each digits of the impaired hand comparing to the functional movement of the healthy hand. *Eric T. Wolbrecht et al.*, [7] alternatively presented a new controller to adaptive control approach in order to learn the patient's abilities and assist in completing movements. *Rui C.V. Loureiro and William S. Harwin* [8] presented the gentle robotic rehabilitation which is a human-machine interaction (HMI), providing and helping arm reaching movement to grasp and release the objects.

Even though there have been numerous rehabilitation robot reported continuously, most rehabilitation robot have focused on mechanics of robot body, but the hand grip stick is simple and may not provide multi-function for concise hand and arm rehabilitation. Fig.1 shows some examples of hand grip stick robotic devices for motor training. It can be seen from Fig.1. that the end-effector type, the exoskeleton type, and a new hand-grip device for self-rehabilitation after stroke are relatively simple. This work alternatively focuses on the design of a new stable gripper as a robot end, which provides full function for training of arm and hand muscles. The design covers a controllable hand stick, a hand ball, and a curvature part for complete exercise. The use of self-rehabilitation also embeds some sensors connecting to smart phones or tablets. Such complements motivate patients to increase repetition of movements with the record outcomes and feedback. In particular, this works attempts to design a cost-effective rehabilitation robot for stroke therapy well as rehabilitation devices, focusing particular features such as capability to repetitive movement, programmable resistance, objective evaluation, and sensing movement.

II. PROPOSED MULTI-FUNCTION HAND GRIP

Fig.2 show the proposed 3-dimentional versatily multi-function hand grip design for rehabilitation robot, which can be used for six main functions. It can be seen from Fig. 2 that the hand grip comprises a hand stick, a hand ball, and a curvature part for complete exercise. For more details, it can

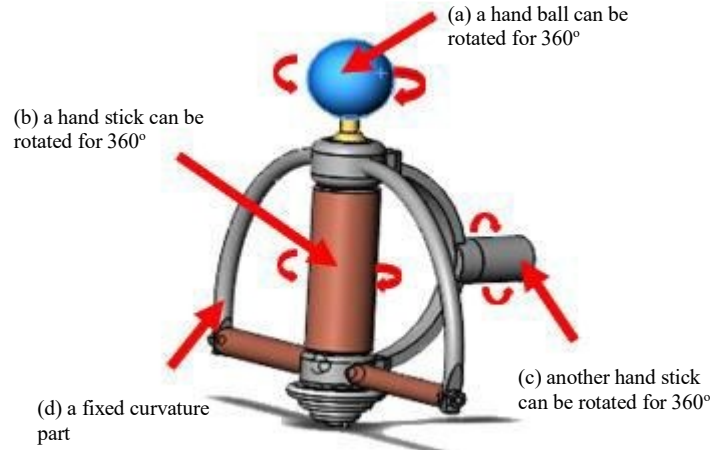


Fig.2. the proposed 3-dimentional versatily multi-function hand grip designed for rehabilitation robot.

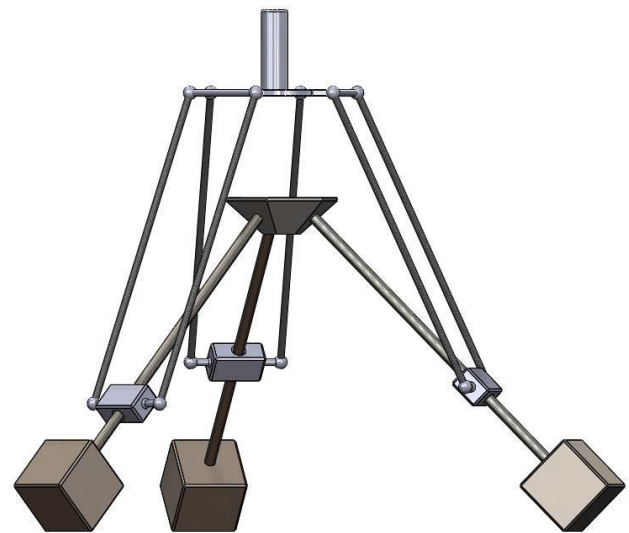


Fig.3. the 3-Dimentional model of the designed robot at normal position where the hand grip will be attached to the top of the robot legs.

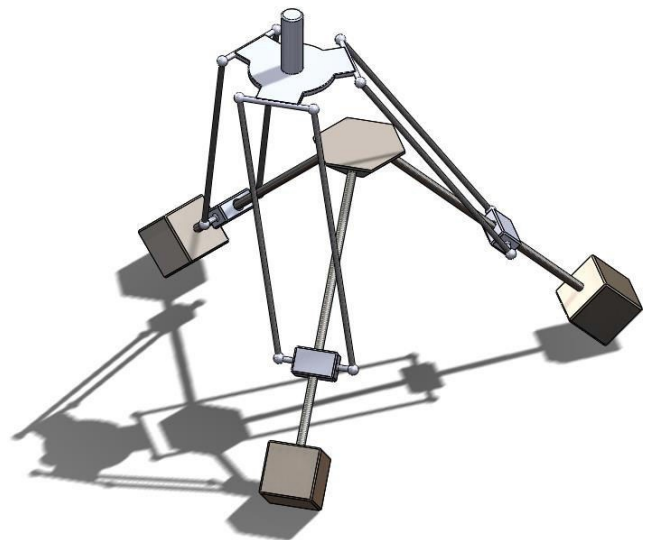
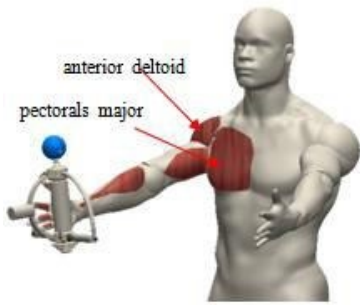
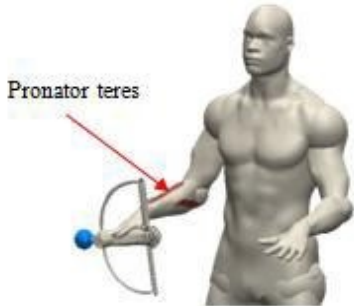


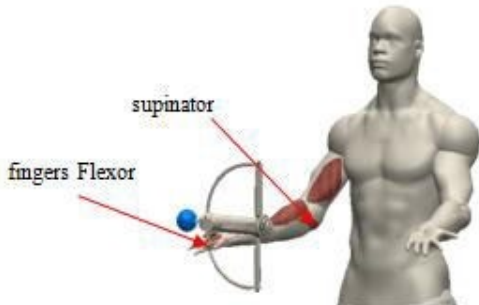
Fig.4. another 3-Dimentional model of the robot at bending position where the hand grip will also be attached to the top of the robot legs.



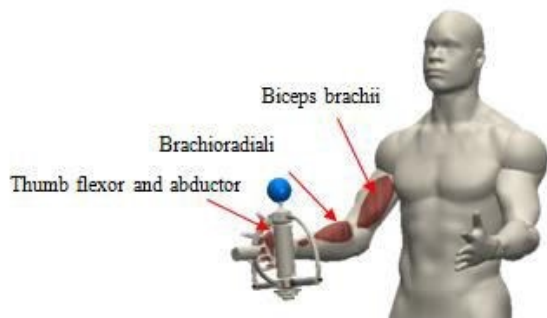
(a) Rehabilitation for Pectorals major and anterior deltoid.



(b) Rehabilitation for pronator teres.



(c) Rehabilitation for finger flexor and supinator.



(a) Rehabilitation for finger flexor and supinator.

Fig.5. Rehabilitation for hand and arm muscles using the proposed hand grip

also be considered in Fig. 2 that there are four features of the designed hand grip, i.e. (a) a hand ball can be rotated for 360°, (b) a hand stick can be rotated for 360°, (c) another hand stick can be rotated for 360°, and (d) a fixed curvature part. Different parts will be used for exercising different hand and arm muscles afterwards. Fig.3 shows the 3-Dimensional model of the designed robot at normal position where the hand grip

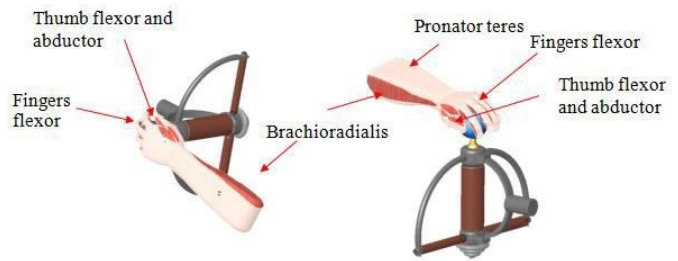


Fig.6. Rehabilitation for fingers, hand and arm muscles using the proposed hand grip at the ball part.

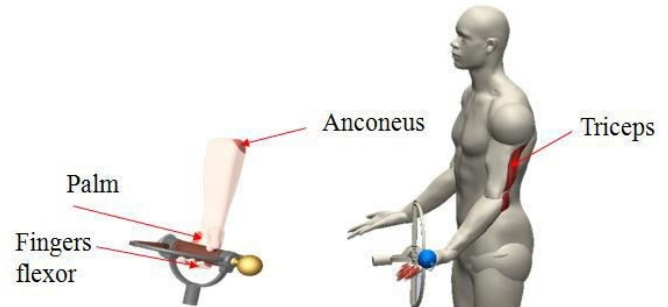


Fig.7. Rehabilitation for fingers, hand and particularly triceps muscles.

will be attached to the top of the robot legs. The design employs three stepping motors with a slider in order to rotate the arm for 180°. For more illustration, Fig.4 depicts another 3-Dimensional model of the robot at bending position where the hand grip will also be attached to the top of the robot legs. In the designed hand grip, some sensors are embedded for measuring body activities and connecting to Wi-Fi network for data collection, monitoring and activity analysis, involving (a) Heart Rate Sensor, (b) Gyroscope, and (c) ESP8266: Wi-Fi Module. The use of sensors will be connected to smart phones or tablets. Such complements motivate patients to increase repetition of movements with the record outcomes and feedback.

V. PHYSICAL IMPACTS OF THE PROPOSED HAND GRIP

In this section, the 6 characteristics of hand grip model will be described in terms of physical impacts through an informational illustration, involving power grip, hook grip, spherical grip, pad-to-side grip, palmer grip, and Tip-to-tip grip. Each function provides different muscle rehabilitation. Fig.5 illustrates rehabilitation for hand and arm muscles using the proposed hand grip. It can be seen in Fig. 5 that the proposed hand grip provides rehabilitation for Pectorals major and anterior deltoid, pronator teres, finger flexor and supinator, and also finger flexor and supinator. Fig.6 depicts the rehabilitation for fingers, hand and arm muscles using the proposed hand grip at the ball part. Additionally, Fig.7 shows the rehabilitation for fingers, hand and particularly triceps muscles. Moreover, the designed hand grip can also be used for adding some small part for particular exercising of fingers, and, and arm of stroke patients. As mentioned earlier, Figs. 8-10 illustrated the muscles are changed corresponding to tip-to-tip grip, pad-to-side grip, and palmer grip, respectively, when the hand grip model position is changed.

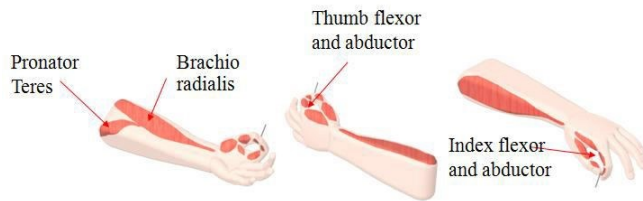


Fig.8. the muscles are changed corresponding to tip-to-tip grip when the hand grip model position is changed.

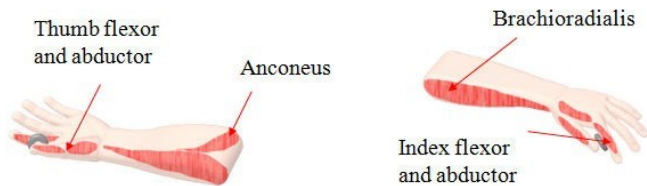


Fig.9. the muscles are changed corresponding to pad-to-side grip when the hand grip model position is changed.

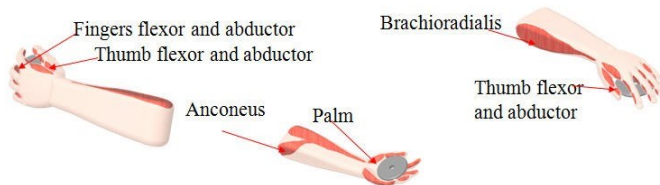


Fig.10. the muscles are changed corresponding palmer grip when the hand grip model position is changed.

VI. DISCUSSIONS AND CONCLUSIONS

Numerous recent studies have heralded the implementation of robotic devices into the field of stroke rehabilitation. Several reports have described the efficacy of robot-assisted therapy for improving motor and ambulatory function in patients with stroke. Most rehabilitation robots have focused on mechanics of robot body and grip stick such as End-effector type (InMotion 2.0 Interactive Motion Technologies, Watertown, MA, USA), Exoskeleton type (Armeo®, Hocoma, Switzerland), or a new hand-grip device for self-rehabilitation after stroke from Imperial College London. However, hand grip strength of the orthopedically challenged and normal persons varied as many factors depending on physical features and particular aspects of stroke patients. Even though, the hand grip may be designed differentially for different category of rehabilitation robot, this work has alternatively attempted to design a versatile hand grip which is compatible to concise arm and hand rehabilitation robot for stroke patients. The design covers a controllable hand stick, a hand ball, and a curvature part for complete exercise. Such a hand grip is capable of providing six main functions, involving power grip, hook grip, spherical grip, pad-to-side grip, palmer grip, and Tip-to-tip grip. The use of self-rehabilitation also embeds some sensors connecting to smart phones or tablets. Such complements motivate patients to increase repetition of

movements with the record outcomes and feedback. The design of cost-effective 3-Dimensional to be implemented will also be introduced. The future work is to implement the actual device and test for further use in hospitals.

VII. ACKNOWLEDGEMENTS

The authors are grateful to Research and Academic Services of Thai-Nichi-Institute of Technology for financial support through a research grant number 1612/A016. The authors would also like to acknowledge Mr. Arnon Thongtem for his useful suggestions.

REFERENCES

- [1] Public Health Statistics, Ministry of Public Health 2015.
- [2] Bulletin of the Thai stroke society: Vol.12, No. 1 January – April,2013. [3] Wansitta Kaewboon, "Arm Rehabilitation", Electricla Engineering, Sonkhla University, Thesis of Academic, Thailand 2013.
- [4] Ricardo Morales, Franciso J. Badesa, Nicolas Garcia-Aracil, Carlos Perez-Vidal, Jose M. Sabater, Eugenia Papaleo, Antonino Salerno, Loredana Zollo, and Eugenio Guglielmelli, "A New Concept of Assistive Robotic Device That Adapts to Individual Users "Patient-Tailored Assistance", IEEE Robotics & Automation Magazine, Volume 21, Issue 3, pp. 123 – 133, 2014.
- [5] Zhibin Song, Shuxiang Guo, Muye Pang, Songyuan Zhang, Nan Xiao, Baofeng Gao, Liwei Shi, "Implementation of Resistance Training Using an Upper-Limb Exoskeleton rehabilitation device for Elbow Joint", Journal of Medical and Biological Engineering, 34(2), pp. 188- 196, 2014.
- [6] Akhlaqur Rahman and Adel Al-Jumaily, "Design and Development of a Bilateral Therapeutic Hand Device for Stroke Rehabilitation", International Journal of Advanced Robotic Systems, Volume 10, pp.1-12, 2013
- [7] Eric T. Wolbrecht, Vicky Chan, David J. Reinkensmeyer, and James E. Bobrow, "Optimizing Compliant, Model-Based Robotic Assistance to Promote Neurorehabilitation", IEEE Transactions on Neural Systems and Rehabilitation Engineering, Volume. 16, Number. 3, 2008.
- [8] Rui C.V. Loureiro and William S. Harwin, "Reach & Grasp Therapy: Design and Control of a 9-DOF Robotic Neuro-rehabilitation System:, In the proceedings of the IEEE 10th International Conference on Rehabilitation Robotics, Noordwijk, Netherlands, June 12-15, 2007.
- [9] Lum PS, Godfrey SB, Brokaw EB, Holley RJ, Nichols D., "Robotic approaches for rehabilitation of hand function after stroke", American Journal of Physical Medicine & Rehabilitation Volume91, pp. S242-254, 2013.
- [10] Mehrholz J, Pohl M., "Electromechanical-assisted gait training after stroke: a systematic review comparing end-effector and exoskeleton devices", Journal of Rehabilitation Medicine, Vo.44, pp. 193-199, 2012.
- [11] <http://www.medscape.com/viewarticle/845170>: Online 25th December 31, 2016.

Development of Thermistor based low cost high sensitive Respiration Rate Measurement System using Audio Software with Audio Input

Tarak Das
Department of
Biomedical Engineering
Netaji Subhash
Engineering College
Kolkata, India
tarakjubme@gmail.com

Sayanti Guha
School of Bioscience
and Engineering
Jadavpur University
Kolkata, India
guhasayanti1@gmail.com

Nisha Banerjee
School of Bioscience
and Engineering
Jadavpur University
Kolkata, India
nisha4evergood@gmail.com

Piyali Basak
School of Bioscience
and Engineering
Jadavpur University
Kolkata, India
piyalibasak@gmail.com

Abstract— Clinical investigation of lungs can be find out by measuring respiration rate. Different methods are present to measure the human respiration rate like Respiratory Rate measurement using Piezoelectric Sensor, Measurement of Respiratory Rate using Laser Doppler Vibrometer, Respiration Rate Measurement System Using Pyroelectric Transducer, Impedance Pneumography Method, Measurement of Respiration Rate by Capnography and Respiratory rate measurement using PPG (Photoplethysmography) signal. However, all of these techniques are very cost effective. We have design a new system using NTC (Negative Temperature Coefficient) type thermistor and Wheatstone bridge and a differential amplifier using IC-741. This system can be used to measure the respiration rate along with display of its waveform in a computer screen. In this system the output signals is taken and after some impedance matching it is used in audio input to a computer. A freely available software Audacity (version 2.1.0) downloaded from internet and installed in to the computer to see the waveform of output signal. The used thermistor is highly sensitive which changes it resistance $-7K\Omega$ per $^{\circ}C$ rise in temperature.

Keywords— NTC Thermistor, wheatstone bridge, OP-741, Respiration rate, software interface, Audacity, wave form.
Introduction

I. INTRODUCTION

The time interval between inspiration and expiration is require to measure the respiration rate^{[1][2]}. It is known to us that the normal respiration is known as eupnea^[8] and when the respiration rate is in higher range it is known as tachypnea and when it goes to below lower range it is known as bradypnea. The normal respiration rate of a healthy person is 14 to 16 cycles in one minute. The respiration rate varies person to person with different ages. During inspiration and expiration fresh air goes inside the lung and there is exchange of carbon dioxide between deoxygenated blood and lung. After this carbon dioxide containing air comes out through lung which is known as expiration. This is the normal technique by which carbon dioxide containing blood convert to oxygenated blood. Human respiration is one of the important parameter of the body for healthy life. Respiration rate also control by brain

through autonomic nervous system. Disease Apnea is one of the important factors which is detect from measurement process of respiration rate. Few important factors can influence the respiration rate. The responsible factors are - Brainstem Rhythmicity Center, Cerebral Cortical Input, Blood Carbon Dioxide, Blood Oxygen, Blood pH, Drugs and Alcohol. Various established methods of measuring respiratory rate are: Piezoelectric sensor based respiratory rate measurement, Laser Doppler Vibrometer based respiratory rate measurement, Using Pyroelectric Transducer based respiratory rate measurement, Impedance Pneumography Method, Capnography method, Photoplethysmography^[5] method. The temperature of inspiration and expiration air during respiration normally varies from room temperature to human body temperature. The thermistor (NTC type) we have used here is highly sensitive to temperature. The Resistance of used thermistor change very rapidly with small change in temperature. Due to its high sensitivity it is very useful to detect both inspiration and expiration phase by using it at one arm of Wheatstone bridge connected with a differential amplifier made by IC-741 and computer interfacing with audacity software. The time period of both the phases and respiration rate also can be measure with high value of accuracy.

II. MATERIALS AND METHODOLOGY

In our work human respiration rate^{[6][7]} is measured simply by using a NTC(Negative Temperature Coefficient) thermistor by placing it in nasal or oral position of a person to cover the patient's mouth and nose and detects the difference in air temperature during inhalation and exhalation. Normal human body temperature is $37^{\circ}C$ but the normal room temperature is 20 to $25^{\circ}C$. This is our new thought to measure respiration rate using NTC type thermistor. Fig:1 represent the block diagram of the system developed by us.

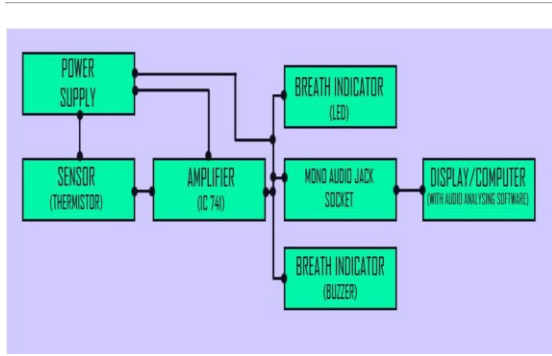


Fig 1 : Block diagram of Respiration Rate measurement device

In circuit, 9V DC power supply from a battery is used as power supply. The sensor that we have used in our work is a thermistor having Negative Temperature Coefficient. It has resistance value above 470k at room temperature. In a NTC type thermistor [9] the resistance decreases with increase in temperature. We have observed that there is decrease in resistance 7kΩ for per degree centigrade rise in temperature. Initially thermistor used at one arm of a Wheatstone bridge and bridge kept in balanced condition.

When we breathe into the thermistor, it causes rise in temperature which lead to decrease in resistance of thermistor and making the bridge unbalanced and the output differential voltage conduct the differential amplifier made by IC 741 [fig:2] for amplification of signals. LED and a Buzzer are used as indicators in this system to detect each breath. The LED will glow each time with incoming breath and the buzzer will buzz until inhalation occurs. During inhalation both the LED and the buzzer will switch off [Fig: 4].

The mono audio jack socket is used to take the output from the amplifier and after impedance matching it feed in to the audio input of a computer for display the wave form and its analysis. In this system as the output amplified signal has large amplitude (4 Volt – 5 Volt), no filtering is required to eliminate noise having low frequency and low amplitude.

The software used for analysis and viewing the signals in the form of audio wave is Audacity [3]. With each inhalation and exhalation there is rise and fall of output voltage which is shown in the form of waveform in the software. The inspiration time period, expiration time period, Respiration rate and also other parameter can be easily analyze from this nature of wave form.

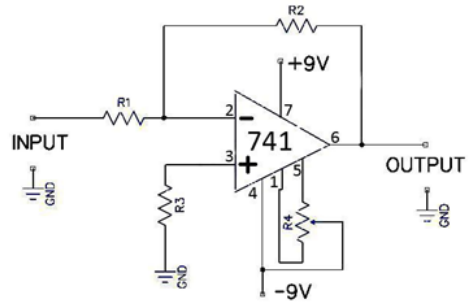


Fig 2: Circuit diagram of IC-741 used as Differential amplifier in this system

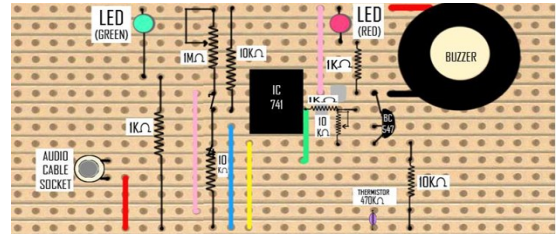


Fig 3: The layout diagram of the circuit in vero board

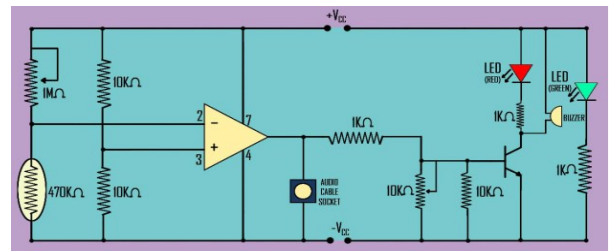


Fig 4: Final diagram of the respiration rate measuring circuit

III. RESULTS AND DISCUSSIONS

Waveform obtained at the audio analyzing software Audacity has distinct positive peaks and negative peaks with a zero baseline in between. The high positive peaks are formed because of the exhalation/expiration and low negative peaks are formed due to the inhalation/inspiration of the subjects. The peak to peak time interval of either 2 consecutive positive peaks or two consecutive negative peaks is the total time taken for one respiration cycle. The time interval between one positive peak and the subsequent zero line is the exhalation period and the time interval between one negative peak and subsequent zero line is the inhalation or inspiratory period. Our work is based on respiratory rate measurement using thermistor and software interfacing. The results are obtained by measuring respiratory rate using a NTC thermistor which is highly sensitive [Fig: 5]. In a NTC thermistor, the temperature is inversely proportional to the resistance and resistance is directly proportion to the voltage.

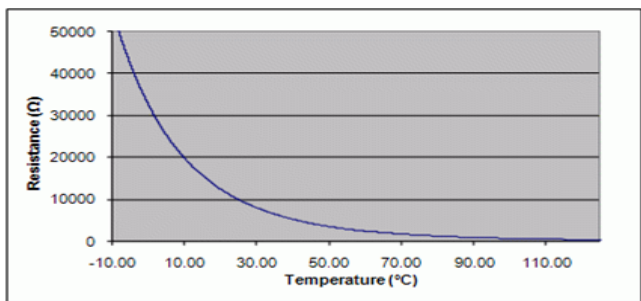


Fig 5: Resistance temperature characteristic of used NTC thermistor

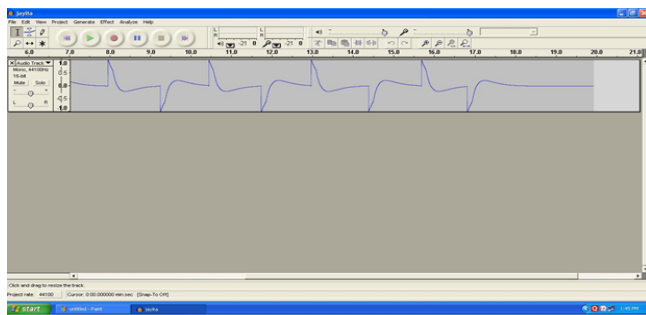


Fig 6: Wave form of Respiration of subject 1 using audacity software

Main advantage of this work is that we can do software interfacing. Output from pin-6 of IC-741^[4] with respect to ground, software interfacing is done. By using audacity software and by converting electrical energy into sound energy using stereo method we get inspiration and expiration curve [Fig: 6].

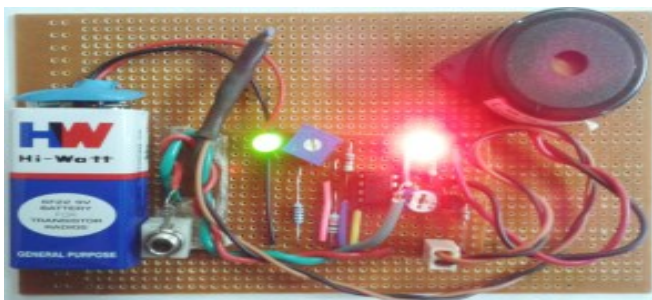


Fig 7: Final picture of the developed respiration rate measuring system

IV. CONCLUSION AND FUTURE SCOPES

Overall, we can conclude that we have successfully observed how this respiration rate measurement system works, which is based on the nasal air flow. By placing a thermistor to conduct when the patient breathes out, and solely depending on heat. This system is very cheaper with respect to the other available systems. After simple modification this circuit can be used as apnea detector. This system is an indicator which can be used to measure the respiration rate of human body. From measurement of respiration rate we can find out several disorder of lung function. Measurement of respiration rate is the initial step to measure the apnea. In this work main aim is

to measure important respiratory rate by using NTC type thermistor, change of its resistance during Inspiration and Expiration very high and very fast due to its high sensitivity. Diagnose of any kind of disturbance in respiratory rate can detect many different diseases, such like Hypertension or Hypotension, Hypothyroidism, Hemochromatosis etc. Audacity is freely available software which can be used to display and measure the respiration rate easily.

ACKNOWLEDGEMENT

We would like to express our special gratitude and thanks to Mr. Tapas Kr. Dawn technical staff of department of Electronic and Communication engineering for providing us information and help in completing the work and designing the circuit. We would like to express our gratitude towards our friends for their kind co-operation and encouragement to complete this work. Finally we would like to express our thanks to all the staff of School of Bio Science and Engineering Jadavpur University for their cooperation with this work.

REFERENCES

- [1] Archita Agnihotri, "Human Body Respiration Measurement Using Digital Temperature Sensor with I2c Interface", in International Journal of Scientific and Research Publications, Volume 3, Issue 3, March 2013.
- [2] K.S. Tan, R. Saatchi, H. Elphick, and D. Burke: Real-Time Vision Based Respiration Monitoring System, 7th International Symposium on Communication Systems Networks and Digital Signal Processing (2010), p. 770-774
- [3] Audacity Team (2008): Audacity (Version 1.3.4-beta) [Computer program]. Retrieved May 5, 2008, from <http://audacityteam.org/>
- [4] LM741, "Texas Instruments", SNOSC25D -May 1998-Revised October 2015
- [5] S. Iamratanakull, J. McNamesl and B. Goldstein: Estimation of Respiration from Physiologic Pressure Signals, Proceedings of the 25th Annual International Conference of the IEEE EMBS (2003), p. 2734-2737
- [6] J. Zhang, and D.Y.T. Goh: A Novel Respiratory Rate Estimation Method for Sound-Based Wearable Monitoring Systems, 33rd Annual International Conference of the IEEE EMBS (2011), p. 3213-3216.
- [7] Michelle A Cretikos, Rinaldo Bellomo, Ken Hillman, Jack Chen, Simon Finfer and Arthas Flabouris, "Respiratory rate: the neglected vital sign", in The Medical journal of Australia, Med J Aust 2008; 188 (11): 657-659.
- [8] R.S Khandpur "Handbook of Biomedical Instrumentation", at McGraw-Hill Education, 2003 - Biomedical engineering - 944 pages
- [9] Maneesh Gupta, Hana Qudsi, "Thermistor Respiratory Monitor", Cornell University, Electrical and Computer Engineering, ECE 4760, 2010
- [10] Karthik Mohan Rao, B.G. Sudarshan, "Design and Development of Real Time Respiratory Rate Monitor Using Non-invasive Biosensor", in International Journal of Research in Engineering and Technology, eISSN: 2319-1163 | pISSN: 2321-7308, Volume: 04 Issue: 06 | June-2015.

Quadcopter based technology for an emergency healthcare

A. Josephin Arockia Dhivya

Department of Biomedical Engineering, School of Bio & Chemical Engineering, Sathyabama University
Old Mahabalipuram Road, Chennai
dhivsahay@yahoo.com

Dr. J. Premkumar

Department of Biomedical Engineering, School of Bio & Chemical Engineering, Sathyabama University
Old Mahabalipuram Road, Chennai
premnsc@gmail.com

Abstract—Several thousands of people die day to day due to the time lag taken by the Ambulance service to reach the accident spot. This happens due to traffic jam, congestion in the city. A prototype of an emergency flying air ambulance or an ambulance drone which can reach the fatal cases faster than a normal ambulance which saves time is designed and it also measures the different health parameters using its measuring devices. When a phone call is given to the emergency number, the emergency operator tracks the location and navigate using global positioning system. The ambulance drone enters the scene in the instant time and real time commands are provided by the operator. The drone consist of a mini patient monitoring system which comprises of variant sensors which can be conveniently attached to the victim body and the important parameters is measured and it is immediately sent to the ambulance as well as to the nearby hospital using global positioning system and ZIGBEE. The particular result helps the paramedics as well as the doctors to evaluate the situation quicker with better diagnostic and therapeutic choices. Therefore, the goal is to develop an all purpose medical toolkit that can be flown to any crisis situation and it is used to give the actual time situation results to the ambulance and the hospital team so that they will be ready to serve to the needs of the patients. This prototype helps to support the routine ambulance rather than replacing the normal ambulance

Keywords— Ambulance, Drone, Sensors , Victim, Lifesaving

I. INTRODUCTION

A drone is a aerial vehicle which is not driven by a human. The more the no of motors and propellers, the maximum thrust it can create. So the best choice to use is the quadcopter as the system comprises of four brushless direct current motors (BLDC) which are used along with the propellers to give them the necessary thrust [2].An 8000mah electrical storage device powers the drone. The drone well equipped with a patient monitoring system is designed to fly to an emergency situation and it is used to extract the victims real time health parameters. The various sensors that we use in our prototype are Temperature sensor, ECG sensor, Respiration sensor. ECG sensor is used to determine the rate and periodicity of heartbeats and also the existence of any mutilation to the heart[4].The Respiration sensor gives the estimation of breaths a individual takes per minute[5].Temperature sensor is used to detect the patient body temperature. Usage of ZIGBEE and global system for

mobile communication protocols in our experiment is mainly for the transmission of data. Zigbee can broadcast data extended areas. The mechanism of Zigbee proposed is to be simpler and less expensive than a wifi and a bluetooth.

II. EXISTING SYSTEM

A hospital wagon drone with a widely reachable defibrillator which can be used during a myocardial arrest during crisis[7]. An emergency air ambulance which serves as a drug delivery system to remote locations. A auxiliary drone support which carries oxygen supply to people who are suffering from respiratory syndrome. These prototypes has a disadvantage of measuring only one parameter. Various measurements cannot be measured. Information regarding patients data cannot be informed to the paramedics immediately.

III. PROPOSED SYSTEM

The prototype that we have proposed is an ambulance drone that can navigate using GPS with a set of sensors that can sense the various physiological parameters of the victim at the ground scene. They are used to send data immediately to the ambulance as well as to the nearby hospitals using ZIGBEE and GSM protocols. This enables them to take a proper decision regarding therapeutic and diagnostic approaches. It also helps the paramedic in the ambulance to track the patient's condition and come prepared accordingly.

IV. ADVANTAGES OF PROPOSED SYSTEM

It progressively reduces the number of mortality cases. This prototype type is well designed for assessment of variant parameters at a determined time limit. It is a life-saving effective process.It can get into an urgent scene quicker than human beings which can save many lives and facilitate the recovery of many patients survival rate. It is ease to use It is portable It is reliable Providing health care in developing countries. Reaching disaster area Caring for patients outside hospitals.

V. BLOCK DIAGRAM

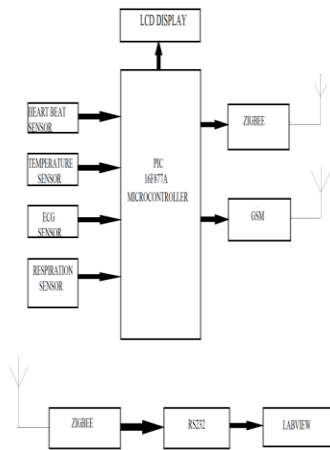


Fig.1:Block diagram of patient monitoring system

VI. MODULE DESCRIPTION

Pic microcontroller, ECG sensor, Temperature sensor, Respiration sensor, Heart beat sensor, ZIGBEE, GSM, GPS.

A. PIC Microcontroller

In our project, we use PIC 16FB77A which has 40 pins. The main advantage of PIC microcontroller is very fast and power consumption is less when compared to other microcontrollers. Interfacing is easy in this type of microcontrollers.[8]

B. ECG Sensor

In our prototype we use AD8232 type ecg sensor is used. This device is used to track the electrical movements and activity of the heart. The output will be in analog form. ECG waveforms are very noisy. So, AD8232 heart rate monitor acts as an operational amplifier to get a perfect signal without any noise. An indicator LED is present to indicate the rate of heart pulse. Here we use 3 lead configuration for measuring ECG. Red colour indicates that it should be connected to right arm. Yellow colour to the left arm. Green colour goes to left leg.



Fig.2:Electrodes used in ECG measurement

C. Temperature Sensor

The temperature sensor which we use is LM-35. This type is widely used for experimental purpose. The average temperature of a human body is 37 degree Celsius. When it increases to a extent it results in hyperthermia which causes fatigue, confusion, fever. It requires +5V DC for proper working.

D. Respiration Sensor

For a healthy adult, proper respiration rate lies from 12-20 breadths per minute. A flexible belt like structure is associated with the sensor and it is strapped around the chest of the individual. When the individual is breathing air into the lungs the resistance of the incorporated rubber cord changes according to the inhalation and exhalation of the person.

E. Heartbeat Sensor

A person's heart beat is determined by the value of contraction and relaxation of heart. A finger probe is present in the sensor kit. The subject should place the finger in the probe and when the LED light glows, the tissue is illuminated with a light source[4]. The amount of light absorbed depends upon the volume of the blood present in that tissue. The output will be in the form of electrical signal. The normal heart beat lies between 60 and 100 beats per minute.

F. Quadcopter

Usage of drones in healthcare is trending nowadays. A quadcopter is a unmanned aerial vehicle or a small helicopter which can be lifted and pushed and it is forwarded by four rotors. Our mini patient monitoring system will be embedded with the quadcopter and when emergency call is given to hospital the operator tracks the location using GPS and the patient real time parameters is measured and they will be sent to the hospital doctors as well as the nurses present in the regular ambulance which will be on the way reaching the scene. These information will be sent to them using GSM. Zigbee is used for data transmission.



Fig.3:Drone embedded with a mini patient monitoring system

VIII. RESULT

This prototype is developed in order to alert the victim's condition to the doctors in the hospital and to the paramedics in normal ambulance. So that those measured parameters details will be sent to them using quadcopter technology before the normal ambulance arrives. The mini patient monitoring system embedded with the quadcopter will reach the scenario and it measures the victim's heart rate, ECG values, temperature and respiration rate. The quadcopter will reach the accident scenario by tracking the location using Global Positioning System(GPS). The real time condition of the patient detail will be sent to the hospital and to the ambulance using GSM technology. The proposed model can be used by drone companies, healthcare companies, government organizations.

IX. FUTURE PLAN

Further advancements can be done in this system by implementing a camera which allows the user and the hospital staffs to view the current situation. Implementing drones in healthcare field is a newly developing field with many opportunities which will be useful for future research.

REFERENCES

- [1] A. Albulbul and A. Chan, "Electrode-skin impedance changes due to an externally applied force", IEEE , pp. 1-4, May 2012.
- [2] A. Nemati and M. Kumar 2014, "Modelling and control of a Single Axis Tilting Quadcopter", American Control Conference (ACC) , June 4-6, 2014.
- [3] Darshana Varma, Virendra Shete, Sunil Somani, "Real Time Self Health Monitoring System", International Journal of Innovative Research in Computer and Communication Engineering(IJIRCCCE), Vol. 3, Issue 6, June 2015.
- [4] Farin, N. , Sharif, S. and Mobin, I, "An Intelligent Sensor Based System for Real Time Heart Rate Monitoring"(HRM), Intelligent Control and Automation, 7, 55-62, May 2016.
- [5] Dr. Firat Güder, Dr. Alar Ainla, Julia Redston, Prof. Bobak Mosadegh, Dr. Ana Glavan, T. J. Martin, Prof. George M. Whitesides, "Paper-Based Electrical Respiration Sensor" Issue 19 , Pages 5727-5732, May 4, 2016.
- [6] Mr. Kalpesh N. Shah, Mr. Bala J. Dutt, Hardik Modh, "Quadrotor – An Unmanned Aerial Vehicle", International Journal Of Engineering Development And Research (IJEDR), Volume 2, Issue 1, 2014.
- [7] Josefín Lennartsson, "Strategic Placement of Ambulance Drones for Delivering Defibrillators to out of Hospital Cardiac Arrest Victims", 2015.
- [8] M. Shanmugasundaram, G Muthuselvi, S Sundar, "Implementation of PIC16F877A Based Intelligent Smart Home System" , International Journal Of Engineering And technology(IJET), Vol5, Issue 2, Apr-May 2013
- [9] Mohamed Fezari, Mounir Bousbia Salah, and Mouldi Bedda, "Microcontroller Based Heart Rate Monitor", The International Arab Journal of Information Technology, Vol. 5, No. 4, October 2008.
- [10] Vinod Ingale, Umar Mulani, "Quadcopter Controlling Using Android Mobile Devices", International Journal of Innovative Research in Computer and Communication Engineering(IJIRCCCE), Vol. 3, Issue 6, June 2015.

Development of Real Time ECG Signal Monitoring System for Telemedicine Application

Mr.S.Bashyam
Department of ECE
SRM University
Kanchipuram, India
bashyam.s@ktr.srmuniv.ac.in

In the recent works many novel architectures[1], algorithms[2]-[3] and software systems [4] are proposed to implement the telemedicine system. The design challenges in

Dr.B.Ramachandran
Department of ECE
SRM University
Kanchipuram, India
ramachandran.b@ktr.srmuniv.ac.in

Abstract—This work presents the development of low cost, portable real time Electrocardiogram (ECG) signal monitoring system with abnormality detection capability. The 3-lead Electrocardiogram device takes the physical pulse input using electrodes stuck to the arms and right leg of the patient under observation. The ECG signal is processed by the microcontroller AT89S52 in the portable wireless unit to count the heart beat for a duration of one minute and the Heart Rate is displayed on LCD display. The amplitude and intervals of some critical components are obtained, processed and displayed in a graphical user interface. If abnormality is detected in the ECG signal, an alert SMS is sent by the system to the doctor through GSM modem to enable him to take appropriate protective measures. The system is intended to use for telemedicine application. Further the system can be improved to monitor multiple physiological signals and to allow patient mobility by transmitting signals wirelessly.

Index Terms—*Real time monitoring system, Electrocardiogram signal (ECG), Heart Rate (HR), Telemedicine.*

I. INTRODUCTION

The foremost causes of disability and precipitate death in the developing countries are non-communicable diseases such as diabetes, chronic respiratory disease and cardiovascular disease. The delay between the first symptom of any cardiac disease and the call for medical assistance has a huge impact among different patients and can have lethal consequences. The exploitation of resources for premature detection and treatment of heart disease has a higher prospective of reducing casualty associated with cardiac disease than superior care after hospitalization. Telemedicine is the utilization of medical information sent from one place to another through communication networks to monitor the health status of the patients. It gives a new approach to deliver health care services when the doctor and patient are separated by long distance.

human physiological signal. In recent works, the received ECG signals from the system is not carrying adequate information about different ECG parameters like amplitude level of p wave, time duration of QRS complex and T wave which helps in diagnosing cardiac arrhythmias, ventricular hypertrophy, myocardial infection and other abnormalities.

A novel non-contact electrode for mobile electrocardiogram, wearable cardiac healthcare System and patient-personalized systems [9]-[13] are implemented for telemedicine application. The cardiovascular disease is well diagnosed if the doctor/ care taker of the patients receives all the extracted ECG parameters [14] in real time without any delay, here the implemented systems lags in transmission of reliable ECG signals with some signal integrity issues. So the monitoring system with reliable signal transmission of vital parameters in real time is indeed for emerging telemedicine application.

In this paper the real time ECG signal monitoring system is proposed to address the above issues. The heart rate is calculated and any abnormality in the heart rate is intimated to doctor through GSM module. Further the duration of different ECG signals are extracted from ECG waveform and displayed in PC which can be accessed by the doctor through remote login procedure when he gets an SMS alert in his mobile phone.

This paper is organized as follows: Section II presents details of the hardware implementation along with software description. The results are discussed in section III. The paper is concluded with future enhancements in section IV.

II. HARDWARE IMPLEMENTATION

The Tele-monitoring system aims for two application scenarios: monitoring at hospital and at home. The wireless monitoring system developed for the present project enables the monitoring of patient at home. The signals from Sensors

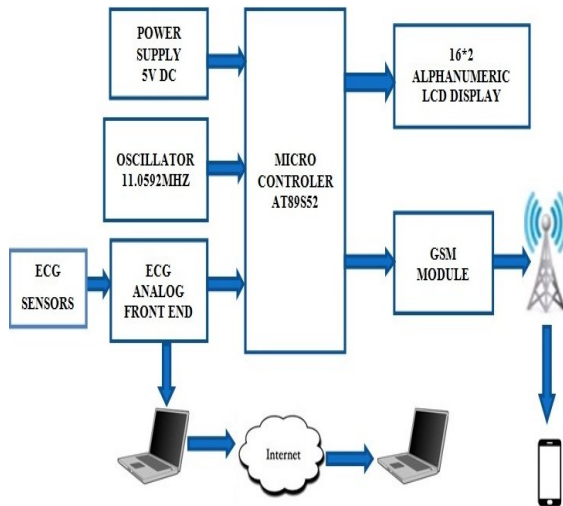


Fig.1. System Architecture

attached to the patient are directed to the ECG analog front end module. It is then processed for heart rate calculation. The architecture is shown in Fig.1.

The microcontroller used is AT89S52 operates at 11.0592 MHz at 5V D.C. The microcontroller obtains the input from the ECG sensors and manipulates the heart beat rate. The abnormality detected in heart rate is sent via SMS using GSM module and displayed on LCD also. The ECG waveform and related parameters are displayed in a PC through graphical interface which can be remotely monitored by the doctor.

A.ECG ANALOG FRONT END

Electrical impulse (waveform of depolarization) is picked up by placing electrodes on patient. The voltage change is sensed by measuring the current change across 2 electrodes. The positive deflection is caused by electrical impulse travels towards the positive electrode whereas the impulse travels away from the positive electrode which results in a negative deflection. The ECG analog front end block is shown in Fig.2.

The pretended ECG signal is generally around 1mV peak-to-peak and is affected by external high frequency noise and common mode voltages. So instrumentation amplifier is used to amplify the signal. The measured electrical potential is an AC signal with frequency range of 0.05Hz to 100Hz in which 50Hz/60Hz noise is suppressed by Notch filter.

The common mode voltages include the 50Hz power-line frequency interferences and DC electrode offset potential. This is the result of the electrode contact with skin, giving rise to a potential difference of up to $\pm 300\text{mV}$. Noise filtering is thus required and it is performed by digital signal processing tool in LabVIEW.

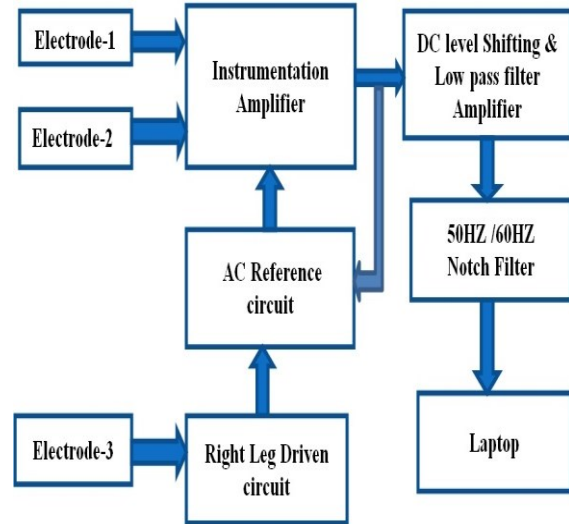


Fig.2. ECG Analog front end circuit

B.SOFTWARE DESCRIPTION

The ECG waveform is also sent to the microcontroller to detect the heart rate. Based on QRS complex received from ECG waveform the heart rate is calculated in beats per minute (BPM). The proteus software is used for simulating the AT89S52 microcontroller with LCD and evaluates heart rate abnormality detection, then send SMS via UART command through GSM module. The simulated output is shown below in Fig.3.

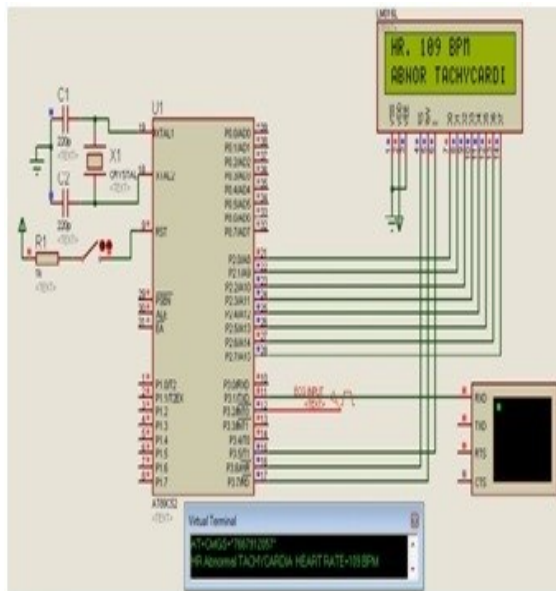


Fig.3. Heart Rate monitor simulation

LabVIEW is a unique software in which bio medical tool kit Package is used to convert the processed electrical impulse signal into a visual representation. The applications are built for baseline wandering removal, noise cancellation, QRS complex detection, heart rate extraction and etc. Usually the ECG signal acquisition hardware can remove the baseline wandering and other wideband noises however, the software scheme is more realistic and it is used for ECG signal processing.

III RESULTS AND DISCUSSION

The Signal produced by the Lub dub simulator is similar to the Real time ECG signal. The system is tested using the Lub dub ECG simulator. The measurement result is shown in Fig.4.

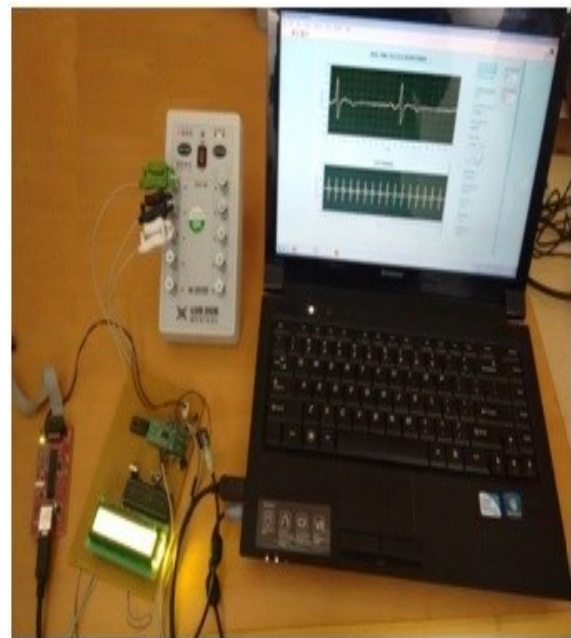


Fig.4. Measured results

The simulated ECG signal given to prototype hardware then tested result is obtained as shown in Table I. The Heart rate between 60 to 100 BPM of patient is considered to be normal. If the heart rate is less than 60 BPM, it is abnormal which is called as bradycardia and if it is above 100 BPM is also indicates abnormality which is called as tachycardia and doctor get alerted by SMS on both cases.

The lab VIEW GUI is designed for real time monitoring ECG signal and to extract the ECG waveform parameters. The web publishing tool is selected from the LabVIEW package and Software web link is launched. It enables doctor to visualize the condition of patient remotely and appropriate treatment measures are communicated to the care taker/junior doctor of the patient at home. The real time tele-monitoring GUI is shown in Fig.5.

TABLE I. HEART RATE INDICATION RESULTS

Simulated ECG signal Heart rate	Analysis result in LCD display	SMS Alert message
60 BPM	HR.060 BPM NORMAL	No

30 BPM	HR.030 BPM ABNORMAL BRADYCARDIA	HR. Abnormal Bradycardia Heart rate=30 BPM
120 BPM	HR.120 BPM ABNORMAL TACHYCARDIA	HR. Abnormal Tachycardia Heart rate=120 BPM

The pulse rate, amplitude level and duration of ECG waveform parameters are extracted and displayed in the Lab View GUI. In Table II the proposed system is compared with some of the existing ECG monitoring systems available. LabVIEW based ECG waveform extraction is new feature in the proposed low cost ECG monitoring system. Also abnormality detection using GSM and remote monitoring of real time ECG signal through online helps patients in diagnosing cardiovascular disease in time



Fig.5. Lab VIEW GUI

TABLE II. COMPARISON OF ECG MONITORING SYSTEM

Ref no.	Signals acquired	Communication technology	ECG waveform extraction	Remarks
---------	------------------	--------------------------	-------------------------	---------

[1]	Heart rate, ECG & Temperature	Internet	Not available	RTOS based architecture enables telecast of Video steaming of the patient.
[7]	ECG, Heart rate	GSM	Not available	FPGA based Arrhythmia detector is proposed.
[8]	ECG, SpO2, Temperature, and BP	GPRS, Internet	Not available	Wireless telemedicine system which integrates sensor, processing & communication unit is proposed.
[10]	ECG, Heart rate	GSM, GPS	Not available	New non-contact electrode circuit is proposed. Heart rate abnormality is intimated.
[11]	ECG, Heart rate	GSM	Available	Wearable Cardiac Healthcare System is proposed. The raw ECG waveform is not monitored remotely.
[13]	ECG, Heart rate, SPO2, PCG & Temperature	Internet, Mobile phone	Available	Vital signs of Patients monitored remotely through internet. The internet access always needed to intimate the abnormal detection of vital signs of the patient.
Presented work	ECG, Heart rate	GSM, Internet	Available	Proposed system enables doctor to remotely monitor ECG waveform. Abnormal detection of heart rate is intimated through GSM module.

IV CONCLUSION

The Real time monitoring system presented in this paper produces reliable ECG waveforms and alerts the doctor for the abnormality in heart rate. In addition ECG waveform extraction is made for premature detection of the cardiovascular related diseases to take precautionary measure. In the future the system can be enhanced by providing wireless connectivity between electrodes with flexible antenna and monitoring portable system that allows arbitrary movement of the patient. Further, development of portable and

low cost multiple health parameters wireless monitoring system will be future scope of our work.

REFERENCES

- [1] M. JagadiswaraRao and M. KameswaraRao, "An RTOS based Architecture for Patient Monitoring System with Sensor Networks", *Indian Journal of Science and Technology*, vol. 9(17), May 2016.
- [2] Christina Orphanidou, Timothy Bonnici, Peter Charlton, David Clifton, David Vallance, and Lionel Tarassenko, "Signal-Quality Indices for the Electrocardiogram and Photoplethysmogram: Derivation and Applications to Wireless Monitoring", *IEEE Journal of Biomedical and Health Informatics*, Vol. 19, pp. 832-838, May 2015.
- [3] Jonathan Herzig, Amitai Bickel, Arie Eitan, and Nathan Intrator, "Monitoring Cardiac Stress Using Features Extracted From S1 Heart Sounds", *IEEE Transactions On Biomedical Engineering*, vol. 62(4), pp. 1169-1178, April 2015.
- [4] Sebastian Thelen, Michael Czaplak, Philipp Meisen, Daniel Schilberg, and Sabina Jeschke, "Using off-the-Shelf Medical Devices for Biomedical Signal Monitoring in a Telemedicine System for Emergency Medical Services", *IEEE Journal Of Biomedical And Health Informatic*, vol. 19, pp. 117-123, January 2015.
- [5] Riccardo Cavallari, Flavia Martelli, Ramona Rosini, Chiara Buratti, and Roberto Verdone, "A Survey on Wireless Body Area Networks: Technologies and Design Challenges", *IEEE Communications Surveys & Tutorials*, vol. 16(3), pp. 1635-1657, third quarter 2014.
- [6] Meng Zhang, Anand Raghunathan, Fellow IEEE, and Niraj K. Jha, "Trustworthiness of Medical Devices and Body Area Networks", *Proceedings of the IEEE*, vol. 102, pp. 1174-1188, August 2014.
- [7] G. Kavya and V. Thulasibai, "VLSI Implementation of Telemonitoring System for High Risk Cardiac Patients", *Indian Journal of Science and Technology*, vol. 7(5), pp. 571-576, May 2014.
- [8] M. Abo-Zahhad, Sabah M. Ahmed, and O. Elnahas, "A Wireless Emergency Telemedicine System for Patients Monitoring and Diagnosis", *International Journal of Telemedicine and Applications*. 2014; <http://dx.doi.org/10.1155/2014/380787>, 2014.
- [9] Boudewijn Venema, Johannes Schiefer, Vladimir Blazek, Nikolai Blanic, "Evaluating Innovative In-Ear Pulse Oximetry for Unobtrusive Cardiovascular and Pulmonary Monitoring During Sleep", *IEEE Journal of Translational Engineering in Health and Medicine*, 2013, vol. 8, Digital Object Identifier 10.1109/JTEHM. 2013.2277870, August 2013.
- [10] Bor-Shyh Lin, Willy Chou, Hsing-Yu Wang, Yan-Jun Huang, Jeng-Shyang Pan, "Development of Novel Non-contact Electrodes for Mobile Electrocardiogram Monitoring System", *IEEE Journal of Translational Engineering in Health and Medicine*. Vol. 4, Digital Object Identifier 10.1109/JTEHM.2013.2253598, June 2013.
- [11] Diptyajit Das, Arnab Pal, Souvik Tewary, Shreyosi Chakraborty, Sauvik Das Gupta, "A Smart and Wearable Cardiac Healthcare System with Monitoring of Sudden Fall for Elderly and Post-Operative Patients", *IOSR Journal of Computer Engineering*. 2014, April, 16(2), pp. 126-133.
- [12] Lei Clifton, David A. Clifton, Marco A. F. Pimentel, Peter J. Watkinson, and Lionel Tarassenko, "Gaussian Processes for Personalized e-Health Monitoring With Wearable Sensors", *IEEE Transactions On Biomedical Engineering*, Vol. 60, pp. 193-197, January 2013.
- [13] Mr. Bhavin Mehta, Ms. Divya Rengarajan, Mr. Ankit Prasad, "Real Time Patient Tele-monitoring System Using LabVIEW", *International Journal of Scientific & Engineering Research*, vol. 3(4), April 2012.
- [14] Carlos Casillas, "Heart Rate Monitor and Electrocardiograph Fundamentals" Freescale Semiconductor. Application Note, Document Number: AN4059, 3/2013.

Hairbrush for Psoriasis Scale Removal

Ravi kant kumar,
School of Electronics
Engineering, VIT
University, Vellore -14

Eunice Esther Lovely
School of Electronics
Engineering, VIT
University, Vellore -14

M, Arpita Kshirsagar,
School of Electronics
Engineering, VIT
University, Vellore -14

Dr. J.B.Jeeva* School
of Electronics
Engineering, VIT
University, Vellore -14
* jbjeeva @vit.ac.in

Abstract - Skin is the largest and vital organ for the protection of internal body from the outer environment. But due to the diseases of the skin, the protectiveness and hygiene of the internal body environment is at risk. Among the prevailing skin problems, psoriasis is being a widespread infection which causes irritation. Many people worldwide are suffering from psoriasis which is a recurring problem. In this paper we have developed a technique for the management of scalp psoriasis and skin psoriasis. People with scalp psoriasis are finding it difficult to take hair washes even once in a week. When high tension is applied on the scalp of patients with psoriasis, there is itching and finally bleeding. Therefore our technique consists of sucking the flakes without any bleeding with the help of a comb like vacuum device. With the help of this device, the vacuum created removes the unattached scalp flakes thereby providing a clean scalp. It also has an added feature of providing phototherapy from an arrangement of UV light emitting diodes integrated in the device which is safe.

Keywords - Skin diseases, Scalp psoriasis, phototherapy, UV-LED.

I. INTRODUCTION

Psoriasis is a dermatological condition in which the skin cells are multiplied 10 times faster than the normal cells. It can be called as an autoimmune disorder with patches of abnormal skin [2]. The common areas affected by psoriasis include the elbows, scalp and the knees, and it can also affect the torso, palms, and soles of the feet. The psoriasis can be of different type. There are 5 types namely Plaque psoriasis, Pustular psoriasis, Inverse psoriasis, Guttate psoriasis and Erythrodermic psoriasis. Amongst these the Plaque Psoriasis is most common one and it mainly affects the forearm, scalp, shin and areas around the belly.

Scalp psoriasis is a skin disorder which is a type of plaque psoriasis. In the affected areas the skin is little raised and appears somewhat reddish in colour with scaly patches. It comes up as a single patch or many, and it can even affect the full scalp. It can spread up to the forehead, the back of the neck, or back side of the ears [5].

Presently there is no cure for Psoriasis. However it can be controlled with the help of shampoo, medicines, oil, Phototherapy and some medication. Maintaining a clean scalp often becomes a challenge for affected people. So to help them

manage this condition we have designed a device which is a hairbrush that cleans the white scales and unattached patches of dead cells from the scalp. This device can also be used to provide phototherapy. Phototherapy can be classified into two types based on the area exposed namely whole body phototherapy and targeted phototherapy.

II. LITERATURE SURVEY

Psoriasis has its origin from the ancient times having different believes. The causes of psoriasis in the early days were thought of due to unbecoming nutrition, disorders in blood, etc. Even the exposure to sunlight causes increased complexity of psoriasis. The ancient people thought that psoriasis was the result of spiritual curse and treated persons affected with psoriasis with scorn. But in the period 460-377 BC, Hippocrates used coal tar as well as topical arsenic for the treatment of psoriasis to increase the skin's sensitivity to natural light. Galen was the first person to coin the word "psoriasis" meaning "to itch". The major breakthroughs in the history of psoriasis were that in the 1st century the classification of skin diseases was done by Jean Louis Ailbert. In 1809, psoriasis was recognized as a specific clinical entity by Dr. Robert William who devoted his life wholly to the study of skin. In 1836, world's first place devoted for the treatment of psoriasis was at Broome Street in New York by Henry Daggett Bulkley [4]. The misconceptions about psoriasis was made clear in 1960, by identifying psoriasis as an autoimmune condition. The treatments for psoriasis was classified into topical, systemic and phototherapy in 1970's. The genes that were responsible for psoriasis were identified in 1990's. In 1998, biologic medications were developed which acted on the enthusiastic immune cells which are the cause for psoriasis [6].

Many centuries ago, treatments by exposure to sunlight (heliotherapy) was performed by ancient Egyptians and Indians. Modern phototherapy can be dated back to 1895 when Neils Finsen treated lupus vulgaris by using a carbon arc. By the introduction of artificial UVB and dithranol by Ingram in 1953, the effectiveness of UVB to treat psoriasis was brought into light. The capability of narrowband UVB was proven by Weelden in 1984. Since then Excimer Lasers are being used in phototherapy. A specific class in phototherapy is targeted phototherapy which was first reported

for psoriasis in 1997 where it can be used to treat difficult areas like scalp, flexures and genitalia [5].

III. DETAILED PROBLEM DEFINITION

In the present scenario of treating scalp psoriasis there are medications such as shampoos, ointments, coal tar, etc. and phototherapy are available. Biologics are used in the first phase of treatment as they are readily available. But they are not approved to be used in children. There are risks associated with using them for a longer time as they cause malignancy and immunosuppressive effect. The response to medication also degrades with time. Also there is no commercially available product in the market as a device to treat psoriasis.

Phototherapy as a solution for Psoriasis treatment is a developing field in which research is going on. The difficulty comes in due to its high cost associated with a single use and that the patient has to visit the clinic whenever he wants the treatment to be done. This makes the procedure a little inconvenient. Taking all these difficulties into consideration, the proposed device uses a novel method to clean the scalp which will not produce any discomfort even in children. In addition to this, treatment through phototherapy is available in the same device which is cost effective, convenient to use and portable [4].

IV. SOLUTION METHODOLOGY

In order to reduce the side effects of medications in the treatment of psoriasis, two techniques have been used. These two techniques which are combined in a single device have been used effectively.

The first technique is the use of vacuum to remove the flakes of the scalp thus providing a clean scalp. The pressure applied on the scalp to suck the flakes is low so that the underlying blood vessels are left undamaged. Thus flake removal through vacuum suction can be used on a daily basis as it is easy to handle, ready to use, low power is consumed and there is no occurrence of erythema.

The next technique that has been utilized is the treatment through phototherapy. This is one of the developing fields that are of interest among the dermatologists. It is generally described as the use of light in a therapeutic way by the application of light energy on the skin. When the skin is exposed to light, there is absorption of photons in the chromophores and finally biochemical reactions takes place in the skin by the absorbed energy. UVA and UVB are the mainly used sources based on their biophysical properties. Since UVA has a long wavelength and low energy radiation, it penetrates into the dermis. Whereas the UVB has short wavelength and high energy radiation penetrates the epidermis to the upper dermis. The UVB produces a stronger immunosuppressive effect and the DNA is damaged by photoproducts released by UVB and hence UVB is used in this paper [1].

In this paper targeted phototherapy has been adopted due to its various advantages. Targeted phototherapy is where only the diseased skin is exposed, thereby the surrounding normal and healthy skin are unaffected by irradiation. The device that has been used to provide light energy is UVB-LED, a low power output device. With the use of UVB-LED, the skin's adaptive immune responses are suppressed and there is induction of photo-adaptation. Since the targeted phototherapy narrows down its exposure to only diseased skin, it is possible to provide UVB for long duration without affecting the nearby skin [3].

V. DESCRIPTION

A. Materials used

As the scalp affected by psoriasis is very sensitive, the material used for the hairbrush is very important. While considering this it was the bristles which was going to be in direct contact, so the material used for bristles should be very soft so that it won't cause bleeding of the scalp blood vessels. The material that we used for the bristles were plastic straws.

The Material that can be used for the manufacture of bristles used should be antistatic rubber. These bristles would be hollow so that they can suck the scalp flakes. It should also be flexible and tough. It was the body of the brush that will house the vacuum suction unit and phototherapy unit composed of UV-B LED. The body of the brush should be made of shock absorbing materials. Materials can be used such as ebony, ABS plastic, nylon etc.

B. Construction and Working

The parts involved in the device were an electric motor, fan, a dust bag, UV-B LEDs, and input port with hollow bristles as shown in Fig.1 When the power was switched ON, the motor turned ON. The motor was used to drive the fan with angled blades. As the blades of the fan rotated they forced the air in forward direction thus the density of the particles in the front side of the fan increased and the density at the back of the fan reduced. This pressure imbalance created suction at the front port. Thus the air was pushed into the intake port and out through the exhaust space. So as long as the fan was running the suction action continued at the intake port. As the input port was attached to the bristles, the bristles caused the suction of white scales when used on scalp.

In between the bristles were the LEDs to provide phototherapy as shown in Fig.2. A switch controlled the use of LEDs so that when it was desired to have phototherapy, this switch was turned ON. The power supply for this phototherapy unit was taken from the same power supply unit that was used for driving the motor.

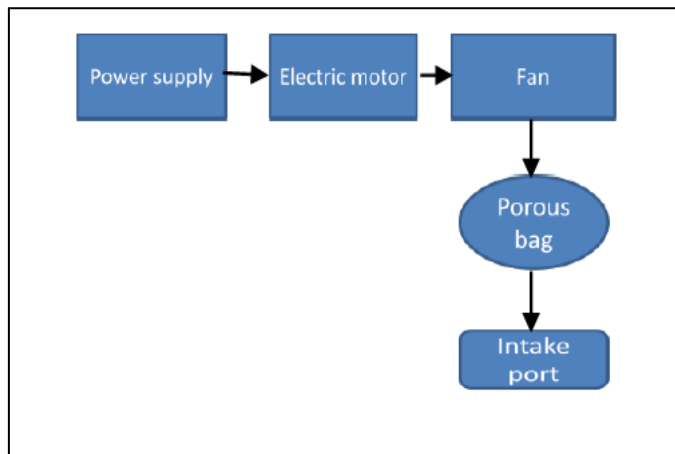


Fig.1 Block Diagram for Vacuum Suction

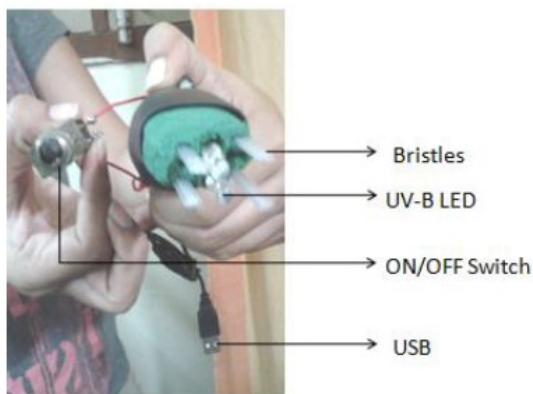


Fig.2 Proposed Device

VI. RESULTS AND DISCUSSIONS

Thus we have successfully implemented the proposed device. This device can clean the scalp by using suction delivered through bristles. An experiment was done in order to determine the maximum particle size that can be sucked by the bristles. It was found that the bristles were able to suck approximately particles that were 3mm in size.

Also the device successfully delivered targeted phototherapy via the UV-B LEDs in the wavelength range of 311-315nm

This hairbrush can be of great use to scalp psoriasis patients to help them maintain a clean scalp. We took the opinion of a dermatologist on the proposed device. According to him it would be of real help to psoriasis and Seborrheic dermatitis patients.

The light delivered by the LEDs is of less power than the available phototherapy lamp, hence it does not produce any heating effect on the scalp. Also the proposed device is portable, easy to use, cost effective, small, and has good tolerability, comfortability and safety.

VII. FUTURE SCOPE

Combination Therapy is useful to treat any kind of psoriasis provided it is a right combination of drug with phototherapy. The therapy is combined in order to increase the clinical response and also the safety associated with phototherapy. Certain combinations like UVB with coal tar causes stains on the area applied, smell and has carcinogenic characteristics. UVB with dithranol though is irritative on the scalp, has higher efficacy than tar. But the effect of UVB with ichthyol has found to be good and it also has several advantages such that it reduces erythema, produces no irritation on the skin and has anti-septic, anti-inflammatory and anti-pruritic properties. Hence addition of a separate port for the delivery of drugs and oil will be attached to the proposed device in the near future.

VIII. CONCLUSION

Patients with scalp psoriasis find it very difficult to take care of their scalp and maintain it without scalp flakes. Use of normal comb would aggravate their sensitive skin on the scalp, since the blood vessels beneath the skin are swollen. With the use of the proposed device this disadvantage of the normal comb can be overcome and the scalp can be clean from flakes on a daily basis. Also the treatment of phototherapy through UV-B LED is a cost effective way and patients can use them at home without the aid of others. Patients can be convenient to use this and no visit to hospital for undergoing phototherapy is required.

REFERENCES

- [1] Alshiyab D, et al, "Targeted Ultraviolet B Phototherapy : Definition, Clinical Indications And Limitations", *Clinical And Experimental Dermatology*, 2015, 40, pp 1-5.
- [2] Farber EM, Nall L, "Natural history and treatment of scalp psoriasis", *cutis*, 1992, 49:396-400.
- [3] Medhat El Mofty, et al, "What is new in phototherapy?", *Journal of Egyptian Women's Dermatologic Society*, 2016, 13:1-6.
- [4] Nina Benakova, "Phototherapy of Psoriasis In The Era Of Biologics: Still In", *ActaBermatovenerot Croat*, 2011, 19(3):195-205.
- [5] Van de Kerkhof PC, Franssen ME, "Psoriasis of the Scalp, Diagnosis and Management", *American Journal of Clinical Dermatology*, 1998, 197:326-34.
- [6] Venkataraman Mysore, "Targeted Phototherapy", *Indian Journal Of Dermatology, Venereology And Leprology*, March-April 2009, Vol 75, Issue 2.

Design of contactless power transfer for Artificial heart

Lidhiya Daniel

*Department of Biomedical
engineering*

Sathyabama University, Chennai
lidhiya2017@gmail.com

Thukkaram Sudhakar *

*Department of Biomedical
engineering*

Sathyabama University, Chennai
corresponding author-
drsudhakar35@gmail.com

Sheeba Abraham

*Department of Biomedical
engineering*

Sathyabama University, Chennai
sheeba8581@gmail.com

Abstract - The transcutaneous power transfer for the artificial heart can be done by the principle of mutual induction. The primary coil and secondary coil present in this transformer should be positioned in such a way to enable the transfer of power from transmitter section to the receiver section wirelessly. The mutual induction process will take place when we keep both the coils parallel. The receiver coil should be positioned inside of the body and transmitter coil should be positioned outside of the body. The voltage regulator will provide or regulate the required output voltage. The Bluetooth technology is used here to observe the charging level of the battery. The inductive power transfer method eliminates the should risk of infection caused due to surgery.

Keywords: Transcutaneous transfer, Mutual induction, pacemaker, Improved mobility, Magnetic flux.

I. INTRODUCTION

In our modern world, the need for wireless electricity is very essential. It helps us in various applications. The concept of wireless electricity can be applied in the healthcare field. Here in this paper, we are able to charge the battery of a pacemaker transcutaneously using mutual induction phenomenon [1]. Mutual induction is the process in which an emf is induced in one circuit when the other circuit is arranged parallel [6]. Wireless power transfer is the process of transferring the energy from its origin into a load without any direct contact. Moreover here the process of wireless power transfer is achieved transcutaneously. It would be helpful for the patients to transfer the energy to the implanted device without any surgery. We need a transcutaneous transformer for the power supply and its secondary coil should be implanted in the body and primary should be kept above the secondary on the exterior body [4]. The distance between the primary coil and secondary coil is directly proportional to the thickness of patients skin. Some transformer has a large air gap between the two coils and it has so much leakage inductance. Hence it can be used for various purposes and it

eliminates the need for wires or cables. This eliminates the risk of infection caused as a result of surgery.

II. LITERATURE SURVEY

H.Y. Leung and team from University of Auckland, New-Zealand made a study about the wireless power system which is used for implantable heart pumps based on energy injection control. Here in this system there is a half bridge energy injection circuit. No extra power components are needed here and it is achieved by using the method of injection of energy into the tank whenever we needed and also it has the presence of air coiled coils [7].

O. Knecht et.al discussed the need of using inductive power transfer for the transcutaneous applications. Transcutaneous energy transfer and the energy losses are the major topics discussed here [6].

Anil Kumar et al discussed wireless power transmission by using the principle of Mutual induction and the loss of power during transmission and they also discussed technological improvements in wireless power transmissions [2].

III. EXISTING SYSTEM

The battery cannot be recharged because it can be used only once. It will be very difficult for the patients to afford high - cost for the surgery each time at the time of battery replacement. Battery level is unknown to the patient because there will not be any record maintained about the pacemaker's battery after the surgery.

IV. DISADVANTAGES

The existing system consists of complex and periodic surgeries for the recharging process. The varying transformer values make the control very difficult in order to gain output voltage regulation when the load varies. There is no visible efficiency and rechargeable batteries are used here. Surgery is

unavoidable. Mobility of the patient gets affected and there is a risk of infection caused by the surgery and the charging level of the battery cannot be obtained.

V. PROPOSED SYSTEM

Battery is rechargeable and can be used multi times. It is a single surgery process and doesn't need to do any surgeries afterward for recharging battery as this can be done wirelessly and transcutaneously and there is less cost for surgery as it is a single process.

VI. ADVANTAGES

Surgery can be avoided for replacing the battery. We can increase the wireless charging distance by adjusting the coils. The charge level can be displayed and cost of surgery is very less. It can stop charging once the battery gets fully charged. The patients improved mobility after the battery recharging process is an important advantage. The wireless power transfer through the skin does not cause any side effects to the body.

VII. BLOCK DIAGRAM

7.1 TRANSMITTER SECTION

TRANSMITTER SECTION

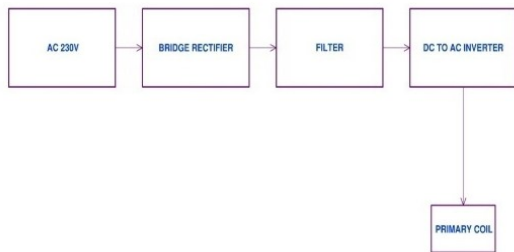


Fig.1 Block diagram of transmitter section

7.2 RECEIVER SECTION

RECEIVER SECTION

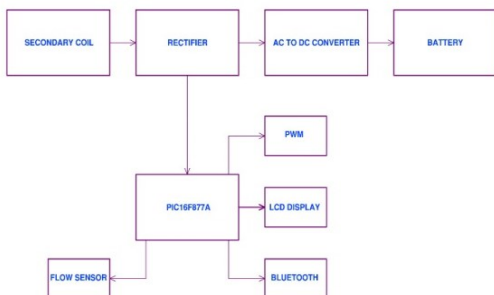


Fig.2 Block diagram of receiver section

VIII. MODULE DESCRIPTION

The proposed transformer prototype model consists of a transmitter coil section and a Receiver coil section. The transmitter section consists of 230v power supply, bridge rectifier, filter, DC to AC converter and transmitter coil. The transmitter coil provides an ac current and it creates a magnetic flux and the bridge rectifier helps in the conversion of ac input to dc output [5].



Fig.3 Flow sensor

The receiver section consists of receiver coil, pic16f877a, microcontroller, max 232, Bluetooth, flow sensor.

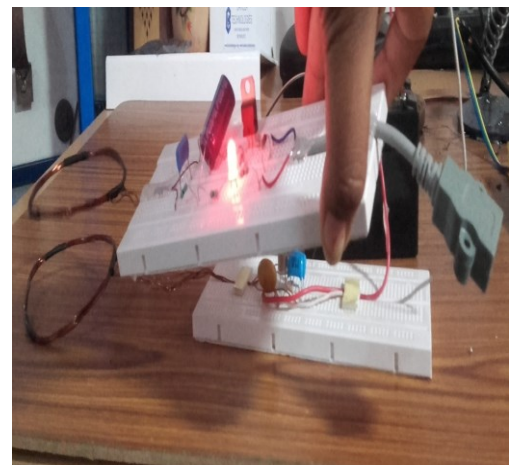


Fig.4 LED glowing in wireless power

The 230V AC current will be converted into 12V DC current using bridge rectifier. The 12V DC current is supplied into the circuit and it converts 12V DC to 5V DC is supplied

into the battery. The magnetic flux from the transmitter section will be received by the receiver section. The Bluetooth used here will transfer the recharging rate to the mobile phone. There is a flow sensor attached to the microcontroller and it is used to measure the rate of flow of blood. This wireless power is used for recharging the battery.

IX. METHODOLOGY AND PERFORMANCE

In this proposed system, the energy transfer is achieved by means of mutual induction among two coils of a transformer kept parallel in face to face direction. The mutual induction leads to an electric flux. The transmitter coil is leaked with an alternating current and when the receiver coil is kept near to the former coil which causes the passing of wireless current. Then the transformed energy can be rectified and filtered to remove ripples and the filter voltage is used to recharge the battery. The battery status is continuously monitored and transmits to the patient's mobile phone through Bluetooth and it shows the level of the battery charge that would be very useful for the patient.

X. SAFETY MEASURES

The wireless power from the transmitter coil should transmit transcutaneously through the distance created by garments, dermis, body fluids etc and it should not cause any power loss and here we are able to reduce the power loss by increasing the efficiency of the coils and even the higher frequencies will interrupt the operation. Another problem is caused due to the wrong positioning of primary and secondary coils and we can eliminate this risk by the use of a flow sensor which can monitor at periodic intervals to make the patients aware.

XI. RESULT

Our aim of the project is to replace the pacemaker implanted patient's surgery by introducing a wireless power transfer method for recharging the battery. We achieved it by using a Mutual induction process. The lithium carbon monofluoride battery is proved for the high density in comparison with other batteries. In this project prototype contactless power transfer model is used for charging. The monitoring of battery level is obtained successfully using a microcontroller, LCD and Bluetooth.

XII. CONCLUSION

The contactless power transfer method for recharging the battery of a pacemaker is achieved through mutual induction process using prototype transformer phenomenon.

ACKNOWLEDGMENTS

We would like to convey our deep sense of gratitude to all those who helped us a lot throughout the course of our work. We thank God Almighty for his grace and mercy that allowed me in the completion of the project.

REFERENCES

- [1] Anand Garg, Lakshmi Sridevi, "Transcutaneous Energy Transmission Based Wireless Energy Transfer to Implantable Biomedical Devices", *International Journal of Innovative Research in Science, Engineering and Technology (IJIRSET)*, Vol.4, Issue 6, pp. 4934 -4938, June 2015.
- [2] Anil Kumar, Rjbir, Arshee Siddqui, "Wireless Power Transmission using Mutual Inductance", *International Journal of Engineering Science and Computing (IJESC)*, Vol 6, Issue No 6, pp. 6301 -6304, June 2016.
- [3] Anisha Cotta, Naik Trupti Devidas, Varda Kalidas Naik Ekoskar, "Wireless Communication using HC-05 Bluetooth Module Interfaced with Arduino", *International Journal of Science, Engineering and Technology Research (IJSETR)*, Vol 5, Issue 4, April 2016.
- [4] Cong.P,N. Chaimanonart,W, H,KO and D.J. Young, "A wireless and Batteryless 130mg 300mw 10b implantable Blood pressure sensing Microsystem for Realtime Genetically engineered Mice Monitoring", *IEEE Transactions on Dig. Tech paper*, 2009.
- [5] Gyu Bum Joung, Bo H.Cho, "An Energy transmission system for an Artificial Heart using Leakage Inductance compensation of Transcutaneous Transformer", *IEEE Transactions on power electronics*, Vol 13, No 6, pp. 1013 -1022, Nov 1998.
- [6] Knecht.O, R.Bosshard, J.N.Kolar and C.T.Starck, "Optimization of Transcutaneous energy transfer coils for high power medical applications", *IEEE Proceedings on control and modelling for power electronics*, pp.p 2-7 1-10, June 22-25, 2014.
- [7] Leung.H.Y, D.M.Budgett, D.Mccormick and A.P.Hu, "Wireless power system for implantable heart pumps based on energy injection control", *Progress in electromagnetic research symposium proceedings Moscow*, pp. 445-449,Aug 19-23,2012.
- [8] Matsuki.H and M.Shiki, "Investigation of coil geometry for transcutaneous energy transmission for artificial heart", *IEEE Trans Magazine*, Vol 28, no 5, pp. 2406-2408, 1992.
- [9] Myers.G.H, G.E.Reed, and A.Thumin, "A transcutaneous power transformer", *IEEE Amer .soc. Artif .Int. Organs*, Vol.14, pp.210-214,1968.
- [10] Schuder.J.C, J.H.Gold, and H.E.Stephenson, "An inductively coupled RF system of the transmission of 1 KW of power through the skin", *IEEE Trans.Bio-Med.Eng.*, Vol.21, pp.612-627, 1983.
- [11] Tarique Salat, Shilpak Raich, Supriya Mahta and Shilpa Togarwar, "A wireless Battery charger for Mobile device", *International Journal of Emerging Trends and Technology in Computer Science(IJETTCS)*, Vol 2, Issue 3, pp.103-105, May-June, 2013.
- [12] Yambe.T, M.Yoshizawa, K.Abe, A.Tanaka, H.Takeda, S.Nitta, "Making Chaos with an artificial heart system", *IEEE Trans .Bio-Med.Eng.*, vol 20,no 3,pp.1561-1564,1998.

Embedding Pressure Sensor in a Footwear for checking the weight distribution during Standing

Nikita Ghosh,
SENSE, VIT University,
Vellore – 14.

Saheli Guha,
SENSE, VIT University,
Vellore – 14.

Sharmila Nageswaran*
SENSE, VIT University,
Vellore – 14.

Abstract: Foot is the basic supporting system of the body. It will bear the weight of body structure and helps us in static and dynamic stability. In our day to day activity, the people from various professions like surgeons, lecturers or common people have a tendency to shift their whole body weight to one foot unknowingly which can cause excess wear and tear in leg. So, if we can design a footwear which can alert the users when there is a distribution of weight mismatch between two legs, it would be of a great clinical need at this hour.

Keywords: *Static stability, Dynamic stability, Wear and tear*

I. INTRODUCTION

Foot is the important anatomical structure which helps us in maintaining surface of interaction with ground. During standing, everyone should maintain stance and stride position for good base of support when equal weight of the body will be evenly distributed in both legs. But, many of the people concentrate their whole body weight to one foot unknowingly which can be the cause of sore feet, heel pain, heel spurs, varicose veins, lower limb problems, back pain, neuropathy, numbness in the neck and shoulder muscles and other health problems. For improvising this situation, in this paper we aim in embedding pressure sensors in footwear to check the distribution of weight during standing.

II. LITERATURE SURVEY

In a research article presented by Stacy J. Morris,[1] the work represents the initial phase of designing an in-shoe sensor system for the evaluation of balance. For this purpose, they strategically mounted a removable insole with sixteen force sensitive resistors and then they recorded the bilateral output. The output confirmed that the sensors can detect small changes during weight distribution of the subject. By analyzing the data, they concluded a strong correlation between

the capability to balance and the condition of health of the subject.

According to Lin Shu [2], for the pathology diagnosis of foot and gait analysis, spatial and temporal plantar pressure distributions are very useful measures. But, plantar pressure measurement systems analysis is more expensive and not comfortable to wear. So, this work present a noble measurement and system analysis for plantar pressure based on the sensor array's textile fabric, which are light weighted, soft and has a very efficient high-pressure sensitivity along with strong durability. The sensors were connected by conductive yarns with a soft polymeric board and mounted into an in-sole. The acquisition system gets wireless transmission of the acquired data with the insole to remote the receiver through the Bluetooth path. These modes of configuration were employed to gain connection with the desktop, laptop, or smart phone, which were configured to work comfortably in research laboratories, hospitals and sport grounds as well as other suitable environments. A real-time display and software analysis are represented to measure different important parameters like mean pressure, peak pressure, center of pressure (COP) and shift speed of COP. Experimental output confirmed that this system is compatible with both dynamic as well as static measurements.

According to another review paper [3], the plantar foot pressure that measures the action between the supporting surface and the foot during every day activity is important in gait as well as posture diagnosing several lower limb problems related to footwear designing and sports biomechanics. A wireless plantar foot pressure measurement was proposed which was suitable for the measurement of high pressure distribution that lies under the foot with high reliability as well as accuracy.

Hence, we should consider different zones of foot pressure, step length and stride length during gait cycle when embedding the pressure sensors in footwear.

III. DETAILED PROBLEM DEFINITION

A person's body is affected by the arrangement of the work area and by the tasks that he or she does while standing. The environment of the workstation, the tools, controls and displays that the worker needs to operate or observe will limit the body positions while standing. As a result, the persons from various professions like sales man, lecturer, traffic surgeons has fewer body positions to choose from, and the positions themselves are more rigid. This gives them less freedom to move around and to rest working muscles. This lack of flexibility in choosing body positions will cause the improper distribution of body weight in both the legs those results in excess wear and tear in either of the leg. So if we can embed pressure sensors in footwear which can measure the weight between two legs and alert the users when there is a distribution of weight mismatch between two legs, it would be of a great clinical need at this hour.

IV. SOLUTION METHODOLOGY

1. According to the above circuit diagram, we have mounted the required components on the bread board.
2. Here we are using pressure sensor which works on 5V battery power having model no FSR400 and can withstand weight up to 10kg.
3. The output of the pressure sensor is connected to the 10K resistor. The output of the resistor goes to Arduino UNO board.
4. Arduino board operates on 9V battery.
5. The Uno is a microcontroller board based on the ATmega328P. It has 14 digital input/output pins, 6 analog inputs, a 16 MHz quartz crystal, a USB connection, and a power jack.
6. We are using Arduino UNO which operates in COM4 mode of the software.
7. The output of the Arduino UNO will be connected to the buzzer which can alert the user when the pressure exceeds the certain threshold value

V. COMPONENTS REQUIRED

TABLE I. COMPONENTS USED

Specifications	Values/ Model	Quantity
Pressure sensor	FSR400	2
Resistor	10K	2
Resistor	56K	2
Resistor	1K	1

Resistor	2.7K	1
OP-AMP	LM358	2
Arduino	ATMega328	1

A. Op-Amp

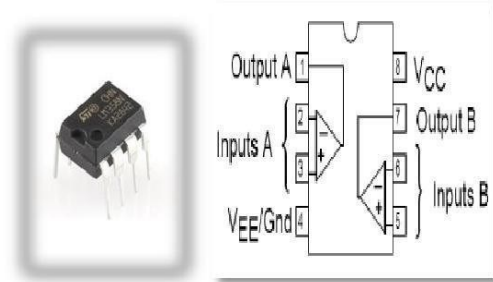


Fig. 1: a) LM358 [7] and b) Pin diagram of the Op-Amp [8]

B. PRESSURE SENSOR

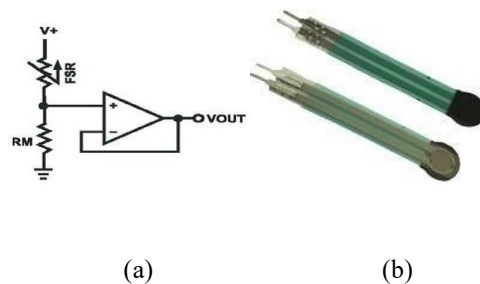


Fig. 2 a) circuit of the pressure sensor and b) FSR400 pressure sensor.

C. CIRCUIT DIAGRAM

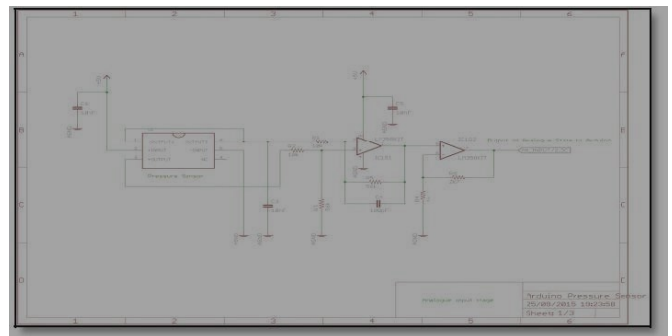


Fig 3: Circuit diagram [9]

For designing the foot wear, we have studied the different pressure zones in foot which is measured by the digital scanner. The red colored area corresponds to highest pressure zones, whereas the lowest pressure areas are indicated by yellow color.

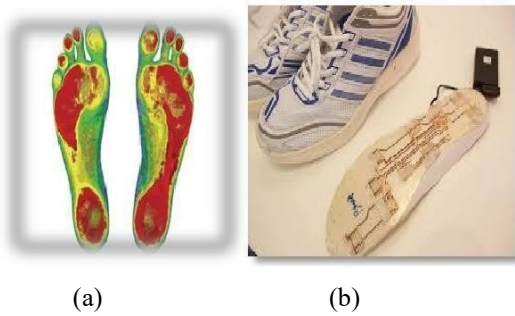


Fig 4: a) Digital Foot Print showing the area's with maximum foot pressure [10] and b) embedded pressure sensor in the shoe [11]

VI. ARDUINO CODING

```

const int analogInPin =
A1; int sensorValue = 0;
float outputValue = 0;
void setup()
{
  Serial.begin(9600);
}

void loop()
{
  sensorValue = analogRead(analogInPin);
  outputValue = map(sensorValue, 15, 1032, 0,
150);
  Serial.print("SENSOR = ");
  Serial.print(SENSORVALUE);
  Serial.print("\tOUTPUT = ");
  Serial.println(OUTPUTVALUE);

  delay(1000);
}
    
```

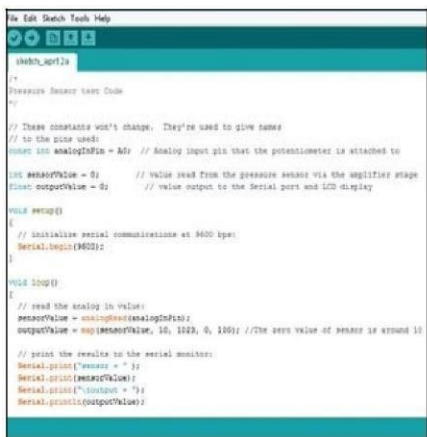


Fig 5: Arduino Coding.

VII. DISCUSSION AND RESULTS

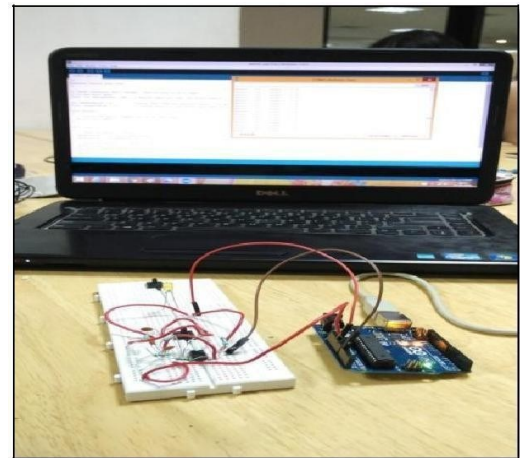


Fig 6: The module connected to the monitor.

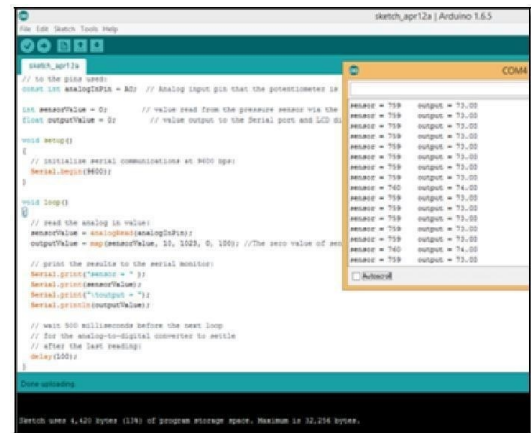


Fig 7: The output seen in Arduino software.

Till now, we have only worked with the sensing part of the circuitry. We are yet to achieve the quantization part. By analyzing the results in Arduino, we see that there is a minor change in voltage variation when are applying pressure into the pressure sensor. When we will place the circuitry in the footwear and exert pressure, then it will show huge variation. The foot which is having more pressure than the threshold value, will alert the user by buzzer system. This system can actually give awareness to the users who have a tendency of shifting weight in one leg and prevent excess wear

REFERENCES

- [1] Stacy J. Morris Bamberg, Member ,IEEE,Paul LaStayo, Lee Dibble, Josh Musselman, and Swama Kiran Dasa Raghavendra(2006), Development of a Quantitative In-Shoe Measurement System for Assessing Balance: Sixteen Sensor Insoles, pp-6041- 6044
- [2] Lin Shu, In-Shoe Plantar Pressure Measurement and Analysis System Based on Fabric Pressure Sensing Array(2010), volume:14, issue:3, pp-767-775
- [3] Abdul Hadi, Abdul Razak, Aladin Zayegh, Rezaul K Begg and Yufridin Wahab, Foot Plantar Pressure Measurement System: A review(2012), pp-988-1012.
- [4] M.J. Mueller, "Application of Plantar pressure assessment in footwear and insert design", J.Orthop.Sports Phys. Therapy, vol.29, no. 12, pp.747-755, 1999.
- [5] E.C. Frederick and K.P. Hartner, "The evolution of foot pressure measurements", Sens. Mag, vol. 10, no. 6, pp. 30-35, 1993.
- [6] R.M. Queen, B. B Haynes, W.M. Hardaker and W.E Garrett, Jr. "Forefoot loading during 3 athletic tasks", Amer. J.Sports Med, vol .35, no.4, pp-630- 636, 2007.
- [7] <https://www.sparkfun.com/products/9456and>
- [8] <http://www.neoembedded.com/lm358-dip.html>
- [9] <http://langster1980.blogspot.in/2014/11/how-to-use-pressure-sensor-with.html?m=1>
- [10] <http://clearchoicechiropractic.com/2010/10/28/orthotics/>
- [11] http://www.hkita.com/html/commopportunities_detail.php?id=120

Experimental Investigations on Capacitive Imaging of Biological Materials

A. S. Sahana
Department of Instrumentation
Engineering,
MIT Campus, Anna University,
Chennai, India.

A. Paramasivam,
Department of Instrumentation
Engineering,
MIT Campus, Anna University,
Chennai, India.

K. Kamalanand
Department of Instrumentation
Engineering,
MIT Campus, Anna University,
Chennai, India

Abstract—Soft tissues found all over our body are highly deformable structures having varied structural arrangements, constituents and composition. Since soft tissues are not easy to handle, tissue mimicking phantoms have been developed that mimics the properties of biological tissues. In this work, an attempt has been made to design a capacitance sensor array for capacitive imaging of biological materials. Further, tissue mimicking Agar-Agar phantoms was developed for testing the developed sensor. In this paper, the objectives, methodology and the observations are presented.

Keywords—soft tissues, tissue mimicking phantoms, capacitance sensor array, agar-agar.

I. INTRODUCTION

Soft tissues are the group of tissues which bind, support and protect the human body. Human soft tissues are highly deformable, and its mechanical properties vary significantly from normal and diseased conditions. Their electrical and mechanical behavior is strongly related to the concentration and structural arrangements. Hence, identification and imaging of the electrical and mechanical properties of soft tissues is highly useful for diagnosis of several diseases [1].

Measurement of capacitive properties of soft tissues suffer from several uncertainties like variable dielectric properties of the test item and environmental conditions. The test results of the dielectric parameters depend on the geometry, chemical composition, morphology and topography [2].

Phantom materials are used for reproduction of the material properties of the real materials under investigation. Tissue mimicking phantoms are materials which are similar to some real soft tissues. Many tissue mimicking phantoms are being developed and researchers have emphasized that these tissue mimicking phantoms play important roles in research on biomedical applications [3, 4].

The objectives of this work is to design a capacitance sensor array for analyzing and imaging the dielectric characteristics of biological materials, using the developed tissue mimicking phantoms

II. METHODOLOGY

A. Design of capacitance sensor array

Size and spacing of the capacitive sensor are both very important to the sensor's performance. A single sided copper clad board is utilized for the sensor design. Required array design is drawn on the board using an etch resistant marker. The single side copper clad board and the marked array design is shown in the Figure 1. Ferric chloride etching solution is used for etching. The board with copper side up is put into a container filled with the etching solution. The exposed copper begins to dissolve and it takes 15-20 minutes for all the exposed copper to dissolve. The marker marks can be removed using thinner to expose the copper clad circuit. The Figure 2 shows the Etch resistant marking and the developed sensor array after the etching process.

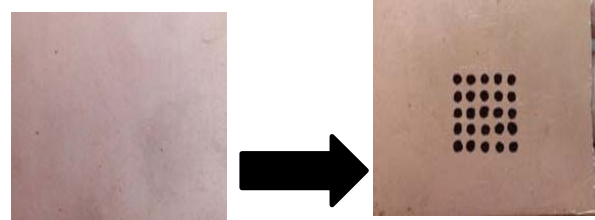


Fig 1. Copper clad board and etch resistant marking for the required sensor array.

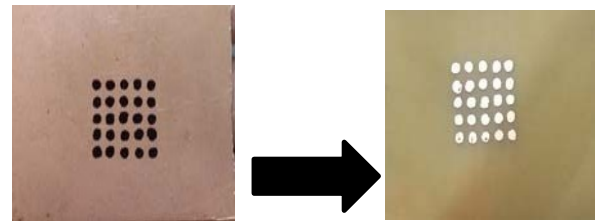


Fig 2. Etch Resistant Marking on the Copper Board and the Developed Sensor Array using Ferric Chloride Solution.

Finally, the 5x5 matrix array on the copper board was obtained after etching as shown in Figure 3.



Fig 3. 5x5 capacitive Sensor Array

The designed sensor array along with another metallic plate (ground plate) acts as a capacitance sensor array. When the material to be analyzed is placed in between the two plates, it acts as dielectric medium. Using this prototype, we can obtain the dielectric characteristics of the given material. A LCR meter is used to obtain the capacitance values from the sensor.

B. Generation of tissue mimicking Agar-Agar phantoms

Agar-Agar is a jelly-like substance, obtained from Polysaccharide Agarose. Agar is a promising material for preparing tissue phantoms [5]. To prepare the phantom, Agar powder (1 gram) is taken and mixed well with 50 ml of distilled water. This forms 2% of Agar solution. A magnetic stirrer is used to achieve uniform distribution. After complete mixing, the mixture is set to boil. When the mixture attains the boiling temperature, they are poured separately in different molds and set to cool. After 5 - 10 minutes, the mixture gets cooled at room temperature and forms as a gel material for mimicking soft tissues. The prepared Agar-Agar gel material is shown in the Figure 4.



Fig 4. The prepared Agar-Agar phantom.

III. RESULTS AND DISCUSSION

The normalized capacitance matrix with cotton fabric as the dielectric medium, at 120 Hz is presented. Measurements were made using an LCR meter:

$$C = \begin{bmatrix} 0.97 & 0.97 & 0.98 & 0.98 & 0.97 \\ 0.97 & 0.96 & 0.97 & 0.97 & 0.97 \\ 0.97 & 0.98 & 0.97 & 1 & 0.97 \\ 0.96 & 0.97 & 0.97 & 0.97 & 0.98 \\ 0.98 & 0.98 & 0.97 & 0.98 & 0.96 \end{bmatrix}$$

Similarly rubber material was analyzed by LCR meter and the normalized capacitance matrix is shown below

$$C = \begin{bmatrix} 0.92 & 0.92 & 0.95 & 0.97 & 0.95 \\ 0.92 & 0.92 & 0.92 & 0.92 & 0.92 \\ 0.92 & 0.95 & 0.97 & 1 & 0.92 \\ 0.92 & 0.92 & 0.92 & 0.92 & 0.95 \\ 0.95 & 0.95 & 0.92 & 0.95 & 0.92 \end{bmatrix}$$

Further, the prepared Agar-Agar phantom was analyzed by the capacitance sensor and the capacitance values were obtained at 1 KHz in. The normalized capacitance matrix is presented below

$$C = \begin{bmatrix} 0.78 & 0.77 & 0.90 & 0.82 & 0.68 \\ 0.77 & 0.86 & 0.88 & 0.93 & 0.88 \\ 0.99 & 0.79 & 0.80 & 0.92 & 0.88 \\ 0.77 & 0.93 & 0.88 & 0.78 & 1 \\ 0.90 & 0.85 & 0.99 & 1 & 0.77 \end{bmatrix}$$

Finally, the capacitance image of the Agar-Agar phantom is shown in Figure 5. Variations in intensity values are observed at different regions of the image which may be due to the topographical variations and variations in the concentration of agar in the phantom. Results demonstrate that the presented method may be efficient in imaging the topography, morphology and chemical composition of the biomaterial under analysis.

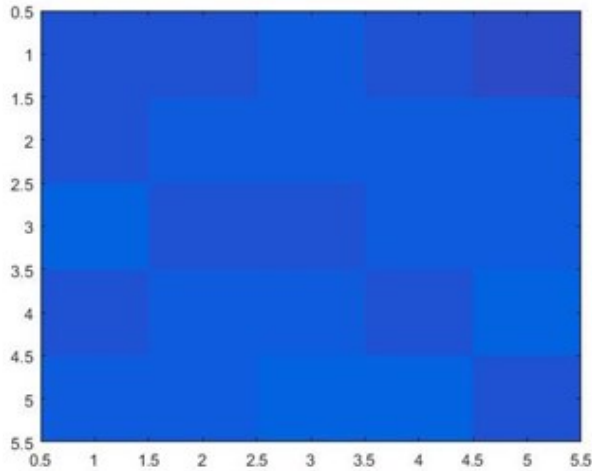


Fig 5. The capacitance image of the developed agar-agar phantom

IV. CONCLUSIONS

In this work, an attempt has been made to develop a suitable capacitance sensor array for imaging and analyzing the biological materials. The sensor consists of a 5x5 matrix sensing array. The array size and spacing can be increased according to our convenience. Using this designed sensor array, ground plate and LCR meter; the capacitance values can be obtained and the capacitance image is formed. For the analysis of biological materials, a tissue mimicking phantom namely the Agar-Agar gel has been developed.

Results demonstrate that the sensor is efficient in imaging the features of biological materials. This work appears to be of high significance since the developed capacitance sensor may further be used for analyzing the non-homogeneity in biological materials.

REFERENCES

- [1] Holzapfel, G. A. (2001). Biomechanics of soft tissue. The handbook of materials behavior models, 3, 1049-1063.
- [2] Assender, H., Bliznyuk, V., & Porfyrakis, K. (2002). How surface topography relates to materials' properties. *Science*, 297(5583), 973-976.
- [3] Kamalanand, K., Sridhar, B. T. N., Rajeshwari, P. M., & Ramakrishnan, S. (2010). Correlation of Dielectric Permittivity with Mechanical Properties in Soft Tissue-Mimicking Polyacrylamide Phantoms. *Journal of Mechanics in Medicine and Biology*, 10(02), 353-360.
- [4] Krishnamurthy, K., Sridhar, B. T. N., Rajeshwari, P. M., & Swaminathan, D. R. (2009). Correlation of Electrical Impedance with Mechanical Properties in Models of Tissue Mimicking Phantoms. In *13th International Conference on Biomedical Engineering* (pp. 1708-1711). Springer Berlin Heidelberg.
- [5] Earle, M., De Portu, G., & DeVos, E. (2016). Agar ultrasound phantoms for low-cost training without refrigeration. *African Journal of Emergency Medicine*, 6(1), 18-23

FPGA based emotions recognition from speech signals

B. Rajasekhar

Ph.D. Scholar, JNTUA &
Associate Professor, ECE Dept.
Gudlavalleru Engineering College
Gudlavalleru, India

M. Kamaraju

Professor & HoD, ECE Dept.
Gudlavalleru Engineering College
Gudlavalleru, India

V. Sumalatha

Professor & HoD, ECE Dept.
JNTU College of Engineering
Ananthapuramu, India

Abstract - Emotion recognition from speech signals has abundant applications in daily life. Particularly in speech-based human machine interaction it is used for improving the naturalness. Speech based emotion recognition is done in two steps namely Gender Recognition and Emotion Recognition. Gender Recognition will give the information about the gender (Male or Female) of the speaker and Emotion Recognition extracts the emotion (happy, sad, angry, and lazy etc.) of the speaker. In emotion recognition step back propagation algorithm under ANN is used as a classifier for classifying the emotions. In this paper, proposes emotion recognition from speech signal using Artificial Neural Networks (ANN) and implemented on FPGA device. The results using ANN are compared with the existing method and observed that ANN has lesser space utilization and improved speed than LDA.

Keywords: Artificial Neural Networks (ANNs), Latent Dirichlet Allocation (LDA).

I. INTRODUCTION

There are many ways of communication between the two human beings among them speech [1] has been proven to be a good indicator of emotional content. In speech based emotion recognition, emotions of the speaker are identified from the given input speech signal. Some of the emotions of the speaker are happy, sad, angry, and lazy. In emotion recognition from speech system, the main objective is to choose the algorithms in order to represent the emotions with good accuracy and less implementation complexity. The speech based emotion recognition system has many applications like medical, security and surveillance [2][3].

The emotion recognition from speech system block diagram is shown in Fig. 1. It consists of four blocks namely Feature extraction, Post processing, Modeling and Recognition.

Over the past years many methods have been proposed for speech feature extraction [20]. All these methods are classified on the ability to use information about human auditory processing and observation, by the robustness to distortions. Human speech is highly redundant and has many speaker-dependent features like pitch, speaking rate and accent [21].

In Feature extraction the features like energy, pitch and frequency coefficients of the speaker are extracted. To provide the good representation of emotional content [4] in speech signal the parameters like activation, valence, and dominance are also considered.

Post processing is used for dimensionality reduction of the speech signal.

The main objective of the emotion recognition from speech is based on choosing the best classifier which gives the best results in emotion recognition framework. The different classifiers available are Hidden Markov Model (HMM) [5], Gaussian Mixture Vector Auto Regressive models (GMVAR) [6], Latent Dirichlet Allocation (LDA) model. LDA is the generative probabilistic model for document preparation which creates one document.

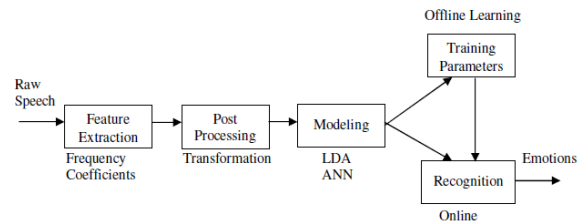


Figure 1. Speech Emotion Recognition System

As each document is divided into topics and every topic is further divided into words and every word is further divided into vocabulary. Similarly in speech emotion recognition framework, speech signal is taken as one document and in that Gender recognition and Emotion recognition are taken as topics. In Gender recognition topic male and female are considered as words, similarly in Emotion recognition topic happy, sad, angry, and lazy are considered as words.

II. ARTIFICIAL NEURAL NETWORKS

Artificial Neural Networks are similar to that of biological nervous system of animals and also motivated by the human computing system in particularly the brain. Different learning mechanisms are available in Artificial Neural Networks to enable the neural network to acquire the knowledge. Depending on the learning mechanisms, neural networks are classified into different types. The learning process in neural networks is called training [19] and the ability to solve the problem is called inference. Backpropagation is training or learning algorithm.

Neural network has three layers namely Input, Hidden and Output layers. This type of networks is called as feed forward networks. The Back Propagation algorithm learns by example, that is, given the input of what the network should do, the

network changes the weights so that, when training is completed, it will give the desired output for a particular input. The network is initialized first by setting all its weights to small random numbers – say between -1 and +1. Secondly, the output is calculated by applying the input pattern, which is called as forward pass. The forward pass gives an output that is completely different from the desired output, because all the weights are random values. This generates the error at each neuron. This error is then considered mathematically to modify the weights at each neuron by which the error will become smaller. This makes each neuron output closer to the target, this process is said as reverse pass. This process is repeated till the error becomes negligible. The simple model of back propagation algorithm is as shown in Fig. 2.

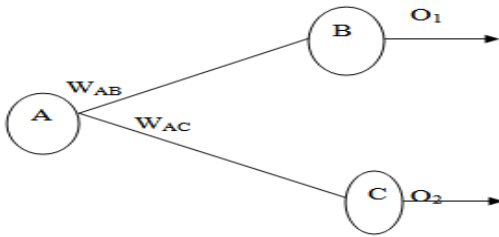


Figure 2. Back propagation algorithm simple network

III. EMOTION RECOGNITION USING ANN

The most important step in emotion recognition system through speech is choosing the best classifier. The emotion recognition from speech system performance depends on the classifier. The classification of emotion can be done by giving different features to the classifier.

In the proposed method ANNs are used as a classifier. To train the network according to our requirement Back Propagation algorithm under ANNs is used.

The steps for the back propagation algorithm are as below:

Step 1: The input layer inputs $\{I\}_I$ and output layer outputs $\{O\}_O$ are represented using “I” and “n” respectively.

Step 2: The number of hidden layer neurons lie between $1 < m < 2l$.

Step 3: The weights connecting to input and hidden neurons are represented as [v] and weights connecting to hidden and output layer neurons are represented as [w].

Step 4: By using linear activation function the input to the input layer is same as that of input layer output.

$$\{O\}_I = \{I\}_I$$

Step 5: Hidden layer input is calculated by multiplying the weights to the input layer output.

$$\{I\}_H = [V]^T \{O\}_I$$

Step 6: The hidden layer outputs are calculated from the sigmoid function.

$$\{O\}_H = \{ 1 / (1 + e^{-\{I\}_H}) \}$$

Step 7: Output layer input is calculated by multiplying corresponding weights to the hidden layer output.

$$\{I\}_O = [W]^T \{O\}_H$$

Step 8: The output layer output is found out by using sigmoid function as

$$\{O\}_O = \{ 1 / (1 + e^{-\{I\}_O}) \} \quad (2)$$

The equation 2 represents the network output.

Step 9: The difference between the Back propagation network output and the target output is the error for the ith training set as follows

$$E_p = \frac{\sqrt{\sum (T_j - o_j)^2}}{n}$$

Step 10: The {d} value is calculated as

$$\{d\} = \{ (T_k - O_k) O_k (1 - O_k) \}$$

Step 11: The Y matrix is calculated by multiplying the hidden layer output with d.

$$[Y] = \{O\}_H \{d\}$$

Step 12: The updated weights are given by

$$[\Delta W]^{t+1} = \alpha [\Delta W]^t + \eta [Y]$$

Step 13: The error is $\{e\} = [w] \{d\}$

$$\{d^*\} = \{e_i (O_{Hi}) (1 - O_{Hi})\}$$

Step 14: Compute the [X] matrix by multiplying the {d} with input layer output.

$$[X] = \{O\}_I \{d^*\} = \{I\}_I \{d^*\}$$

Step 15: Updated weights for input to hidden neurons and output to hidden neurons is given by

$$[\Delta W]^{t+1} = [W]^t + [\Delta W]^{t+1}$$

$$[\Delta V]^{t+1} = [V]^t + [\Delta V]^{t+1}$$

Step 16: Find the error rate by

$$\text{Error rate} = \frac{\sum E_p}{n_{set}}$$

Step 17: Steps 4-16 are repeated till the error gets negligible.

IV. RESULT ANALYSIS

The RTL schematic of emotion recognition from speech system is as shown in Fig. 3. In this the inputs are 8 bit data, clock, reset, load and the outputs are female, male, angry, happy, sad, and lazy of the speaker.

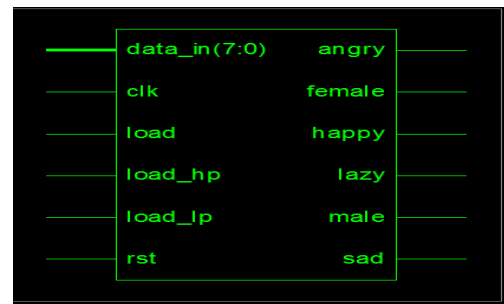


Figure 3. RTL schematic of speech emotion recognition system.

The expanded view of RTL schematic is as shown in Fig. 4. RTL schematic is the top level view of our design. RTL schematic consists of basic gates (AND, OR), adders and multipliers.

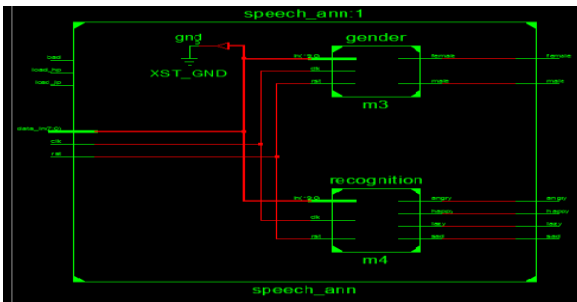


Figure 4. Expanded RTL schematic of speech emotion recognition system

TABLE I. DEVICE UTILIZATION

Device Utilization Summary			
Logic Utilization	Used	Available	Utilization
Number of Slices	2817	4656	60%
Number of slice flip flops	2916	9312	31%
Number of 4 input LUTs	2900	9312	31%
Number of bonded IOBs	16	232	6%
Number of GCLKs	1	24	4%

The summary of Device Utilization using ANN is shown in Table I. It consists of number of devices available and number of devices used. The device utilization summary gives the information about total area under utilization.

TABLE II. COMPARISON BETWEEN LDA AND ANN

Device Utilization Summary		
Parameters	LDA (Device Utilization)	ANN (Device Utilization)
Number of slices	75%	60%
Number of slice flip flops	75%	31%
Number of 4 input LUTs	72%	31%
Number of bonded IOBs	8%	6%
Number of GCLKs	4%	4%
Gate Delay	4.04 ns	2.4286 ns

The comparisons between LDA and ANN for device utilization and delay are as shown in Table II. From Table II, it is observed that, the device utilization and gate delay are decreased using ANN as compared to LDA, which says decrease in space utilized and increase in computational speed by using ANN.

V. CONCLUSION

Speech based emotion recognition from speech signal using Artificial Neural Networks (ANN) is implemented on FPGA device. Back propagation algorithm under ANN is proposed as a classifier for classifying the emotions of the speaker in the given speech signal. The Emotions recognized are happy, sad, angry, and lazy. The obtained results using ANN are compared with the existing method using Latent Dirichlet Allocation (LDA) and found that device utilization as 75% in LDA method where as it is 60% for ANN, delay as less as 2.4286ns for ANN.

REFERENCES

- [1] R. Cowie and R.R. Cornelius, "Describing the emotional states that are expressed in speech," *Speech Communication*, vol. 40, no. 1, pp. 5-32, 2003.
- [2] M. Shah, B. Mears, C. Chakrabarti, and A. Spanias, "Lifelogging: Archival and retrieval of continuously recorded audio using wearable devices," *IEEE International Conference on Emerging Signal Processing Applications*, pp. 99-102, 2012.
- [3] M. Shah, B. Mears, C. Chakrabarti, and A. Spanias, "A top down design methodology using virtual platforms for concept development," *13th International Symposium on Quality Electronic Design*, pp. 444-450, 2012.
- [4] M. Grimm, K. Kroschel, E. Mower, and S. Narayanan, "Primitives-based evaluation and estimation of emotions in speech," *Speech Communication*, vol. 49, no. 10, pp. 787-800, 2007.
- [5] B. Schuller, B. Vlasenko, E. Eyben, G. Rigoll, and A. Wendemuth, "Acoustic emotion recognition: A benchmark comparison of performances," *IEEE Workshop on Automatic Speech Recognition & Understanding*, pp. 552-557, 2009.
- [6] M.M.H. El Ayadi, M.S. Kamel, and F. Karray, "Speech emotion recognition using Gaussian mixture vector autoregressive models," *IEEE international Conference on Acoustics, Speech and Signal Processing*, vol. 4, pp. 957-960, 2007.
- [7] D.M. Blei, A.Y. Ng, and M.I. Jordan, "Latent Dirichlet allocation," *The Journal of Machine Learning research*, vol. 3, pp. 993-1022, 2003.
- [8] D. Ververidis and C. Kotropoulos, "Emotional speech recognition: Resources, features, and methods," *Speech Communication*, vol. 48, no. 9, pp. 1162-1181, 2006.
- [9] E. Burkhardt, A. Paeschke, M. Rolfes, W. Sendlmeier, and B. Weiss, "A database of German emotional speech," *Proceedings of Inter speech*, pp. 1517-1520, 2005.
- [10] S. Young, G. Evermann, D. Kershaw, G. Moore, J. Odell, D. Ollason, V. Valtchev, and P. Woodland, "The HTK book," *Cambridge University Engineering Department*, vol. 3, 2002.
- [11] L. Dagum and R. Menon, "OpenMP: an industry standard API for shared-memory programming," *IEEE Computational Science & Engineering*, vol. 5, no. 1, pp. 46-55, 1998.
- [12] M.J. Beal, "Variational algorithms for approximate Bayesian inference (PhD thesis)," *The Gatsby Computational Neuroscience Unit, University College London*, pp. 65-66, 2003.
- [13] B.C. Russell, W.T. Freeman, A.A. Efros, J. Sivic, and A. Zisserman, "Using multiple segmentations to discover objects and their extent in image collections," *IEEE Conference on Computer Vision and Pattern Recognition*, vol. 2, pp. 1605-1614, 2006.
- [14] C. Wang, D. Blei, and E.E. Li, "Simultaneous image classification and annotation," *IEEE Conference on Computer Vision and Pattern Recognition*, pp. 1903-1910, 2009.
- [15] T. Huynh, M. Fritz, and B. Schiele, "Discovery of activity patterns using topic models," *Proceedings of the 10th International Conference on Ubiquitous Computing*, pp. 10-19, 2008.
- [16] E.C. Lin, K. Yu, R.A. Rutenbar, and T. Chen, "Moving speech recognition from software to silicon: the in silicovox project," *Proceedings of Inter speech*, pp. 2346-2349, 2006.
- [17] E.C. Lin, K. Yu, R.A. Rutenbar, and T. Chen, "A 1000 word vocabulary, speaker-independent, continuous live-mode speech recognizer implemented in a single FPGA," *Proceedings of the 15th International Symposium on Field programmable gate arrays*, vol. 18, no. 20, pp. 60-68, 2007.
- [18] B. Rajasekhar, M. Kamaraju, V. Sumalatha, "Gender Driven Emotion Recognition System for Speech Signals Using Neural Networks", *proceedings of the 6th International Advanced Computing Conference (IACC 2016), IEEECS, Feb 2016*, pp 31.
- [19] S. Rajasekaran, G.A. Vijayalakshmi Pai, "Neural Networks, Fuzzy logic, and Genetic Algorithms".
- [20] S. Sravan Kumar, T. Ranga Babu, "Emotion and Gender Recognition of Speech Signals Using SVM," *International Journal of Engineering Science and Innovative Technology*, Volume 4, Issue 3, May 2015.
- [21] S. Sravan Kumar, K. Baby Swapna, "A DNN-HMM Approach Towards Gender and Age Recognition," *International Journal of Engineering & Science Research*, Sept. 2015, Vol-5, Issue-9/1210-1218.



A Study to differentiate normal and hypertensive subjects based on dynamic thermogram features.

Jayashree Ramesh¹
 Department of Biomedical
 SRM University
 Chennai, India
 jayashree94music@gmail.com

Dr.Jayanthi Thiruvengadam²
 Department of Biomedical
 SRM University
 Chennai, India
 Jayanthi.t@ktr.srmuniv.ac.in

Abstract—Hypertension also familiarized as high or raised blood pressure. It is a condition where the blood vessels have continuously raised pressure. It is a condition where the systolic pressure is 140 mm/Hg or above and the diastolic pressure is 90 mm/Hg or above. According to the statistics of Directorate General of Health Services, Ministry of Health and Family Welfare, Government of India, the overall prevalence of hypertension in India by 2020 will be 159.46/1000 population. This paper aims to study the potential of Dynamic thermogram in differentiating normal and hypertensive subjects. In this technique the dynamic Infra-red (IR) thermogram of selected body regions like hand (left and right) and neck (left and right) are obtained for about 60secs using IR thermal camera from 50 subjects (normal = 25 and age and sex matched hypertensive = 25). The average temperature for each and every millisecond in these selected body regions is measured using ResearchIR software. The T-Test value shows a significant difference in almost all the parameters between normal and hypertensive subjects. The percentage difference is high for the rate of temperature change in the neck left region (92.5%).

Keywords—Dynamic thermal imaging, T-Test, hypertension, mean, energy, kurtosis.

I. INTRODUCTION

Hypertension also familiarized as high or raised blood pressure. It is a condition where the blood vessels have continuously raised pressure [1]. It is a condition where the systolic pressure is 140 mm/Hg or above and the diastolic pressure is 90 mm/Hg or above. Hypertension paves the way for stroke deaths and coronary heart diseases which are 57% and 24%. According to the statistics of Directorate General of Health Services, Ministry of Health and Family Welfare, Government of India, the overall prevalence of hypertension in India would be 159.46/1000 population by 2020 [2]. About 75 million of people in U.S suffer from hypertension [3]. It costs about \$46 billion each year for the nation to diagnose and treat hypertensive people. Hypertension paves the way

for all cardiovascular disease if left untreated. This work mainly focuses on differentiating dynamic thermogram between normal and hypertensive subjects. The conventional process of inflation, deflation, examining korotokoff sounds with astethoscope can be replaced by the technique of continuous dynamic thermal imaging. Thus this technique can be used for mass and initial screening. Sergey Y. Chekmenev et al. developed a model that matched thermogram with pulse rate [4]. Hence our work focuses on differentiating normal and hypertensive subjects through dynamic thermogram features. Thermal Imaging is a non-invasive and non-contact method where the temperature patterns in the skin are studied using a thermal Camera. Thermal imaging has a wide variety of application in medical field diagnosis that includes inflammatory diseases, complex regional pain syndrome and Reynaud's phenomenon, breast cancer, various types of arthritis, injuries and other traumas [5, 6, and 7].

II. MATERIALS AND METHODS

A. Population Concentrated

A health camp was conducted in a private hospital where about 50 subjects registered both men and women participated. Subjects in the age group of 39±5.01 (normal and known hypertensive were included in the study. The following parameters like BP (mm/Hg), Ultrasound Doppler scan, SpO₂ (%), sex, age (cm), hip and waist circumference (cm) and height (cm) and weight (Kg) were obtained. The consent form was obtained from all the subjects. And details of this procedure were clearly explained. Institutional Ethical clearance was obtained from the Institutional Ethical clearance committee letter dated 1034/IEC/2016.

B. Pressure Measurement

The subjects were made to relax in sitting position and his blood pressure both systole (mm/Hg) and diastole (mm/Hg) was measured using standard sphygmomanometer. Only a trained technician took the measurements for all 50 subjects.

C. Thermal Imaging

The thermal camera was placed on the stand and connected to the laptop. The initial setting for taking video was taken care. A standard approach as proposed by the International Association of Certified Thermographers was followed during the entire procedure [8]. The process was carried out in a full air conditioned maintained at 25°C. The subjects were made to stay in the room for 15 minutes. The subjects were asked to stand, and their left and right hand were stretched and held in support while the video signal was taken. Similarly, the subjects were made to move their head left and right side for the neck images. The data was taken using thermal camera Therma Cam A305sc, FLIR Systems, USA. Then the average temperature was measured using FLIR tool. The noise removal and decomposition process was done using Wavelet transform with a level of db4. The change in temperature signal for a minute before and after noise removal is shown in figure 1.

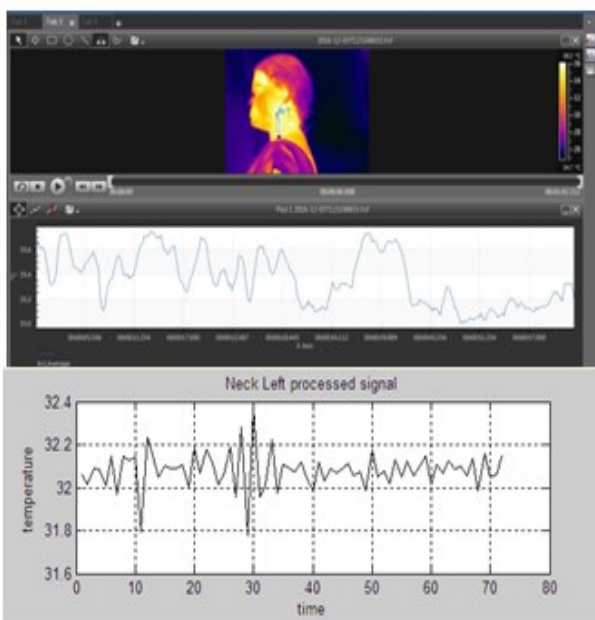


Fig. 1. Original and processed hand left signal

After the noise removal the rate of temperature change was calculated using equation [9]:

$$C = \frac{F_{AT} - I_{AT}}{F_{RT} - I_{RT}} (\text{°C/Min}) \quad (1)$$

C - Rate of change in Temperature

F_{AT} - Final Average Temperature

I_{AT} - Initial Average Temperature

F_{RT} - Final Relative Time

I_{RT} - Initial Relative Time

D. Ultrasound Doppler Scan

The subject was made to lie on the bed, and the ultrasound Doppler images and flow patterns were obtained. The ultrasound Doppler scans of right and left Common Carotid Artery

was taken using MINDRAY DC-N3 Doppler machine. The rate of blood flow was calculated from mean velocity and vessel diameter [10]. The formula to calculate flow rate was:-

$$Q = \pi * D^2 / 4 * V_m * 60 \text{ (ml/min)} \quad (2)$$

Q - Flow rate

π - 3.14

D - Vessel Diameter (cm)

V_m - Mean Velocity (cm/s)

A correlation study was performed between flow rate that was obtained for left and right common carotid artery and features derived from thermal imaging. This study shows the relationship between blood flow rate and skin surface temperature change.

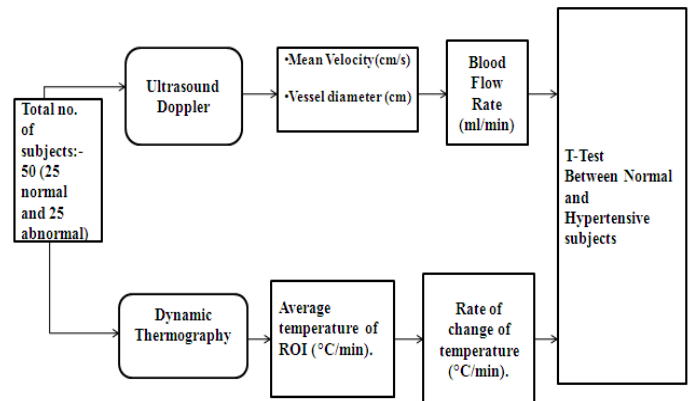


Fig. 2. Methodology

Fig.2 shows the overall methodology of the work. The ultrasound and dynamic thermogram were taken for normal (n=25) and hypertensive subjects (n=25). The mean velocity and vessel diameter were obtained from ultrasound Doppler scan, and an average temperature of the region of interest was plotted from dynamic thermogram. The blood flow rate (ml/min) and rate of change of temperature (°C/min) were calculated, and TTEST was performed between the normal and hypertensive population.

III. RESULTS

A. A t-test between the rate of temperature change and features from dynamic thermogram for normal and hypertensive subjects with mean and standard deviation.

From the Table 1, it is evident that almost all parameters show a significant difference between normal and hypertensive subjects except neck right mean and neck right median. The percentage difference is high for hand left (80), hand right (90), neck left (92.5) and neck right (76.9) rate of temperature change. Among the features extracted from dynamic thermogram the percentage difference is high for hand left (51.1), hand right (42.3), neck right kurtosis (46.9). All features extracted from the right and left hands



show significant difference. The chart depicting the percentage difference is shown below in figure 3.

II. DISCUSSIONS

The brachial artery is one of the important arteries in measuring blood pressure [11, 12, 13, 14]. From the table it is inferred that there exist a significant difference between normal and hypertensive subjects in hand left and right regions, from where pressure could be measured [15]. Kurtosis physiologically relates to volatility [16]. Baroreceptors monitor sudden changes in blood pressure; they buffer these changes to intercept rise and fall in blood pressure. Failure of the baroreflex leads to volatility in blood pressure, thus leading to orthostatic hypotension and supine hypertension [17]. Hence significant difference in kurtosis can lead to the prediction of hypertension and hypotension. Blood pressure could be measured from the carotid and brachial artery for hypertensive subjects in order to know various stages of coronary heart disease [18]. Likewise in our study also we have obtained the dynamic thermogram features from carotid and brachial artery regions of left and right side to differentiate hypertensive subjects from normal subjects.

Table 1:-T-Test significance, mean and standard deviations of rate of temperature change and features from dynamic thermogram

Region	Features	Normal Mean & Standard Deviation	Abnormal Mean & Standard Deviation	% diff.	Sig. Diff.
Hand Left	Rate of temp. change	0.01±0.05	0.05±0.02	80	0.01
	Kurtosis	2.2±0.9	4.5±0.7	51.1	0.01
	Mean	45.2±2.0	46.9±1.3	3.6	0.01
	Median	46.1±2.1	47.2±1.2	2.3	0.05
	Energy	22.9±1.5	24.8±1.5	7.7	0.01
Hand Right	Rate of temp. change	0.2±0.2	0.02±0.01	90	0.01
	Kurtosis	3±0.5	5.2±1.0	42.3	0.01
	Mean	44.6±1.9	47.5±0.6	6.1	0.01
	Median	46.3±1.5	47.3±0.8	2.1	0.05
	Energy	22.4±1.1	24.6±1.3	8.9	0.01
Neck Left	Rate of temp. change	0.4±0.4	0.03±0.02	92.5	0.01
	Kurtosis	2.8±0.9	2.1±0.6	25	0.05
	Mean	47.2±0.9	48.7±1.1	3.1	0.01
	Median	47.5±0.7	48.6±1.0	2.3	0.01
	Energy	22.3±1.1	25.1±1.1	11.2	0.01
Neck right	Rate of temp. change	0.03±0.01	0.13±0.11	76.9	0.01
	Kurtosis	3.2±1.2	1.7±0.4	46.9	0.01
	Mean	47.0±1.3	46.8±1.2	0.4	NS
	Median	47.0±1.4	47.0±1.6	0	NS
	Energy	22.3±1.0	25.2±1.7	11.5	0.01

NS- Not Significant

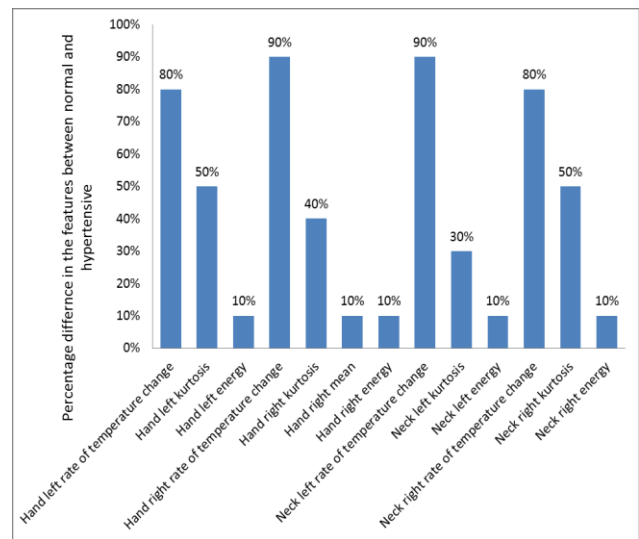


Fig 3:- Bar chart depicting the percentage difference

III. CONCLUSION

As this work shows a significant difference between the normal and hypertensive subjects, this method would be able to predict hypertension. The higher significance in hand regions adds on a point in using this method for prediction of diagnosis. The camera can be replaced by thermal sensors, and it can be used as an add-on device with mobile applications and independent portable devices.

REFERENCES

- [1] <http://www.who.int/topics/hypertension/en/>
- [2] Singh, Manoj Kumar, BhaskarSingamsetty, and JithendraKandati. "An epidemiological study of the prevalence of hypertension and its risk factors in a rural community of Nellore, Andhra Pradesh, India." *International Journal Of Community Medicine And Public Health* 3.12 (2016): 3408-3414.
- [3] <https://www.cdc.gov/bloodpressure/facts.htm>.
- [4] Chekmenev, Sergey Y., Aly A. Farag, and Edward A. Essock. "Thermal imaging of the superficial temporal artery: An arterial pulse recovery model." *2007 IEEE Conference on Computer Vision and Pattern Recognition*. IEEE, 2007.
- [5] Ring, E. F. J., and K. Ammer. "Infrared thermal imaging in medicine." *Physiological measurement* 33.3 (2012): R33.
- [6] Hildebrandt, Carolin, Christian Raschner, and Kurt Ammer. "An overview of the recent application of medical infrared thermography in sports medicine in Austria." *Sensors* 10.5 (2010): 4700-4715.
- [7] Qi, Hairong, and Nicholas A. Diakides. "Thermal infrared imaging in early breast cancer detection-a survey of recent research." *Engineering in Medicine and Biology Society, 2003. Proceedings of the 25th Annual*



- International Conference of the IEEE*. Vol. 2. IEEE,
- [8] Ring, E. F. J., and K. Ammer. "The technique of infrared imaging in medicine." *Infrared Imaging*. IOP Publishing, 2015.
- [9] <https://www.physicsforums.com/threads/rate-of-temperature-change.616194/>
- [10] Benetos, A., et al. "Pulsed Doppler: an evaluation of diameter, blood velocity and blood flow of the common carotid artery in patients with isolated unilateral stenosis of the internal carotid artery." *Stroke* 16.6 (1985): 969-972.
- [11] Borow, Kenneth M., and Jane W. Newburger. "Noninvasive estimation of central aortic pressure using the oscillometric method for analyzing systemic artery pulsatile blood flow: comparative study of indirect systolic, diastolic, and mean brachial artery pressure with simultaneous direct ascending aortic pressure measurements." *American heart journal* 103.5 (1982): 879-886.
- [12] Beevers, Gareth, Gregory YH Lip, and Eoin O'Brien. "Blood pressure measurement: Part II--conventional sphygmomanometry: Technique of auscultatory blood pressure measurement." *British Medical Journal* 322.7293 (2001): 1043.
- [13] Braunwald, Eugene, and Charles J. Frahm. "Studies on Starling's law of the heart IV. Observations on the hemodynamic functions of the left atrium in man." *Circulation* 24.3 (1961): 633-642.
- [14] Issa, Ziad, John M. Miller, and Douglas P. Zipes. *Clinical Arrhythmology and Electrophysiology: A Companion to Braunwald's Heart Disease: Expert Consult: Online and Print*. Elsevier Health Sciences, 2012.
- [15] Dr. T. Jayanthi, Dr. M. Anburajan" Non-invasive cuffless diagnosis of Hypertension using dynamic thermal imaging features." *Vol. 14 CIC 2016 Special Issue International Journal of Computer Science and Information Security (IJCSIS)*. ISSN 1947-5500.
- [16] Jondeau, Eric, and Michael Rockinger. "Conditional volatility, skewness, and kurtosis: existence, persistence, and comovements." *Journal of Economic dynamics and Control* 27.10 (2003): 1699-1737.
- [17] Aung, Thein, Wuqiang Fan, and Mahesh Krishnamurthy. "Recurrent syncope, orthostatic hypotension and volatile hypertension: think outside the box." *Journal of Community Hospital Internal Medicine Perspectives* 3.2 (2013).
- [18] Safar, Michel E., and Augustine Kakou. "Carotid and brachial blood pressure-measurements in hypertensive subjects." *Revista Brasileira de hipertensao* 15.3 (2008): 122-124.

Analysis of Neuromuscular Control In Human Arm

Jan Thomas

MTech: Department of Biomedical Engineering
SRM University
jan.thomas15@hotmail.co
m

P.Vinupritha

Asst Prof: Department of Biomedical Engineering
SRM University

Abstract—The central nervous system directs a large number of muscles to produce complex motor behaviors. By using Artificial neural networks (ANNs) where more number of hidden layers are used for learning a specific task, we propose a method to understand the representations of neuromuscular control in the central nervous system as representations of movement plans that are eventually executed by the spinal cord and muscles in the periphery. In this report, we provide our results in attempting to build a neural network that enables muscle activation implemented in OpenSim- a biomechanical software to simulate the right upper arm of a human body. It is expected that this project will provide fundamental insights into the neuromuscular control.

Keywords—Neural network; OpenSim; Muscle activation

I. INTRODUCTION

The last decade saw studies that shed light on motor control and the problems underlying the generation of multi joint movement. Consider tasks that make up daily human activities like reaching, grasping, bending, walking etc. Neural Networks have also gained popularity in their usage in fields such as Natural Language Processing, Computer Vision, reinforcement learning, and even animation. This paper will discuss its application to approximating and controlling muscle activation. The only goal of this paper is to see if we could achieve values using the above strategy. We have selected a musculoskeletal model that we will use for our Neural Network approximation. In order to achieve our goal, we generate random movements in an allowable range in order to train and test our neural network.

A. OpenSim

OpenSim is a software framework designed to build and share musculoskeletal models, simulate movements, and analyze and visualize those movements using specialized tools. This framework contains, amongst other things, a graphical user interface (GUI) written in java, various built-in musculoskeletal models developed and published by an open source community of researchers and users, a software development kit, APIs and other various tools that are used by researchers or hobbyists for analysis. OpenSim has many open source musculoskeletal models available in their repository.

These include human and animal models that can vary in complexity and scope. In our case, we are only looking at the right arm of a human. There are multiple arm models that are available and we have the liberty of choosing one that we believe can achieve our objective simply and effectively. There are many tools available on the platform that can be used to analyze muscle actuation and joint position. We use an arm model whose muscles are based on Hill's muscle model

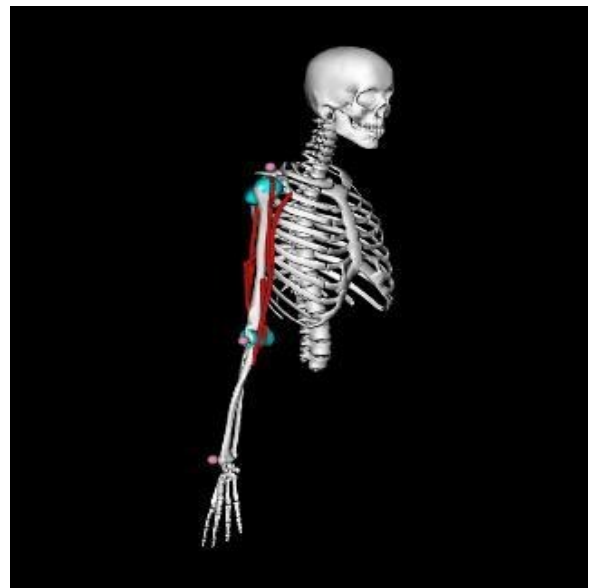


Fig. 1: OpenSim's Arm model

It consists of 2 degrees of freedom, with 6 muscles and muscle elements such as bones, ligaments, etc. and provides a dynamic graphical simulation to visualize and analyze moments about the joints of a human arm.

II. BACKGROUND

The primary motivation of this study is the work 'Computational schemes and neural network models of human arm trajectory control' where Flash et al discuss the control of multijoint movements by the CNS to perform complicated transformations from the desired behavioural goals into appropriate neural commands to muscles. The evidence for the above view was also discussed and neural network model was developed to understand the internal organisation of movement generation. In 'Formation and Control of Optimal Trajectory in

Human Multijoint Arm Movement' Kawato et al discusses what criterion is adopted for trajectory determination. Several researchers measured the hand trajectories of skilled movements and found common invariant features. For example, when moving the hand between a pair of targets, subjects tended to generate roughly straight hand paths with bell-shaped speed profiles. On the basis of these observations and dynamic optimization theory, a mathematical model was proposed which accounts for formation of hand trajectories. This model is formulated by defining an objective function, a measure of performance for any possible movement: square of the rate of change of torque integrated over the entire movement.

III. METHODOLOGY

A. Scaling

Scaling is performed based on a combination of measured distances between x-y-z marker locations and manually-specified scale factors. The marker locations are usually obtained using motion capture equipment. The motion capture device used for this study was Qualisys motion capture system (Qualisys Inc) with Qualisys Track Manager (QTM) allows users to perform 2D, 3D and 6DOF capture of data in real-time by the way of C3D data which is then converted into in a

.trc file which provides the distances between markers on the model and experimental marker positions which are compared and determined by the scaling factors. For this study the scaling factor was set to 1.0 which is the default scaling factor used in OpenSim software. The experimental markers set for 15 healthy subjects were right acromium; right humerus epicondyle and right styloid process of radius to match with the generic marker in model. The unscaled model has a set of virtual markers placed in the same anatomical locations as the experimental markers.

B. Inverse kinematics

The IK tool goes through each time step (frame) of motion and computes generalized coordinate values which positions the model in a pose that "best matches" experimental marker and coordinate values for that time step. Mathematically, the "best match" is expressed as a weighted least squares problem, whose solution aims to minimize both marker and coordinate errors; where the marker error is the distance between an experimental marker and the corresponding marker on the model when it is positioned using the generalized coordinates computed by the IK solver. Each marker has a weight associated with it, specifying how strongly that marker's error term should be minimized. The IK solver is given by the following equation as the weighted least squares problem solved by IK

$$\min_{q \in \text{markers}} [\sum w_i \| x_i^{\text{exp}} - x_i(q) \|^2 + \sum_{j \in \text{unprescribed coords}} \omega_j (q_j^{\text{exp}} - q_j)^2] \quad (1)$$

where q is the vector of generalized coordinates being solved for, x_i^{exp} is the experimental position of marker i, $x_i(q)$ is the position of the corresponding marker on the model (which depends on the coordinate values), q_j^{exp} is the experimental value for coordinate j. This generates motion file with the times histories of joint angles.

TABLE 1: MOTION FILE

Time	Joint 0	Joint 1	Joint n
t0	θ00	θ01	θ02
t1	θ10	θ11	θ12
t2	θ 20	θ21	θ 22
tm	θm1	θm2	θ m3

Each of the positions are in units of radians. For our model, we have 2 Degrees of Freedom (joint angles) that correspond to 2 joints, namely glenohumeral (GH) and elbow (EL). Each joint has a minimum and maximum value for position expressed as radians.

C. Forward dynamics and Muscle activation

The Forward Dynamics Tool can drive a forward dynamic simulation. A forward dynamics simulation is the solution (integration) of the differential equations that define the dynamics of a musculoskeletal model. By focusing on specific time intervals of interest, and by using different analyses, more detailed biomechanical data for the trial in question can be collected. From Newton's second law, we can describe the accelerations (rate of change of velocities) of the coordinates in terms of the inertia and forces applied on the skeleton as a set of rigid-bodies: This is given by the following equation

$$\ddot{q} = [M(q)]^{-1} \{ \tau + C(q, \dot{q}) + G(q) + F \} \quad (2)$$

Where \ddot{q} is the coordinate accelerations due to joint torques τ Coriolis and centrifugal forces, $C(q, \dot{q})$ as a function of coordinates q ,and their velocities \dot{q} , gravity $G(q)$, and other forces applied to the model F, and $M[(q)]^{-1}$ is the inverse of the mass matrix. The state of a model is the collection of all model variables defined at a given instant in time that are governed by dynamics. The model dynamics describe how the model will advance from a given state to another through time. In a musculoskeletal model the states are the coordinates and their velocities and muscle activations and muscle fiber lengths. The dynamics of a model require the state to be known in order to calculate the rate of change of the model states (joint accelerations, activation rates, and fiber velocities) in response to forces and controls. This generates the controls file which gives the time histories of muscle excitations.



IV. NEURAL NETWORK ARCHITECTURE

Neural Network architecture is imbibed from the computational phenomenon of the brain. In the brain neurons are connected to each other and fire when the sufficiently appropriate stimuli are presented. Inputs gathered by the Neuron and then passed through an activation function which produces an output from the neuron. These outputs are then propagated throughout the neural network and in the final stage, combined into a output value used to interpret the relevant state of the application.

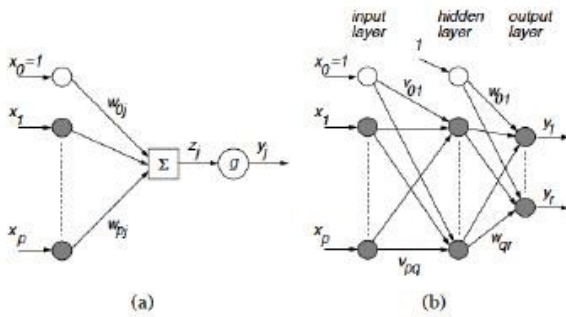


Fig.2 (a) Neuron (b) Neural Network configuration

Neurons are arranged in layers labeled as input, hidden, or output. Input layers represent the inputs to the neural network. The hidden layers are between the inputs and outputs. The output layer is the observable. Each neuron in layer l receives weighted inputs from layer $l-1$ and sums them together along with a bias before passing them through activation function. The bias shifts the input sums along the sigmoid function and can be beneficial to biasing the output towards a particular value. The activation function may change depending on the situation of the neural network, but typically it is the sigmoid function expressed as:

$$g(z) = 1/(1+e^{-z}) \tag{3}$$

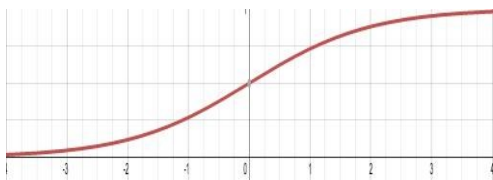


Fig.3 Sigmoid function

A. Sampling

The sampling required a control data in (xml file) and state data in storage (.sto) file. The states file contains the time histories of model states, including joint angles, joint speeds, muscle activations, muscle fiber lengths, and more. These states are used by the Forward Dynamics Tool to set the initial states of the model for forward integration. Muscle states can be estimated by solving for tendon and muscle fiber force equilibrium when the Solve for equilibrium for actuator states is checked.

TABLE 2:STATE FILE

Time	r_ shoulder_elev	r_elbow_flex	r_ shoulder_elev_u	r_elbow_flex_u
t1	θ11	θ12	θ13	θ14
t2	θ21	θ22	θ23	θ24
t3	θ 31	θ32	θ33	θ34
t4	θ 41	θ42	θ43	θ44
t5	θ 51	θ52	θ53	θ54
t6	θm1	θm2	θm3	θm4

The control file contains the time histories of the model controls (e.g., muscle excitations) to the muscles and/or joint torques, for this study Triceps long, medial and lateral head and biceps long head was considered. It is possible to specify the controls as .sto files instead, with columns corresponding to desired excitations.

TABLE 3:CONTROL FILE

Time	Triceps_Jong	Triceps_med	Triceps_lat	Biceps_long
t1	Excitation 11	Excitation 12	Excitation 13	Excitation 14
t2	Excitation 21	Excitation 22	Excitation 23	Excitation 24
t3	Excitation 31	Excitation 32	Excitation 33	Excitation 34
t4	Excitation 41	Excitation 42	Excitation 43	Excitation 44
t5	Excitation 51	Excitation 52	Excitation 53	Excitation 54
t6	Excitation 61	Excitation 62	Excitation 63	Excitation 64

B. Training

The training is carried out by the steepest descent gradient for backpropagation algorithm using the neural network toolbox of Matlab 2014 software (Mathworks Inc). The weights and biases are updated in the direction of the negative gradient of the performance function. The algorithm for training is as follows:

A random training example from training pool is chosen. Pass training input through the network and determine objective loss.

for

Calculate each nodes in output layer by

- 1) Computing gradients with respect to biases

- 2) Computing gradients with respect to weights
- 3) Computing gradients with respect to previous layer

end for (Calculate gradients with respect to outputs backwards

through the layers)

Repeat using output gradients from the next layer for:

- 1) Computing gradients with respect to biases
- 2) Computing gradients with respect to weights
- 3) Computing gradients with respect to previous layer until input layer is reached
- 4) Update all weights and biases based on the computed gradients by a stepsize

end for

For each neuron output:

$$O_j^l = g(\sum(O_i^{l-1}W_{ij}^l) + b_j) \quad (4)$$

g is the sigmoid activation function. O_j^l is the output of node j in layer l where O_i^{l-1} is the output from the previous layer and W and b are the weights and biases of the current layer respectively.

The gradients for weight, biases and previous output are as follows:

$$\partial O_j^l / \partial W_{ij}^l = g'(\sum(O_i^{l-1}W_{ij}^l) + b_j^l) O_i^{l-1} \quad (5)$$

O_i^{l-1} contributes to all of the outputs in the next layer and so in order to back propagate the contribution, we have to average all of its contributions as follows:

$$\partial O_j^l / \partial O_i^{l-1} = 1/N \sum (g'(\sum(O_i^{l-1}W_{ij}^l) + b_j^l) W_{ij}^l) \quad (6)$$

The chain rule is applied to find the gradients with respect to the weights and biases of previous layers as follows:

$$\partial O_j^l / \partial W_{ij}^{l-1} = \partial O_j^l / \partial O_i^{l-1} * O_i^{l-1} / W_{ij}^{l-1} \quad (7)$$

$$\partial O_j^l / \partial b_i^{l-1} = \partial O_j^l / \partial O_i^{l-1} * O_i^{l-1} / b_i^{l-1} \quad (8)$$

C. Results of performance function

Fig.6 The above result shows the performance of 0.0246203 at 1000 epochs with gradient of 0.0523

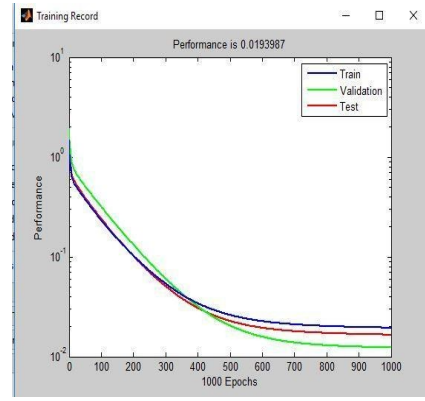
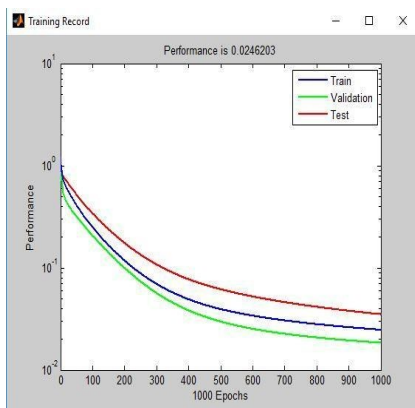


Fig.7 The above result shows performance of 0.0194 at 1000 epochs with gradient of 0.0155

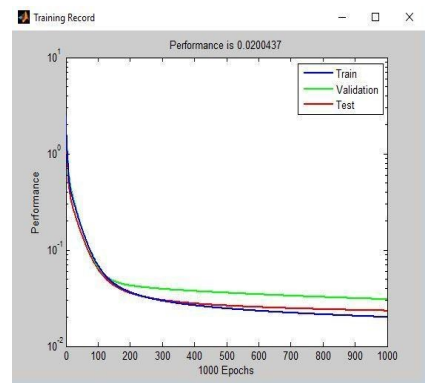


Fig.8 The above result shows the performance of 0.0200 at 1000 epochs with gradient of 0.0234

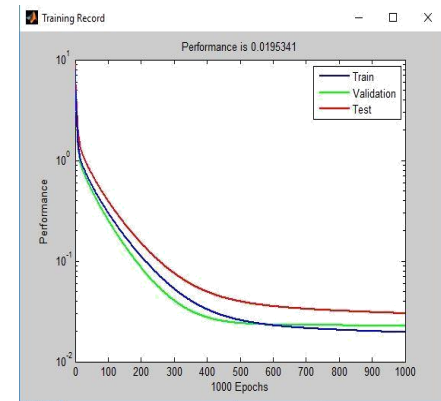


Fig.9 The above result shows the performance of 0.0195 at 1000 epochs with gradient of 0.0211.

V. CONCLUSION

This project enables the simulation of neuromuscular control through the use of ANN (artificial neural networks) in an effort to mimic the execution and motor planning of the brain when performing simple tasks. Feed forward neural network is used along with backpropogation by gradient descent to compute the muscle activation profile.

REFERENCES

- [1] Scott L. Delp*, Frank C. Anderson, Allison S. Arnold, Peter Loan, Ayman Habib, Chand T. John, Eran Guendelman, and Darryl G. Thelen et al., "OpenSim: Open-Source Software to Create and Analyze Dynamic Simulations of Movement" .IEEE Transactions on biomedical engineering, vol. 54, no. 11, november 2007.
- [2] David Sussillo, Mark M Churchland, Matthew T Kaufman & Krishna V Shenoy et al, "A neural network that finds a naturalistic solution for the production of muscle activity" Nature Neuroscience volume 18 , number 7, july 2015.
- [3] Tamar Flash, Michael J Jordan, "Computational schemes and neural networks model of human arm trajectory control". World congress of neural networks, November 1999 pp.76-83.
- [4] Mitsuo Kawato, "Formation and Control of Optimal Trajectory in Human Multijoint Arm Movement". Biol.Cybernetics 61, 80-89. 1989.

Preliminary Big Data Analytics of Hepatitis Disease by Random Forest and SVM Using R- Tool

Visali Lakshmi P R

Electronics and Instrumentation Engg.
St. Joseph's College of Engineering
Chennai, India
visali1553@gmail.com

Shwetha G

Electronics and Instrumentation Engg.
St. Joseph's College of Engineering
Chennai, India
gshwetha1812@gmail.com

N.Sri Madhava Raja

Electronics and Instrumentation Engg.
St. Joseph's College of Engineering
Chennai, India
nsrimadharaja@stjosephs.ac.in

Abstract—In the growing era of technology, concentration is on the analysis of large amount of structured and unstructured data. The processing applications are inadequate to deal with these data are termed as BigData since in large amounts. In this work, an initial stage for analysing medical informatics using R-studio by R programming is attempted by two algorithms. The biomedical data is used because they are concerned with the real time usage and is an open access journal aiming to facilitate the presentation, validation, use, and re-use of datasets, and can be modifiable with focus on publishing biomedical datasets that can serve as a source for simulation and computational modelling of diseases and biological processes. Random forest technique and support vector machine (SVM) techniques are used to derive features from the database and are able to differentiate various disease supports. The aim of this paper is to provide a comparison between the various techniques that are involved in the field of sorting the data and analysing them in large numbers. For this the process of data mining is used. Data mining is the process of extracting valuable information from a large set of databases. The latter technique produces more appropriate results that has less deviation from the reference taken from the hepatitis profile. By this method one can get the lead vision of the results that are produced by medical science. Therefore the SVM technique can be implemented practically in the medical field.

Keywords—*BigData; Hepatitis; Random forest; SVM; Error analysis*

I. INTRODUCTION (HEADING 1)

In the recent years of medical field, database management has become an important part of the disease analysis. BigData[1] plays an important role in the analysis of the large datasets. Due to the increase in use of social networking, surveillance cameras, and satellite images the amount of data has grown. Big data gives the optimal results on analysis [2] of huge amount of database that are considered. In hepatitis, there are various enzymes that are involved in the secretion of the bile serum[3]. Hence they are sorted using BigData. Many techniques are used to analyse the medical informatics. Random Forest and SVM are widely used to differentiate biomedical data of normal and abnormal states. First is the Random Forest[4] technique that are used to sort and it provides a error rate which is higher to be accepted practically. It is manipulated using BigData since it produces higher resolution. The second one is the Support Vector Machine (SVM)[5] technique which is used to manipulate the

distributed data. Since here the decision trees and its nodes deal with real data they are sorted using BigData. There is a difference in the error rate between both the techniques. The latter produces results that are more appropriate to those obtained from the reference.

II. DATABASE OF HEPATITIS ANALYSIS

The hepatitis is caused due to the inflammation of the liver. Cholyglycine (CG) and sulfolithocholyglycine (SLCG) in fasting and postprandial serum were determined in patients with liver diseases by radioimmunoassay also in diseases like cancer, etc. These are the two vital parameters that are used to classify to form the decision trees. In liver disease, serum bile acids [3] were elevated in both the acute and the chronic disorders. The greatest increase was found in acute viral hepatitis [6] but moderate or slight increase was also found in chronic active hepatitis, liver cirrhosis, and hepatoma and in others. Insignificant elevation of bile acids was found postprandially in patients with liver diseases as well as normal controls and postprandial bile acids were not more sensitive than fasting ones, hence taken in both cases. It has also been suggested that measuring serum bile acids two hours after a meal was the method of choice for detecting hepatobiliary disease [7] rather than conventional liver function testing. Thus the enzyme levels are taken in both the stages since there is a variation in the secretion of the bile serum [8]. The values are obtained from the profile of acid range in liver disease from the literature [3], where they had described the estimated levels of bile acids various stages. These values are taken within a set of range and to validate them in BigData by using various techniques which are generated.

III. METHODOLOGY

The considered is subjected to study based on the confusion matrix where the database is generated synthetically with the preferred values of the hepatitis. After the prediction of factors from the plot, the techniques are applied.

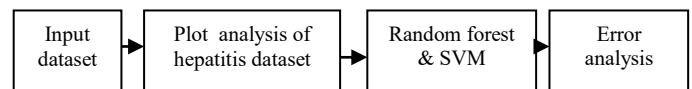


Fig.1 Sequence of database analysis

This section presents the methodology adapted for the work. The Fig.1 represents the sequence of analysis of database.

A. Random forest:

Random Forest [4] is one of the ensemble method used for the sorting of the data based on the estimated description. The methodology includes the construction of the decision trees for the training ones that are taken from the reference and comparing them with the testing ones. It is used to rank the importance of variables in the situation. For that ranking, set $D_n = \{(X_i, Y_i)\}_{i=1}^n$ is used to fit the data. The i^{th} variable gives the importance of the testing ones. However the importance lies in the computation of the averaging the difference rates before and after the permutation is being done.

The decision tree [9] formation is done by the tree bagging system, where the training algorithm for the random forest is obtained by the given formula.

Given training set $X = x_1, \dots, x_n$, with the response $Y = y_1, \dots, y_n$

The bagging is done for B times, for $b=1 \dots B$

The samples are replaced with n training samples from X, Y, call these X_b, Y_b and the number of regression trees are f_b .

After training the predictions for the sample x' ,

$$f' = \frac{1}{B} \sum_{b=1}^B f'_b(x') \tag{1}$$

Normalization of the permuted data can be done by the standard deviation. The features [4] that produces more difference are important than those ones that produces a less difference to enhance the proximity of the results. The various steps that are involved in the construction are as follows. Let the number of the testing variables be 'n' and the number of sample be 'm'. Next the number of input variables be 'p' which is always lesser than 'm'. Choose the training data k times that the 'n' variable by the bootstrapping. It is the method separation of the various variables based on certain estimation that are grouped together. By this method a tree can be formed where the variables occupy their own respective characteristics and divide themselves. By this tree formation, each node has some similar character that can be easily split with the trained ones [10]. Pruning is done which means the act of cutting the leaf nodes to make it grow further. The tree with the least error is the best tree that which produces a minimum deviation from the training data.

B. Support vector machine:

Support vector machine(SVM)[5] is the one of the classification algorithms used for the pattern analysis. From the different types of SVM [11], the Radial Basis Function kernel is taken for the analysis. The RBF kernel [12] has two samples x and x' , represented in the feature space in some input space is defined as,

$$k(x, x') = \exp\left(-\frac{\|x - x'\|^2}{2\sigma^2}\right) \tag{2}$$

$\|x, x'\|^2$ is the squared Euclidean distance

$$\sigma \text{ is free parameter involves in } \gamma = \frac{1}{2\sigma^2}$$

In this, the 'gamma' parameter [12] defines how much the radial length reaches the sample, with low values means 'far' and high values means 'near'. The behavior of the model mainly depends on the 'gamma' parameter. It involves the area fitting in SVM. The size of the kernel in RBF be like $k(x, y) = \exp(-\gamma \|x - y\|^2)$ (3) and its corresponding feature is infinite dimension. In the processing it takes the two inputs and split out how similar they are.

Since the value of the RBF kernel decreases with distance and ranges between 0 and 1 ($x = x'$) is to be represented by feature space that the infinite number [13] of dimension $\sigma = 1$, is defined as

$$\exp\left(-\frac{1}{2} \|x - x'\|^2\right) = \sum_{j=0}^{\infty} \frac{(x^T x')^j}{j!} \exp\left(-\frac{1}{2} \|x\|^2\right) \exp\left(-\frac{1}{2} \|x'\|^2\right) \tag{4}$$

It works mainly with the feature vector. It is a machine learning algorithm [14] usually represented with the dot products and these dot products are replaced with the kernel in the future. By doing this, the feature vector can be neglected. It reduces the complexity and improves the efficiency of computation. By this method, the even cost function the computation time of the results and the levels of the results are predicted. The kernel can also be understood by the dimensional conversion in the graph method.

C. Plot analysis

In this analysis the database are plotted by using three different plots [15]. A bar graph [16] is the first plot which consists of vertical parallel bars that shows the distribution graphically for the quantitative samples. Here BigData is used since they are so large or complex that traditional data processing applications are inadequate to deal with them. The next is the ggplot [17] where the database is plotted. ggplot2 is a plotting system for R, which tries to take the good parts of base and lattice graphics and none of the bad parts. It takes care of many of the minute details that make plotting a hassle (like drawing legends) as well as providing a powerful model of graphics that makes it easy to produce complex multi-layered graphics. This plot is used because it provides plot specification at a higher level of prediction and also it completes the graphics system. So, they are analysed using BigData. The psych plot [18] is an initiative plot that just indicates how the distribution has taken place. It gives the



values that are more appropriate and by this the change in the prediction can be done.

IV. RESULTS AND DISCUSSION

A. Factor analysis by plot prediction

In the hepatitis disease analysis the important part is the plot prediction [3]. It helps to analyze the factors which are important for the result analysis. Here the comparison of the various factors which is taken for the result analysis in the datasets is provided. The main factors are age, CG and SLCG in pre and post prandid stage.CG and SLCG are the main factors which are used for the clinical analysis of liver disease hepatitis. The results of the disease are based on the normal and abnormal states of the patient. The Fig.7 defines the consolidated plot of all the parameters. They are represented in the diagonal axis. It gives the comparative results of the normal and abnormal rate of the patient. The results are the main factor in the synthetic data it is to be compared with all the parameters in the datasets.

The Fig.2 describes the distributions of the age and results. The comparison between the age and results gives the equal distribution of the normal and abnormal rate. The important part of the factor analysis is the distribution range of the values through the parameters. The final value of the confusion matrix is also taken for the consideration. In the case of the age analysis to the results normality is equally distributed in all the range. The Fig.3 and Fig.4 is the plot between CG and SLCG pre prandid and results. Normalization of the plot can be obtained between the set of range. In this more people are fall under the abnormal category of less than 40 and the people above this are normal in CG and incase of SLCG below 10 is abnormal and remaining is highly normal range. In Fig.5 and Fig.6 gives the detailed description of post prandid analysis of CG and SLCG. In these plots CG is abnormal for less than 40 and remaining are normal and in SLCG it is vice versa. This graphical analysis is mainly for the factor selection for the future algorithm results. From the overall results of the plot analysis and confusion matrix formation age, CG pre prandid, SLCG pre prandid, CG post prandid, SLCG post prandid are taken as the factors for the future analysis. The final distribution of the normal and abnormal rate is based on the considered literature. These parameters are selected as factors because they have high distributed value in the final confusion matrix formation. The matrix prediction is obtained from the pshyc plot.

B. Error analysis:

	Abnormal	Normal	Class.error
Abnormal	272	4	0.014%
Normal	17	358	0.045%

Table1. final predicted values of random forest algorithm

Prediction	Abnormal	Normal
Abnormal	272	2
Normal	4	373

Table2. Final predicted values of support vector machine algorithm

The final error values [19] are tabulated for both the algorithm. The error prediction is to be done by analysis the testing data prediction of the datasets with the training data. The predicted normal results by the random forest is 93.23% and the error rate of SVM is 96.65%. The error in the normal abnormal range of predicted output is high in the random forest. In comparing the results of the both the algorithm support vector machine is highly optimal when compared to random forest.Finally SVM concluded as the optimal for the result prediction.

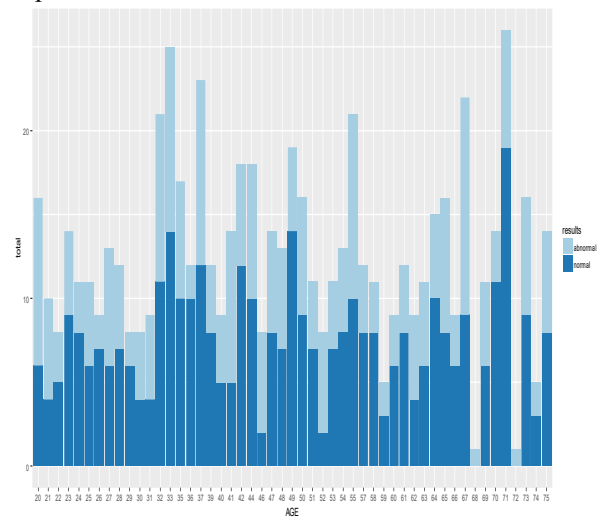


Fig.2 Plot analysis between the age and results



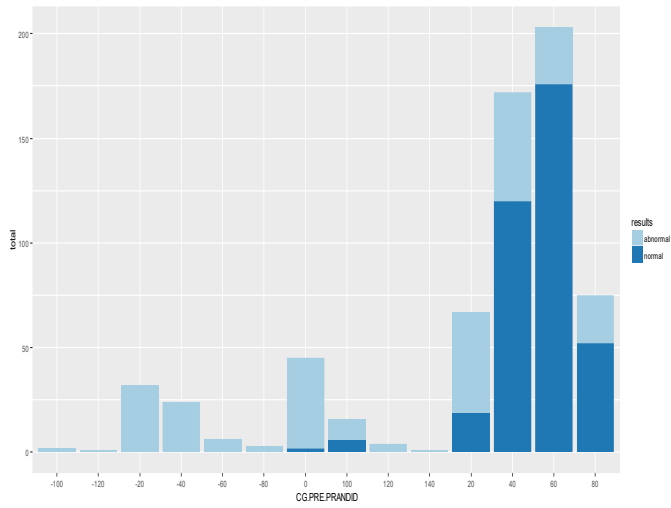


Fig.3 Plot analysis between CG.PRE prandid and results

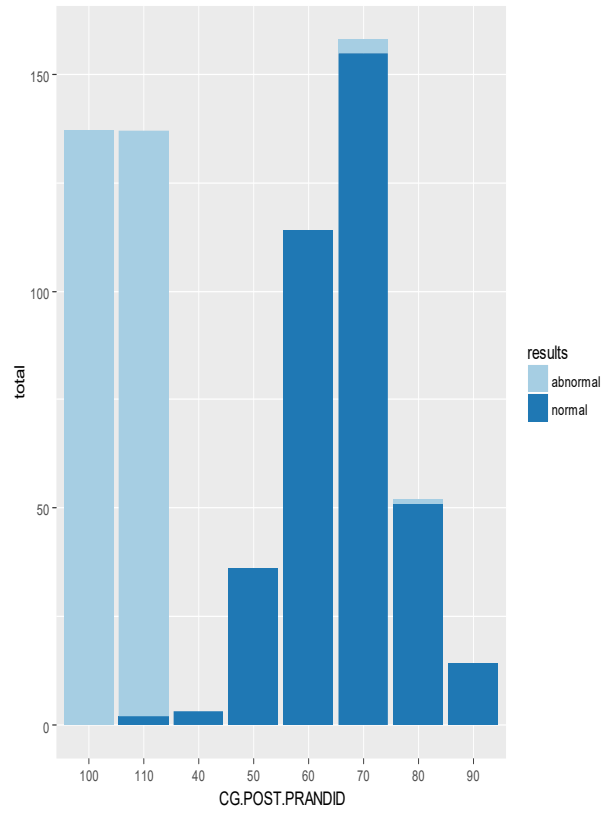


Fig.5 Plot analysis between CG.POST prandid and results

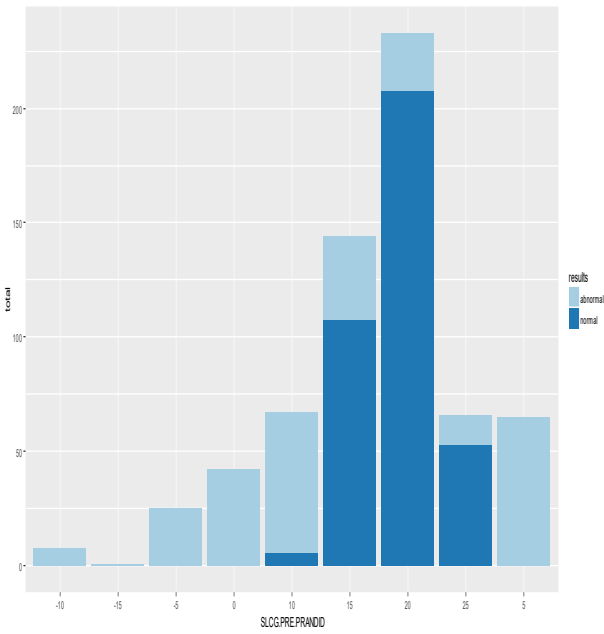


Fig.4 Plot analysis between SLCG.PRE prandid and results

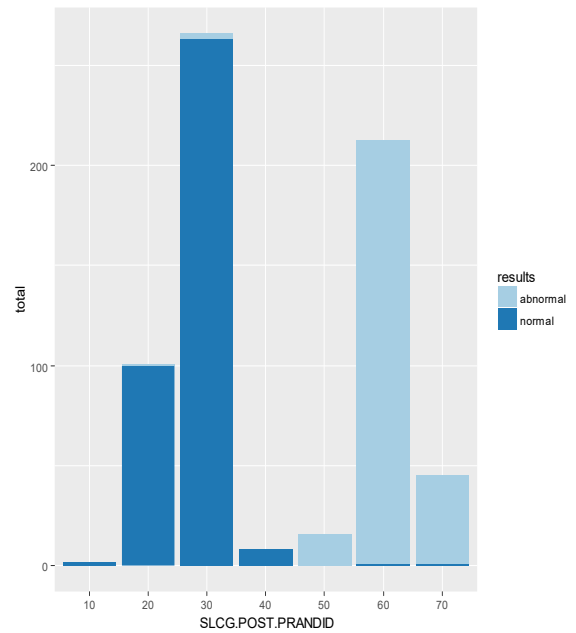


Fig.6 Plot between SLCG.POST prandid and results

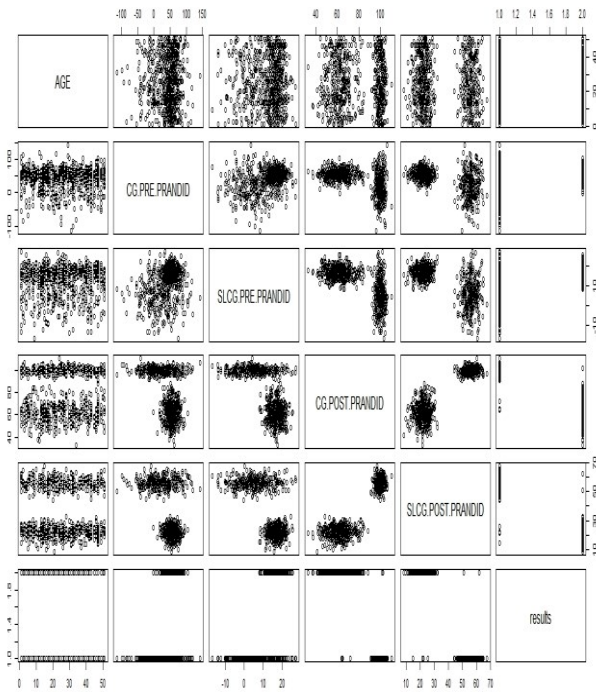


Fig.7. Combined plot for hepatitis datasets using R tool

V. CONCLUSION

In this analysis, the bioinformatics are used for the prediction and computation. Since, the current medical field are concerned with the natural data from the patients, these algorithms can be used for classification for any medical data. The factors being obtained from the generalized plot is tabulated and the results are obtained by the two algorithms. From these results the deviation can be predicted from the matching of techniques. However, a small deviation exists between the error rates by the two methods. Since in the medical field a minute deviation can produce a larger impact and thereby its consequences are large. So, this minute error has to be considered. By this analysis, the SVM technique proves more efficient and gives a normalized result. In future, more optimization can be obtained by the other techniques.

References

- [1] Gali Halevi & Henk F.Moed, "Evolution of BigData as Research and Scientific Topic: overview of literature", in Biometrics, September 2012.
- [2] Kuo Lane Chen, Huei Lee, "The Impact of BigData on the Healthcare Information system", Tranction of the International Conference on health information technology advanvement, 2013
- [3] Min Ja Kim, Dong Jin Suh, "Profile of Serum Bile Acids in Liver Disease", korrean J intern med, PMC
- [4] T R Prajwala, " A comparative study on Decision Tree and Random forest using R tool", IJRCCE, vol.4, issue 1, January 2015.
- [5] Alexandros Karatzoglou, David Meyer, Kurt Hornik, "Support vector machine in R", journal related on statistical software, april 2006, vol.15, issue 5, by Alexandros Karatzoglou
- [6] Olusegun Adekanle, A.Dennis, Samuel Anu Olowookere, Oluwasegun Ijarotimi, and Kayode Thaddeus Ijadunola, "Knowledge of Hepatitis B Virus Infection, Immunization with Hepatitis B Vaccine, Risk Perception, and Challenges to Control Hepatitis among Hospital Workers in a Nigerian Tertiary Hospital", Volume 2015 (2015), Article ID 439867, 6 pages.
- [7] Sara Romani, Seyed Masoud Hosseini, Seyed Reza Mohebbi, Shabnam Kazemian, Shaghayegh Derakhshani, Mahsa Khanyaghma, Pedram Azimzadeh, Afsaneh Sharifian, and Mohammad Reza Zali, "Interleukin-16 Gene Polymorphisms Are Considerable Host Genetic Factors for Patients' Susceptibility to Chronic Hepatitis B Infection", Volume 2014 (2014), Article ID 790753, 5 pages
- [8] M .Mostafa , E. Behairy , M. Azza , A. Sameh , and E.Ehab , "Serum Inter-Alpha-Trypsin Inhibitor Heavy Chain 4 (ITIH4) in Children with Chronic Hepatitis C: Relation to Liver Fibrosis and Viremia", Volume 2014 (2014), Article ID 307942, 7 pages
- [9] C .Salperwyck, V. Lemaire , "Incremental decision tree based on order statistics Neural Networks", The 2013 International Joint Conference on Neural Networks, DOI:10.1109/IJCNN.2013.6706907, Pages-1-8, Publication Year :2013
- [10] Hong Bo Li, Wei Wang, Hong Wei Ding, Jin Donh, "Trees Weighting Random Forest Method for Classifying High-Dimensional Noisy Data", IEEE 7th International Conference, Publication Year: 2010, pages:160-163
- [11] K .Durgesh , Srivastava, Lekha Bhambh , "Data classification using support vector machine", journal of theoretical and applied information technology
- [12] http://scikitlearn.org/stable/auto_examples/svm/plot_rbf_parameters.html
- [13] Biwaj Goankar and Christos Davatzikos, "Analytic estimation of statistical significance maps for SVM based multi-variate image analysis and classification", in PMC ,2013 sep:78:270-283.
- [14] Jason Brwle, "SVM for machine leaning", machine learning algorithm, april 2016
- [15] <http://www.statmethods.net/graphs/>
- [16] <https://www.r-bloggers.com/stacked-bar-charts-in-r/>
- [17] <https://www.rstudio.com/wp-content/uploads/2015/03/ggplot2-cheatsheet.pdf>
- [18] William Revele, dept. of psychology, North western university, "How to use the psych package for factor analysis and data reduction"
- [19] R-blogger, "Initial Impression of Range Lab" by Derek Joans, 2011

122 Finite Element Analysis of Palmaz -Schatz Stent and Express Stent Using Three Dimensional Models

Keerthana.S
 Department of Biomedical Engineering
 Sri Ramakrishna Engineering College
 Coimbatore, India
keerts.official@gmail.com

Visalakshi.cho
 Department of Biomedical Engineering
 Sri Ramakrishna Engineering College
 Coimbatore, India
sala19cho@gmail.com

Abstract—The paper reviews the Finite Element Analysis (FEA) on three dimensional models of two different types of stents namely Palmaz-Schatz stent and Express stent. The simulations are performed for 2 cases: first is stents made of 316 LN Stainless Steel material and L605 Cobalt Chromium alloy. FEA analysis is a computerised method that numerical uses Numerical techniques to analyse the behaviour of a Stent. A CAD model of the stents is generated that are divided into small and simpler elements known as Finite Elements. The stent CAD model is meshed, then it undergoes simulation process .The results are been Post-processed. From finite element analysis of stents the post processed results of Von Mises Stress were studied for strength analysis

Keywords— *Finite Element Analysis, Palmaz-Schatz stent, Express stent, Von Mises Stress.*

I. INTRODUCTION

A stent is a tiny wire like mesh tube, that are been inserted in an atherosclerotic vessel to treat the weak and narrow arteries. The stents are expanded and clean up the plaque formation allowing normal flow of blood. The two different kinds of biomaterials used for stent comparison are 316 LN Stainless Steel material and L605 Cobalt Chromium alloy. 316LN is a low carbon, nitrogen-enhanced version of Type 316 molybdenum-bearing austenitic stainless steel. They have high creep, stress-rupture and tensile strength at elevated temperature. L605 is a cobalt-chromium-tungsten-nickel alloy. It has good formability, high strength to 1500°F (816°C). Finite Element Analysis (FEA) on three dimensional models of two different types of stents namely Palmaz-Schatz stent Figure 1 and Express stent.

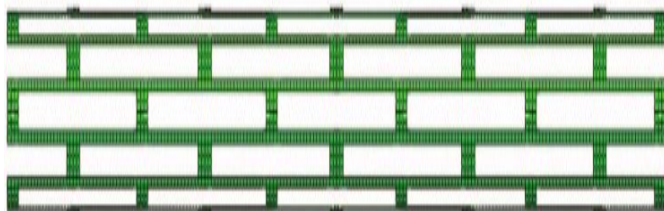


Figure 1: Palmaz-Schatz stent



Figure 2: Express stent

For accurate result CAD model is been prepared which is meshed then the boundary conditions are been applied and post processing is done.

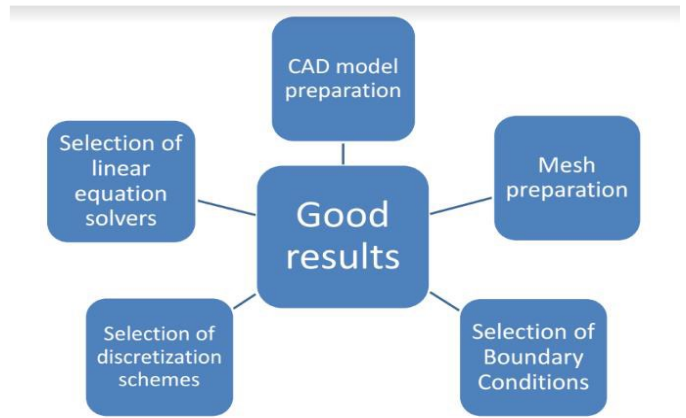


Figure 3: requirements for a good analysis result

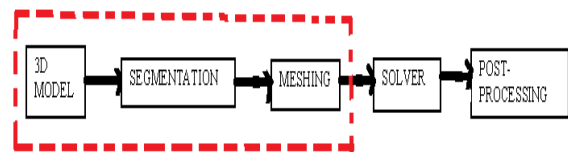


Figure 4: Steps involved in FEA analysis

By above steps Figure 4 results are scrutinised.

II. MODELLING PROCEDURE

A. Meshing

The mesh been used for FEA analysis of stents are Tetrahedral Parametric Mesh .Meshing designates the cells or elements known as finite elements on which the flow is solved. Is a discrete representation of the geometry of the problem. Has cells grouped into boundary zones where boundary conditions are been applied. In Tetrahedral Parametric Mesh, the mesh consists only triangular faces. Mesh Refinement is been adapted for enhanced accuracy and to eliminate the error.

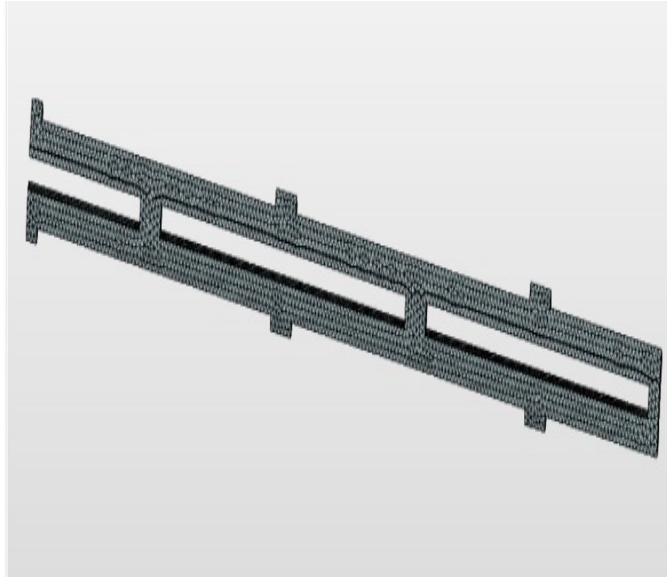


Figure 5: meshing result of Palmaz-Schatz stent

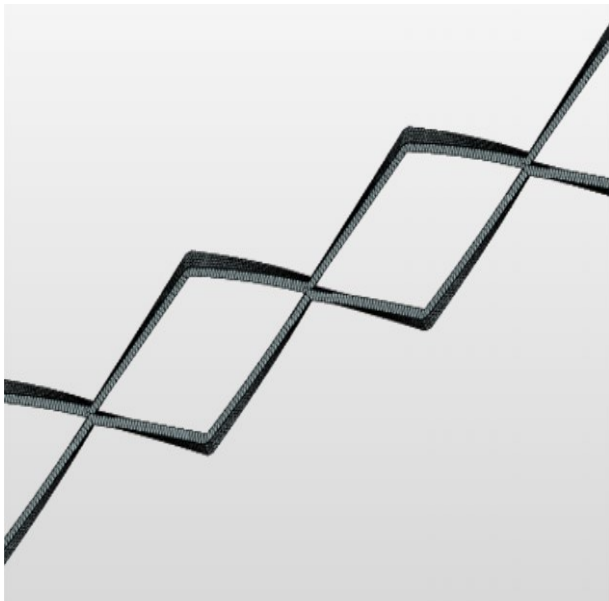


Figure 6: meshing result of Express stent

Due to cyclic symmetry only a portion of geometry will be considered. This helps in the analysis on a smaller mesh that would take less computational time and power.

B. Simulation

The analysis type 'Static analysis - advanced' under 'Solid mechanics'. The simulation run for each cases is performed. For the ease we will create topological sets in order to use them further in our boundary conditions. The topological sets which we will create will be based on the figure below which explains all the boundary and loading conditions.

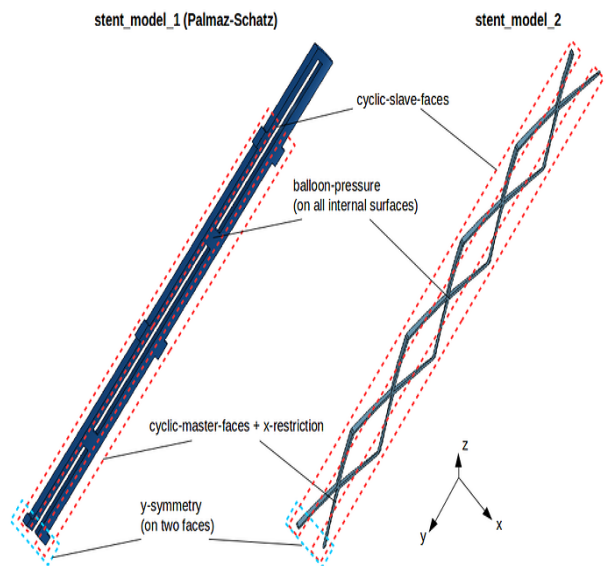


Figure 7: Topological sets of all boundary and loading conditions

The laminar flow module is used for this purpose, which uses Navier-Stroke's equation. Here blood is assumed to be an incompressible fluid with density 1060 kg/m³. Both Newtonian and Non-Newtonian was considered. For Newtonian behaviour, the blood viscosity is chosen to be 0.004 Pa.S. For non-Newtonian behaviour of blood, the power law model was considered for analysis.

C. Post Processing

Post-Processing involves extracting the desired stent properties from the computed field. The computed stent properties are then compared to results. The magnitude of von Mises stress can be viewed. In order to know which portion of the stent are yielded, the Von Mises stress values from 0 to 205e6 is rescaled.

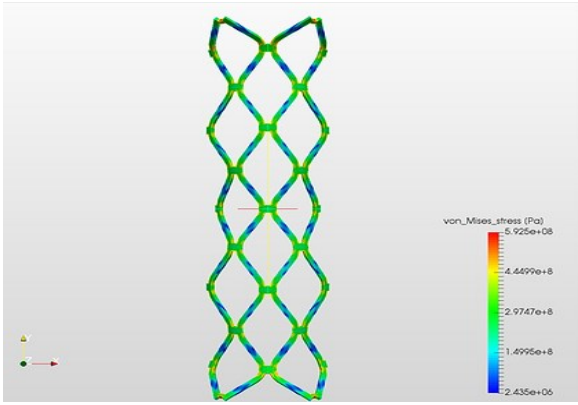


Figure 8: Post processing result for case 1

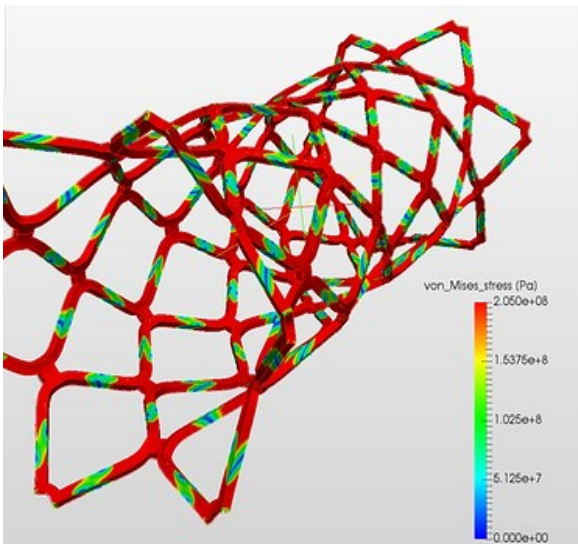


Figure 9: Post processing result for case 2

III. ANALYSIS OF VON MISES STRESS

Von Mises stress is used here to analyse whether stents can withstand the cyclic loading. Von Mises stress of the stent should be greater than the yield strength of the material. Yield strength of the 316L stainless steel is 205MPa and the yield strength of cobalt chromium is 450MPa. The Von Misses stress springs up from distortion energy failure theory.

Von Misses stress is expressed by,

$$\left[\frac{(\sigma_1 - \sigma_2)^2 + (\sigma_2 - \sigma_3)^2 + (\sigma_3 - \sigma_1)^2}{2} \right]^{1/2} \geq \sigma_y$$

Where

$$\left[\frac{(\sigma_1 - \sigma_2)^2 + (\sigma_2 - \sigma_3)^2 + (\sigma_3 - \sigma_1)^2}{2} \right]^{1/2} = \sigma_v$$

The above equation is Von Mises stress

Thus the failure analysis can be analysed by arriving at this equation

$$\sigma_v \geq \sigma_y$$

Von Mises stress of the should be greater than the yield strength of the material so it can withstand a maximum load capacity .With the post processing results the Von Mises stress is been compared with yield strength of the material to scrutinize the results.

IV. CONCLUSION

Comparison of the results is worth noting that the second model of stent is expanded considerably less compared to the first model case. Also the size of the second model become nearly half along y-axis compared to the first model case. But the second model expansion is more uniform than the first one.

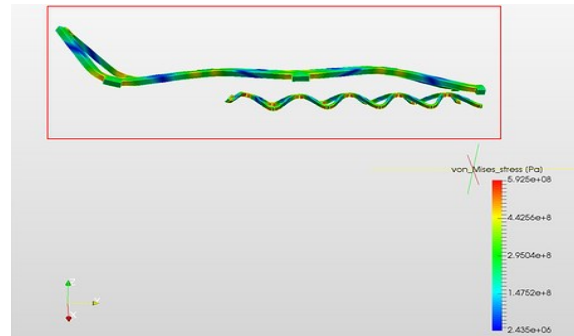


Figure 10: The stent model comparison of two cases

By using solid mechanics it's easier to analyse the static advanced behaviour of each stent which helps the surgical procedure easier and this seems to be a useful for scrutinizing the various stent materials for different application by non-invasive technique.

REFERENCES

- [1] AURICCHIO*, Ferdinand, M. Di Loreto, and E. Sacco. "Finite-element analysis of a stenotic artery revascularization through a stent insertion.5".
- [2] Computer Methods in Biomechanics and Biomedical Engineering 4.3 (2001): 249-263.
- [3] Poncin, P., et al. "Comparing and optimizing Co-Cr tubing for stent applications.3" Proceedings of the materials and processes for medical devices conference. 2004.
- [4] Vogel, T; Shindelman, L.; Nackman, G.; Graham, A. (2003). "Efficacious Use of Stents in the Femoral and Popliteal Arteries.".Journal of Vascular Surgery.38 (6): 1178–1183.
- [5] Céline Bilardo. "Hans Wallsten, inventor of the stent". Invivo Magazine. Retrieved 28 September 2016.
- [6] Effect of rapid solidification and heat treatment on Co-20 wt. %Cr alloy for biomedical applications A L Ramirez-Ledesma1 , M A Aguilar-Mendez , R A Rodriguez-Diaz , J A Juarez-Islas.

A Preliminary Study on the Control of Nano Acrylamide Polymerization Reaction

N. Priyadharshini

Department of Instrumentation Engineering
MIT Campus, Anna University
Chennai, India

K. Kamalanand

Department of Instrumentation Engineering
MIT Campus, Anna University
Chennai, India
Email: kamalanand@mitindia.edu

Abstract—In this work, an attempt has been made to develop a control system for controlling the nano acrylamide polymerization reaction for mimicking the optical properties of soft tissues in ultraviolet spectrum. The nano acrylamide polymerization reaction process was modeled using an ARX model. Further, a proportional-Integral (PI) controller was designed to control the reaction. It is observed that the developed control scheme is suitable for control of the nano acrylamide polymerization reaction since the absorbance can be controlled to different levels in order to mimic various human soft tissues. This work appears to be clinically significant since the development of optical phantoms is highly useful for medical diagnostic applications.

Keywords—Acrylamide polymerization; nanotechnology; tissue mimicking materials; control systems.

I. INTRODUCTION

Light has the ability to penetrate a tissue, interact with the tissue components and to escape the tissue. The detected light is the key to diagnosis of several diseases and also for several therapeutic applications. Hence measurement and analysis of the optical properties of a tissue helps in properly designing devices, interpreting measurements and therapy planning [1].

Tissue-mimicking phantom play an important role in diagnostic research and development of diagnostic equipment without the requirement of using animal experiments. Tissue mimicking phantoms are materials that mimic a body tissue under analysis [2].

Polyacrylamide tissue mimicking phantoms are highly efficient for mimicking the properties of actual tissues under investigation. Further, nano acrylamide polymers exhibit enhanced tissue mimicking properties when compared to conventional polymers [3-5]. The objective of this work is to develop a suitable control scheme for the nano acrylamide polymerization reaction for tissue mimicking applications.

II. METHODOLOGY

In this work, an attempt has been made to develop a nano acrylamide polymer for mimicking the optical properties of

soft tissues in ultraviolet spectrum. The nano acrylamide/bis-acrylamide particles were generated using a planetary ball milling machine. The particle size of the milled material was estimated using a Scanning Electron Microscope (SEM) and Particle Size Analyzer(PSA). It was found that the milled particles were in nanometric dimensions. Further, the tissue mimicking phantoms of 20% concentration was prepared as per the standard protocol described by Kamalanand *et al* [3] and the UV absorbance was measured using a UV spectrophotometer in the wavelength range of 310 to 430 nm.

The inputs given to the nano acrylamide polymerization reaction is a step change in temperature (25°C and 24.8°C) and 20% concentration. The outputs are absorbance and Transmittance. An autoregressive model with exogenous terms was used to model the nano acrylamide polymerization reaction, using the prediction error method.

Further, a feedback control scheme was employed to control the nanoacrylamide polymerization reaction using a PI controller. The PI parameters were tuned using genetic algorithms. Figure 1 shows the block diagram of the adopted control scheme.

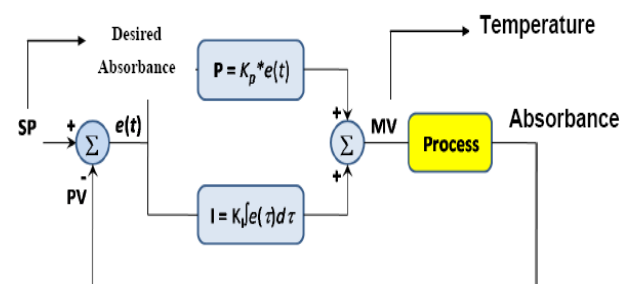


Figure 1. Block diagram representation of feedback control of the nano acrylamide polymerization reaction

III. RESULTS AND DISCUSSION

Figure 2 shows the set point or the desired absorbance and the controlled process output. It is observed that the developed PI based control scheme has the ability of set point tracking. The set point given to the control system was

2.01 Absorbance. Results demonstrate that the developed PI based control scheme is efficient in developing nano acrylamide polymers whose absorbance can be controlled to the desired level so that different tissues can be mimicked.

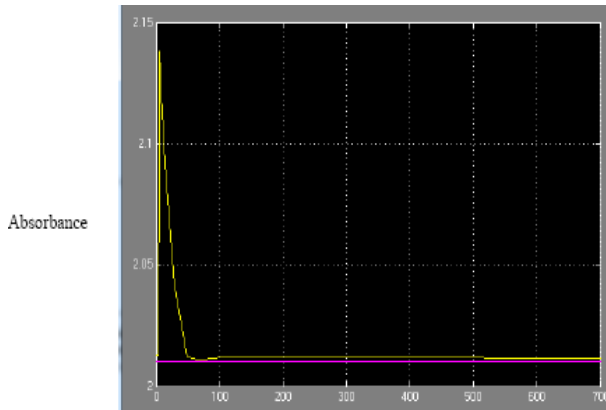


Figure 2. Variation of process output and the set point shown as a function of time in seconds

IV. CONCLUSIONS

The optical absorption properties of the tissue such as absorbance relates to the ability of light to interact with the tissue structures and components. In particular, many diagnoses are highly efficient when carried out in the

ultraviolet wavelength range. In this work, an attempt has been made to develop control system for the nano acrylamide polymerization process for mimicking the optical properties of soft tissues in ultraviolet spectrum. Results demonstrate that the developed control scheme is suitable for control of the nano acrylamide polymerization reaction since the controller is able to track the set point and the absorbance can be controlled to different levels in order to mimic various human soft tissues. This work appears to be clinically significant since the development of optical phantoms is highly useful for medical diagnostic and therapeutic applications.

REFERENCES

- [1] Jacques, Steven L. "Optical properties of biological tissues: a review." *Physics in medicine and biology* 58.11 (2013): R37.
- [2] Othman, N. S., Jaafar, M. S., Rahman, A. A., Othman, E. S., & Rozlan, A. A. (2011). Ultrasound speed of polymer gel mimicked human soft tissue within three weeks. *International Journal of Bioscience, Biochemistry and Bioinformatics*, 1(3), 223.
- [3] Kamalanand, K., Sridhar, B. T. N., Rajeshwari, P. M., & Ramakrishnan, S. (2010). Correlation of Dielectric Permittivity with Mechanical Properties in Soft Tissue-Mimicking Polyacrylamide Phantoms. *Journal of Mechanics in Medicine and Biology*, 10(02), 353-360.
- [4] Krishnamurthy, K., Sridhar, B. T. N., Rajeshwari, P. M., & Swaminathan, D. R. (2009). Correlation of Electrical Impedance with Mechanical Properties in Models of Tissue Mimicking Phantoms. In 13th International Conference on Biomedical Engineering (pp. 1708-1711). Springer Berlin Heidelberg.
- [5] Zhang, L., & Webster, T. J. (2009). Nanotechnology and nanomaterials: promises for improved tissue regeneration. *Nano Today*, 4(1), 66-80.

A Study on Time and Frequency Domain Analysis of Two Class Motor Imagery Signals

S. Sridevi

Department of Production
Technology
Madras Institute of Technology,
Anna University
Chennai 600044, India
sridevi2012608023@gmail.com

P. Karthikeyan

Department of Production
Technology
Madras Institute of Technology,
Anna University
Chennai 600044, India
karthi_209170@yahoo.com

S. Ramakrishnan

Biomedical Engineering Group,
Department of Applied Mechanics
Indian Institute of Technology
Madras
Chennai 600036, India

Abstract— Development of human body motion classification method gains a foremost consideration in several applications for disabled communities. Essentially in brain computer interface (BCI), the electroencephalogram (EEG) signals possess valuable information about various functions of human body including motor movements. Various motor imagery tasks are classified by acquiring and analyzing the oscillatory and dynamic signals of brain. In this work classification of movement of right hand (task-1) and feet movement (task-2) is studied using two class motor imagery (002-2014) data set. Raw EEG data were recorded using 15 channels from 14 subjects (four females and 9 BCI novices aged between 20 to 30 years). Surface Laplacian filter (SL) is used to preprocess the raw EEG signal and elliptical 6th order band pass filter is used to separate various sub-bands such as delta, theta, alpha, beta and gamma. Statistical features like bandpower, kurtosis, mean, median, mode, root mean square (RMS), skewness, standard deviation (STD) and variance are extracted for both time domain and frequency domain signals and classified using K nearest neighbor (KNN) and Support Vector Machine (SVM) classifiers. The result shows that, mean and median give maximum average classification accuracy 54.3% compared to existing work.

Keywords— BCI, EEG, motor imagery, KNN, SVM, hand, foot

I. INTRODUCTION

Recent days BCI takes an importance to control and communicate with external world for hand and foot impaired communities. The Rehabilitation Engineering Group at University of Campinas (Unicamp) Brazil, aimed to optimization of various techniques to achieve artificial movement, artificial sensations are generated from restored movements and investigation of motor control strategies in normal subjects and adaptation of these algorithms to neuromuscular electrical stimulation (NMES) systems. As a part of the above strategies, described NMES systems were used to restore upper and lower limb functions in spinal cord injuries. In order to achieve functional hand movement to execute some basic activities such as drinking, eating, writing and typing etc., hand muscle activation sequences were identified. 16 channels simulator used to implement complex algorithm. Neural network and ruled based substates algorithms implemented into one hybrid control system and present good results [1, 2]. In [3], have examined that

topographies of mu and beta rhythm in motor imagery and actual movements. Over sensorimotor cortices, mu topographies exposed bilateral foci of de-synchronization, whereas over the vertex, beta topographies exposed peak de-synchronization. Using continuous wavelet transform salient spatio-temporal features extracted to classify various wrist movements [4]. In [5], classified left or right hand imaginary movements using type-2 fuzzy logic approach (T2 FL). When compared to linear discriminant analysis (LDA), T2 FL proved that has been given favorable classification accuracy and has been exposed more robust during presence of noise. In [6], classified imagined left-right movement using wavelet transform and auto-regressive (AR) parameter model. Mean of absolute values, standard deviation and average power were the features used to find feature vector for each sub-bands. To estimate AR model, Burg's method was used. This technique was more accurate and showed better resolution without the problem of spectral leakage. To develop BCI system, [7] classified right and left motor imagery based on bispectrum for that four coefficients of AR model, four features related to PSD and four features related to third order statistics were extracted. LDA, SVM and NN classifiers were used to classification. From the experimental results, minimal misclassification rate was given by SVM classifier. [8] recognized right and left motor imageries using harmonic wavelet transform (HWT) for that Graz BCI data set used that is open data set available for analyzing motor imagery. Alpha rhythm has sensory motor task signals that can change the cortex functional connectivity. This phenomenon leads to amplitude suppression or an amplitude enhancement. Feature vector has developed using bispectrum and PSD. LDA classifier used to classify the data. In [9], classified various wrist movements such as extension, pronation, flexion and supination of both right and left hands. To extract features wavelet pocket transform that partitions the frequency axis not only toward the low frequency but also toward the high frequency, thereby giving a balanced tree. For classification, radial basis function used. This paper targets to examine whether difference in statistical features that could be used to discriminate right hand movement and feet movement. For this reason, we use statistical features both time and frequency domains that are extracted from five different frequency bands from three channels. This paper is organized as follows.

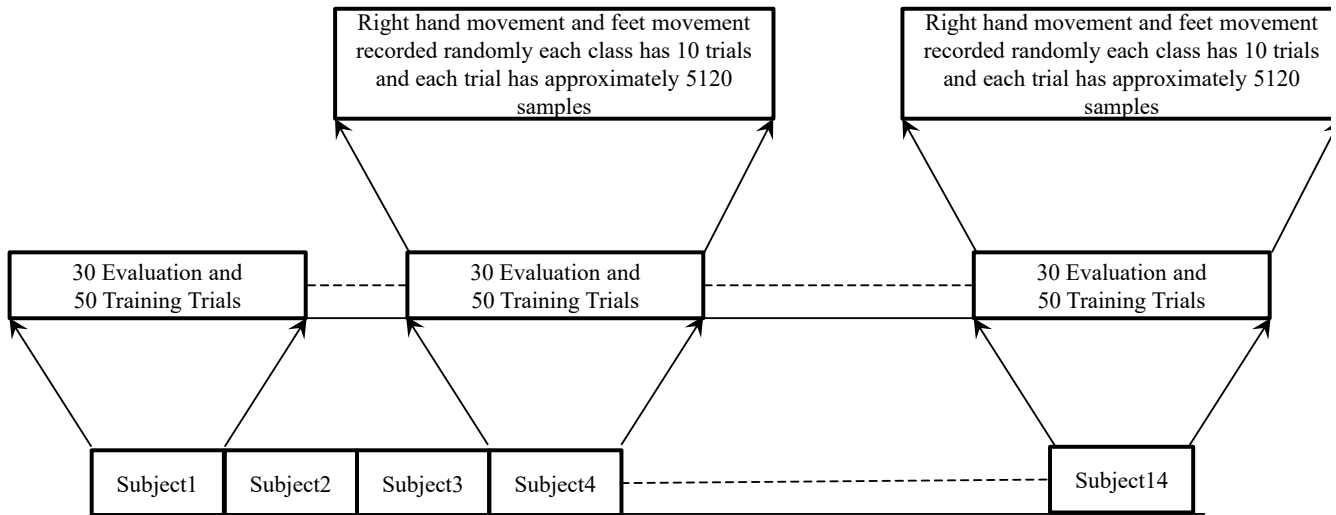


Fig. 1 Schematic representation of the protocol

Section II describes about material used to analysis that includes dataset and participants, movement stimulus method and signal acquisition. Section III presents methodology that consists of filtering, signal processing about time domain and frequency domain analysis, feature extraction, feature vector and classification methods. Section IV describes results and discussion of this analysis.

II. MATERIALS USED

A. Dataset and Participants

All data used in this study is downloaded from <http://bnci-horizon-2020.eu/database/data-sets>. These data sets consist of 112(14*3 evaluation and 14*5 training) EEG recordings taken from 14 subjects. Each subject performed 8 experimental runs: each run consists of ten right hand movement and ten feet movement trials [10]. Detailed version of the experiment protocol is shown in fig 1.

B. Movement Stimulus Method and Signal Acquisition

Visual stimuli were used to obtain EEG signals. In this data set has two classes of motor movement imagery dynamic brain signals, namely Task – 1 (class 1) and Task – 2 (class 2). The EEG signals were recorded from 15 electrodes positioned as shown in the fig.2. Center electrodes were positioned at C3, Cz and C4 where Laplacian derivations were calculated. Each signals sampled at 512 samples per second [10].

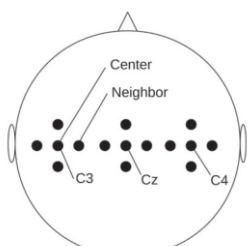


Fig. 2 Electrodes positions

III. METHODOLOGY

The fig. 3 illustrated that the block diagram of motor imagery recognition. All signals were preprocessed i.e filtered using SL filter and sub bands are segmented using 6th order band pass elliptical filter with sampling frequency is 512Hz and the pass band ripple is 1dB that are delta (δ : 1–4 Hz), theta (θ : 4–8 Hz), alpha (α : 8–13 Hz), beta (β : 13–30 Hz), and gamma (γ : 30–49 Hz) are shown in the fig. 4 [11]. Then features extracted both time domain and frequency domain and classified using machine learning methods. A brief description on each block is given below.

A. Filtering

Even though EEG is aimed to acquire brain activity but also it records various signals say artifacts over various positions in the scalp. It can be divided into two groups they are physiologic and extraphysiologic artifacts. Physiological artifacts can be generated from subjects body other than brain (ie, tongue, eye movement) and extraphysiologic artifacts arises from outside the body [12]. To get pure EEG signal, these types of noises should be removed. While removing noises certain useful information from EEG signals may be removed. So, familiarity is essential to interpret EEGs clinically [13].

To remove artifacts, SL filter is used in this work. EEG signal is generated by brain based on neural activities. It possesses different spatial frequencies. SL filter is extracted the possibly useful information from the middle frequencies. The SL can be defined as the second order spatial derivative of the potentials acquired from surface. Because of its intrinsic spatial high-pass filtering characteristics, the SL is used to reduce the volume conduction effect by improving the high-frequency spatial resolution than surface potentials [14]. The mathematical modeling of SL filter is given as

$$X_{new} = X(t) - \frac{1}{N_E} \sum_{i=1}^{N_E} X_i(t) \quad (1)$$

Where, X_{new} : signal after filtering; $X(t)$: raw EEG signal; NE : number of neighbor electrodes(4 electrodes).

B. Signal Processing

To extract features, EEG signal processing includes following two methods of analysis:

- Time domain analysis and
- Frequency domain analysis

1. *Time Domain Analysis*: Raw EEG signals have spatial information, temporal information of the signal and various noises. Noises are eliminated using SL filters.

The parameters are computed from time domain signal, as contrasting to other features that are measured using frequency domain. These factors are capable to differentiate various mental tasks [15].

over the time and its uniformity. Autocorrelation and cross-correlation uses in finding synchronicity between channels. Time domain features offer only spatial information, but it eliminate temporal information [16].

2. *Frequency Domain Analysis*: Frequency domain analysis can be defined as the representation of frequency components and estimations of all correlated features from the frequency of a signal. Fast Fourier Transform (FFT) method is used to analysis features. When a signal is studied in frequency domain, its temporal information will lose [17]. Occurrence of various events in specified time can be measured by its frequency. Non-stationary EEG signals consist of events at different frequencies. Power Spectral Density (PSD) is the utmost frequently used feature in frequency domain which is used to understand local stationary behavior. Also used to acquire time progressing nature of EEG [16]. Spectrum estimation is estimated by nonparametric technique which deals with the approximation of the autocorrelation from a given data set. The power spectrum is then estimated by Fourier transformation of the estimated autocorrelation sequence [18] . Fig 5. Shown the PSD of sub bands.

1. *Non parametric method*: To evaluate the power spectrum, Welch method is popularly used. The sequences are permitted to overlay and a data window (Hamming window) is applied to each sequence. Over all data is segmented into 8 segments with 50% overlap. Let, be the sequence, where $d=1, 2, 3, \dots, L$ are the signal intervals and each interval length is M . So, the Power Spectral Density (PSD), according to Welch is given by:

$$\widehat{P}_d(f) = \frac{1}{MU} \left| \sum_{n=0}^{M-1} x_d(n)w(n)e^{-j2\pi fn} \right|^2 \quad (2)$$

where, U =normalization factor for the power in the windowing function, selected as:

$$U = \frac{1}{M} \sum_{n=0}^{M-1} |w(n)|^2 \quad (3)$$

where, $w(n)$ =windowed data. The welch power spectrum is the average over these modified periodograms that is:

$$\widehat{P}_{Welch}(f) = \frac{1}{L} \sum_{i=0}^{L-1} \widehat{P}_d(f) \quad (4)$$

where \widehat{P}_{Welch} is the periodogram of the EEG signal of each interval [18].

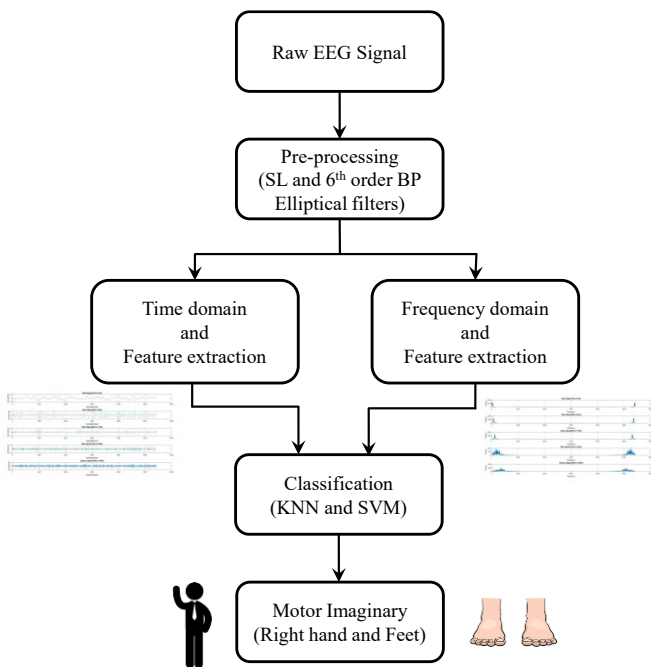


Fig. 3 Block diagram of the motion recognition system

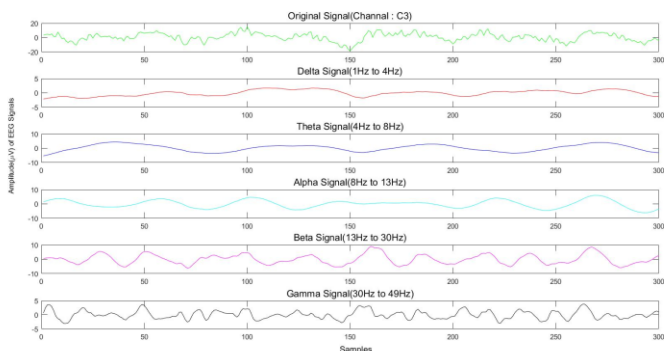


Fig. 4 Sub bands of the EEG signal

By calculating mean, one can get an idea related to amplitude of a particular signal at a particular time interval. Variance and STD shows that in what way the signal extents

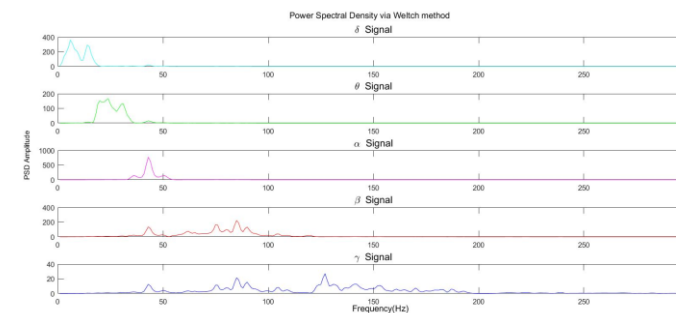


Fig. 5 PSD estimation of sub bands

C. Feature Extraction

Signals are a composition of several sub bands. Each sub band has its own characteristics. To characterize the signal, it should decompose into various sub bands. In this study, conventional features are extracted, classified using KNN and SVM classifiers and are compared.

- Conventional features: For classifying motor imaginary signals, set of statistical features (band power, kurtosis, mean, median, mode, root mean square, skewness, standard deviation and variance) are extracted from various sub bands. Description of statistical features discussed in table 1.

Table.1 Description of statistical features

Features	Description
Band Power	How much power is the licensee permitted to emit within its band and geographic area of an EEG signal.
Kurtosis	Kurtosis measures the tailedness of the probability distribution as opposed to the peakedness in the centre
Mean	Mean corresponds to the center of a set of potentials
Median	The median is the value separating the higher half of electrode potentials, from the lower half.
Mode	A potential that appears most often is the mode.
Root Mean Square	The root mean square value of a quantity is the square root of the mean value of the squared values of the quantity taken over an interval
Skewness	Skewness tells us about the direction of variation of the data set.
Standard Deviation	Measures the deviations of electrodes potential from the mean value[13]
Variance	Measures the variability of electrodes potential [13]

D. Feature Vector

50 training trials and 30 evaluation trials were recorded per class per subject. 700 (14 subjects * 50 training trials) training trials and 420 (14 subjects * 30 evaluation trials) evaluation trials were considered per class for all subjects. 1120 trials were processed per class for all subjects. Time taken to acquire per trials is ten seconds i.e approximately 5120 samples per trial.

EEG signal acquired from 15 electrodes. Laplacian derivations calculated from three central electrodes namely C3, Cz and C4. Five sub bands extracted from each electrodes. Features are computed from 15 sub bands (5 sub bands * 3 electrodes). Nine features per sub band are computed. So, totally 135 feature vectors (9 features * 15 sub bands) are extracted for classification.

E. Classification

It's important to identify best classifiers among various classifiers, to classify the input data into correct class during data analysis. For that the data analyzers can review the

literature to recognize about classifiers family outside of their domain of knowledge. In this work we identify, KNN and SVM classifiers will be best classifiers based on the review [19].

1. *KNN Classifier*: KNN is well known supervised learning algorithms. Where the class of a new input data is predicated based on neighboring training samples existing in the feature vector. The distance is calculated using the Euclidian distance method[20]. In general, vector calculation solves by considering direction and magnitude. But in Euclidian distance only the physical distance is calculated.
2. *SVM Classifier*: SVM is widely used supervised learning algorithms. It develops a hyper plane to separate data classes where the margin is maximized in each sides of the hyper plane by selecting suitable support vectors. Therefore, the separating hyper plane is oriented perpendicular to the shortest line separating the convex hulls of the training data for each class, and it is located midway along line [21].
3. *Performance Measures*: Performance of both classifiers is calculated by assessing sensitivity (Sn) or recall, specificity (Sp), positive predictive value (PPV) or precision and accuracy (Acc). Definition of performance measures discussed in table 6.

Table 6. Definition of Performance Measures

Sensitivity (Sn)	The proportion of actual positive cases which are correctly identified.
Specificity (Sp)	The proportion of actual negative cases which are correctly identified.
PPV	The proportion of positive cases that were correctly identified.
Accuracy (Acc)	The proportion of the total number of predictions that were correct

Equations (4)–(7) are used to determine the performance measures. Where TP stands for True Positive, TN stands for True Negative, FP stands for False Positive and FN stands for False Negative [35].

$$Sensitivity (Sn) = TP / (TP + FN) \quad (4)$$

$$Specificity (Sp) = TN / (TN + FP) \quad (5)$$

$$PPV = TP / (TP + FP) \quad (6)$$

$$Accuracy (Acc) = (TP + TN) / (TP + TN + FP + FN) \quad (7)$$

IV. RESULTS AND DISCUSSION

According to the planned methodology, the feature vectors were organized to send two different classifiers. In such a non-linear data classification problems, a train data grouped and a test data grouped where in this analysis the data set consists of EEG samples taken from 14 subjects. Each subject has 50 testing trials per class and 30 evaluation trials per class. 15 electrodes are used to acquire EEG signals. Five different sub bands are extracted from three electrodes namely C3, Cz and C4. Nine features are extracted from sub bands for three

electrodes. The classification is performed by two different motor imaginary signals right hand and feet.

Table 2. Performance measures of KNN classifier for time domain

Feature	Sn(%)	Sp(%)	PPV(%)	Acc(%)
Bandpower	38.5	66.1	53.2	52.3
Kurtosis	52.1	53.6	52.9	52.9
Mean	56.4	50.0	53.0	53.2
Median	51.4	51.4	51.4	51.4
Mode	72.2	57.1	52.0	51.8
RMS	40.7	64.3	53.3	52.5
Skewness	47.5	59.3	53.8	53.4
STD	40.4	65.0	53.6	52.7
Variance	42.5	62.5	53.1	52.5

Table 3. Performance measures of SVM classifier for time domain

Feature	Sn(%)	Sp(%)	PPV(%)	Acc(%)
Bandpower	99.6	1.1	50.2	50.4
Kurtosis	87.9	14.6	50.7	51.2
Mean	60.0	49.6	53.8	54.3
Median	67.9	40.7	53.4	54.3
Mode	7.5	96.4	67.7	52.0
RMS	72.5	30.7	51.1	51.6
Skewness	52.5	52.1	52.3	52.3
STD	45.4	57.1	51.4	51.2
Variance	9.6	93.6	60.0	51.6

Table 4. Performance measures of KNN classifier for frequency domain

Feature	Sn(%)	Sp(%)	PPV(%)	Acc(%)
Bandpower	51.8	52.5	52.2	52.1
Kurtosis	50.7	52.4	51.6	51.6
Mean	25.6	76.3	51.9	50.9
Median	30.5	69.4	49.9	50.0
Mode	52.1	49.3	50.7	50.7
RMS	52.3	49.4	50.8	50.8
Skewness	54.7	49.5	52.0	52.1
STD	54.1	49.6	51.8	51.9
Variance	37.3	63.6	50.6	50.4

Table 5. Performance measures of SVM classifier for frequency domain

Feature	Sn(%)	Sp(%)	PPV(%)	Acc(%)
Bandpower	89.2	1.1	50.1	50.4
Kurtosis	58.6	48.7	53.3	53.6
Mean	40.8	59.5	50.2	50.1
Median	41.5	59.8	50.8	50.7
Mode	51.3	13.5	50.8	51.3
RMS	50.1	1.1	50.0	50.1
Skewness	50.9	52.5	51.7	51.7
STD	89.2	11.3	50.2	50.3
Variance	55.3	46.3	50.7	50.8

The comparison of Table 2, Table 3, Table 4 and Table 5 shows that performance measures of various features for both time and frequency domain. In time domain the maximum classification accuracy is achieved with SVM classifier for mean and median is 54.3%. The comparisons of other features are low. Maximum sensitivity is 99.6% obtained for bandpower. Maximum specificity is 96.4% is achieved for

mode and the maximum precision is 67.7% is obtained for mode.

In frequency domain the maximum classification accuracy is achieved with SVM classifier for kurtosis is 53.6%. The comparisons of other features are low. Maximum sensitivity is 89.2% obtained for bandpower and STD. Maximum specificity is 59.8% is achieved for median and the maximum precision is 53.3% is obtained for kurtosis.

V. CONCLUSION

In this work binary class classifications of two motor imagery tasks of EEG signals are examined through KNN and SVM classifier. With the aim of construct a fast and active BCI, a finest classification scheme is investigated with the basic statistical features. Results are shown that based on features extraction. SVM classifier gives better result than KNN. Upcoming works will plan to acquire EEG data from various healthy subjects and various right or left hand motor imagery and also planned to include higher order statistical features to reduce misclassification rate.

ACKNOWLEDGMENT

The authors would like to thanks to Prof. A. Jothilingam, Head of the Department, Prof. G. Muralidharan and all Department staff members, Production Technology, MIT-Campus, Anna University, Chennai. Also we would like to thank Dr. R. Yuvaraj.

REFERENCES

- [1] Antonio A. F. Quevedo, Francisco Sepulveda, Maria C.F. Castro, Francois X. Sovi, Percy Nohama, and A. C. Jr., "Development of control strategies for restoring function to paralyzed upper and lower limbs," in *Engineering in Medicine and Biology Society, 1997. Proceedings of the 19th Annual International Conference of the IEEE*, 1997, pp. 1946-1949 vol.5.
- [2] Ferrari de Castro, M. Claudia, Cliquet, and Alberto, "Artificial Grasping System for the Paralyzed Hand," *Artificial Organs*, vol. 24, pp. 185-188, 2000.
- [3] McFarland D. J., Miner L. A., Vaughan T. M., and Wolpaw J. R., "Mu and beta rhythm topographies during motor imagery and actual movements," *Brain Topogr.*, vol. 12, 2000.
- [4] H. Lakany and B. A. Conway, "Classification of Wrist Movements using EEG-based Wavelets Features," in *2005 IEEE Engineering in Medicine and Biology 27th Annual Conference*, 2005, pp. 5404-5407.
- [5] P. Herman, G. Prasad, and T. M. McGinnity, "Investigation of the Type-2 Fuzzy Logic Approach to Classification in an EEG-based Brain-Computer Interface," *Conf Proc IEEE Eng Med Biol Soc*, vol. 5, pp. 5354-7, 2005.
- [6] B. Xu, A. Song, and J. Wu, "Algorithm of Imagined Left-Right Hand Movement Classification Based on Wavelet Transform and AR Parameter Model," in *2007 1st International Conference on Bioinformatics and Biomedical Engineering*, 2007, pp. 539-542.
- [7] S.-M. Zhou, J. Q. Gan, and F. Sepulveda, "Classifying mental tasks based on features of higher-order statistics from EEG signals in brain-computer interface," *Information Sciences*, vol. 178, pp. 1629-1640, 2008.
- [8] Renhuan yang, Aiguo song, and Baoguo xu, "Feature Extraction of Motor Imagery EEG Based on Wavelet Transform and Higher-Order Statistics," *International Journal of Wavelets, Multiresolution and Information Processing*, vol. 08, pp. 373-384, 2010.
- [9] Y. U. Khan, "Imagined wrist movement classification in single trial EEG for brain computer interface using wavelet packet,"

- International Journal of Biomedical Engineering and Technology*, vol. 4, pp. 169-180, 2010.
- [10] D. Steyrl, R. Scherer, J. Faller, and G. R. Muller-Putz, "Random forests in non-invasive sensorimotor rhythm brain-computer interfaces: a practical and convenient non-linear classifier," *Biomed Tech (Berl)*, vol. 61, pp. 77-86, Feb 2016.
- [11] R. Yuvaraj, M. Murugappan, N. M. Ibrahim, K. Sundaraj, M. I. Omar, K. Mohamad, *et al.*, "Optimal set of EEG features for emotional state classification and trajectory visualization in Parkinson's disease," *Int J Psychophysiol*, vol. 94, pp. 482-95, Dec 2014.
- [12] Selim R Benbadis and Helmi L Lutsep, "EEG Artifacts : Overview, Physiologic Artifacts, Extraphysiologic Artifacts," *Medscape References*, 2015.
- [13] M. Murugappan, N. Ramachandran, and Y. Sazali, "Classification of human emotion from EEG using discrete wavelet transform," *Journal of Biomedical Science and Engineering*, vol. 3, p. 390, 2010.
- [14] T. Al-ani and D. Trad, *Signal Processing and Classification Approaches for Brain-computer Interface*: INTECH Open Access Publisher, 2010.
- [15] M. Vourkas, S. Micheloyannis, and G. Papadourakis, "Use of ANN and Hjorth parameters in mental-task discrimination," in *2000 First International Conference Advances in Medical Signal and Information Processing (IEE Conf. Publ. No. 476)*, 2000, pp. 327-332.
- [16] V. K. Harpale and V. K. Bairagi, "Time and frequency domain analysis of EEG signals for seizure detection: A review," in *2016 International Conference on Microelectronics, Computing and Communications (MicroCom)*, 2016, pp. 1-6.
- [17] V. Azimirad, M. Alimohammadi, A. Joudi, A. Eslami, and M. Farhoudi, "Analysis of PSO, AIS and GA-based optimal Wavelet-Neural Network classifier in Brain-Robot Interface," *IRBM*, vol. 36, pp. 240-249, 8// 2015.
- [18] D. P. Subha, P. K. Joseph, U. R. Acharya, and C. M. Lim, "EEG signal analysis: a survey," *J Med Syst*, vol. 34, pp. 195-212, Apr 2010.
- [19] M. Fern, #225, ndez-Delgado, E. Cernadas, Sen, #233, *et al.*, "Do we need hundreds of classifiers to solve real world classification problems?," *J. Mach. Learn. Res.*, vol. 15, pp. 3133-3181, 2014.
- [20] K. Palanisamy, M. Murugappan, and S. Yaacob, "Multiple physiological signal-based human stress identification using non-linear classifiers," *Elektronika ir elektrotechnika*, vol. 19, pp. 80-85, 2013.
- [21] U. R. Acharya, S. V. Sree, S. Chattopadhyay, and J. S. Suri, "Automated Diagnosis of Normal and Alcoholic EEG Signals," *International Journal of Neural Systems*, vol. 22, p. 1250011, 2012.

Selection of Dominant Voice Features for Accurate Detection of Parkinson's disease

Spriha Chandrayan
Department of
Electronics and
Communication
Engineering
Birla Institute of
Technology, Mesra
priha.chandrayan@gmail.com

Aarushi Agarwal
Department of
Electronics and
Communication
Engineering
Birla Institute of
Technology, Mesra
aarushiagarwal27@gmail.com

Mohammad Arif
Department of
Electronics and
Communication
Engineering
Birla Institute of
Technology, Mesra
web2arif@gmail.com

Sitanshu S. Sahu
Department of
Electronics and
Communication
Engineering
Birla Institute of
Technology, Mesra
sssahu@bitmesra.ac.in

Abstract— Parkinson's disease (PD) is a widespread chronic neurological disease prevalent in old age. Speech is found to be an effective marker for the identification of Parkinson's disease. In the following paper, we have proposed using factor analysis to select meaningful and dominant features from the speech signals, which are relevant for prediction of Parkinson's disease. We infer that along with the jitter variants, shimmer variants and noise to harmonic ratio, pitch period entropy (PPE), the recurrence period density entropy (RPDE), and spread parameters are important in identifying PD. For classification, Support Vector Machine (SVM) is used. The proposed model discriminates Parkinson afflicted individuals from healthy ones with an average accuracy, sensitivity and specificity of about 90%. Further, from the study, it is inferred that sustained phonations carry sufficient information for predicting Parkinson's disease.

Keywords—Parkinson's disease (PD), Support Vector Machine (SVM), Factor analysis.

I. INTRODUCTION

Parkinson's disease (PD) is a neurological malady affecting the central nervous system, is named after Doctor James Parkinson, who described PD as "shaking palsy" in 1817 [1]. It is progressive in nature, caused by the loss of dopamine generating neurons and mainly affects people above 60 years of age [2]. During its course, Parkinson leads to several motor and non-motor symptoms which include loss of muscle control, rigidity, tremor and cognitive impairment along with thinking and behavioural problems [3].

One of the non-motor symptoms is hypokinetic dysarthria (HKD) which refers to reduced movement of the speech producing muscles [4]. HKD affects respiration, phonation, resonance and articulation in speech. Respiration problems disturb voice loudness in the patients. Vocal folds vibration during phonation creates periodic pattern in voice and Parkinson affects the periodicity of voice leading to variation in jitter, shimmer and harmonicity parameters. Resonating system determines richness of the voice while Parkinson affects the nasal quality of the voice. Imprecise articulation in PD is attributed to the reduced movement or lack of

coordination of face muscles. Clinical diagnosis is the most confirmatory approach of Parkinson identification but is invasive, time consuming as well as expensive. Thus, in recent years, researchers have focused their studies on speech signals because speech impairment is an early indicator of the disease, affecting around 75-90% of its patients [5]. Moreover, speech analysis is non-invasive, comparatively cheaper and easier to process.

Various quantitative analyses have been reported for PD detection using voice signals. Tsanas *et al.* used voice signals to prognosticate the progressive tendency of PD and demonstrated UPDRS assessment. They used signal processing algorithms to extract meaningful voice features and identified the useful features [6]. In another work, they have used selected features and have employed SVM and random forest to discriminate diseased from healthy subjects with an overall 99% classification accuracy in the generated dataset [3]. Little *et al.* have presented an evaluation of the nonstandard measures as compared to existing traditional for distinguishing Parkinson diseased people from healthy by detecting dysphonia with an accuracy of 95% [2]. In another paper, they have proposed the use of recurrence and fractal scaling along with bootstrapped classifier to achieve an overall accuracy of 91.8% [7]. Shahbakhi *et al.* used genetic algorithm (GA) and support vector machine for classification between healthy and Parkinson afflicted people, using voice samples with 14 features, predicting with an accuracy of 94% [8]. Indira R. *et al.* used pattern recognition and C-means clustering based approach for the discrimination between healthy and Parkinson's disease affected people [9]. Derya Avci *et al.* used wavelet kernel extreme learning machine and genetic algorithm. The best correct diagnosis rate found, on using the suggested GA-WK-ELM method was 96.81% [10]. Chen *et al.* proposed two classifiers- Nested-RF and Nested-SVM classifier with Nested-SVM classifier showing the best accuracy which was found to be 93% [11]. Benba *et al.* used compression of the MFCCs frames to extract the voiceprints from individuals, concluding that it is a good parameter for the detection of voice disorder in the context of Parkinson's disease [12]. Prashanth *et al.* proposed Support Vector Machine (SVM) and classification tree methods with olfactory

loss feature and SPECT features and provides accuracy of 85.48% [13].

In this paper, we have focused on the selection of relevant and dominant features from speech signals, which are used to build a predictive model with SVM for discriminating Parkinson diseased from healthy subjects.

II. MATERIALS & METHODS

We propose a system in which the voice samples are collected from the subjects, and then relevant dominant features are extracted and fed to SVM for building the model to distinguish PD subjects from healthy ones. The complete flow graph of the detection methodology is shown in Fig. 1.

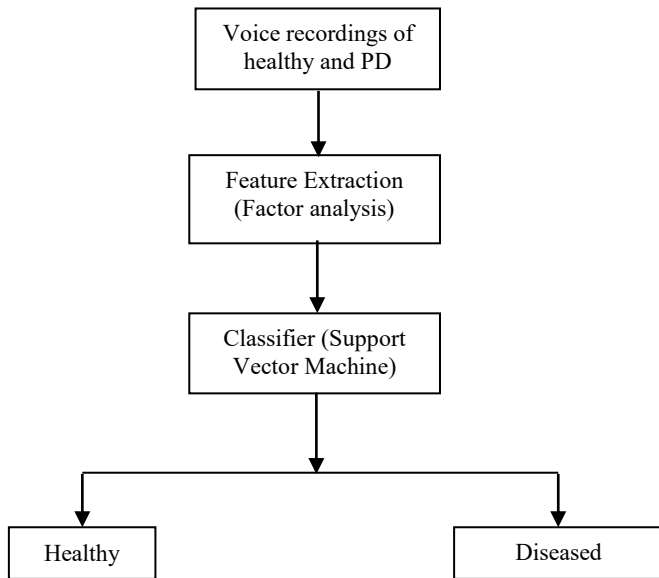


Fig. 1. Parkinson's disease detection process.

A. Factor Analysis

Many authors have proposed several dysphonia features from the speech signal. [2 3 14]. It has been found that, frequency (jitter), amplitude (shimmer), fundamental frequency parameters, harmonicity parameters, dynamic complexity parameters, signal fractal scaling component, non-linear parameters (such as pitch period entropy (PPE)), pitch parameters, voicing parameters and pulse parameters are relevant for identifying the Parkinson's disease.

Selection of dominant features can decrease the complexity of the predictive model. For this purpose, a statistical method called factor analysis is used to analyze the voice parameters. It provides underlying, latent variables from the observed variables thereby establishing a relation among all the variables. Each factor is represented as:

$$A_n = \lambda_n f + e_n \quad (1)$$

Where, A_n represents the n^{th} feature, f is the latent or underlying variable called factor, λ_n is the factor loading which represents the correlation between factors and variables when

only a single common factor is involved and e_n gives the specific variation of the variable from the factor.

Factor analysis can be described in matrix notation by

$$R = PCP' + U^2 \quad (2)$$

Where, P is the loading matrix, R is correlation coefficients of the observed variables matrix, C is the correlation among common factors, and U is the diagonal matrix or unique variances of the factors [15].

B. Support Vector Machine

Support Vector Machine (SVM) is a class of machine learning techniques, from statistical learning theory, based on optimization principle [16]. It separates the input data while maintaining maximum possible margin, with a reasonable computing efficiency. In an SVM classifier the data points which are not linearly separable in the current space are projected in to a higher dimensional feature space, where the different classes become linearly separable. This is achieved by constructing an optimal separating hyperplane in the feature space, which maximizes the margin between the two classes and thereby separating the data into different classes. The hyperplane is defined as:

$$f(x) = w^T x + b = 0 \quad (3)$$

In equation (3), w is an adjustable weight vector and b is a bias. The hyperplane is found by minimizing the following cost function:

$$J(w) = \frac{1}{2} w^T w = \frac{1}{2} \|w\|^2 \quad (4)$$

This is subjected to the constraints:

$$d_i [w^T x_i + b] \geq 1, \quad i = 1, 2, \dots, N \quad (5)$$

In order to make the optimization efficient, the kernel trick is used. Kernels are nothing but the dot products in the feature space, used to make the non-linear feature map. From an empirical study it has been inferred that, the radial basis function (rbf) is superior among other kernels in support vector machine.

C. ROC Curve

Receiver Operating Characteristics (ROC) curve graphically represents the performance of the classifier, by varying the threshold. It is a plot of true positive (TP) rate versus the false positive (FP) rate. In the ROC plot, the best value of threshold is given by the point in the upper left corner which denotes 100% specificity and 100% sensitivity. The area under the curve (AUC) denotes the likelihood that a classifier will place a randomly chosen negative sample lower than a positive sample, which indicates that greater value of AUC, is desirable for Parkinson detection.

D. Evaluation Parameters

Cross validation is a measure of assessment of the predictive methods. It splits the data in training set and testing set such that every instance of the original dataset has equal probability of appearing in the training and testing set. In this

paper, we have used Leave-one-out Cross Validation, in which k-fold is taken to its logical extreme such that k takes the value equal to the count of the samples in the dataset.

The parameters used to assess the efficiency of classification techniques are:

a) *Overall Accuracy*: It denotes the ratio of correctly predicted subjects (both PD and healthy) to the total predictions made.

$$Accuracy = \frac{TP+TN}{TP+FP+TN+FN} \quad (6)$$

b) *Specificity*: It denotes the ratio of healthy subjects accurately predicted as healthy to the total predictions which are healthy.

$$Specificity = \frac{TN}{FP+TN} \quad (7)$$

c) *Sensitivity*: It is the ratio of PD accurately predicted as PD to the total predictions which are diseased.

$$Sensitivity = \frac{TP}{TP+FN} \quad (8)$$

True positive (TP) is the number of Parkinson's afflicted individuals accurately detected as diseased; false negative (FN) is the number of Parkinson's afflicted individuals detected as healthy; false positive (FP) is the number of healthy individuals prognosticated as diseased and true negative (TN) is the count of healthy subjects accurately prognosticated healthy.

III. RESULTS AND DISCUSSION

A. Data Source

The dataset used has been created by Max Little et al. and comprises of the voice samples from 31 subjects, with 23 PD patients. Six recordings were collected from each subject such that there are 195 voice recordings having 22 features each, consisting of fundamental frequency parameters, jitter, shimmer, harmonicity parameters, dynamic complexity parameters, signal fractal scaling component and non-linear parameters [7].

B. Experimental Results

The uniformity of the speech samples is maintained by normalizing all the features between 0 and 1. All the experimental studies have been carried out using MATLAB. The factor loading of the extracted features is listed in Table 1.

TABLE I. FACTOR ANALYSIS RESULTS

Features	Total Samples	Healthy subjects	PD subjects
Fo	-0.09	0.07	0.06
Fhi	0.007	0.02	0.08
Flo	-0.14	-0.33	0.05
Jitter (%)	0.78	0.51	0.76
Jitter(abs)	0.71	0.35	0.68

Jitter(RAP)	0.77	0.53	0.75
Jitter(PPQ)	0.81	0.48	0.79
Jitter(DDP)	0.77	0.53	0.75
Shimmer	0.99	0.99	0.99
Shimmer(dB)	0.98	0.97	0.98
Shimmer(APQ3)	0.98	0.99	0.98
Shimmer(APQ5)	0.98	0.92	0.97
Shimmer(APQ)	0.94	0.85	0.94
Shimmer(DDA)	0.98	0.99	0.98
NHR	0.73	0.42	0.73
HNR	-0.84	-0.71	-0.85
RPDE	0.44	0.035	0.42
D2	0.16	-0.16	0.11
DFA	-0.65	-0.17	-0.62
Spread1	0.45	0.017	0.38
Spread2	0.50	0.57	0.44
PPE	0.69	0.19	0.66

It is observed from Table 1 that jitters and shimmer variants are dominating features. From the harmonicity parameters, noise to harmonicity ratio is an important feature but harmonicity to noise is not. Also, PPE (Pitch Period Entropy), RPDE (Recurrence Period Density Entropy), and non-linear parameters spread1 and spread2 are useful in discriminating PD patients. Thus, 16 dominant features are selected to assess the prediction model.

TABLE II. PERFORMANCE EVALUATION OF SVM ON ALL 22 FEATURES

SVM Parameters		Overall Accuracy	Specificity (Healthy)	Sensitivity (PD)
σ	C			
5	50	92.82	95.83	91.83
5	100	93.33	93.75	93.19
5	200	94.45	91.66	95.25

We have carried out a study of SVM model, in which $\sigma=5$ and $C=200$ was found best for prediction giving an accuracy of 94.45 % as shown in Table 2. The ROC curve for the model is shown in Figure 2 and the area obtained under the ROC curve is found to be 0.98377.

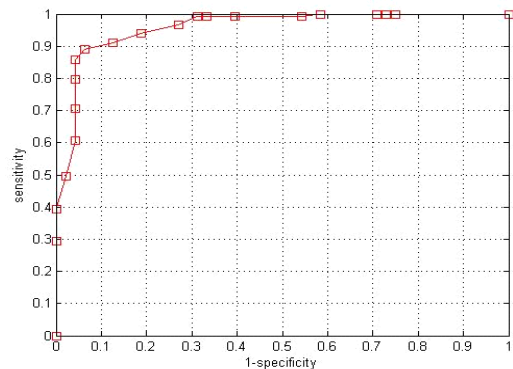


Fig. 2. ROC curve for all 22 features.

The performance of the model was assessed with the selected dominant features using factor analysis. The model built using these features provided an accuracy of 89.74% as listed in Table 3. It is inferred from the result that the selected dominant features are sufficient to discriminate PD from healthy.

TABLE III. PERFORMANCE EVALUATION OF SVM ON DOMINANT 16 FEATURES

SVM Parameters		Overall Accuracy	Specificity (Healthy)	Sensitivity (PD)
σ	C			
5	50	89.23	89.51	89.11
5	100	89.23	89.51	89.11
5	200	89.74	89.58	89.79

The ROC curve for the model of 16 dominant features is shown by the Figure 3. The area under the curve (AUC) was found to be 0.95642.

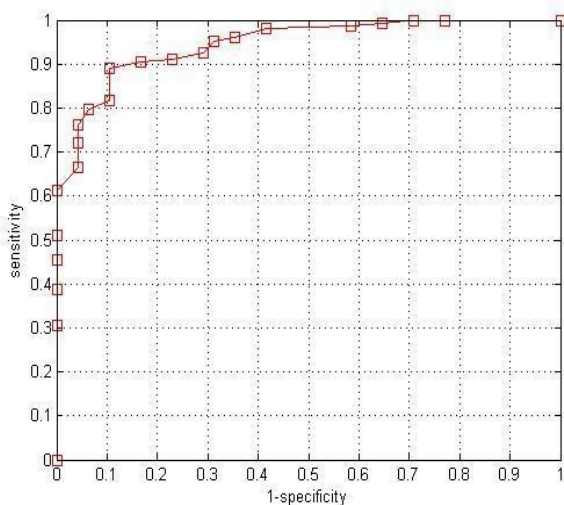


Fig. 3. ROC curve for 16 dominant features.

IV. CONCLUSION

In the following paper, we have implemented SVM as a robust technique to build an accurate predictive model for discriminating PD and healthy. From our extensive study, SVM gives an average accuracy of 90%, making it a reliable method for prediction. In agreement with previous findings, sustained vowels carry sufficient information to identify Parkinson diseased patients. We infer that along with the jitter variants, shimmer variants and noise to harmonic ratio, the RPDE, PPE and spread parameters are important in identifying PD. In conclusion, future research can be carried out on this technique by incorporating new features and

different datasets and extending its applicability to other biomedical fields.

REFERENCES

- [1] J. W. Langston, "Parkinson's disease: current and future challenges", *Neuro Toxicology*, vol. 23, no. 4-5, pp. 443-450, 2002.
- [2] M. A. Little, P. E. McSharry, E. J. Hunter, J. Spielman, and L. O. Ramig, "Suitability of Dysphonia Measurements for Telemonitoring of Parkinson disease", *IEEE Transactions on biomedical engineering*, vol. 56(4), 2009.
- [3] A. Tsanas, M. A. Little, P. E. McSharry, J. Spielman, and L. O. Ramig, "Novel Speech Signal Processing Algorithms for High-Accuracy Classification of Parkinson's Disease", *IEEE transactions on biomedical engineering*, vol. 59(5), 2012.
- [4] K. M. Rosen, R. D. Kent, A. L. Delaney and J. R. Duffy, "Parametric Quantitative Acoustic Analysis of Conversation Produced by Speakers with Dysarthria and Healthy Speakers", *J. Speech, Language and Hearing Research*, vol. 49, pp. 395-411, 2006.
- [5] A. K. Ho, R. Janssek, C. Marigliani, J. Bradshaw, and S. Gates, "Speech impairment in large sample of patients with Parkinson's disease," *Behav. Neurol.*, vol. 11, pp. 131-137, 1998.
- [6] A. Tsanas, M. A. Little, P. E. McSharry and L. O. Ramig, "Accurate Telemonitoring of Parkinson's Disease Progression by Non invasive Speech Tests ", *IEEE transactions on biomedical engineering*, vol. 57(4), 2010.
- [7] M. A. Little, P. E. McSharry, SJ Roberts, DAE Costello, IM Moroz, "Exploiting Nonlinear Recurrence and Fractal Scaling Properties for Voice Disorder Detection", *Bio Medical Engineering OnLine*, 2007.
- [8] Shahbakhi, M., Far, D.T. and E. Tahami, "Speech Analysis for Diagnosis of Parkinson's Disease Using Genetic Algorithm and Support Vector Machine", *J. Biomedical Science and Engineering*, vol 7, pp. 147-156, 2014.
- [9] Rustempasic, Indira, & M. Can, "Diagnosis of Parkinson's Disease using Fuzzy C-Means Clustering and Pattern Recognition ", *South East Europe Journal of Soft Computing*, vol 2(1), 2013.
- [10] Derya Avcı and Akif Dogantekin, "An Expert Diagnosis System for Parkinson Disease Based on Genetic Algorithm-Wavelet Kernel-Extreme Learning Machine", *Hindawi Publishing Corporation Parkinson's disease*, vol. 2016, Article ID 5264743.
- [11] A. H. Chen, C. H. Lin & C. H. Cheng, "New approaches to improve the performance of disease classification using nested-random forest and nested-support vector machine classifiers", *Research Notes in Information and Service Sciences*, vol. 14(0), 2013.
- [12] A. Benba, A. Jilbab, and A. Hammouch, "Detecting Patients with Parkinson's disease using Mel Frequency Cepstral Coefficients and Support Vector Machines", *International Journal on Electrical Engineering and Informatics*, vol. 7(2), 2015.
- [13] R. Prashanth , Sumantra Dutta Roy, Pravat K. Mandal, and Shantanu Ghosh, High-Accuracy Detection of Early Parkinson's Disease through Multimodal Features and Machine Learning, *International Journal of Medical Informatics*, Vol. 90, p.13-21, 2016.
- [14] B. E. Sakar, M. E. Isenkul, C. O. Sakar, A. Sertbas, F. Gurgen, S. Delil, H. Apaydin, and O. Kursun, "Collection and Analysis of a Parkinson Speech Dataset with Multiple Types of Sound Recordings", *IEEE J. Biomedical And Health Informatics*, vol. 17(4), pp. 828-834, 2013.
- [15] A. G. Yong and S. Pearce, "A Beginner's Guide to Factor Analysis: Focusing on Exploratory Factor Analysis", *Tutorials in Quantitative Methods for Psychology*, vol. 9(2), pp. 79-94, 2013.
- [16] V. Vapnik, "The Nature of Statistical Learning Theory", NY: Springer-Verlag, 1995.



EEG Signal Analysis using Sparse Approximations

Palakurthi Ravali

Electronics and Communication Engineering
Kakatiya Institute of Technology and Science
Warangal, Telangana 506015
ravali.palakurthi@gmail.com

J. Sheshagiri Babu

Electronics and Communication Engineering
Kakatiya Institute of Technology and Science
Warangal, Telangana 506015

Abstract—Electroencephalogram (EEG) is physiological signal generated in the brain. Electroencephalography is a method to record the electrical activity of the brain in order to detect the abnormalities of the brain. However, EEG also detects the signals which are not originated from the brain called artifacts. This paper deals with the analysis and extraction of EEG signals in sparse representation using sparse algorithms Orthogonal Matching Pursuit (OMP) and LASSO. OMP is an iterative greedy algorithm which replaces optimization problem in each step of Matching Pursuit (MP), an earlier algorithm for solving sparse approximation problems by least squares minimization. LASSO is an optimization technique which involves regression analysis concepts. Sparse approximations are used in practical applications like feature extraction, Denoising, Inpainting etc.

Keywords—EEG; artifacts; sparse approximations; orthogonal matching pursuit; LASSO

I. INTRODUCTION

Physiological signals are generated by the body during the functioning of various bio-electrical systems. Hence physiological signals hold information which can be extracted from these signals to find out the state of the functioning of these bio-electrical systems. Physiological signals generated in the brain are EEG signals. Electroencephalography is used for monitoring the electrical activity in the brain both for clinical and research purposes. It is performed by placing electrodes on the scalp which acquires EEG signals and transmits to recording system.

Usually, EEG test is conducted for diagnosing brain abnormalities like brain tumor, epilepsy, dementia etc as mentioned in [1]. When measured on the scalp, the strength of the EEG signal is about 100 μ V and 1-2 mV when measured on surface of the brain. Its frequency is about 0.1Hz to 500Hz. This range is divided into different frequency bands based on various brain states these are; delta, theta, alpha, beta and gamma waves. Firstly, delta waves are high amplitude waves and the range of frequency is about 0.1 Hz to 3Hz. These waves are observed during deep sleep. Secondly, theta waves are associated with rapid eye movement in adults. Excess theta waves represent abnormal activity of the brain. The frequency range of these waves is 4Hz to 7Hz and amplitude is 10 μ V. The third classification is alpha waves occur during relaxation periods. The frequency of these waves is 8 Hz to 12 Hz and the amplitude is about 20-200 μ V. Beta waves are

characterized by low amplitude ranging 5-10 μ V and frequency range is about 12 Hz to 30 Hz. These waves represent when the person is anxious. Lastly, gamma waves correspond to frequency range 30-100Hz which are detected when the person is in thinking process.

Signals which are detected by the EEG but not originated from the brain are called artifacts. Artifacts play major role during acquisition of EEG signals since the amplitude of artifacts are quite greater than the brain signals that are considered for study. There are different types of artifacts; some common artifacts are power line artifact, electrocardiogram (ECG), electrooculogram (EOG). Power line artifact is the most common artifact which contaminates the EEG signals by introducing 50Hz frequency and higher strengths to the original signals. So, dealing with artifacts effectively is the most challenging task for the technologist.

The term sparse depicts measurable property of a vector in which the number of zero entries is greater than the non-zero entries. Sparse approximations solve a system of linear equations approximately for a sparse vector. In other words, sparse approximation algorithms convert the signal to sparse representation i.e. the data content of the input signal gets sparsified. So, for storing the content, it requires less space as the data is sparse. Hence, sparse approximations have huge practical applications. To understand sparse approximation algorithms, linear algebra concepts are essential. In this paper, sparse approximations are applied to an under-determined system of linear equations. In under-determined system, the number of equations is less than the number of unknowns i.e. when a matrix is considered, the number of rows (m) is less than the number of columns (n) ($m < n$). For both the algorithms in this project, input is EEG signal and the output obtained is sparse vector of the input signal.

Orthogonal matching pursuit is an iterative greedy method as stated in [4] and used for solving the sparse approximation problem. In each iteration, the column vectors of measurement matrix which are similar to the input vectors are picked. These selected vectors are combined for building the required solution. Least absolute shrinkage selector operator replaces the sparse approximation problem by a convex problem. Generally, LASSO is an optimization

principle rather than an algorithm. Hence, to analyze LASSO concepts of regression analysis are required.

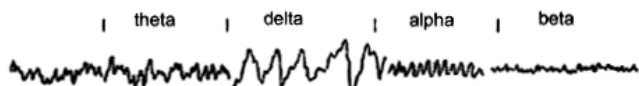


Fig.1. Different EEG frequency bands

II. RELATED WORK

For detection of brain abnormalities according to acquired EEG signal, a method was proposed in [1]. This method includes pre-processing, feature extraction, feature selection and classification. The authors in [3] discussed about the orthogonal matching pursuit algorithm which is used in this paper. In [3], the orthogonal matching pursuit is compared with previous algorithm matching pursuit. Results are compared with different dictionaries like Bernoulli's and Gaussian. Sparse signal recovery using sparse random matrix is focused in [5]. The use of sparse random matrix in recovery provides low computational complexity. [7] implements orthogonal matching pursuit algorithm with noise. [7] can be used for separating noise from required EEG signal. Multipass LASSO algorithm is proposed in [8] for sparse signal recovery.

III. BACKGROUND

A. Definitions

A dictionary of a signal space is finite collection of unit norm vectors that spans the whole space. The members of dictionary are called atoms. There are different types of dictionaries. Depending on their properties, dictionaries are used in different applications.

A dictionary is redundant if there is more than one possible representation of the signal. If the size of the dictionary is high, the errors in representing the signal will be minimum.

Representation of a signal is the linear combination of atoms that is same as signal. Without loss of generality, all the coefficients in representation are assumed to be nonzero. Generally, a p-term representation is a representation that involves p atoms.

Over a redundant dictionary every signal can be represented in infinite number of distinct ways. The problem of approximating a signal with the best linear combination of elements from a redundant dictionary is called sparse approximation or highly nonlinear approximation.

The aim of this paper is to identify the exact representation of the input signal that uses the least number of atoms .i.e. the sparsest one.

B. Significance of Sparse Approximations

As discussed earlier, there is wide range of applications of sparse approximation practically. Sparsity deals with the number of non-zero entries in a vector. So, for a sparse vector the space required to store it is very less since the position and value of the non-zero entries are stored instead of whole matrix. Hence, storage space reduces to the fraction of what is needed originally. These sparse algorithms are used to analyze how the column vectors in a given dictionary are related and combined to produce the data.

In feature extraction, sparse approximations are used to analyze data when only one particular feature of that data is to be considered. Matrices with columns which have same properties as of desired are used to approximate the desired features.

Sparse approximations can also be used in de noising. There are many ways in which the required data can get contaminated by the noise. De-noising is the process of separating the noise from the desired content. For EEG signal acquisition, artifacts get added with the desired signals. Sparse approximations like orthogonal matching pursuit can be used for de noising artifacts from the EEG signal.

In inpainting, sparse algorithms are used for retrieving the information by ignoring the missing content and constructing the solution from the remaining data.

IV. ORTHOGONAL MATCHING PURSUIT

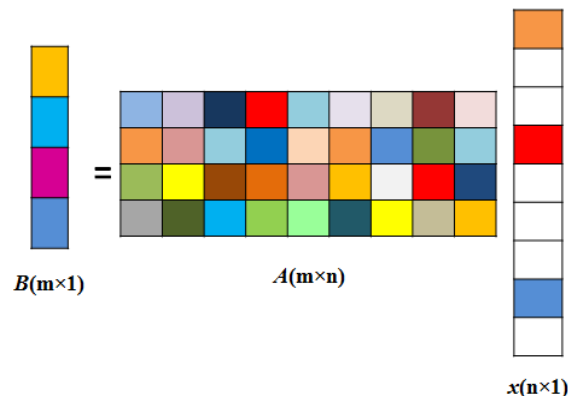


Fig.2. Problem model

As in Fig.2, the defined system is under-determined system as the number of rows is very less than the number of columns. B is the input EEG signal with order m-by-1, x is the sparse representation of the input EEG signal with order n-by-1 and A is the random measurement matrix with order m-by-n and its columns are denoted by $\{a_1, a_2, \dots, a_n\}$. The number of non-zero entries i.e. the sparsity level is also given as input k. As Orthogonal Matching Pursuit (OMP) is an iterative algorithm, in each step it builds a locally optimum solution. This can be done by finding the vectors in the measurement matrix A which are similar to the residual vector R. For the

first iteration residual vector is equal to the input vector $B = v$. After each iteration, residual vector is updated depending on the previously chosen vector. Then it subtracts off its contribution to v and iterate on the residual. After k iterations, the desired solution is generated.

A. Algorithm

INPUT:

1. An m -by- n measurement matrix (A)
2. An m -dimensional data vector (B)
3. The sparsity level k of the ideal signal.

OUTPUT:

1. An estimate \hat{s} in \mathbf{R}^n for the ideal signal
2. A set P_k containing k elements from $\{1, \dots, n\}$
3. An m -dimensional residual $r_k = v - q_k$

PROCEDURE:

- 1) Initialize the residual $r_o = v$, the index set, $P_o = \emptyset$ and the iteration counter $t = 1$.
- 2) Find the index λ_t that solves the easy optimization problem.

$$\lambda_t = \arg \max_{j=1,2,\dots,n} |\langle r_{t-1}, a_j \rangle|$$

Augment the index set and the matrix of chosen atoms: $P_t = P_{t-1} \cup \{\lambda_t\}$ and $A_t = [A_{t-1} a_{\lambda_t}]$. We use the convention that A_o is an empty matrix.

- 3) Solve a least squares problem to obtain a new signal estimate:

$$x_t = \arg \min_x \|v - A_t x\|_2$$

- 4) Calculate the new approximation of the data and the new residual

$$q_t = A_t x_t$$

$$r_t = v - q_t$$

- 5) Increment t , and return to step 2 if $t < k$.
- 6) The estimate \hat{s} for the ideal signal has non zero indices at the components listed in P_k .

B. Explanation

Step 1: Iteration counter t is initialized to 1, residual initialized to input data vector $v=B$ and the index set (which contains the k elements in the output) is first initialized to null set.

Step 2: In this step, optimization problem (maximizing or minimizing a real function by systematically choosing input values from within an allowed set and computing the value of the function) is performed. The inner product of each column of A is done with residual r_{t-1} and the value of j at which the

inner product becomes maximum is stored in index λ_t i.e. is the index of the column of A at which the inner product becomes maximum. For the first iteration, the inner product of data vector v with all the columns of A is performed.

Step 3: Update the index set P_t and matrix set A_t . Index set P_t is updated with the index λ_t (the index in step 2) and A_t is updated with the λ_t th column of A i.e. the column which produces maximum inner product with residual.

Step 4: Finds the least squares solution x_t by minimizing the error between v and $A_t x$ in L_2 norm. Least squares solution is calculated by using QR decomposition. Here A_t is decomposed to Q (Orthonormal matrix) and R (Upper triangular matrix).

Step 5: New approximations of data and new residual for further iterations are calculated. r_t is the new residual which is always orthogonal to A_t .

Step 6: Iteration counter t is incremented and if t is less than the sparsity level k , then go to step 2 for next iteration, otherwise stop the process.

V. REGRESSION ANALYSIS

There are different types of regression analysis for determining the regression co-efficients. Few of them are –

1. Ordinary least squares regression
2. Ridge regression
3. LASSO regression

A. Ordinary least squares regression

Ordinary least squares regression is a method of estimating the estimator from the predictors by linear approximation of data nothing but minimizing the error between estimator and predictor in L_2 norm by calculating $\bar{\beta}$.

$$\bar{\beta}_{OLS} = \arg \min_{\beta} \|v - A\bar{\beta}\|_2$$

OLS is more efficient for two regression co-efficients i.e. for the model $y = \beta_0 + \beta_1 X_1$. If the estimators are highly correlated (Possible when more than one independent variable exists), OLS model fails as the variation between the regression co-efficients is high.

B. Ridge regression

Ridge regression is similar to OLS regression except there is a constraint on the minimizing function. The constraint is on the regression co-efficients in L_2 norm. For ridge regression to be performed there must be minimum two estimators with high correlation.

$$\vec{\beta}_{Ridge} = \mathop{\text{argmin}}_{\vec{\beta}} \|Ax - \vec{\beta}\|_2 \text{ subject to } \|\vec{\beta}\|_2 \leq c$$

As the constraint is in L₂ norm, the predictor value must lie on the boundary formed by $\vec{\beta}$ or inside the boundary. Hence, for a set of values of $\vec{\beta}$, solution lies on the circumference of the circle for two dimensional case. This regression can also be represented as following for easy computations.

$$\vec{\beta}_{Ridge} = \mathop{\text{argmin}}_{\vec{\beta}} \|Ax - \vec{\beta}\|_2 + \lambda \|\vec{\beta}\|_2$$

where λ is Lagrange multiplier.

C. LASSO regression

LASSO is acronym for Least absolute shrinkage selector operator. It is similar to Ridge regression but the constraint on $\vec{\beta}$ is in L₁ norm. For a set of values of $\vec{\beta}$, solution lies on the circumference of the rhombus for two dimensional case.

$$\vec{\beta}_{LASSO} = \mathop{\text{argmin}}_{\vec{\beta}} \|v - A\vec{\beta}\|_2 \text{ subject to } \|\vec{\beta}\|_1 \leq c$$

Least number of non-zero entries is required to represent the solution in LASSO. i.e. LASSO sparsifies the $\vec{\beta}$ regression co-efficients which is the required condition. LASSO finds the approximations rather than the representations. This regression can also be represented as following for easy computations.

$$\vec{\beta}_{LASSO} = \mathop{\text{argmin}}_{\vec{\beta}} \|v - A\vec{\beta}\|_2 + \lambda \|\vec{\beta}\|_1$$

where λ is Lagrange multiplier.

VI. RESULTS

For Orthogonal matching pursuit, the inputs are EEG delta signal B as shown in fig.3, sparsity level k(Required number of non-zero entries in the result) and random measurement matrix A. Result is recovered sparse EEG signal x with k number of non-zero entries. When the resultant sparse signal is multiplied with measurement matrix, the signal is same as input EEG signal. For the given input, the sparsity level is 200 and the sparse signal x is as shown in fig.4. and the EEG signal is shown in fig.5. For LASSO, the inputs are EEG delta signal as in fig.6, random measurement matrix A and Lagrange multiplier lambda. Output is recovered sparse signal which is similar to OMP sparse signal and shown in fig.7. The

recovered EEG output is obtained when multiplied with matrix A, shown in Fig. 8.

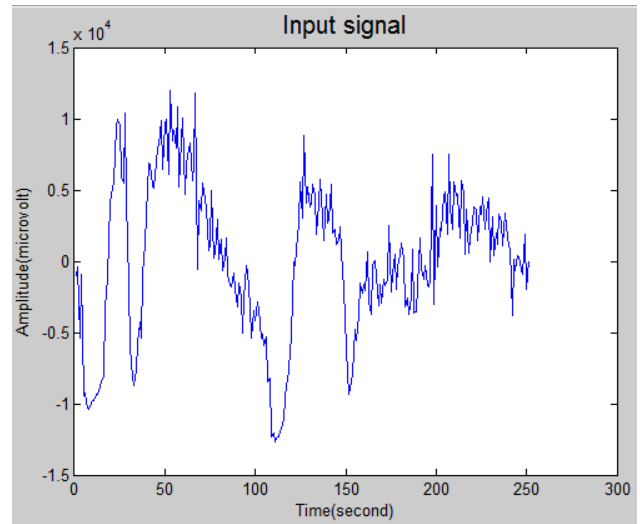


Fig.3. EEG Input for OMP

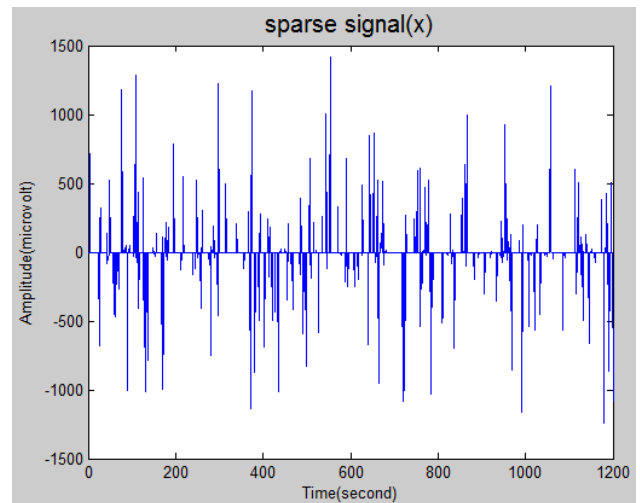


Fig.4. Sparse output for OMP

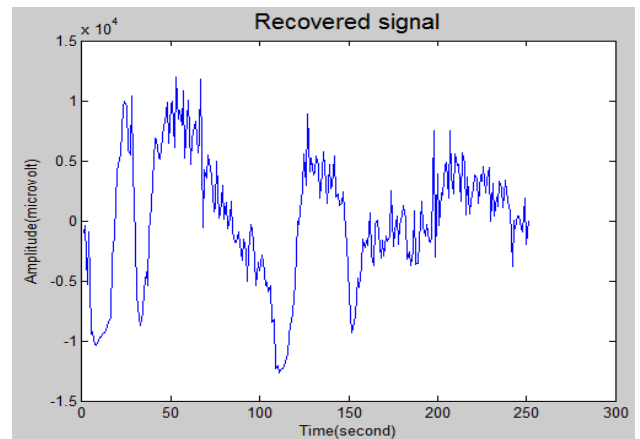


Fig.5. EEG output for OMP



VII. CONCLUSION

From the results, the original input signal is recovered in sparse representation using the both algorithms OMP and LASSO with random measurements. OMP is easy to implement and the results are improved compared to matching pursuit. Using these conclusions, the artifacts in EEG signals can be removed using Orthogonal Matching Pursuit including noise algorithm.

REFERENCES

- [1] Kalaivani, M., V. Kalaivani, and V. Anusuya Devi. "Analysis of EEG Signal for the Detection of Brain Abnormalities." *at International Journal of Computer Applications*® year (2014).
- [2] Arman, Sabbir Ibn, Arif Ahmed, and Anas Syed. "Cost-effective eeg signal acquisition and recording system." *International Journal of Bioscience, Biochemistry and Bioinformatics* 2.5 (2012).
- [3] J. A. Tropp and A. C. Gilbert, "Signal Recovery From Random Measurements Via Orthogonal Matching Pursuit," in *IEEE Transactions on Information Theory*, vol. 53, no. 12, pp. 4655-4666, Dec. 2007.
- [4] J. A. Tropp, "Greed is good: algorithmic results for sparse approximation," in *IEEE Transactions on Information Theory*, vol. 50, no. 10, pp. 2231-2242, Oct. 2004.
- [5] A. Gilbert and P. Indyk, "Sparse Recovery Using Sparse Matrices," in *Proceedings of the IEEE*, vol. 98, no. 6, pp. 937-947, June 2010.
- [6] D. Needell and R. Vershynin, "Signal Recovery From Incomplete and Inaccurate Measurements Via Regularized Orthogonal Matching Pursuit," in *IEEE Journal of Selected Topics in Signal Processing*, vol. 4, no. 2, pp. 310-316, April 2010.
- [7] T. T. Cai and L. Wang, "Orthogonal Matching Pursuit for Sparse Signal Recovery With Noise," in *IEEE Transactions on Information Theory*, vol. 57, no. 7, pp. 4680-4688, July 2011.
- [8] Y. Jin and B. D. Rao, "MultiPass lasso algorithms for sparse signal recovery," *2011 IEEE International Symposium on Information Theory Proceedings*, St. Petersburg, 2011, pp. 1417-1421.
- [9] E. J. Candes and T. Tao, "Decoding by linear programming," in *IEEE Transactions on Information Theory*, vol. 51, no. 12, pp. 4203-4215, Dec. 2005.
- [10] S. G. Mallat and Zhifeng Zhang, "Matching pursuits with time-frequency dictionaries," in *IEEE Transactions on Signal Processing*, vol. 41, no. 12, pp. 3397-3415, Dec 1993.
- [11] D. L. Donoho, Y. Tsaig, I. Drori and J. L. Starck, "Sparse Solution of Underdetermined Systems of Linear Equations by Stagewise Orthogonal Matching Pursuit," in *IEEE Transactions on Information Theory*, vol. 58, no. 2, pp. 1094-1121, Feb. 2012.
- [12] Tibshirani, Robert. "Regression shrinkage and selection via the lasso." *Journal of the Royal Statistical Society. Series B (Methodological)* (1996): 267-288.
- [13] Tropp, Joel A., Anna C. Gilbert, and Martin J. Strauss. "Algorithms for simultaneous sparse approximation. Part I: Greedy pursuit." *Signal Processing* 86.3 (2006): 572-588.
- [14] S. C. Wu and A. L. Swindlehurst, "Matching Pursuit and Source Deflation for Sparse EEG/MEG Dipole Moment Estimation," in *IEEE Transactions on Biomedical Engineering*, vol. 60, no. 8, pp. 2280-2288, Aug. 2013
- [15] Needell, Deanna, and Joel A. Tropp. "CoSaMP: Iterative signal recovery from incomplete and inaccurate samples." *Applied and Computational Harmonic Analysis* 26.3 (2009): 301-321.

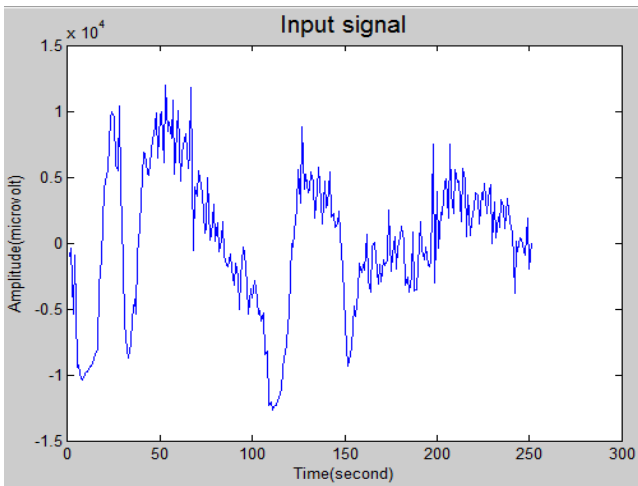


Fig.6. EEG Input for LASSO

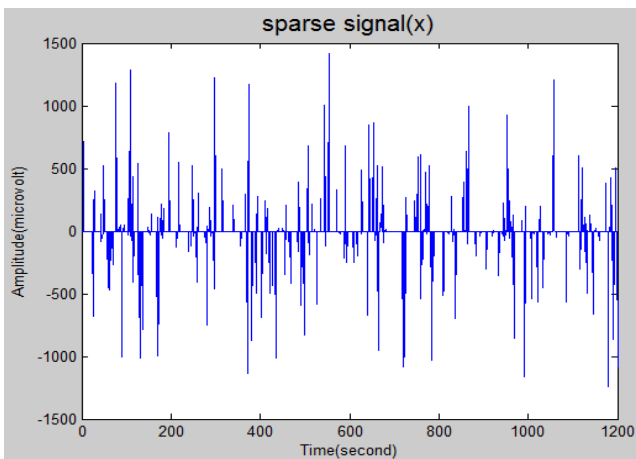


Fig.7. Sparse output for LASSO

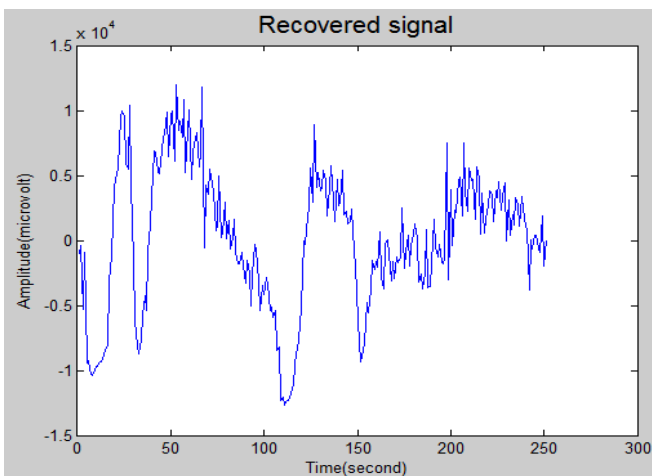


Fig.8. EEG output for OMP

Impact Assessment of Mental Subliminal Activities on the Human Brain Through Neuro Feedback Analysis

Munyaradzi C. Rushambwa

Department of Sensors and Biomedical Engineering, School
of Electronic Engineering Vellore Institute of Technology
Vellore Institute of Technology
Vellore Tamil Nadu,632014, India.

Asaithambi Mythili

Department of Sensors and Biomedical Engineering, School
of Electronic Engineering Vellore Institute of Technology,
Vellore Institute of Technology
Vellore Tamil Nadu,632014, India.
such as reading, reasoning and concentration.

Abstract—Neuro feedback is a type of biofeedback phenomena that shows the activity on the human brain through Electroencephalogram (EEG). EEG measure the electrical activity of the human brain by electrodes placed on different parts of the brain cortex. Since the human brain has complex circular firing wave patterns, EEG allows us to non-invasively measure the electrical activity of the brain waves. The intensities of these human brain waves vary from individual to individual and changes due to various physiological, mental and physical state of the human body. This work explores the effects of sleep, attention and music on the human brain. Analysis of these activities is used to show the correlation between specific EEG patterns and the aforementioned activities.

Keywords—Brain, electrical activity, EEG, neuro feedback.

I. INTRODUCTION

THIS work analyzes the effects of physical and mental subliminal activities on the human brain waves. The human brain waves are measured using EEG, which may be configured in various ways, depending on the region of the brain to be assessed. EEG measures the electrical activity of the human brain by electrodes placed on different parts of the brain cortex. For the EEG signals the main focus of this work is on alpha and beta waves, in which the beta waves represents the awakening/reasoning state, whilst alpha is associated with meditation and relaxation[1].

According to the IEEE standards, the recommended practice for neuro feedback system, it follows that:

TABLE 1: IEEE recommended practice for neuro feedback systems

Brain Wave	Range
Delta	0.1-4 Hz
Theta	4-8 Hz
Alpha	8-13 Hz
Beta	13-30 Hz
Gamma	36-44 Hz

The physical and mental subliminal activities analyzed are music, sleep, attention which involves various other activities

A. Music.

Music consists of tones of varying amplitude and frequencies which changes over time. Music non-invasively enhances the cognitive functions of an individual and thus has positive effects on brain waves because of its changing frequency nature [2]. The positive impact of music on the brain waves differs among individuals due to differences in age, taste and type of music, and emotional intelligence. When one listens to music, the frontal left and right brainwaves reflect theta, alpha and beta waves of almost the same magnitude to signify a balance. As a result of this balance a conclusion can be made that there is a relationship between the frequency of the waves and the power emitted by the music in brainwaves [3]. This relationship is illustrated by the equation 1

$$p(t) = p_0 \sin(2\pi ft) \quad (1)$$

$p(t)$ = instantaneous sound pressure.

p_0 = maximum amplitude component in $p(t)$.

f = frequency (Hertz).

t = time (seconds).

Not all music is good, but selecting music that has frequency components (f) as in equation 1 can have a good role in therapeutic rehabilitation [4]. The relaxed state of the brain after listening to music helps in the information capturing process thereby enhancing learning and cognitive task performance.

B. Sleep and Attention

The profundity of sleep as examined by the easiness to arouse a human being with a standard stimulus such as sound and reading correlates perfectly with the state of the EEG. Deep phases of sleep are characterized by delta waves and the subject will be having, low blood pressure, decreased muscle tone, low heart rate low respiration rate, low temperature and the absence of rapid eye movement [5]. The reason being the

fact that sleeping is a physiological and physical renewal and reformation, consolidating memory cells, discharging emotions and enhancing cognitive functions. This in turn means that poor sleep results in poor cognitive function such as organization and planning, poor academic performance, subsequent memory loss and slows healing process. This can be seen in Fig. 1 where one emits high frequency alpha waves when relaxed, mid frequency theta waves when drowsy and very low frequency delta waves when asleep.

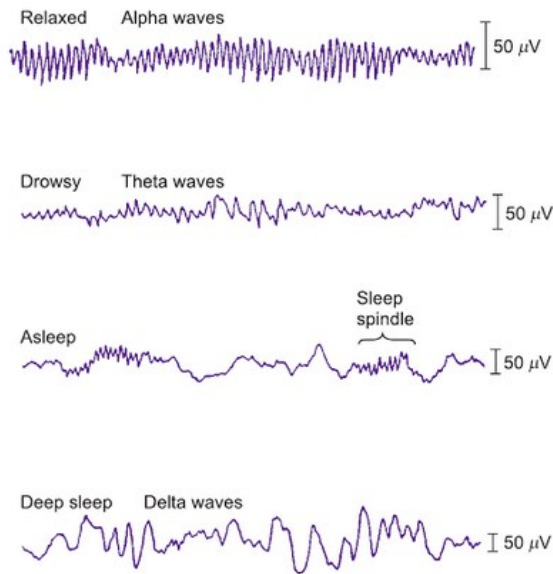


Fig. 1. Brainwaves versus human activity

Attention is the fundamental activity on the human brain which is altered by both music and sleep. When one is awake and alert, EEG signals shows high frequency waves in the range 20-50Hz with a low voltage amplitude of 10-20uV [6]. This characteristic of the human brain represents the beta wave component of an individual. Closing the eyes and gradually sleeping results in reduced attention and low frequency and high amplitude patterns may be seen from Fig. 2:

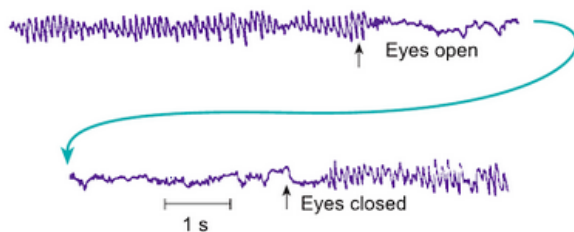


Fig. 2. Frequency and eye movement

In Fig. 2, the closed eye pattern has a brainwave signal of higher amplitude in the range 20-40uV and lower frequency in the range 8-12Hz. This characteristic of the human brain represents the alpha rhythm component of an individual. More drowsiness and sleep leads to a wave of greater amplitude in the range 40-80Hz and low frequency pattern in the range 4-7Hz. Deep sleep is characterized by slow frequency patterns of less than 3Hz and high amplitude levels in the range 100-200uV [7]. This characteristic of the human brain represents the delta rhythm component of an individual.

II. MATERIALS AND METHODOLOGY

Fig. 3 shows the implementation of the system to measure the EEG signals. A Neurosky brain wave sensor with an ear clip for grounding, a headband that clings to the human head and an EEG frontal lobe sensor is used to acquire the EEG signals for further processing. The brainwave sensor is a MEMS type sensor embedded with a signal conditioning unit and a Bluetooth transceiver unit which communicates with the controller via UART protocol. The sensor is placed above the eye on the fp1 position as per the 10-20 configuration standards. The raw signal and the EEG power spectrum is extracted from the brain wave sensor and sent via Bluetooth to the controller where Fast Fourier Transform (FFT) and signal separation is done. The resultant values are digitized values of the various EEG components (alpha, beta, delta and theta) represented on a scale of 0-100.

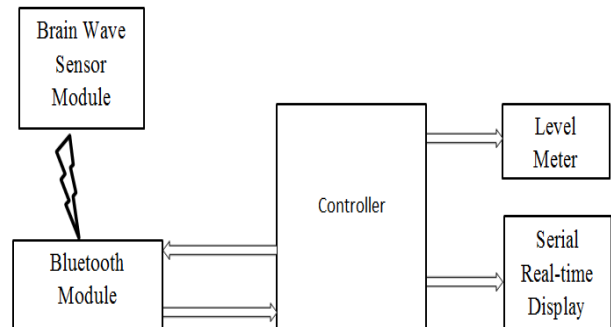


Fig. 3. Block diagram of the system

The Bluetooth module used in this work is an HC05 module which receives data wirelessly from the brainwave sensor and relays it via UART to the controller. The controller is an Arduino UNO-R3 board which controls the level of the LED array. The LED array acts as a level meter indicating the subject's state of mental alertness. In design it consists of an array of different colored LEDs mounted on a board with 220ohm resistors connected to each LED. LED colors from yellow, green and red represents the variation of the alertness

on a 0-100 percentage scale. The value of the subject's alertness is displayed in real time using serial monitor software component of Arduino.

III. SOFTWARE IMPLEMENTATION

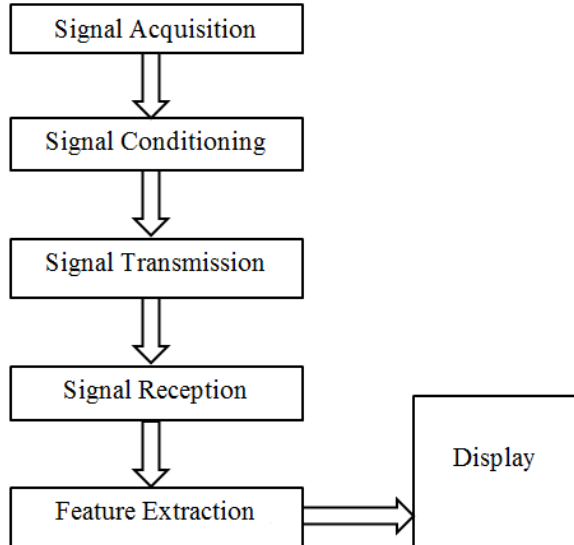


Fig. 4. Signal Flow Diagram

In Fig. 4 signal acquisition and transmission is implemented by the brainwave sensor which has one electrode placed on the frontal lobe. The electrode is used to pick the voltage from the brain and the ear electrode is used as the reference ground. This voltage is subtracted through common mode rejection and converted into a mono channel EEG signal. The signal measured therefore is low in amplitude and a gain of 2000 is used to enhance the faint EEG signal. Digital low and high pass filters are used to amplify the signal to get the required signal range of 1-50Hz. At a sampling rate of 512Hz, fast fourier transform is performed such that the various components of the EEG signal may be extracted.

A. Bluetooth HC05 Configuration

HC05 Bluetooth module automatically pair with brainwave sensor so that it can receive the digitized signal. Through AT commands it can be configured to work as a TTL master/slave transceiver using the serial UART method for communication. In this case it the HC05 module was configured using Cool term software via AT commans.

TABLE 1. AT commands used to configure the Bluetooth module

AT Command	Comment
AT	Status check
AT+NAME= PROJECT	Naming the module
AT+UART=57600,0,0	baud rate

AT+ROLE=1	Set as master
AT+CMODE=0	bound address connection
AT+BIND=0HF5:2C:57B6	Auto pairing
AT+IAC=9E8B33	Interpretation
AT+CLASS=0	device class
AT+INQM=1,9,48	access patterns

B. Signal Processing and Feature Extraction

The data transmitted by the brainwave has encoded values which come as a serial stream of bytes through the standard Bluetooth serial port profile (SPP). The baud rate at which this data is transmitted is 57600 as defined from the AT command. Values of poor signal quality, attention and meditation are extracted though FFT from the serial stream of the encoded values.

1) Poor Signal Quality

Poor signal is represented by an unsigned one byte integer indicating how poor the signal measured by the brainwave is. Poor signal indicates the presence of artifacts in the signal which may be due to improper grounding, improper electrode placement and rapid eye movement, excessive motion by an individual or some electrostatic noise from the environment.

2) Attention and Meditation

Attention and meditation values are calculated after feature extraction and each level of the two is shown on a scale of 0-100 as a percentage. The value of attention level is an unsigned one byte value which reports the state of the human brain as it is affected by alertness. The value of attention level is an unsigned one byte value which reports the state of the human brain as it is affected by calmness and relaxation.

3) Brain Wave Visualizer

Brainwave visualizer is a windows application that shows the variation of the brain waves in real time as the subject listens to different genre of music. In Fig. 6 below the visualizer shows how music with varying frequency affects the attention and meditation values on a meter calibrated from 0 to 100 as can be seen in Fig. 5.

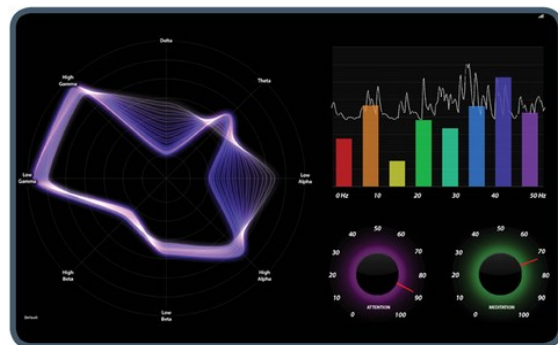


Fig. 5. Brainwave visualizer application

IV. HARDWARE IMPLEMENTATION

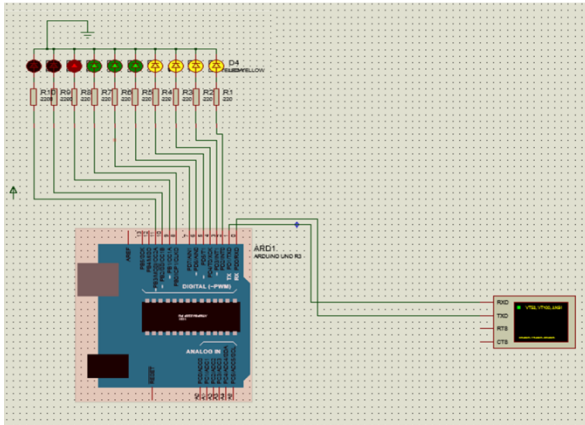


Fig. 6. System Circuit

Hardware circuitry was implemented in Proteus software as can be seen in Fig. 6. The LED array is glowing showing some alertness level. The brainwave sensor connects wirelessly via Bluetooth to the Arduino board using an HC05 Bluetooth module and is simulated using virtual terminal.

V. RESULTS AND DISCUSSION

The data acquisition part of the project was simulated using the Arduino IDE serial monitor which showed the polled output every second of the attention and meditation value in real time as seen from the screenshot in Fig. 7.

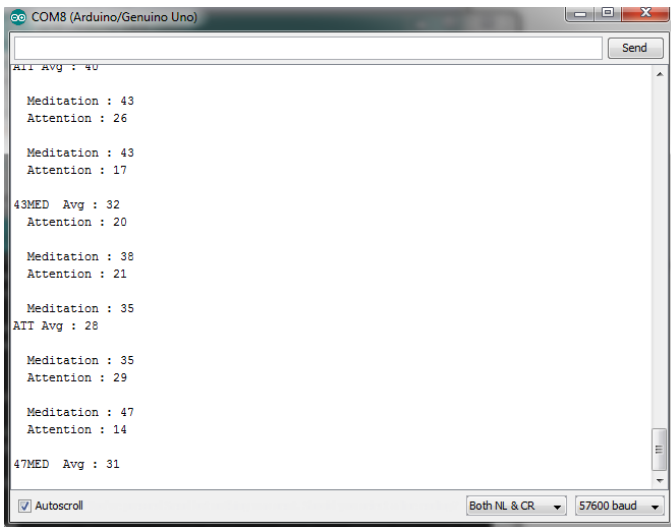


Fig. 7. Serial Monitor Output

Of the 5 subjects used in this exploration, average values of attention and meditation were recorded against each activity. A graph of the brain activity for 1 minute was plotted to show the variations of the attention values and is given in Fig. 7 below:

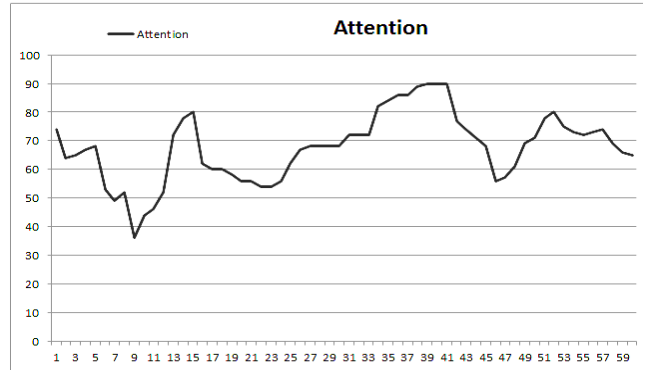


Fig. 8 . 60 seconds Attention Value Variation Test Plot

Table 2 shows the results of one subject after listening to various kinds of music with varying frequencies. The music was played whilst the attention and meditation levels were being recorded and shown on output on serial monitor in real time. The average value was computed for the period which the subject was listening to the music.

TABLE 2. Impact of music on brain waves

Music Type	Attention (%) Average value	Meditation (%) Average value
Rock	82	32
Soul	59	27
Jazz	67	23
Violin	57	34
Funky	29	17

Table 3 shows the results of one subject when reading one paragraph, one page, more than one page, reading an interesting story and reading a sad story.

TABLE 3: Impact of music on brain waves

Reading section	Attention (%) (Average value)	Meditation (%) (Average value)
Paragraph	41	46
Page	69	51
More than 1 page	77	55
Interesting story-page	67	34
Sad story-page	72	17

Table 4 shows the variation of attention and meditation when the subject was at first just closing the eyes for 2 minutes,

when the subject feels sleepy and drowsy (“sleepy state”) and when the subject is in deep sleep.

TABLE 4: Impact of music on brain waves

Sleep State	Attention (%) Average value	Meditation (%)
Eye closing for more 2 minutes	32	46
Drowsiness	23	45
Deep sleep	12	34

VI. CONCLUSION AND FUTURE WORK

A. Analysis

A relatively low cost system was implemented to assess the impact of music, sleep and reading on the brain waves focusing mainly on attention and meditation. The signal was successfully acquired from the frontal lobes using the 1 channel EEG electrode. For music assessment it can be concluded that low frequency music like violin and jazz decreases the attention levels of an individual. On the other hand, high frequency music generally increases the attention levels of a human being. As for reading there is a general increase in the attention value as the amount of text being read increases. When the subject was reading a sad story the attention level average value for the 5 subjects was more than the attention level value when one is reading an interesting story. Meditation level average when one is reading increased as the amount of text being read increases. When the subjects closed their eyes the average value of attention was slightly lower than that of meditation indicating low frequency components in both the attention and mediation values. This value of attention and mediation kept on decreasing as the subjects went on to deep sleep.

VII. FUTURE WORK

As future work there is need to do a comparative assessment for the whole EEG spectrum with the possibility of analyzing how different body functions such as muscle movement, emotions, external environment exposure (5 senses) and sickness and injuries affect the human brain.

REFERENCES

- [1] Ed. Joseph D. Bronzino, The Biomedical Engineering Handbook, Second Edition. Boca Raton: CRC Press LLC, 2000. page 253-256.
- [2] Petersen Bjørn, Weed Ethan, Sandmann Pascale, Brattico Elvira, Hansen Mads, Sørensen Stine, Derdau, Vuust Peter. Brain Responses to Musical Feature Changes in Adolescent Cochlear Implant Users. *Frontiers in Human Neuroscience* Volume9,2015. <http://journal.frontiersin.org/article/10.3389/fnhum.2015.00007>. DOI:10.3389/fnhum.2015.00007, ISSN=1662-5161
- [3] Gillian Pocock, Christopher D. Richards, David A. Richards. *Human Physiology, Oxford University Press*, 30139780199574933U. <https://books.google.co.in/books?id=pSxYM5-PrmgCD> 2013 I OUP Oxford
- [4] Särkämö Teppo, Altenmüller Eckart, Rodríguez-Fornells Antoni, Peretz Isabelle. *Music, Brain, and Rehabilitation: Emerging Therapeutic Applications and Potential Neural Mechanisms. Frontiers in Human Neuroscience* Volume10,2016. <http://journal.frontiersin.org/article/10.3389/fnhum.2016.00103>. DOI=10.3389/fnhum.2016.00103, ISSN=1662-5161
- [5] Rangayyan, Rangaraj M. *Biomedical signal analysis*. Vol. 33. John Wiley & Sons, 2015. pages 28-35.
- [6] Kanagasabai Adalarasu, 1Mohan Jagannath and 2Naidu Keerthiga Ramesh. EEG Based Neurophysiological Responses To Music Among Sleep Disorder Patients. *International Journal of Recent Scientific Research* Vol. 3, Issue, 5, pp.360 - 365, May, 2012
- [7] Adalarasu, K., Jagannath, M. and Keerthiga, S. and Geethanjali, B. 2011. A review on influence of music on brain activity using signal processing and imaging system. *International Journal of Engineering Science and Technology*, 3(4): 3276–3282.
- [8] Bringas Maria L., Zaldivar Marilyn, Rojas Pedro A., Martinez-Montes Karelia, Chongo Dora M., Ortega Maria A., Galvizu Reynaldo, Perez Alba E., Morales Lilia M., Maragoto Carlos, Vera Hector, Galan Lidice, Besson Mireille, Valdes-Sosa Pedro A. Effectiveness of music therapy as an aid to neurorestoration of children with severe neurological disorders. *Frontiers in Neuroscience*. Volume 9,2015. URL=<http://journal.frontiersin.org/article/10.3389/fnins.2015.00427>, ISSN=1662-453X
- [9] K.Crowley, A.Sliney, I.Pitt, D.Murphy," Evaluating a Brain-Computer Interface to Categorise Human Emotional Response", IEEE, 2010.
- [10] Boris Gutmann, Andreas Mierau, Thorben Hülsdünker, et al., "Effects of Physical Exercise on Individual Resting State EEG Alpha Peak Frequency," *Neural Plasticity*, vol. 2015, Article ID 717312, 2015. doi:10.1155/2015/717312
- [11] K. R. Scherer, "Which Emotions Can be induced by Music? What Are the Underlying Mechanisms? And How Can We Measure Them?" *Journal of New Music Research*, vol. 33, no. 3, pp. 239–251, Sep. 2004..
- [12] L. A. Schmidt and L. J. Trainor, "Frontal brain electrical activity (EEG) distinguishes valence and intensity of musical emotions," *Cognition & Emotion*, vol. 15, no. 4, pp. 487–500, Jul.2001.[Online]. Available:<http://dx.doi.org/10.1080/02699930126048>
- [13] J. Kim and E. Andr'e, "Emotion recognition based on physiological changes in music listening." *IEEE transactions on pattern analysis and machine intelligence*, vol. 30, no. 12, pp.206783,Dec.2008.[Online]. Available:<http://www.ncbi.nlm.nih.gov/pubmed/18988943>
- [14] Michael Linden, 2 Thomas Habib, and Vesna Radojevic A Controlled Study of the Effects of EEG Biofeedback on Cognition and Behavior of Children with Attention Deficit Disorder and

- Learning Disabilities, Biofeedback and Self-Regulation, Vol. 21, No. 1, 1996
- [15] N Mandeep Singh, Mahak Narang Department of Electrical & Instrumentation Engineering, Thapar University, Patiala, INDIA, Changes in Brain wave rhythms during tasks involving Attention and Working memory, IJITKMI Volume 7 • Number 2 • Jan– June 2014 pp. 71-97 (ISSN 0973-4414)
- [16] Nithiya Amirtham .S*, Dr.K. Saraladevi, Analysis of Attention Factors and EEG Brain Waves of Attention Deficit and Hyperactivity Disorder (ADHD) - A Case Study Report , IJSRP, Volume 3, Issue 3, March 2013 Edition [ISSN 2250 3153]
- [17] Balgemann, Claire Evelyn, "Effects of Acute Exercise, Mindfulness Meditation, and Mindfulness Meditation Neurofeedback on Stroop Performance" (2015).Master's Theses. Paper 4621
- [18] K. Suresh Manic1,*, Aminath Saadha1, K. Pirapaharan2, Aravind C.V, Characterisation And Separation Of Brainwave Signals, Journal of Engineering Science and Technology EURECA 2014 Special Issue January (2015) 32 – 44 © School of Engineering, Taylor's University
- [19] MindSet Communications Protocol June 28, 2010 Step-By Step Guide to Parsing a Packet June 28, 2010 | © 2009-2010
- [20] Chow, Theodore, "Mindfulness Meditation versus EEG-Alpha Neurofeedback: The Role of EEG-Alpha Enhancement in Attentional Control" (2014). Electronic Thesis and Dissertation Repository. Paper 2302.
- [21] Aftanas, L.I., Goloshekin, S.A. (2003). Changes in cortical activity in altered states of consciousness: the study of meditation by high-resolution EEG. *Human Physiology*, 28, 2, 143-151
- [22] Basar, E., Schurmann, M., Basar-Eroglu, C., Karakas, S. (1997). Alpha oscillations in brain functioning: an integrative theory. *International Journal of Psychophysiology*, 26, 5-29.

AUTHORS

First Munyaradzi C. Rushambwa received a B.Tech. Degree in Electronic Engineering from Harare Institute of Technology, Harare, Zimbabwe in 2015. He is currently pursuing the M. Tech. degree in Biomedical Engineering at Vellore Institute of Technology, 632014 Vellore India. His research interest lies in the development of neuro feedback systems for use in assisting in neurodegenerative diseases. (e-mail: mrushambwa@yahoo.com).

Second Dr.A.Mythili

Asaithambi Mythili is with Vellore Institute of Technology, Department of Sensor and Biomedical Technology, 632014, Tamil Nadu, India. She received a PhD Degree at Madras Institute of Technology, Anna University, Chennai, India. Previously she had completed her Master's degree in Biomedical Instrumentation from the same university. Her current interests are respiratory biomechanics and medical imaging. (e-mail: mythiliasaithambi@gmail.com).

Diagnosis of Epilepsy-A Systematic Review

Vetrikani.R

Department of Electrical and Electronics
Engineering,
East Point College of Engineering and Technology
Bengaluru,India
vetrikani@gmail.com

T. Christy Bobby

Department of Electronics and Communication
Engineering
M S Ramaiah University of Applied Sciences
Bengaluru, India
christy.ec.et@msruas.ac.in

Abstract: Epilepsy is the most common chronic disorder affecting nearly 50 million people worldwide and is associated with periodic loss of consciousness characterized by recurrent seizures with the abnormal electrical activity of the brain. According to Bangalore Urban Rural Neuro-epidemiological Survey (BURNS) approximately 51502 urban and 51055 rural people are affected with epilepsy in Bangalore. The prime requirement for successful predetermination and diagnosis of epilepsy is the selection of optimal treatment to benefit the patients who need extreme care. Recently, most of the research has been initiated to prevent and diagnose the epilepsy. In this paper detection of epilepsy based on both signal and image processing have been reviewed along with the comparison of performance of different feature extraction methods and classifiers. Multi model approaches have also been discussed which improves the specificity of the system reduces fault detection and retrieves more information about disorder in the brain.

Keywords: epilepsy, signal processing, image processing, multimodal tool.

I. INTRODUCTION

Epilepsy is defined as a neurological disorder due to transient occurrence of abnormal neuronal activity in almost any part of the brain [1]. Seizure is the main symptom of epilepsy and is defined as a brief change in the movements, behaviour, feeling or awareness which elongates from few seconds to few minutes. The illness affecting both the hemispheres of a brain is called generalized seizure whereas illness affecting only one hemisphere is called partial seizure. Both these kinds are termed as convulsive seizures and absence seizure is termed as non-convulsive seizure. Among 50 million people affected with epilepsy worldwide, 60% are affected by convulsive seizure and 40% are affected by non-convulsive seizure. The basic cause of continuous seizure is an imbalance between inhibitory and excitatory activities of neuro transmitters arising due to severe head injury, brain infection, genetic disease, stroke, oxygen deprivation, birth trauma, in the temporal lobe. This imbalance will make the person to feel that they are self-conscious and unable to act [2].

Epilepsy existed 3000 years ago but has been realized in the last few hundred years. Presently abundant amount of research is going on in the area of diagnosis, prevention and treatment of epilepsy due to the availability of large number of medical facilities [3].

A few signal and image processing techniques which help in the predetermination and diagnosis of brain disorders are EEG (electroencephalogram), video EEG telemetry, MEG (magneto encephalography), CT (computed tomography), MRI (magnetic resonance imaging), FS MRI (flow sensitive MRI), fMRI (functional MRI), MRA (MRI Angiography), MRS (magnetic resonance spectroscopy), PET (positron emission tomography), SPECT (single photon emission computed tomography) [4].

An EEG can evaluate the electrical activity in the brain. It is a painless procedure which records electrical signals from brain in the form of wavy lines wherein abnormal spikes or patterns can be quickly assessed leading to the identification of seizures or any other brain disorders [6-9]. Video EEG telemetry is a continuous technique performed for a long period of time to provide enough information regarding the source of seizures. MEG measures the magnetic fields generated by nerve cells and can be combined with the information provided by other types of diagnosis treatment.

A CT scan provides X-rays of any parts of the body at different angles which is further fed into the computer to bring the information together. MRI scanner uses magnetic field signals to provide necessary information of the brain, whereas FS MRI is used for combining fMRI images with CSF (cerebrospinal fluid) for surgical removal of tumors. Compared to MRI, fMRI is a faster technique indicating the change in the blood flow in the brain while performing perceptual and cognitive tasks. MRA uses a series of MRI scans to outline the blood vessels and follow the blood flow in the brain. MRS shows the patterns of activity with the help of functions rather than shapes to determine the advancement of the tumor. PET uses a dye having radioactive tracers injected into the vein to determine the grade of tumor whereas SPECT complements the information captured from other scans by providing 3D pictures of the organ. Also many multimodal approaches are carried out for the accurate diagnosis of seizure [4].

In this paper, significant researches have been reviewed that are associated with early detection and diagnosis of epileptic seizures by signal, image and hybridization of both signal and image processing techniques.

II. SYSTEMATIC REVIEW

In either signal or image processing techniques, the datasets are first pre-processed, segmented and then the features are extracted and classified using a suitable classifier to determine the performance parameters like accuracy, specificity, sensitivity, etc.. Feature selection is a process of reducing the set of extracted features, by choosing a subset of relevant features called as feature vectors. Extraction and selection of features are very important in spike classification tasks. These parametric features are used for spike detection through a threshold or by a general classifier. Three categories of features in signal processing system are time domain, frequency domain and time frequency domain. In signal processing techniques, discriminative parameters are collected from the time series signal by feature extraction process. A common approach is to look into the signal data with either spike or correlated events associated with epilepsy. Fourier Transform (FT) and Wavelet Transform (WT) [10]-[12] are the main approaches for wave analysis. FT is based on frequency changes and is suitable for periodic and linear time invariant signals whereas WT decomposes the signal in terms of scale factor and time shift factor of mother wavelet and scaling function. The Daubechies order 4 (Db4) [13]-[14] is the most recurrent wavelet basis used to decompose the raw data. Other feature extraction techniques such as morphological [15]-[16], mimetic [17]-[18], statistical [19] and parametric [20]-[21] are also used.

The image processing methods such as histogram model, transforms, clustering, partial differential equation, multi spectral or multi scale approaches, segment the entire brain image into small imbrications. For the segmented imbrications, various feature extraction techniques such as GLCM (Gray Level Co-occurrence Matrix), SGF (Structured Graph Format), Texture, Shape, GLRLM (Gray Level Run Length Matrix), Local Binary Patterns, histogram are used to extract the feature vectors to differentiate normal and abnormal brain images [22].

A multi class classification technique is required to test the unknown patterns using the information related to known patterns. Various classifiers such as Threshold based classifier, LM (Language Model) classifier, GC (Granular classifiers), SVM (support vector machines) [23], ANN (artificial neural network) [24]-[25], Fuzzy system [26], are used to classify the feature vectors derived from brain images captured using various imaging modalities. The performances of the various methods used for epilepsy analysis are tabulated in table 1.

Around 0.6 to 0.8% of Indian population is affected by seizure, of which 30% were not diagnosed correctly. K-Nearest Neighbour algorithm (KNN) and Linear Discriminate Analysis (LDA) were used to detect the dissipated intuitive feelings of human through EEG signals. The features of basic rhythms in EEG signals were automatically integrated into virtual EEG device by using Gabor transform with the help of basic rhythm frequency band relative intensity ratio (BRIR). Fast Fourier Transform (FFT) algorithm was developed and

recorded from 4 channels filtered using Band Pass Filter. 20 subjects in age group of 22 to 40 years using 64 channels was used to generate a database. This algorithm was useful to differentiate the healthy and unhealthy subjects by frequency repetition between them whereas the frequency variation after the occurrence of first seizure cannot be analysed [27].

Petit mal epilepsy has been demonstrated using 3 spike per second wave discharge method. Along with other existing diagnostic method, it was used as an adjoin method for diagnosis and management of patients with epileptic seizures. In this method the entire cortex has been synchronously triggered to generate enough voltage for the changes in EEG measurement and may lead to fault diagnosis. As temporal sampling was limited and spatial sampling was incomplete, EEG measurements taken may not be sufficient to differentiate the regular and irregular activities of the patients. Diagnostic errors may occur because interictal epileptiform discharge (IED) which was not shown in the short duration of EEG recordings. Around 10% of epileptic seizure patients may not have epileptiform discharges in their EEG measurements [28].

Recurring seizures affects almost 1% of world's population. Discrete Wavelet Transform (DWT) was used to analyse the signal at different frequency bands and statistical features were extracted from the wavelet subbands. To differentiate normal and seizure subjects ANFIS (Adaptive Neuro Fuzzy Inference System) and BPN (Back Propagation Network) algorithms were used. Compared to BPN algorithm, ANFIS algorithm has more specificity, sensitivity and accuracy [29].

EEG signal classification based on machine learning methods and individual emotional states were classified using Bayes classifier. EEG signal of 23 subjects with an average age of 25 to 6 years with an average time of 12 minutes was recorded with 19 electrodes according to 10-20 international system. Total 1902 statistical features were extracted for individual patient with time resolution of 1 sec using 4 levels of decomposition and Mother Wavelet Db4 Shannon's entropy. 5 fold cross validation was performed on the obtained features and class errors are computed for all the subjects. The subject having the least cross validation error was considered for SOM (self-organizing map) visualization. The SOM was trained and trajectory was observed indicating change in person's brain activity over time. The mean accuracy obtained to detect the emotional states using this method is 75%. In this method, the universal features were not selected for classification of all subjects due to inter-individual differences in the signal [30].

MRI image is used to visualize the internal structure and functionality of the brain for identifying the source of epilepsy. Three categories of textural features such as statistical, GLCM and GLRLM were extracted from the MRI data acquired from epileptic patients. Two classifiers SVM with RBF (radial basis function) kernel and fast single shot multiclass proximal SVM (PSVM) were used for classification purpose. The output of these two classifiers was described in terms of error rate and learning time. The average

performance of these models in terms of learning time for PSVM was 1.16 sec whereas for SVM it was 1.37 sec, which indicates that PSVM reduces the complexity without affecting the performance and requires only matrix equation solver [22].

Corpus callosum is a neural fibre connecting the left and right hemispheres of the brain is responsible for communication between the hemispheres, eye movement, maintaining the balance of arousal and attention and tactile localization. Images were taken from oasis dataset and pre-processing was performed using threshold grayscale interval method. Multi-scale segmentation was used to segment the corpus callosum whereby an accuracy of 91.51% and execution time of 0.86 sec was obtained. The considered images were subjected to edge based, k-means clustering, region growing, marker controlled watershed and wavelet db16 segmentation techniques and shape features like callosal

bending angle, mean thickness and callosal length were extracted using watershed transform. Case based reasoning classification model provides better performance with sensitivity 97%, specificity 89% and accuracy 96.7% [32].

In medical imaging, multiple medical images were fused into a new image to improve the information required for diagnosis in terms of visual quality and peak signal to noise ratio (PSNR). Wavelet and curvelet transform were used for image fusion to obtain high resolution image where WT represents linear edges and curvelet transform improves the accuracy of curve localization. CT scan that can visualize dense structures and MRI images that can depict the morphology of soft tissues were fused and compared with individual images of CT and MRI to calculate the performance characteristics. Improvement in PSNR value of

TABLE 1
COMPARISON OF FEATURE EXTRACTION AND CLASSIFICATION METHODS FOR BRAIN DISORDER

Ref No	Signal/Image Analysed	Feature Extraction / Selection Method	Classification Method	Performance Estimation
[10]	EEG Signal	Mexican Hat Wavelet – Normalized Wavelet Power	Threshold	Sensitivity: 70 % Selectivity: 67 %
[11]	EEG Signal	CWT	ANN	Accuracy: 90 %
[12]	EEG Signal	CWT	Threshold	Sensitivity: 84 % Selectivity: 12 %
[13]	EEG Signal	Db4	Adaptive Threshold	Accuracy: 91 %
[14]	EEG Signal	Feature Transformation	MLP ANN	Accuracy: 95 %
[17]	EEG Signal	Mimetic	Adaboost classifier	Accuracy: 90 %
[18]	EEG Signal	Mimetic	ANN	Sensitivity: 95 % Specificity: 76 %
[19]	EEG Signal	Statistical – Linear Discriminant Analysis	Fisher’s Linear Discriminant	Sensitivity: 98 % Selectivity: 96 %
[21]	EEG Signal	Parametric	Parameters fit	Sensitivity: 92 % Selectivity: 84 %
[22]	MRI Image	GLCM, Statistical, GLRLM	PSVM, SVM	Sensitivity: 93 % Specificity: 89 % Accuracy: 96 %
[22]	MRI Image	Texture, GLCM, GLRLM	SVM PSVM	Learning time: 1.37 sec Learning time: 1.16 sec
[24]	EEG Signal	Db4	Bayesian, MLP/FF ANN	Sensitivity: 47 % Specificity: 86 %
[25]	EEG Signal	Morphological	Spatial context, ANN	Accuracy: 95 %
[29]	EEG Signal	DWT	ANFIS, BPN	Accuracy: 85 %
[30]	EEG Signal	MW, Db4, Shannon’s entropy	Bayes Classifier, Machine Learning Methods	Sensitivity: 90 % Specificity: 69 % Accuracy: 75 %
[31]	EEG Signal	Wavelet Scale Selection	ANN	Sensitivity: 83 % Selectivity: 90 %
[32]	Corpus Callosum Image	Callosal length, callosal bending angle, mean thickness	Case based reasoning	Sensitivity: 97 % Specificity: 89 % Accuracy: 97 %
[33]	MRI & CT Fusion	WT	PSNR	MRI PSNR : 14 dB CT PSNR : 23 dB
[33]	MRI & CT Fusion	Curvelet transform	PSNR	MRI PSNR : 15 dB CT PSNR : 25 dB
[35]	MRI & SPECT Fusion	Z score or threshold, mean, standard deviation	3D Gaussian smoothing kernel	Sensitivity: 88 % Specificity: 87 %
[36]	EEG & MRI Fusion	DWT, ROI analysis	SVM with Gaussian kernel	ERP Accuracy: 75 % MRI Accuracy: 90 % Fusion Accuracy: 94 %
[37]	MRI & PET Fusion	Binary indicator variables, vector concatenation and conditional dependence	Single and multi-modality with leave one out cross validation	MRI Accuracy: 53 % PET Accuracy: 51 % VC Accuracy: 39 % CD Accuracy: 52 %

fused image over MRI varies from 12.1 dB to 14.3 dB using wavelet transform and PSNR varies from 12.5 dB to 15.2 dB using curvelet transform. Similarly improvement in PSNR value of fused image over CT varies from 14.6 dB to 22.8 dB using wavelet transform and PSNR varies from 16.5 dB to 24.9 dB using curvelet transform. The curvelet fusion results were better than wavelet fusion results because of higher improvement in the value of PSNR [33].

fMRI is a unique new imaging technique is combined with EEG may provide restricted information with respect to irritative and seizure onset zones. This method combines spatial resolution of MRI with temporal resolution of EEG to improve pre-surgical evaluation. In focal epilepsy, approximately 50% of patients with interictal epileptiform discharges correlated with BOLD (Blood Oxygen Dependent Level) signal and changes were recorded. A group of 6 out of 29 patients had activation on EEG-fMRI underwent surgical resection who were rejected for surgery by frequent IEDs. General linear model (GLM) was used to identify IED related BOLD changes [34].

Subtraction ictal SPECT co-registered to MRI (SISCOM) is used to identify the epileptogenic focus and evaluate patients for surgery. Consistent, reliable and successful analysis of SISCOM data was obtained by a proper selection of z-score or threshold with various values of 1, 1.5, 2 or 2.5. Epileptic patients who underwent temporal or extra-temporal resection from Cleveland clinic epilepsy center were observed and recordings were taken with ictal and interictal SPECT images, pre-operative and post-operative MRI images. Various z-score values were used for interpretation and decision making. The inter ictal image of SPECT was subtracted from ictal image and was smoothed using 3D Gaussian smoothing kernel were transformed into z-score using mean and standard deviation. The mean activation map was co-registered for pre-operative MRI measurements for anatomical localization and then for cortical localization. The SISCOM images were reviewed and the blinded portion was localized with post-operative MRI images, if the final decision taken by the reviewers lies within the surgical resection then the localization decision was considered to be correct. The sensitivity and specificity of various z-scores were observed to vary from 76.5% to 87.8% and 93.8% to 86.6% [35].

Event related potentials (ERP) obtained from different scalp locations of EEG are combined with MRI images for early diagnosis of various brain disorders. Oddball paradigm was used to acquire ERPs whose features reflect physiological changes whereas MRI based features reflect anatomical changes. ERP and MRI images were acquired for normal and abnormal subjects. ERP signals were decomposed into constituent frequency bands using DWT and MRI images were segmented using region of interest (ROI) analysis of density map. Totally 24 features were extracted from 12 brain regions. An ensemble of classifiers was trained to form the "ERP expert" that consists of one classifier for each source. From 5 electrode locations, analysed at 3 different frequency bands with 2 types of stimuli, 30 sources of ERP signals per patient were generated. 30 SVM classifiers with Gaussian

kernel were trained from 30 ERP signals using leave one out (LOO) cross validation method. These 30 classifiers were then combined using weighted majority voting (WMV) to determine the performance of validation data. The average of all individual LOO trials gives the overall classification performance. Similarly, an "MRI expert" was created where another 30 SVM classifiers with Gaussian kernel were trained considering random subset of 18 out of 24 features of MRI data using random subspace method and were combined using MWV. Ensemble of classifiers approach was used to reduce the total error and also to combine heterogeneous data from different sources. Finally two tier LOO cross validation was used for training, validation and testing. The obtained diagnostic performance measures were accuracy 74.70% for ERP, 89.16% for MRI and 93.98% for ERP + MRI fusion, sensitivity 75.51% for ERP, 85.71% for MRI and 93.88% for ERP + MRI fusion [36].

Two multimodal computer aided diagnostic methods such as vector concatenation (VC) for statistical modelling and conditional dependence (CD) to model the clinical decision process were used to improve the diagnostic accuracy by considering data from seizure disorder patients based on their long term video EEG and neuroimaging techniques like MRI, PET. All the patients were grouped based on their clinical studies into temporal lobe epilepsy, focal onset epilepsy, generalized onset epilepsy, unspecified epilepsy and non-epileptic seizures. Few patients were excluded based on inconclusive video EEG recordings who also had activated measurements in MRI and PET imaging techniques. The MRI findings were simplified into binary indicator variables and PET findings were simplified into indicators of hypo or hyper metabolism from real world clinical archives and the data found were then classified by both single and multi-modality classifiers with Leave One out Cross Validation (LOOCV) based on c4.5 decision tree and the performance was compared using permutation tests. Accuracy of single modality classifier for MRI and PET imaging techniques were 53.1% and 51.1% respectively. VC and CD accuracy using the fusion of MRI and PET were observed to be 39.2% and 51.8% [37].

III. CONCLUSION

The existing approaches for the prediction and diagnosis of epilepsy depends mostly either on signal processing or image processing techniques. It has been observed that without using the multimodal tools there is a possibility of fault identification which leads either to false treatment or delayed treatment and may also end up to death. It has been identified that there is an improvement in the accuracy of fused approaches compared to its constituent signal or image. Hence fusion of image and signal helps to retrieve more information about disorder in the brain. Also multimodal approaches improves the specificity of the system and minimize the fault identification with any combinations of EEG or MEG signals with CT, MRI or fMRI images for brain disorders.

REFERENCES

- [1] Suruchi Sharma and Vaishali Dixit, "Epilepsy-A Comprehensive Review", *International Journal of Pharma Research & Review*, Dec 2013.
- [2] L.Orosco, A.G.Correa and E.Laciar, "Review: A Survey of Performance and Techniques for Automatic Epilepsy Detection", *Journal of Medical and Biological Engineering*, vol. 33, issue 6, pp. 526-537, Feb 2013.
- [3] E.Mgiorkins, A.Diamantis, K.Sidiropoulou and C.Panteliadis, "Highlights in the history of epilepsy: the last 200 years", *Epilepsy research and treatment*, vol. 2014, 2014.
- [4] Types of brain scans, [Online]. Available: <http://www.abta.org/brain-tumor-information/diagnosis/types-of-brain-scans.html>.
- [5] Tzallas, Alexandros.T et al., "Automated Epileptic Seizure Detection Methods: A Review Study", *Epilepsy- Histological, Electroencephalographic and Psychological Aspects*, Feb 2012.
- [6] Devarajan.K, Jyostna.E, Jayasri.K and Balasampath.V, "EEG Based Epilepsy Detection and Prediction", *IACSIT International Journal of Engineering and Technology*, vol. 6, no. 3, June 2014.
- [7] M.Z.Parvez and M.Paul, "Prediction and Detection of Epileptic Seizure by Analysing EEG Signals", *Chapter 4*, October 2015.
- [8] De Moraes, F.D. and Callegari, D.A., "Automated Detection of Interictal Spikes in EEG: A Literature Review", March 2014.
- [9] Sharanreddy.M and P.K.Kulkarni, "Review of Significant Research on EEG based Automated Detection of Epilepsy Seizures and Brain Tumor", *International Journal of Scientific & Engineering Research*, vol. 2, issue 8, August 2011.
- [10] M.Latka, Z.Was, A.Kozik and B.J.West, "Wavelet Analysis of Epileptic Spikes", *Physical Review E*, May 2003.
- [11] H.Goelz, R.D.Jones and P.J.Bones, "Wavelet Analysis of Transient Biomedical Signals and its Application to Detection of Epileptiform Activity in the EEG", *Clinical EEG*, Oct 2000.
- [12] G.Calvagno, M.Ermani, R.Rinaldo and F.Sartoretto, "A Multi-resolution Approach to Spike Detection in EEG", *IEEE Int. Conf. Acoust. Speech Signal Process*, 2000.
- [13] K.P.Indiradevi, E.Elias, P.S.Sathidevi, S.D.Nayak and K. Radha krishnan, "A Multi-level Wavelet Approach for Automatic Detection of Epileptic Spikes in the Electroencephalogram", *comput. Biol. Med.*, vol. 38, 2008.
- [14] Y.Kutlu, M.Kuntalp and D.Kuntalp, "Optimizing the performance of an MLP classifier for the automatic detection of epileptic spikes", *Expert Syst. Appl.*, vol. 36, May 2009.
- [15] G.Xu, J.Wang, Q.Zhang and J.Zhu, "An Automatic EEG spike detection algorithm using morphological filter", *IEEE Int. Conf. Autom. Sci. Eng.*, 2006, pp. 170-175.
- [16] J.Gotman, "Quantitative measurements of epileptic spike morphology in the human EEG", *Electroencephalography and clinical neurophysiology*, vol. 48, issue 5, pp. 551-557, May 1980.
- [17] Y.C.Liu, C.C.K.Lin, J.J.Tsai and Y.N.Sun, "Model based spike detection of Epileptic EEG data", *Sensors (Basel)*, vol. 13, Jan 2013.
- [18] C.F.Boos, Fernando.M. de Azevedo, Geovani.R. Scolaro and Maria do carmo, V.P., "Automatic detection of Paroxysms in EEG signals using Morphological Descriptors and Artificial Neural Networks", *Biomedical Engineering Trends in EC and Software*, 2011.
- [19] A.K.Keshri, A.Singh, B.N.Das and R.K.Sinha, "LDA Spike for Recognising Epileptic spikes in EEG", *I.J. Inf. Eng. Electron*, October 2013.
- [20] J.Pardey, S.Roberts and L.Tarassenko, "A review of parametric modelling techniques for EEG analysis", *Med. Eng. Physics*, 1996, vol. 18(1), pp. 2-11.
- [21] N.Acir and C.Guzelis, "Automatic Spike Detection in EEG by a two stage procedure based on support vector machines", *Comput. Biol. Med.*, vol. 34, Oct 2004.
- [22] Sujitha.V, Sivagami.P and Vijaya.M.S, "Predicting Epileptic Seizure from MRI using Fast Single Shot Proximal Support Vector Machine", *IEEE international test conference*, 2011.
- [23] Support vector machines vs artificial neural network, [Online]. Available: <http://www.svms.org/>.
- [24] J.Halford, R.Schalkoff and J.Zhou, "Standardized database development for EEG epileptiform transient detection: EEG net scoring system and machine learning analysis", *J. Neurosci.* vol. 212, issue 2, pp. 308-316, 2013.
- [25] Mohd Zuhair, et al., "Automatic Identification of an Epileptic Spike Pattern in an EEG signals using ANN", *Proceedings of Third international conference on soft computing for problem solving*, 2014, vol. 258, pp. 915-923.
- [27] Meenakshi, R.K.Singh and A.K.Singh, "Frequency Analysis of Healthy & Epileptic Seizure in EEG using Fast Fourier Transform", *International Journal of Engineering Research & General Science*, vol. 2, issue 4, June-July 2014.
- [28] S.J.M.Smith, "EEG in the Diagnosis, Classification and Management of patients with Epilepsy", *J Neurol Neurosurg Psychiatry*, 76(suppl II):ii2-ii7, 2005.
- [29] D.Najumnisna and T.R.Rangaswamy, "Detection & Classification of Epileptic Seizures using Wavelet Feature Extraction & Adaptive Neuro-Fuzzy Inference System", *International Journal of Computational Engineering Research*, vol. 2, issue 3, May-June 2012.
- [30] M.Macas, M.Vavrecka, V.Gerla and L.Lhotska, "Classification of the Emotional states based on the EEG signal processing", *IEEE international technology and applications in biomedicine*, Jan 2010.
- [31] M.Nuh, A.Jazidie and M.A.Muslim, "Automatic detection of epileptic spikes based on wavelet neural network", *Circuits and Systems*, Jan 2003.
- [32] P.T.selvy, V.Palanisamy and S.Elakkiya, "A novel approach for the prediction of epilepsy from 2D medical images using case based reasoning classification model", *WSEAS transactions on computers*, issue 6, vol. 12, June 2013.
- [33] F.E.Ali, I.M.El-Dokany, A.A.Saad and F.E.Abd El-Samie, "Fusion of MR and CT images using the Curvelet Transform", *Progress in electromagnetic research C*, 2008, vol. 3, pp. 215-224.
- [34] Thornton.R et al., "EEG correlated fMRI and post-operative outcome in Focal Epilepsy", *National Society for Epilepsy MRI unit*, 2011.
- [35] C.R.Newey, et al., "optimizing SPECT SISCOM analysis to localize seizure onset zone by using varying z scores", *international league against epilepsy*, epilepsy, vol. 54, issue 5, pp. 793-800, April 2013.
- [36] Patel.T, Polikar.R, Davatzikos.C and Clark.CM, "EEG and MRI data fusion for early diagnosis of Alzheimer's disease", *30th annual international IEEE EMBS conference*, August 2008.
- [37] Kerr.WT., et al., "Multimodal diagnosis of epilepsy using conditional dependence and multiple imputation", *International workshop pattern recognition neuroimaging*, June 2014.

A Review on Systemic Approach of the Ultra Sound Image to Detect Renal Calculi Using Different Analysis Techniques

V.Velmurugan¹,
Assistant Professor, Department of
ECE, Agni College of Technology,
Thalambur,
Chennai-600130

M.Arunkumar²
Assistant Professor, Department of
ECE, Agni College of Technology,
Thalambur,
Chennai-600130

P.Gnanasivam*
Professor & Head, Department of
ECE, Agni College of Technology,
Thalambur,
Chennai-600130
ecehod@act.edu.in

Abstract - This paper proposes to develop the image segmentation method by appraising the various image analysis techniques. The effective method had been examined and degree of justification was carried out in various clinical concerns. Currently, we scrutinize a classification of methodology in terms of previous data. New ideas had been obtained from additional papers and demonstrated about clinical efficiency or potential specific to the ultrasound segmentation of the renal calculi.

Keywords: *Ultrasound image, Kidney stone, Regional grow, Renal calculi*

I. INTRODUCTION

Ultrasound image segmentation is powerfully assertive by the quality of information and continuous development of computer technology, digital systems, portability and modern medical imaging technology has been utilized widely in clinical applications. It involves X-ray imaging techniques, Computerized Tomography (CT), Magnetic Resonance Imaging (MRI), Ultrasonic Imaging (US), Infrared Thermal Imaging (Thermal Imaging), Endoscope imaging (Endoscope), micrograph imaging (Micrograph), Positron Emission Tomography (PET), Digital Subtraction Angiography (DSA) and so on. An improved image segmentation method based on region growing algorithm was surveyed. Initially, growth rule is determined by the result of automatic scan. Based on the growth rule, a seed point is chosen in the region of kidney. Segmentation results are optimized using image morphology. The basic operations of image morphology are opening and closing of images by Region Growing Algorithm. The figure 1(a) and 1(b) shows normal left and right kidney of ultra sound image.

The first comprehensive review of ultrasound segmentation methodology issues across different clinical applications in terms of preceding modeling was implemented

in this paper. There is large number of papers which describes the general segmentation of ultrasound images without any specific reference to the image formation.

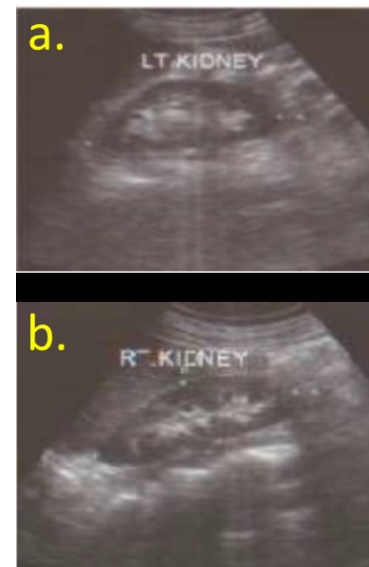


Fig. 1 Ultrascan image of the Kidney. (a) Normal left kidney image. (b) Normal Right Kidney

Abouzar Eslami et.al proposed an electronic access for cyst segmentation in ultrasound image [1-5]. It comprises three steps: ending a seed point in the object abusing the Gibbs random, detecting the boundary based on multi resolution and edge running, shape model features extraction. This approach will help us in fast and less complex to suit ultrasound exploration. Three different errors were assessed in our automated segmentation processes: the Mean of Error (ME), the False Positive (FP), and False Negative (FN).

A Region Indicator with Contour Segmentation (RICS) method was approached by P. R. Tamilselvi et.al. [2, 6-8]. The usage of ANFIS in this method made it more efficient than the previous techniques. And also this proposed method provides accurate detection of renal calculi with less computational time. The performance of RICS method was analyzed and it was seemed to produce less relative error. The RICS segmentation method provided 99.98% accuracy, 95.60% sensitivity and 99.98% specificity value.

S. A. Hojjatol eslami et.al put forth new region growing methods for discovering the boundaries of blobs [3]. A unique feature in this method is, in each step at least a pixel must exhibit the required properties to join the region. To control the growing process, two novelties were used to measure discontinuities: Average contrast and Peripheral contrast. This makes the direction of region growing process more predictable, more reliable and consistent than other method.

Ultra sound is one of the modality choice in kidney image processing was approached by R.Anjit Raja et.al. [4]. US images are used to measure the size and outer shell of the kidney, also to detect kidney stones, congenital anomalies, swelling and blockage of urine flow. More than 200 kidney stone ultrasound images had been tested using this method. They conducted a texture analysis with kidney stone images; the performance of segmentation method was analyzed with less relative error.

Lokesh B.et.al proposed a new approach for Computer Aided Diagnosis (CAD) system with automatic contouring and texture analysis to aid the classification of breast lesions using ultrasound [5]. The precise contour of breast lesions were automatically extracted by a morphological watershed transform in bus images segmentation. These techniques are used in CAD system to support the detection and diagnosis of breast lesion in bus image.

Prema. T Akkasalyar et.al preprocessed ultrasound kidney images using two types of filters: Median filters and Wavelet filter. Segmentation of renal calculi was carried out by Seeded Region Growing algorithm [6]. From the segmentation results, region properties are extracted. The average accuracy of the proposed method for both normal and calculi image are as 95% and 90%. The drawback of the ultrasound imaging has poor quality, presence of speckle noise and disturbance will degrade the quality of images.

Ultrasonography is often more desirable than another medical imaging formations because it is non-invasive, portable, utilization etc. It does not use ionizing radiations and is comparatively low cost. The main intention is to classify the kidney stone with ultrasound scan. For fine resolution 2D B-Mode images, image enhancement algorithm based on filtering and noise reduction procedure was proposed by PSJ Kumar, Indranil Sarkar et.al. [7]. Finally, it can be noted that the proposed algorithm could be adapted without any difficulty for purpose of despeckling of several types of

biomedical images. The disadvantage of ultrasound scan is poor quality, so speckle noise arises.

The proposal of this paper is given: in section 2, ultrasound image segmentation is classified by clinical application as most of the researchers are interested in segmentation for a given clinical problem. Section 3, describes the performance assessment and clinical validation that has been done in these areas up-to-date. Section 4, gives importance to the researchers working on new segmentation algorithm development. Section 5, by listing performance metric. Ultrasound segmentation was concluded in terms of new ideas and validation.

II. RELATED WORK

Texture is a primary feature which presents considerable information for an image. The main aim of image segmentation process is clustering the pixels in the region which is equivalent to individual surface, objects or ordinary parts of objects and to simplify the delegation of an image into something that is more consequential and easier to analyze. For efficient detachment, sharp and fine edge of the segmented portion of the images are developed using MTIS algorithm [8, 9-14].

For early detection of diseases in medical diagnosis, artificial networks are used as an impressive fussy classifier. The main purpose is to diagnose kidney stone by using different neural networks algorithm which have different architecture and distinctive. This helps in early recognition of kidney stone in victim and reduces the analysis time. Finally, we conclude that multilayer perception competent with back propagation is one of the algorithms for kidney stone diagnosis.

Image segmentation by region growing method is robust, fast and very easy to implement, but it suffers from: threshold trouble, sensitivity to noise. Genetic algorithm is used to get over the threshold problem. Genetic algorithm follows three steps to solve a problem: finite chain of chromosomes are formed by coding potential solution, a selective function allowing a good discrimination between chromosomes are found and genetic operators must be defined. The algorithm result provides good performance and threshold problem is eliminated.

The semi-automated segmentation method of US images helps the physician by providing accurate location of abnormal region. SRG technique is widely used for segmentation process and it isn't affected by the speckle noise. The results are correlated with marker based water-shed segmentation and morphological segmentation. It is found that the efficiency of renal calculi is achieved by using SRG technique. The above technique was used in various medical fields.

III.REGIONAL GROW METHOD BLOCK DIAGRAM

A region growing method is used for identifying the renal calculi in ultrasound scan (US). Since US images accommodate noise, it is removed using background removal and filtering.

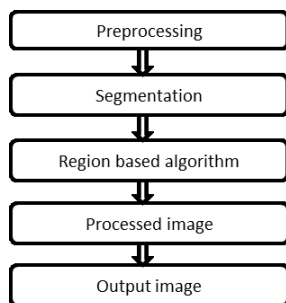


Fig. 2 Processing Block diagram

The regions that have the same properties are separated correctly by region growing method shown in figure 2. This method provides good segmentation in the original images with clear edges. This concept has a simple algorithm. The seed point and the criteria can be determined very easily by us. Various techniques are used for finding bright spots from the image, but all intense spots are not calculi. Calculi are differentiated from shadows by two phases: In first phase, images are scanned line by line and a pixel with higher intensity value is selected as seed point. The pixel values which has the same intensity value of seed are clustered together to form a complete region. This method identifies all the intense spots. The second phase comprehends the calculi from these white spots and analyzes the kidney stones using shadow. The region below the analyzed intense spots is taken as polygon. A 3X3 mask of unit weight is enforced in polygon region. If the value lies between the upper and lower limit of seeded pixels then it is examined as a shadow point. The presence of calculi is identified by connecting all shadow points in the neighborhood was shown in figure 3a and 3b.

Evaluation of texture is based on features like coarseness, smoothness, granulation, randomness, regularity and used for identifying the depth and orientation of renal calculi. There are three major approaches for texture evaluation: 1. Spectral Approach is based on Fourier spectrum. The parameters are used for analyzing the image are peak energy in percentage, laplacian peak, peak angle, peak area, peak distance from origin and angle between two highest peaks. 2. Statistical Approach are used to find the autocorrelation functions, texture edges, structural elements, spatial moments and spatial coordinates.

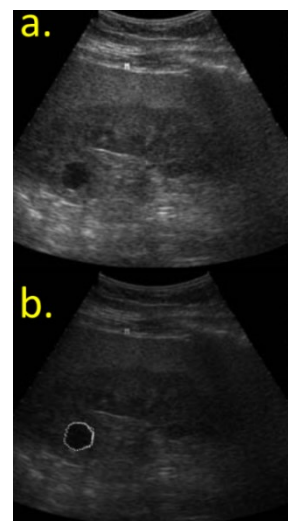


Fig. 3 Segmentation of the Renal calculi (a) before segmentation (b) after segmentation

3. Structural Approach deals with the Primitives (connected pixels are characterized by attributes) and their spatial relationships are taken into consideration to identify renal stones. The shape based segmentation techniques was shown in figure 4.

This develops a multi-scale wavelet based on Bayesian speckle suppression method for ultrasound kidney image. The logarithmic transformation of the original image was evaluated into the multi-scale wavelet domain. The US image remains as a challenge due to speckle noise and various other antiquities.

Ultrasound imaging is non-ionizing, fast, portable, in expensive and capable of real time imaging. A novel speckle suppression method for medical ultrasound images are used to remove speckle noise. The system set up multi-resolution technique to decompose kidney image into several scale by employ the 2D wavelet transform [9]. Since there is no need to align the imaging plane with the anatomical area of interest, evaluation of the surface area can be performed more rapidly.

Advantages of using region growing segmentation method are by using defined properties, the region is separated correctly using region growing method [10, 15-20]. From region growing method [21, 22], we can get clear edges and gives good segmentation results in original images. The concept used in this is, we will first seed a point in image and we will grow the region with same pixels value which is a simple process. The seed point which we want can be determined by us. For selecting the seed point, multiple criteria can be chosen in a single region. Even though there is noise in the image, segmentation method performs well compared with other method.

For adequate speckle suppression and detection of calculi in sonographic kidney images, wavelet based method is developed in applied mathematics image structures. The wavelet based method provides most important content descriptive parameters to identify and classify the kidney stones with ultrasound scan. Fuzzy c means clustering [23-25] is used for unsupervised image segmentation. Kidney stone is detected by using Back Propagation Neural Network (BPNN) and it saves the radiologist time, increases efficiency. The experimental results shows that the proposed algorithm considerably improves the subjective image quality without generating a noticeable artifact, and provide better performance compared with the actual improvement schemes.

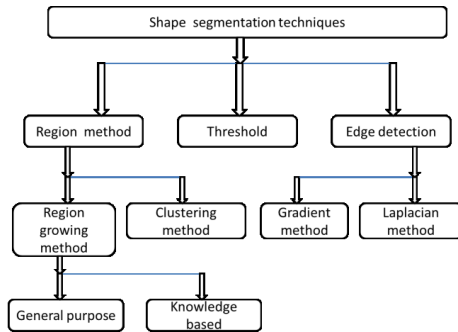


Fig. 4 Major classification of the shape Segmentation techniques

TABLE I. COMPARISON OF THE OTHER METHODS MERITS AND DEMERITS

S.No.	Algorithm Types	Merits	Demerits
1	Watersheds Algorithm	<ul style="list-style-type: none"> Mathematical morphology is used. Helps to improve the capture area. 	Over segmentation
2	Inverse dynamics algorithm	<ul style="list-style-type: none"> Inputs are very good Animation is of high quality Using a nonlinear optimizer 	Many different EMG patterns can produce the same kinematic output.
3	Active contour algorithm	<ul style="list-style-type: none"> Use active contour models Preserves global line shapes perfectly 	Only find gradients to drive the contour. Inaccuracy in image boundaries and image noise.
4	Threshold model Algorithm	<ul style="list-style-type: none"> Try to find edge pixels while dispose of the noise influence. To find the potential edge pixels they use gradient magnitude. 	The detected edges are consisted of discrete pixels and may be inadequate or discontinues. Computationally this algorithm is expensive.
5	Novel edge-based Algorithm	<ul style="list-style-type: none"> Algorithm based on an energy minimization procedure. 	Depends on the deduction the deformation and movement of the tracked object is small between the frames.
6	Pattern recognition Algorithm	<ul style="list-style-type: none"> Pattern recognition fields used to achieve the segmentation. The method used to model relationships between inputs and outputs. 	Restriction on shape parameters. Problematic.
7	Topological alignments algorithm	<ul style="list-style-type: none"> Improve the filtration efficiency. Using linkage clustering. 	Neural networks are Complicated.

IV. K-MEANS ALGORITHM

Earlier for the extraction of sequential properties of US kidney images like registration and segmentation are applied separately. The existing image algorithm are watersheds algorithm [26], Inverse dynamics algorithm [27], Active contour algorithm [28], Generic algorithm [29], Threshold model algorithm [30], Novel edge-based Algorithm, Pattern recognition Algorithm, Topological alignments algorithm, Fuzzy multi scale image, RICS algorithm, IOREWS algorithm, ESRANFIS Algorithm. The comparison of the different algorithms was shown in the Table I, II, III and IV. The average gray level intensity inside the kidney region is determined. K means Algorithm will overcome the problems with 3D models due to moving parts. GFR measurement is done by using voxel deformation which is important parameter in diagnosis. Finally, the diagnosis of renal diseases is expected by using the standard sets of rules are still to be defined. K-means algorithm proposes to cluster the object by grouping them with their nearest mean value. This algorithm splits unspecified data into fixed number of clusters. The center point in the cluster is called as centroid [11, 26].

V. PERFORMANCE COMPARISON OF K-MEANS WITH OTHER METHOD

TABLE II. COMPARISON OF PERFORMANCE METRICS OF ULTRASOUND (US) IMAGE

Kidney Images	Mn	Dn	Vn	En	Ep	Journal	Author	ISSN	year
US image	15.3	6.6	2.3	20.1	18.4	Journal of computer science	P.R.Tamilselvi et.al.,	15449-3636	2011
Kidney stone	24.1	10.4	4.1	32.3	25.6				
Early Detection	21.5	8.3	3.2	20.2	23.2				
Early Calculi	22.1	6.1	2.3	20.1	18.4	IOSR-Journal of computer Engineering	A.Irsathahamed et.al.,	2278-0661	2014
Medium calculi	25.3	8.5	4.1	20.1	18.4				
Early Calculi	27.1	11.3	7.3	20.1	18.4				

TABLE III. COMPARISON OF PERFORMANCE METRICS OF COMPUTED TOMOGRAPHY (CT) SCAN IMAGE

Kidney Images	PPV	Sen	DSC	DIST	DEV	Journal	Author	ISSN	year
Min	0.937	0.924	0.95	0	1	IEEE image processing	F.Khalifa et.al.,	9781-4577	2011
Max	0.995	0.952	0.92	3.12	2.12				
Mean	0.984	0.938	0.993	1.25	2.25				
St.Dv	0.038	0.038	0.0199	0.68	1.68				

TABLE IV. COMPARISON OF PERFORMANCE METRICS OF MAGNETIC RESONANCE IMAGE (MRI)

Kidney Images	PPV	Sen	DSC	DIST	DEV	Journal	Author	ISSN	year
Min	0.947	0.934	0.94	2.22	2.42	IEEE Human machine systems	M.Emmanouils kounakis et.al.,	9871-4677	2014
Max	0.985	0.942	0.93	3.12	3.12				
Mean	0.974	0.978	0.993	2.25	2.35				
St.Dv	0.982	0.068	0.99	2.68	2.58				

Note: The comparison of output values among ultra sound image, MRI image and CT scan image. The parameters are Mean pixel rate (Mn), Dispersion pixel rate (Dn), Variance Pixel Rate (Vn), Energy Joules(En),Entropy rate (Ep) for CT images, Positive Predictive Value (PPV), Sensitivity (Sen), Dice Similarity Co-efficient (DSC), Stands for Distance (DIST), Deviation (DEV) of the image.

VI. CONCLUSION

We compared the performance metrics of US images, MRI image and CT image. By using segmentation method, the calculi area in the kidney scan images was identified correctly. It provides feature extraction and high detection certainty. The segmentation accuracy of renal calculi achieved by the region growing method is adequate for using in various medical fields.

ACKNOWLEDGMENT

The work reported in the paper was fully supported by the

grant of BIRAC SRISTI PMU -2016/0082 through the Gandhi young Technical Innovation (GYTI 0082). We are getting scan images from MEDILABS. The authors would like to thank the head of department and our institution.

REFERENCES

- [1] A. Eslami, S. Kasaei and M. Jahed “Radial Multi-scale cyst Segmentation in Ultrasound Image of Kidney”.
- [2] P. R. Tamilselvi and Dr. P. Thangaraj “Segmentation of Calculi from Ultrasound Kidney Image by Region

- Indicator with Contour Segmentation Method”, *Global Journal of Computer Science and Technology*, vol. 11, Issue 22, Version 1.0, December 2011.
- [3] S. A. Hojjatoleslami and J. Kittler “Region Growing: A New Approach”, *IEEE Transaction on Image Processing*, vol. 7, No 7, July 1998.
- [4] R. Anjit Raja and J. Jennifer Ranjini “Segment Based Detection And Quantification of Kidney Stone And Its Symmetric Analysis Using Texture Properties Based On Logical Operators With Ultra Sound Scanning”, *International Journal of Computer Applications*, 2013.
- [5] A. Lokesh and K. Shailaja “Segmentation and Classification of Based Lesions in Ultrasound Images”, *International Journal of Scientific & Technology Research*, Vol. 3, Issue 6, P.No: 238 – 242, June 2014.
- [6] T. Prema Akkasalyar and S. shruti Karakalman “Abnormality Detection in Kidney Ultrasound Imaging”, *International Journal of Engineering and Computer*, Vol. 4, Issue 7, July 2015.
- [7] P. S. J. Kumar and I. Sarkar “Speckle Reduction of Ultrasound Images Using Wavelet Transform”, *International Journal of Computer Engineering and applications*, Vol. 8, Issue II – Part I – December 2014.
- [8] S. Rizwana and Dr. S. Pannirselvam “Massive Regional Texture Extraction for Aerial and Natural Images”, *IOSR Journal of computer engineering*, Vol. 11, Issue 5, PP 40-46, May - June 2013.
- [9] P. S. Anushalin and J. Samson Isaac “Ultrasound Image Analysis of Kidney Stone Using Wavelet Transform”, *International Journal of Bioscience and Engineering*, vol.1, 39-49 August 2014.
- [10] T. Pavlidis and Y. Tay Liow “Integrating region growing and edge detection”, *IEEE trans.*, vol. 12, March 1990.
- [11] Kewal Krishnan and Sukhjit Singh “Colour Image Segmentation Using Improved Region Growing & K-Means Method”. *IOSRJEN*, Vol. 4. May 2014.
- [12] Jie Wu, Skip Poehlman, D. Michael Noseworthy and V. Markad Kamath “Texture feature based automated seeded region growing in abdominal MRI segmentation”, *JBISE*, February 2009.
- [13] P.R. Tamilselvi “Detection of Renal Calculi Using Semi Automated Segmentation Approach”, *International Journal of Engineering and Innovative Technology*, vol. 2, Issue 3, May 2013.
- [14] Saman Ebrahimi and Vladimir Y. Mariano “Image Quality Improved in Kidney Stone Detection of CT Images”, *Journal of Image and Graphics*, vol. 3, NO.1, June 2015.
- [15] R. Nevatia and K. Babu “Linear feature extraction and description *Computer Graphics and Image Processing*”, Vol. 13, 1980.
- [16] R. Saurin Shah, D. Manhar Desai and Lalit Panchal “Identification of Content Descriptive Parameters for Classification of Renal Calculi”, *International Journal of Signal and Image Processing*, Vol.1, No. 4, pp. 255-259, 2010.
- [17] Hafizah, W.M. Supriyanto and E. J. Yunus “Feature Extraction of Kidney ultrasound images based on intensity histogram and Gray Level Co-occurrence Matrix”, *Modelling Symposium (AMS)*, Sixth Asia Publication, pp. 115 - 120, 2012.
- [18] G. M. Nasira and M. Ranjitha “A Combinational Approach For Noise Removing And Smoothing Ultra Sound Kidney Images”, *International Journal Of Computer Engineering & Technology (IJCET)*, Vol. 5, Issue:3, pp:138-147, March 2014.
- [19] Jun Xie, Yifeng Jiang and Hung-tat Tsui “Segmentation of Kidney From Ultrasound Images Based on Texture and Shape Priors”, *IEEE Transactions On Medical Imaging*, Vol. 24, No. 1, pp. 45-56, January 2005.
- [20] P.R. Tamilselvi and P. Thangaraj “Improved Gabor Filter for Extracting Texture in Ultrasound Kidney Image”, vol.4, No.4, April 2010.
- [21] P.R. Tamilselvi and P. Thangaraj “Improved Gabor Filter for Extracting Texture in Ultrasound Kidney Image”, vol.4, No.4, April 2010.
- [22] Ahmad EL Allaoui and M. Barek Nasri “Threshold Optimization by Genetic Algorithm for Segmentation of Medical Image by Region Growing”, *International Journal of Emerging Trends & Technology in computer Science*, vol.1, Issue.2, July-August 2012.
- [23] Y. Frank Shih and Shouxian Cheng “Automatic Seeded Region Growing for Colour Image Segmentation”, *IMAVIS*, May 5, 2005.
- [24] Rubble Birdi and Er. Jyothi Gill “3D Tumor Detection from Kidney Using Ultra sound Images”, *An International Journal of Engineering Science*, Issue 2, vol. 2, December 2014.
- [25] Nikita Derle and Prof. Devidas Dighe “4D Images Analysis and Diagnosis of Kidney Diseases Using DCE-MRI Images”, *International Journal of Innovative Science, Engineering & Technology*, vol. 2, Issue 4, April 2015.
- [26] M. Lawrence Lifshitz and M. Stephen Pfizer “A Multi resolution Hierarchical Approach To Image Segmentation Based on Intensity Extreme”, *IEEE Transaction on Pattern Analysis And Machine Intelligence*, vol. 12, No 6, June 1990.
- [27] Jicksy Susan Jose, R. Siva kami, N. Uma Maheshari and R. Venkatesh “An Efficient Diagnosis of Kidney

- [28] Images Using Association Rules”, International journal of Computer Technology And Electrical Engineering, vol. 2, Issue 2, April 15, 2012.
- [29] V. S. Roshni, G. Raju and RavindraKumar “Texture Gradient From Images For Segmentation”, IJCSC, June 2011.
- [30] Jitendra Malik, Serge Belongie, Jianbo Shi and Thomas Leung. “Textons, Contour And Regions : Cue Integration In Image Segmentation”, IEEE, September 1999.
- [31] Anju Dahiya, R. B. Dubey “Survey of Some Multilevel Thresholding Techniques For Medical Imaging”, IJSER, July 2015.

Proceedings of the

3rd International Conference on Bio Signals, Images and Instrumentation (ICBSII 2017)

Biomedical Engineering is a field of study that integrates two dynamic professions, Medicine and Engineering. It has recently established itself as an independent field with the objective of assisting medicine towards the betterment of society, through research.

Being an interdisciplinary science, it has associations with various other subjects such as Electrical Engineering, Mechanical Engineering, Chemical Engineering and Biotechnology. The spectrum of Bio-medical research aims to unite these disciplines in synergy, leading to new possibilities thus enabling the development of technology that could save lives.

The 3rd International Conference on Bio Signals, Images and Instrumentation (ICBSII-2017) was conceived with the thought of bringing together scientists, engineers and researchers from various domains all over the world. It has been a platform where some of the greatest minds of the country and abroad could interact, exchange ideas and work together towards a common goal.

Research papers were received from diverse areas such as Physiological Modeling, Medical Imaging, Medical Robotics, Biomechanics, Biomedical Instrumentation and Nano-materials amounting to a total of 62 papers. After a rigorous review process by an expert review committee, 42 papers that displayed quality in idea and work were selected for final presentation at the conference, of which 34 papers are scheduled for the presentation session.

This conference is the fruit of a vision of the Management, faculty and students of the Department of Biomedical Engineering, SSN College of Engineering in association with the Centre for Healthcare Technologies (CHT), a multi-disciplinary R&D centre, who worked unanimously towards materializing it and were instrumental in its success.

The Department of Biomedical Engineering, since its inception in 2005, has been a pioneer in the field of biomedical technology, instrumentation, and administration. The department has excellent infrastructure, experienced faculty members and motivated students. It also has collaborations with several industries such as L&T Medical System, Texas Instruments, National Instruments, Materialize, Chettinad Hospitals and Sri Ramachandra Medical College. To add feather to the crown, the department has conducted two International conferences (ICBSII) in 2013, 2015 and two national conferences (NCABES) in 2014, 2016.